

ספריות הטכניון *The Technion Libraries*

בית הספר ללימודי מוסמכים ע"ש ארווין וג'ואן ג'ייקובס
Irwin and Joan Jacobs Graduate School

©

All rights reserved to the author

This work, in whole or in part, may not be copied (in any media), printed, translated, stored in a retrieval system, transmitted via the internet or other electronic means, except for "fair use" of brief quotations for academic instruction, criticism, or research purposes only. Commercial use of this material is completely prohibited.

©

כל הזכויות שמורות למחבר/ת

אין להעתיק (במדיה כלשהי), להדפיס, לתרגם, לאחסן במאגר מידע, להפיץ באינטרנט, חיבור זה או כל חלק ממנו, למעט "שימוש הוגן" בקטעים קצרים מן החיבור למטרות לימוד, הוראה, ביקורת או מחקר. שימוש מסחרי בחומר הכלול בחיבור זה אסור בהחלט.

Topological Properties of Quasiperiodic Chains: Structural and Spectral Analysis

Eli Levy

Topological Properties of Quasiperiodic Chains: Structural and Spectral Analysis

Research Thesis

Submitted in partial fulfillment of the requirements
for the degree of Doctor of Philosophy

Eli Levy

Submitted to the Senate
of the Technion — Israel Institute of Technology
Sivan 5776 Haifa June 2016

This research was carried out under the supervision of Prof. Eric Akkermans and Dr. Amnon Fisher, in the Faculty of Physics.

List of Publications

Some results in this thesis have been published as articles by the author and research collaborators in conferences and journals during the course of the author's doctoral research period, the most up-to-date versions of which being:

- [1] E. Akkermans, G. Dunne, and E. Levy. Wave propagation in one dimension: Methods and applications to complex and fractal structures. In Luca Dal Negro, editor, *Optics of Aperiodic Structures: Fundamentals and Device Applications*, chapter 10. Pan Stanford, 2013.
- [2] E. Levy, A. Barak, A. Fisher, and E. Akkermans. Topological properties of Fibonacci quasicrystals: A scattering analysis of Chern numbers. arXiv preprint arXiv:1509.04028, 2015 (submitted to PRL).
- [3] F. Baboux, E. Levy, A. Lemaître, E. Galopin, I. Sagnes, L. Le Gratiet, A. Amo, J. Bloch, and E. Akkermans, (to be submitted to PRL 2016).
- [4] A. Dareau, E. Levy, M. Bosch Aguilera, R. Bouganne, E. Akkermans, F. Gerbier, and J. Beugnon (submitted to Science 2016).

Acknowledgements

My thanks are given to

Eric Akkermans, for an admirable demonstration of a thorough theoretical research and a persistent quest for a significant understanding.

Amnon Fisher, for his optimism and support through the scientific and administrative rough patches.

Shimrit, for being a stable companion and for offering me her uncompromising support, from the beginning of the road as a new partner until now as my wife and the mother of my children Maayan and Gilad.

The generous financial help of the Technion is gratefully acknowledged.

Contents

List of Figures

Abstract	1
Abbreviations and Notations	3
1 Introduction	7
1.1 Context and motivation	7
1.2 Some chronology	9
1.3 How to read this manuscript	11
2 Structural analysis of quasiperiodic chains	13
2.1 Structural generation method	13
2.1.1 The Fibonacci chain - methods for generation	13
2.1.2 Generation methods: Concatenation rule	13
2.1.3 Generation methods: Substitution rules	14
2.1.4 Generation methods: Characteristic function	15
2.1.5 Generation methods: Cut and Project (C&P) method	16
2.1.6 Generation methods: Co-numbering method	17
2.1.7 Substitution rules structures properties	20
2.1.8 Characteristic function (and C&P) quasiperiodic structures properties	22
2.1.9 Structural properties of the Fibonacci chain and other C&P chains	23
2.1.10 Generalization to 1D Aubry-Andre-Harper (AAH) model	25
2.2 The modulation phase ϕ for a finite size Fibonacci chain	25
2.2.1 Structural effect of scanning ϕ on the Fibonacci chain	25
2.2.2 ϕ -driven fractional translation	35
2.2.3 ϕ -driven fractional inversion	36
2.2.4 The ϕ -driven palindromicity cycle	37
2.2.5 Generalization to 1D Aubry-Andre-Harper (AAH) model	41
2.3 Reciprocal space properties	42
2.3.1 Bragg peaks analysis of 1D structures	42
2.3.2 The role of irrationality in reciprocal space	44

2.3.3	Generalization to the Aubry-Andre-Harper model	46
3	Spectral analysis of quasiperiodic chains	49
3.1	Tools and methods: Scattering analysis of 1D structures	49
3.1.1	Background	49
3.1.2	Wave equations	50
3.1.3	Scattering matrix formalism	51
3.1.4	Transfer matrix formalism	54
3.1.5	Scattering and transfer matrix calculations	58
3.1.6	Scattering computer code properties	60
3.1.7	Illustrative Examples of Layered Systems: Free space	61
3.1.8	Illustrative Examples of Layered Systems: Fabry-Perot structure	62
3.1.9	Illustrative Examples of Layered Systems: Periodic structure - photonic crystal	63
3.1.10	Illustrative Examples of Layered Systems: Random structure	67
3.1.11	Illustrative Examples of Layered Systems: Aperiodic structures - "Fractal" Cantor set structure	68
3.1.12	Illustrative Examples of Layered Systems: Aperiodic structures - the Fibonacci quasiperiodic structure	70
3.2	Gap modes in quasiperiodic structures: A Fabry-Perot approach	73
3.2.1	An example: Defect modes in photonic crystal structure	73
3.2.2	A general classification for gap mode producing schemes	75
3.2.3	The artificial palindrome structural scheme	76
3.3	The effective Fabry-Perot model	77
3.3.1	Formulation, and Resonant mode conditions	77
3.3.2	Fabry-Perot cavities with wavelength dependent effective length	79
3.3.3	Spatial symmetry prediction	81
3.3.4	Calculation of gap modes for a hetero-structure	87
3.4	The topological spectrum of substitution chains	90
3.5	Spectral gaps and Bragg peaks	92
3.6	Independent phases of the scattering matrix	93
3.6.1	Two independent phases	93
3.6.2	Scattering analysis of a hetero-structure	95
4	Topological properties of quasiperiodic chains: theory and experiment	97
4.1	Topological invariants: Further introduction	97
4.1.1	topological invariants in physical problems	97
4.1.2	The physics of topological edge states	99
4.1.3	Topological properties of quasicrystals	99
4.2	Topological properties of Fibonacci quasicrystals: A scattering analysis of Chern numbers	100

4.2.1	Preface	101
4.2.2	Semi-quantitative numeric description	102
4.2.3	Quantitative description	110
4.2.4	Generalizations to other C&P slopes and the Aubry-Andre-Harper model (artificial palindrome scattering)	115
4.3	Experimental measurement of Chern numbers using the edge states of Fibonacci polaritonic quasicrystals	115
4.4	Direct measurement of Chern numbers in the diffraction pattern of a Fibonacci chain	119
4.4.1	Optical setup	126
4.4.2	Noise generation	127
4.5	The structural origin of Chern numbers in quasiperiodic chains	128
4.5.1	Diffraction amplitudes for various structural schemes	128
4.5.2	The phase term $\theta_q(\phi)$	129
4.5.3	Generalizations to other C&P slopes and the Aubry-Andre-Harper model (artificial palindrome diffraction)	131
4.5.4	Diffraction peak splitting - an Intuitive explanation	133
4.5.5	Chern numbers - structural origin	135
4.5.6	Generalizations to other C&P slopes and the Aubry-Andre-Harper model (topological map)	140
4.5.7	Derivation of p_l and q_l for a structure of length $N = \mathcal{F}_j$	140
4.6	The importance of keeping $N = \mathcal{F}_j$	142
5	Summary and outlook	145
5.1	The story	145
5.2	Our contribution	147
5.3	Outlook	149
5.3.1	Structural and spectral understanding of aperiodic order.	149
5.3.2	The effective Fabry-Perot model	150
5.3.3	Generalizations	150
5.3.4	What about p ?	150
5.3.5	Is the palindromic cycle necessary?	150
	Hebrew Abstract	i

List of Figures

- 2.1 The first generations of the Fibonacci chain, S_j ; $j = 0, 1, 2, 3, 4, 5, 6$. . . 14
- 2.2 examples of 2D substitution quasiperiodic structures. (a) Rectangular substitution, and (b) Ammann-Beenker tilings generated using non-rectangular substitution .From [Jol13]. 15
- 2.3 The Cut and Project (C&P) method. (a) The “cut”: a \mathbb{Z}^2 -lattice (red circles) is crossed by a line Δ defined by $y = \tau^{-1}x + const$ (magenta) and acceptance window Ω (green double arrow). Only points within Ω are selected. The origin is taken as the intersection point between the lattice and Δ (green ellipse). (b) The “project”: Selected points are projected onto Δ (black lines), and the projections are recorded (black dots). The distribution of nearest projection distances is two valued with uneven occurrence (inset). If the possible distances are termed “A” and “B”, and we record the first 13 letters, we obtain the chain $S_6 = ABAABABAABAAB$. (c) C&P process for the rational slope $2/3$. The line Δ crosses multiple lattice points, thus defining the unit cell of a periodic structure ABAB ABAB ABAB.... (d) C&P process for the Fibonacci slope with a slight change in ϕ , resulting in the structure $AABABAABABAAB \neq S_6$. The origin is still the green ellipse, but the intersection point with the lattice has shifted along Δ . This shows that scanning ϕ is equivalent to an origin shift along S_∞ 18
- 2.4 The co-numbering method (a simple example). The \mathbb{Z}^2 lattice is crossed by the line Δ (solid magenta line) defined by $y = \frac{3}{5}x$. The intersection point is marked by a green circle. The thin blue lines orthogonal to Δ mark the physical boundary of the unit cell, and the dotted magenta line notes the C&P allowance band Ω . The generator g is found as the first nonzero intersection of the line $y = \frac{2}{3}x$, and this lattice point is marked as “1”. A sequential vectorial addition of g labels $p + q = 8$ times maps all $p + q - 1 = 7$ in-band lattice points with a co-numbering index. Alternating black and blue arrows account for the addition of the generator g , the winding around the unit cell boundaries is indicated by the dashed arrows, and the first two points are labeled to illustrate the method. 19

- 2.5 Components of the characteristic function. (a) The behavior of $\cos(2\pi\tau^{-1}x)$ in blue and of $\text{sign}[\cos(2\pi\tau^{-1}x)]$ in red, where $x \in \mathbb{Z}$. The resultant rectangular function in red is balanced between +1 (A) and -1 (B). (b) The behavior of $\cos(2\pi\tau^{-1}x) - \cos(\pi\tau^{-1})$ in blue and of $\text{sign}[\cos(2\pi\tau^{-1}x) - \cos(\pi\tau^{-1})]$ in red, where $x \in \mathbb{Z}$. Due to the positive offset, the resultant rectangular function in red favors +1 (A) over -1 (B). (c) The same functions as in (b), under-sampled such that $x \in \mathbb{N}$ (green diamonds for the full function and black circles for the sign function). The under-sampling makes the discrete structure to sometimes skip one oscillation. The positive offset makes sure that the -1 (B) half-cycle is never skipped (i.e. no BB doublet). The resulting structure is: ABAABABAABAAB which is identical to S_6 (generated through concatenation or substitution). 24
- 2.6 Occurrence of finite Fibonacci segments along S_∞ . (a)-(b) Occurrence of the segments $\vec{F}_8(\phi_F)$ and $\overleftarrow{F}_8(\phi_F)$ in blue and red respectively. These segments regularly occur (but not periodically) along S_∞ . The two segments occur at a constant distance from each other as depicted in (c), showing the difference between the occurrence coordinates of $\vec{F}_8(\phi_F)$ and $\overleftarrow{F}_8(\phi_F)$. (d)-(f) The same plots for $\vec{F}_{34}(\phi_F)$ and $\overleftarrow{F}_{34}(\phi_F)$ 26
- 2.7 (a)-(b) The same as figure 2.6 for a 34 letter long C&P segments with slope $1/\sqrt{5}$. (c)-(d) The same plots for slope π^{-1} 26
- 2.8 (a)-(b) The same as figures 2.6 and 2.7 for a 58 letter long segments of the Thue-Morse Pisot substitution. (c) The same plot for the non-Pisot substitution discussed previously. There are no occurrences of the mirrored segment. 27
- 2.9 A continuous scan of ϕ in the characteristic function for the Fibonacci chain causes the structure to change. Here plotted the counter of these changes for \vec{F}_{89} as a function of ϕ . Inset: a closer look. 28
- 2.10 ϕ -driven phason-flips in the Fibonacci chain $\vec{F}_{13}(\phi)$: the C&P picture. The structure origin is indicated by a green ellipse. (a) The original chain $S_6 = \vec{F}_{13}(\phi_F)$. Orange arrows indicate the location of the first expected flip (for an increase in ϕ equivalent to dragging the "cut" band downwards). (b) The chain $\vec{F}_{13}(\phi_F + \Delta\phi)$ differing from S_6 by a single phason-flip. Orange and green arrows indicate the location of the previous and the next expected flip (for an additional increase in ϕ). (c) The chain $\vec{F}_{13}(\phi_F + 2\Delta\phi)$ differing from S_6 by a two phason-flips, marked with orange and green arrows. (d) Top to bottom, the resultant structures of (a), (b) and (c). The orange brackets indicated the identical phason flips equivalent to the inversion of a single 6-letters segment $BAABAB \leftrightarrow BABAAB$ 29

2.11 An x - ϕ colormap of $\{\vec{F}_N(\phi)\}$, with $N = 89$ for the Fibonacci chain as a function of ϕ . Black slabs stand for “B”, and white slabs stand for “A”.	30
2.12 The same map as in figure 2.11. Red circles indicate the location of the 89 identical phason-flips.	30
2.13 The same map as in figure 2.11 for other C&P slopes. (a) slope is $1/\sqrt{5}$. (b) slope is $2/\pi$	31
2.14 The Fibonacci chain as a function of ϕ . Equivalent translation for the $N = 89$ segments of the infinite chain chosen through scanning of ϕ (by the resultant segment index in $\{\vec{F}_N(\phi)\}$). (a) The equivalent translation for the first occurrence of each segment (in blue dots). (b) The same, for the second occurrence (in green). (c) The same, for the third occurrence (in red). (d). A superposition of (a)-(c). .	31
2.15 Other C&P chains as a function of ϕ . Equivalent translation for the $N = 89$ segments of the infinite chain chosen through scanning of ϕ for C&P slopes $1/\sqrt{5}$, and $1/\pi$. (a) C&P slope of $1/\sqrt{5}$. The equivalent translation for the first occurrence of each segment (in blue dots). (b) The same, for the four first occurrences (in blue, green, red and cyan, respectively). (c)-(d) The same as (a)-(b) for C&P slope of $1/\pi$. .	32
2.16 Equivalent value of ϕ for translations in the $N = 89$ segments of the infinite chain for C&P slopes: (a) τ^{-1} , (b) $1/\sqrt{5}$, and (c) $2/\pi$	33
2.17 The $2D$ map of figure 2.16(a) is a perfect torus. Here it is used as the unit cell of a 3×3 periodic array to show the toroidal properties. . .	33
2.18 The $2D$ map of figure 2.16(b) is a perfect torus along the $\Delta\phi$ direction (y-axis), but not along the x-axis. If we shorten the segment to have $N = 84$, it becomes a torus. Here it is used as the unit cell of a 3×3 periodic array to show the toroidal properties.	34
2.19 The $2D$ map of figure 2.16c is a perfect torus along the $\Delta\phi$ direction (y-axis), but not along the x-axis. If we enlarge the segment to have $N = 354$, it becomes a torus. Here it is used as the unit cell of a 3×3 periodic array to show the toroidal properties.	34
2.20 (a) The spatial correlation between the segment $\vec{F}_{89}(\phi)$, and some target structure such as $\vec{F}_{89}(\phi = \pi)$, as a function of ϕ . (b) the same plot for the C&P slope $1/\sqrt{5}$	35
2.21 (a) The fractional inversion between the segment $\vec{F}_{89}(\phi)$, and some target structures such as $\vec{F}_{89}(\phi = \phi_F)$ in blue, and $\vec{F}_{89}(\phi = \phi_F + 0.4\pi)$ in red as a function of ϕ . The lowest fractional inversion plateaus at the value of $0.236 = 2\tau^{-1} - 1$. (b) the same plot for the C&P slope $1/\sqrt{5}$. 37	37

2.22 Behavior of $\eta(\phi)$ (for $N = 89$). The saturation at $\eta \simeq 0.76$ is specific to Fibonacci through the $[AA]$ doublet occurrence, $2\tau^{-1}-1$. (a) Behavior of $\eta(\phi - \phi_F)$, where the value at $\phi - \phi_F = 0$ represent the deviation from a palindrome for S_{10} (b) The same plot for $\eta(\phi - \phi_{pal})$	39
2.23 Behavior of $\eta(\phi)$ (for $N = 89$) for other C&P slopes. (a) $1/\sqrt{5}$, (b) $2/\pi$, and (c) $10/17$	39
2.24 The Aubry-Andre-Harper structure dependence on ϕ . (a) An $x-\phi$ colormap of $\{\overrightarrow{AAH}_N(\phi)\}$, with $N = 89$ as a function of ϕ . This time the colormap is continuous in the interval $[-1, 1] - \cos(\pi\tau^{-1})$. (b) Behavior of $\eta(\phi - \phi_{pal})$	42
2.25 The Diffraction pattern of a Fibonacci chains (generated by substitution/concatenation) S_{10} (a) and S_{14} (b), in blue solid lines. The spatial frequency axis is normalized as described in chapter 4. Red dotted lines mark possible values for the diffraction peaks k_q predicted by (2.13).	43
2.26 A colormap depicting the diffraction spectrum such as presented in figure 2.25 for multiple values of the C&P slope. The Fibonacci chain slope, τ^{-1} is indicated by a red arrow.	44
2.27 The same colormap as presented in figure 2.26, with inverted axes. The labels $[q, p]$ for several lines are indicated by white arrows.	45
2.28 Top: the diffraction spectrum for the Fibonacci chain S_{14} from figure 2.25. Bottom: A section of the colormap from figure 2.26 around the Fibonacci slope $\tau^{-1} \cong 0.62$ and the corresponding line labels $[q, p]$ as presented in figure 2.27. These labels are now assigned to the diffraction peaks, and corroborate (2.13).	45
2.29 The diagram in figure 2.26 redone for the Aubry-Andre-Harper (AAH) model with the smooth transition parameter β (axes are omitted for clarity - they are identical to those in figure 2.26). Panel (a) is for the true AAH model. Panels (b)-(f) correspond to $\beta = 0.3, 1, 2, 5, 10$ respectively.	47
3.1 The scattering problem. (a) A sketch for the notations of incoming and outgoing waves. (b) The amplitude notations for two possible experiments: incoming waves from the right or from the left.	52
3.2 Setup and wave propagation notations for the dielectric scattering geometry problem. $\{i_L, o_L\} \equiv \{E_L^{(\rightarrow)}, E_L^{(\leftarrow)}\}$ denote the electric field amplitudes of incoming and outgoing waves at the left boundary, respectively. Similarly, $\{i_R, o_R\} \equiv \{E_R^{(\leftarrow)}, E_R^{(\rightarrow)}\}$ are defined outside the right structure boundary.	56
3.3 Setup of notations for the continuity relations at an interface BA or BA (a), and for the free propagation through a slab A or B (b).	57

3.4	The normalized density of modes (left part) and the transmission spectrum (right part), for free space (no scattering structure).	61
3.5	Left panel : the electric field amplitude $k - z$ map for free space. Right panel: a cross section of the map along the entire stack at a single frequency ($L/\lambda = 3$).	62
3.6	The normalized density of modes (left part) and the transmission spectrum (right part), for a Fabry-Perot resonator.	62
3.7	Left panel : the electric field amplitude map for a Fabry-Perot resonator. Right panel: a cross-section of the map along the entire stack at a frequency of an allowed mode ($2L = 6\lambda$) in blue and of a forbidden mode ($2L = 7.5\lambda$) in red.	63
3.8	Periodic Bragg system of 10 unit cells. The band structure is calculated using both the Chebychev polynomials (3.23) and via the transfer matrix numeric approach (3.18). Right part is a close up on the long wavelength band edge mode.	64
3.9	The transmission spectrum for a 40 slab long photonic crystal whose structure is illustrated in the inset.	65
3.10	The transmission spectrum for a 40 slab photonic crystal. The figure on the right shows a close-up on the long wavelength band edge mode.	65
3.11	The normalized density of modes spectrum for a 40 slab photonic crystal. The figure on the right shows a close-up on the long wavelength band edge mode.	65
3.12	The electric field amplitude $k - z$ map for a 40 slab photonic crystal. Spatial boundaries of each slab are indicated by dashed gray lines. Bottom figures are a close-up on the long (bottom left figure) and short (bottom right figure) band edge modes.	66
3.13	The electric field amplitude cross section for the long and short wavelength band edge modes in a 40 slabs photonic crystal. Electric field of the short and long wavelength modes concentrate on different slab types.	66
3.14	The normalized density of modes (left part) and the transmission spectrum (right part), for a weakly disordered structure.	67
3.15	The normalized density of modes (left part) and the transmission spectrum (right part), for a strongly disordered structure.	67
3.16	The electric amplitude map for disordered structures. (a) a weakly disordered structure. (b)-(d) a strongly disordered structure, with increasing close-up view of a resonant mode.	68
3.17	A schematic view of generations 0-5 of a triadic Cantor set.	69
3.18	The normalized DOM (left part) and the transmission spectrum (right part), for the 4th generation triadic Cantor set structure with $n_B = 1.5n_A$	69

3.19 A close-up on the transmission curve (left) and electric field intensity map (right) for a resonant mode in figure 3.18.	70
3.20 The normalized density of modes (left part) and the transmission spectrum (right part), for the Fibonacci chain S_{10}	71
3.21 Transmission spectrum and stack structure for S_9 (a) ,and S_{12} . Structures are illustrated above the spectra. The self similarity of the spectra is evident in the close-up on the middle part of the two spectra. . . .	71
3.22 Self similarity in the counting function (a) The counting function $\mathcal{N}(k)$ for S_{12} . (b) A close-up on the middle part of panel (a). (c) A close-up on the middle part of panel (b).	72
3.23 (a) Density of modes spectrum and stack structure for S_{16} . (b) A numerical of the quantity $\mathcal{N}(\Delta k)$ in (3.27)	72
3.24 The electric field intensity map for the Fibonacci chain S_8 . Left- full spectrum. Other plots: close up zoom on some isolated modes. Spatial localization and spatial self-similarity are apparent.	72
3.25 The normalized density of modes (left part) and the transmission spectrum (right part), for a photonic crystal hosting a single defect. . . .	74
3.26 A close-up on the transmission curve (left part) and the electric field intensity map (right part) for the resonant defect mode in the photonic crystal structure.	74
3.27 (a) A gap mode associated with a defect in a periodic chain (the red line illustrates the gap mode electric intensity envelope). (b) The same as (a) with “closed” boundary. The refractive index of the continuum is smaller than the chain’s, and the dotted red line signifies evanescent decay. (c) The same as (a) with a periodic hetero-structure.	75
3.28 (a) The artificial palindrome for the Fibonacci segment \vec{F}_N , hosting gap modes in the interface indicated by the dotted line. (b) A Fibonacci segment \vec{F}_N bounded from the right with a metallic mirror, hosting gap modes at the edge. (c) A Fibonacci segment \vec{F}_N bounded from the right by a continuum with refractive index smaller than the chain’s, hosting gap modes at the edge. The arithmetic operators symbolizes the fact that the artificial palindrome is a generalized mirror.	76
3.29 The first 5 Fabry-Perot resonant mode (and symmetry) for various mirror schemes. (a) The case with two index mismatch phase conserving mirrors (gray vertical strips represent the mirrors). (b) The case with two metallic phase flipping mirrors (golden diagonal stripes represent the mirrors). (c) The hybrid case with a metallic mirror on one side, and an index mismatch mirror on the other.	80

3.30 A sketch of the same cases as in figure 3.29 explained by replacing metallic mirrors by a phase conserving mirror, retracted by a quarter wavelength, i.e. explained by a frequency dependent cavity length.	80
3.31 Density of modes (in blue) for a 55 letter periodic chain with a central defect (inset). The Effective Fabry-Perot model finds a solution within the spectral gap: $k_2 = 0.5$ fitting the scattering method calculated spectrum.	82
3.32 The Electric field strength of the gap mode presented in figure 3.31 (in blue) on top of the structural detail.	82
3.33 Density of modes (in blue) for a 55 letter periodic chain with a 30 letter long central defect (inset). The Effective Fabry-Perot model finds 9 solutions within the spectral gap $\{k_m\} m = 17, 18, \dots, 25$ fitting the scattering method calculated spectrum.	82
3.34 The Electric field strength of the gap mode presented in figure 3.33 (in blue) on top of the structural detail.	83
3.35 The Fibonacci chain S_9 with a non central single letter defect. (a) Density of modes for the undisturbed structure (in blue) compared to the same structure with single non central defect (in red). The 2 effective Fabry-Perot model intra-gap solutions with $\{k_m\} m = 2, 3$ is in purple circles. (b) The Electric field strength of the defect gap modes $m = 2$ (in red) and $m = 3$ (in blue) on top of the structural detail.	83
3.36 The Fibonacci chain S_9 with a reflective boundary conditions, and in the artificial palindrome scheme. Density of modes for S_9 based artificial palindrome (in blue), for S_9 with a reflective boundary condition (index mismatch $n_{continuum} \ll n_B$) (in dashed green), and for S_9 with a reflective boundary condition (index mismatch $n_{continuum} \gg n_B$) (in dashed red). The effective Fabry-Perot model intra-gap solutions $\{k_m\}$ is in purple circles.	84
3.37 The Electric field intensity profile and spatial symmetry for selected gap modes of the structures of figure 3.36. (a) S_9 based artificial palindrome. (b) The S_9 chain with a reflective boundary condition (index mismatch $n_{continuum} \ll n_B$). (c) The same as (b) for a metallic reflective boundary, $n_{continuum} \gg n_B$	84

3.38	The Fibonacci chain S_9 with a reflective boundary conditions, and in the artificial palindrome scheme with a geometrical cavity length. (a) Density of modes for artificial palindrome with a 48 letter geometrical cavity (in blue), compared to the undisturbed structure (in red). The effective Fabry-Perot model intra-gap solutions $\{k_m\}$ is in purple circles. (b) Density of modes for the chain S_9 with a reflective boundary condition (index mismatch $n_{continuum} \ll n_B$) with a 24 letter stand-off (in blue), compared to the undisturbed structure (in red). The effective Fabry-Perot model intra-gap solutions $\{k_m\}$ is in purple circles. (c) The same as (b) for a metallic reflective boundary, $n_{continuum} \gg n_B$.	85
3.39	The Electric field intensity profile and spatial symmetry for selected gap modes of the structures of figure 3.38. (a) S_9 based artificial palindrome with a 48 letter geometrical cavity. (b) The S_9 chain with a reflective boundary condition (index mismatch $n_{continuum} \ll n_B$) with a 24 letter stand-off. (c) The same as (b) for a metallic reflective boundary, $n_{continuum} \gg n_B$.	86
3.40	$\varphi(\theta_{cav}, \mathfrak{R})$ as calculated from (3.41). The relation $\varphi = -\theta_{cav}$ holds only for perfect reflectance.	90
3.41	The behavior of the phases $\varphi(\theta_{cav}(k), \mathfrak{R})$ and $\theta_{cav}(k)$ as a function of k for the artificial palindrome $\left[\overrightarrow{S}_{10} \overleftarrow{S}_{10} \right]$ with a dielectric contrast of 25%, at different spectral gaps (gap edges are indicated by red bars, and the gap mode frequency is indicated by orange arrows). (a) Gap at $k \approx 1 - \tau^{-1}$ given by (2.13), with $\mathfrak{R} = r ^2 \approx 0.98$. (b) Gap at $k \approx 2\tau^{-1} - 1$, with $ r ^2 \approx 0.25$.	91
3.42	Normalized IDOS for the Fibonacci chain S_{10} , with a dielectric contrast of $(n_{high} - n_{low})/n_{low} = 15\%$. The location of 8 selected gaps using their topological numbers $[p, q]$ are indicated in accordance to (3.45).	92
3.43	A reciprocal space and scattering analysis of the Fibonacci chain S_{10} . The relations between the spatial frequency of observable diffraction peaks (a), and the frequency of the spectral gaps in the transmission spectrum (b), where the contrast is 100%.	93
4.1	A sketch of the topological properties of a sphere (a) and a torus (b)	98
4.2	(a) The scattering setup. A finite chain is inserted in between perfect dielectric media supporting incoming (i_L, i_R) and outgoing waves (o_L, o_R) . Displayed case: $\mathcal{P} \equiv \overrightarrow{F}_N \overleftarrow{F}_N$ (\uparrow indicates the interface) (b) The chain \overrightarrow{F}_N with a reflecting boundary condition (golden bar), is equivalent to the unfolded open structure \mathcal{P} in (a). (c) Complex amplitudes corresponding to a wave incident respectively on the right or left side of the chain.	101

4.3	Colormap: $ \alpha(\phi, k) $ for \vec{F}_N ; $N = 89$. On top: The transmittance spectrum for the structure. On the left: the structural palindromic symmetry cycle.	103
4.4	(a) The colormap of figure 4.3, at k values inside the gap $q = -1$. (b) A cut through the colormap in (a) at mid-gap (blue circles), compared the structural palindromic symmetry cycle (green line).	103
4.5	(a) The colormap of figure 4.3, at k values inside the gap $q = 2$. (b) A cut through the colormap in (a) at mid-gap (blue circles), compared the structural palindromic symmetry cycle (green line).	104
4.6	(a)-(f) The colormap of figure 4.3, at k values inside the gaps $q = 3, 4, 5, 6, 7, 8$, respectively.	105
4.7	In the center: The integrated density of states (IDOS) of \vec{F}_N ; $N = 89$, with gap labels $[p, q]$ using (3.45). On both sides: $\alpha(\phi, k)$, at k values within the gaps $q = \pm 1$ (compared to the palindromic symmetry cycle).	106
4.8	In the center: The integrated density of states (IDOS) of \vec{F}_N ; $N = 89$, with gap labels $[p, q]$ using (3.45). On both sides: $\alpha(\phi, k)$, at k values within the gaps $q = \pm 2$ (compared to the palindromic symmetry cycle).	107
4.9	In the center: The integrated density of states (IDOS) of \vec{F}_N ; $N = 89$, with gap labels $[p, q]$ using (3.45). On both sides: $\alpha(\phi, k)$, at k values within the gaps $q = \pm 3$ (compared to the palindromic symmetry cycle).	107
4.10	$\alpha(\phi, k)$, at $k = 13\tau^{-1} - 8$, labeled by $q = 13$	108
4.11	In the center: The integrated density of states (IDOS) of \vec{F}_N ; $N = 89$, with gap labels $[p, q]$ using (3.45). On both sides: $\vec{\theta}_{\vec{F}}(\phi, k)$, at two different k values within the gaps $q = \pm 1$ (compared to the palindromic symmetry cycle).	108
4.12	$\vec{\theta}_{\vec{F}}(\phi, k)$, at $k/\pi = 25\tau^{-1} - 15$, labeled by $q = 25$	109
4.13	Topological gap modes in the spectrum of the artificial palindrome $\mathcal{P} \equiv \vec{F}_N \overleftarrow{F}_N$; $N = 89$. (a) A semi 3D plot of the density of states as a function of ϕ and k for the structure \vec{F}_N ; $N = 89$. The ϕ -independent gaps with $q = \pm 1, \pm 4$ are marked with dashed red ellipse. (b) The same as (a), for the structure $\mathcal{P} \equiv \vec{F}_N \overleftarrow{F}_N$; $N = 89$. Gap modes and their traverse as a function of ϕ is observable.	109
4.14	Topological gap modes in the spectrum of the artificial palindrome $\mathcal{P} \equiv \vec{F}_N \overleftarrow{F}_N$; $N = 89$. Eight selected gap modes frequencies as a function of ϕ is in colored markers, compared to the transmission spectrum below, and the palindromic symmetry cycle on the left.	110

- 4.15 Topological gap modes in the spectrum of the artificial palindrome $\mathcal{P} \equiv \vec{F}_N \overleftarrow{F}_N$; $N = 89$. (a) The integrated density of states (IDOS) of \vec{F}_N ; $N = 89$, with gap labels $[p, q]$ using (3.45). (b) Eight selected gap modes relative in band frequencies as a function of ϕ is in blue (gap edges are in light green), compared to the palindromic symmetry cycle on top and to the gap Chern number q . Red bars split the ϕ axis to guide the eye in estimating the Harmonic. 111
- 4.16 Topological gap modes in the spectrum of the structure $\vec{F}_N \overleftarrow{F}_N \vec{F}_N$; $N = 89$. The eight selected gap modes (see figure 4.15) relative in band frequencies as a function of ϕ is in blue for the first interface, and magenta for the second (gap edges are in light green), compared to the palindromic symmetry cycle on top and to the gap Chern number q . Red bars split the ϕ axis to guide the eye in estimating the Harmonic. 112
- 4.17 Left to right: a comparison between the colormaps for $\alpha_q(\phi)$, $\theta_{cav}(\phi, k)$, and $\vec{\theta}_{\vec{F}}(\phi, k)$ for the structure $\mathcal{P} \equiv \vec{F}_N \overleftarrow{F}_N$; $N = 89$ within the gap $q = -1$ 113
- 4.18 Topological gap modes in the spectrum of the artificial palindrome $\mathcal{P} \equiv \vec{F}_N \overleftarrow{F}_N$; $N = 89$. (a) Colormap of $\theta_{cav}(\phi, k)$ within the gap $q = -1$. Light green areas correspond to the resonance condition (4.1). (b) Crossover of the gap mode $k_m(\phi)$. Relative spectral location (red) is compared to the resonance condition (4.1) in blue, and to the palindromic symmetry cycle (green). (c)-(d) The same as (a)-(b) for $q = 2$ 113
- 4.19 Contrast dependence of the topological gap modes trajectory as a function of ϕ for the structure $\mathcal{P} \equiv \vec{F}_N \overleftarrow{F}_N$; $N = 89$. (a) The spectral location of gap modes $k_m(\phi)$ as for the $q = -1$ gap with a 15% dielectric contrast and (b) The same as (a) for a 80% dielectric contrast. . . . 114
- 4.20 The effect of a single phason-flip on the scattering chiral phase $\alpha_q(\phi)$, for the structure $\mathcal{P} \equiv \vec{F}_N \overleftarrow{F}_N$; $N = 144$, and $q = -1$. (a) The phason flip counter compared to a properly unwrapped $\alpha_q(\phi)$ as a function of ϕ (inset: a close-up view). (b) The effect of a single phason-flip on the scattering chiral phase $\alpha_q(\phi)$ as a function of its distance from the center for two values of dielectric contrast (15% and 80%) in Linear scale (c) The same as (b) in logarithmic y -scale. 114

- 4.21 (a) Illustration of the C&P method dependence on the phason ϕ . (b) Nominal energy potential corresponding to a laterally modulated 1D cavity. (c) Scanning electron microscopy (SEM) image of a portion of a 1D cavity reproducing the Fibonacci based sequence $\mathcal{P} \equiv \overleftarrow{F}_N \overrightarrow{F}_N$. The letters A and B correspond to two different widths of the cavity. (d) SEM image showing the full view of 3 fabricated Fibonacci structures, corresponding to 3 different values of the phason. Vertical blue arrows indicate the position of phason-flips in the sequences. 116
- 4.22 (a)-(b) Energy-resolved emission from $\mathcal{P}(\phi)$ with $\phi = 0.6\pi$ in real space (a) and in momentum space (b). Edge states are visible in the two lowest energy gaps, characterized by $q = +2$ and $q = -1$. These states are localized at the central interface ($x = 0$). (c) Integrated density of states (IDOS) obtained by wave-vector integration of the spectrum of panel (b). (d) Spatial profile of the edge state of gap $q = +2$ measured in a series of structures of same width $w_A = 3.5m$ of letters A, but various widths w_B of letters B, yielding different contrasts for the Fibonacci potential. 117
- 4.23 Measured energy of the edge states of gaps $q = +2$ and $q = -1$ as a function of the phason ϕ . The energy of the lowest bulk mode is denoted as E_0 , and the solid lines indicate the gap boundaries. 118
- 4.24 Measured energy of the edge states of gaps $q = +2$ and $q = -1$ as a function of the phason ϕ for three values of contrast (determined by w_B). The energy of the lowest bulk mode is denoted as E_0 , and the solid lines indicate the gap boundaries. 119
- 4.25 Measured spatial symmetry of the edge states of gaps $q = +2$ and $q = -1$ as a function of the phason ϕ . The spatial symmetry flips between alternating gap mode traverses. 119
- 4.26 Experimental setup. (a) A sketch of the optical setup. A collimated laser beam at a wavelength of $532nm$ diffracts off a grating programmed on a Digital Mirror Device (DMD). The far-field diffraction pattern is measured on a CCD camera. (b) A sketch of the DMD mirrors. (c) When the grating is structured following a Fibonacci sequence along the horizontal x direction (and uniform along the vertical y direction), we observe diffraction peaks characteristic of the quasi-periodic structure of the chain. 120
- 4.27 Grayscale map: measured diffraction pattern for the structure $\overleftarrow{F}_N \overrightarrow{F}_N$; $N = 89$. Each ϕ value corresponds to a different diffraction experiment. The global pattern, which is almost independent of ϕ , is compared to the transmission of an \overleftarrow{F}_N dielectric structure (above) calculated using scattering analysis of chapter 3. Chern numbers labeling the transmission gaps (and diffraction peaks) through (3.45) are indicated above. 121

- 4.28 Grayscale map: measured diffraction pattern for the structure $\mathcal{P} \equiv \vec{F}_N \overleftarrow{F}_N$; $N = 89$. Each ϕ value corresponds to a different diffraction experiment. The global pattern, showing a dependence on ϕ , is compared to the transmission of an \vec{F}_N dielectric structure (above) calculated using scattering analysis of chapter 3, and to the purely structural palindromic symmetry cycle of chapter 2 (on the right). Chern numbers labeling the transmission gaps (and diffraction peaks) through (3.45) are indicated above. 122
- 4.29 A close-up view on the diffraction pattern of figure 4.28 for peaks labeled with $q = 1, -3$. The oscillatory behavior of the diffraction intensity at the original peak frequency as a function of ϕ is shown. . 123
- 4.30 A close-up view on the diffraction pattern of figure 4.28 for the peak labeled with $q = 2, 4$. The oscillatory behavior of the diffraction intensity at the original peak frequency as a function of ϕ is shown. 123
- 4.31 Grayscale map: measured diffraction pattern for the structure $\vec{F}_N \overleftarrow{F}_N \vec{F}_N$; $N = 89$. Each ϕ value corresponds to a different diffraction experiment. A close-up view for the vertical stripes of Chern numbers $q = -3, 2, -1, 4, -4, 1, -2, 3$ (from left to right). 124
- 4.32 Grayscale map: measured 2D diffraction pattern (in a single measurement) for $\{\vec{F}_N(\phi)\}$; $N = 89$. The axes are calibrated to directly display the diffraction pattern as a function of k_x and $k_y = k_\phi$. We observe peaks at the k_x values obeying (2.13) but shifted along the vertical axis to $k_\phi = q \times 2\pi/aN$. The asymmetry between the intensity of the diffraction peaks for positive and negative k_ϕ values is due to the envelope of the diffracted intensity from the DMD, originates from the form factor of the micromirrors. 125
- 4.33 A close-up view of figure 4.32 126
- 4.34 Colormap: robustness of the topological features against structural disorder. (a) Diffraction pattern of the structure $\mathcal{P} \equiv \vec{F}_N \overleftarrow{F}_N$ at $\phi = 0$ for different levels of noise μ . Each value of μ corresponds to a different diffraction experiment. The three white dotted lines correspond to three specific values of μ , namely $\mu = 0.73, 0.83, 0.93$ chosen as examples. (b)-(d) Evolution of the diffraction pattern when varying ϕ for three different noise levels, respectively. Note that only the $[0, \pi]$ interval of the period of ϕ is scanned. 127
- 4.35 A numerical plot of the phase $\theta_q(\phi)$ of the diffraction amplitude $A_q^{\vec{F}_N}(\phi)$, as a function of ϕ for the structures \vec{F}_N (in blue) and \overleftarrow{F}_N (in red) and for the diffraction peaks k_q for various q values. (a)-(b) $q = \pm 1$, respectively. (c)-(d) $q = \pm 2$, respectively. (e)-(f) $q = \pm 3$, respectively. (g)-(h) $q = \pm 4$, respectively. 130

4.36 Colormap: $ \gamma(\phi, k) $ for \vec{F}_N ; $N = 89$. Completely analogous to $ \alpha(\phi, k) $ of figure 4.3, including the complete synchronization with the diffraction peaks in the k -axis, and to the structural palindromic symmetry cycle on the ϕ -axis.	131
4.37 (a) Colormap: $ \gamma(\phi, k) $ for a C&P structure with $N = 89$ and a slope $5^{-1/2}$ (with k and ϕ axes as before). Regions with a regular behavior of $ \gamma(\phi, k) $ with integer windings, correlated to the palindromic symmetry cycle are easily observable. (b) Grayscale map: calculated diffraction pattern for two structure the artificial palindrome based on the structure describes in (a). Each ϕ value corresponds to a different diffraction spectrum. The global pattern, showing an integer winding in agreement with (a). Blue line indicates the ϕ value where no diffraction split exists.	132
4.38 Colormap: calculated diffraction pattern for an artificial palindrome based on the Aubry-Andre-Harper (AAH) structure with $N = 89$ and a slope τ^{-1} (with k and ϕ axes as before). (a) Pure AAH structure (b) A modified AAH with $\beta = 3$. The global pattern appears to be a limited version of the Fibonacci case (and the limitation is a function of β).	133
4.39 (a) Calculated diffraction pattern (in blue) for an undisturbed periodic structure (given above in a grayscale map). The inset gives a close up view of the single diffraction peak. (b) The same as (a) for a periodic structure with a single slab separation.	134
4.40 (a)-(f) A close up view of the single diffraction peak (in blue) for an increasing amount of separation (shown in the inset). The imbalance of the split is periodic in the amount of separation.	135
4.41 (a) Grayscale map: the periodic grating with a semi-continuously increasing separation. (b) Grayscale map: the calculated diffraction pattern for the structure set given in (a). Each " ϕ " value corresponds to a different diffraction calculation	136
4.42 Structural properties of the 2D set $\{\vec{F}_N(\phi)\}$ for $N = 89$. (a) The structural $x - \phi$ map created through the Cut & Project method forms a tilted 2D crystal with a 2D unit cell indicated by red and blue squares. The fact that $p_l : q_l = 5 : 8$ is easy to deduce. This map is a torus obtained by wrapping the map along both axes, so that the four blue squares coincide. (b) An illustration of the resulting torus.	137

- 4.43 Construction of the torus QBZ_N for $N = \mathcal{F}_{j=10} = 89$ with the corresponding values $p_l = 5$ and $q_l = 8$. The red circles define the corners of the torus QBZ_N which encloses $\mathcal{F}_{10} = 89$ points (lattice coordinates $[m, n]$ are given). The fundamental k_ϕ value, δk_ϕ , corresponding to Chern number equal to 1, is represented by the green circle (along with the lattice coordinates $[m, n]$). This lowest non zero value of k_ϕ in this case is obtained using the predecessor approximant (p_{l-1}, q_{l-1}) in the Farey series. (a) An emulated lattice angled at φ (to set notations). (b) Colormap: the actual 2D Fourier transform of $\{\vec{F}_N(\phi)\}$ for $N = 89$ 138
- 4.44 A properly unwrapped torus QBZ_N for $N = \mathcal{F}_{j=10} = 89$. The red circles define the 4 corners of the torus QBZ_N of figure 4.43. The fundamental k_ϕ value, δk_ϕ , corresponding to Chern number equal to 1, is represented by the green circle. k_ϕ values now come in pairs of equal magnitude and opposite sign. (a) An emulated lattice angled at φ . (b) Colormap: the actual 2D Fourier transform of $\{\vec{F}_N(\phi)\}$ for $N = 89$ 139
- 4.45 (a) The convergence of δk_x in the Fourier transform of $\{\vec{F}_N(\phi)\}$ as a function of structure length (as expressed by the Farey generation describing the reciprocal lattice) to τ^{-1} (represented by the 15th Farey approximant). (b) In black dots the reciprocal lattice of the 15th Farey approximant (representing the true quasiperiodic structure). In red squares the 89 reciprocal lattice points of the 4th Farey approximant. In magenta diamonds the 233 reciprocal lattice points of the 5th Farey approximant. The level of convergence in the k -axis is indicated in the colored arrows in (a) 141
- 4.46 Colormap: topological map for the C&P structure with $N = 89$ and a slope $5^{-1/2}$ (with k and ϕ axes as before). Axes were discarded for clarity 142
- 4.47 Colormap: topological map for the Aubry-Andre-Harper structure with $N = 89$ and a slope τ^{-1} (with k and ϕ axes as before). Axes were discarded for clarity. (a) Pure AAH structure (b) A modified AAH with $\beta = 3$. The global pattern appears to be a limited version of the Fibonacci case (and the limitation is a function of β). 143
- 4.48 Topological gap modes in the spectrum of the artificial palindrome $\mathcal{P} \equiv \vec{F}_N \overleftarrow{F}_N$. Eight selected gap modes relative in band frequency as a function of ϕ is in blue (gap edges are in light green), compared to the palindromic symmetry cycle on top and to the gap Chern number q . Red bars split the ϕ axis to guide the eye in estimating the Harmonic. (a) $N = 93$. (b) $N = 89$ 144

4.49 Topological gap modes in the spectrum of the artificial palindrome $\mathcal{P} \equiv \vec{F}_N \overleftarrow{F}_N$ as predicted by the scattering phase θ_{cav} . The gap with $q = -1$ is investigated for the existence and frequency of gap modes using θ_{cav} (colormaps) and specifically the condition $\theta_{cav} = 0$ (blue lines with circles), and compared to the structural palindromic symmetry cycle (green lines with circles). (a)-(b) $N = 93$. (c)-(d) $N = 93$ 144

Abstract

The topological properties of quasiperiodic chains are revisited. Chern numbers known to label the infinite set of spectral gaps and diffraction peaks for infinite chains, are shown to be related to the underlying structural palindromic symmetry of finite chains. The deviation from this symmetry forms a periodic cycle as a function of a structural degree of freedom ϕ , driven by a series of structural events termed phason-flips. Topological classification of spectral gaps is related to the two independent phases of the scattering matrix: the scattering total phase shift describing the frequency spectrum and the scattering chiral phase carrying topological information in a winding number as a function of ϕ . Conveniently designed edge states of a generalized edge perform a spectral winding (as a function of ϕ) directly related to the Chern numbers, allowing to scan these phases. A full quantitative description of these states by an effective topological Fabry-Perot cavity, and a first experimental measurement of these predictions in a cavity polariton setup are presented for the Fibonacci chain. An identical analysis was carried out in reciprocal space. Topological classification of diffraction peaks is related to a diffraction chiral phase, found to carry the topological information (labeling the diffraction peaks) in a winding number as a function of ϕ . A splitting of diffraction peaks in a generalized edge setup performs a spectral winding (as a function of ϕ) directly related to the Chern numbers and allows to scan this phase. A first experimental observation of this winding and its robustness against disorder, performed in a programmable optical grating setup, is presented for the Fibonacci chain. The purely structural origin of the topological labeling of spectral gap and diffraction peaks is also revisited. A two-dimensional structural map of phason-flips as a function of ϕ in a finite chain is shown to form a perfect torus. This property constitutes an internal periodic boundary conditions with respect to ϕ , and leads to the definition of a quasi-Brillouin zone in reciprocal space. A quantitative formulation for the allowed number of Chern numbers, and the deviation of the spectral gaps/diffraction peaks from the infinite chain values are given. A first experimental observation of the quasi-Brillouin zone is given for the Fibonacci chain, capturing 89 different Chern numbers in a single measurement. A general discussion is presented regarding the role of true quasiperiodicity in the properties predicted and observed, and also regarding the role of the quasiperiodic chain natural lengths. This work has relied on

the Fibonacci quasiperiodic chain as a leading example, but the results presented extend to a very large family of quasiperiodic chains, and expected to be generalizable to higher dimensions.

Abbreviations and Notations

g genus (in geometrical topology), or the co-numbering generator

χ Euler-Poincare characteristic

χ_n a characteristic function element (letter)

σ_H Hall conductance

\mathcal{C} Chern number

$\#D$ #-dimensional

\mathcal{F}_j the j th generation Fibonacci length (Fibonacci number)

S_j the j th generation Fibonacci chain

k an integer or outside wave-number (in the scattering of waves), or the spatial frequency (in the Fourier transform or diffraction pattern), or an integer

k_x spatial frequency (in the Fourier transform or diffraction pattern) along the x direction

k_ϕ spatial frequency (in the Fourier transform or diffraction pattern) along the ϕ direction

k_q spatial frequency (in the Fourier transform or diffraction pattern) of a diffraction peak labeled by the integer q

k_m gap mode frequency

τ the golden mean $\frac{1+\sqrt{5}}{2} \cong 1.618$

p an integer

q an integer

m an integer

n an integer or refractive index

j generation number, or slab number along a chain

\mathcal{N} counting function (integrated density of states)

$\xi(\mathcal{A})$ a substitution rule for a letter out of an alphabet.

ϕ the modulation strength a.k.a. the phason

ϕ_0 a general origin preset for ϕ

ϕ_F a specific origin preset to obtain S_j

ϕ_{pal} a specific origin preset to obtain a palindromic segment

\vec{F}_N a segment of length N of the infinite Fibonacci chain. A function of ϕ .

\overleftarrow{F}_N the mirror image of \vec{F}_N

$\mathcal{M}_\#$ the occurrence matrix for the $\#$ th super-letter

$V_\#$ occurrence vectors. Eigenvectors of $\mathcal{M}_\#$

x location along the quasiperiodicity direction.

C&P cut and project.

AAH Aubry-Andre-Harper.

IDOS integrated density of states.

$\eta(\phi)$ deviation (or violation) of palindromic symmetry.

β AAH smoothing parameter.

S the scattering matrix

$o_{L(R)}$ outgoing wave from the boundary $L(R)$.

$i_{L(R)}$ incoming wave from the boundary $L(R)$.

t transmitted complex amplitude.

θ_t transmitted amplitude phase.

\vec{r} reflected complex amplitude for incoming waves from the left

\overleftarrow{r} reflected complex amplitude for incoming waves from the right.

$\vec{\theta}$ reflected amplitude phase for incoming waves from the left

$\overleftarrow{\theta}$ reflected amplitude phase for incoming waves from the right.

ρ density of states.

$\delta(k)$ scattering total phase shift.

M transfer matrix.

E electric field.

z location along the quasiperiodicity direction.

n_A refractive index for slab A.

n_B refractive index for slab B.

d_A slab thickness for slab A.

d_B slab thickness for slab B.

λ wavelength.

a scaling parameter.

b scaling parameter.

\mathbb{F} a general periodic function of period 1.

\mathcal{P} artificial palindrome.

L geometric cavity length.

\mathcal{L} effective cavity length.

θ_{cav} cavity phase.

\mathfrak{R} mutual reflectance.

α scattering chiral phase.

\mathcal{W} winding number.

γ diffraction chiral phase.

Chapter 1

Introduction

1.1 Context and motivation

The investigation of topological features has long been recognized to be a powerful tool both in mathematics and (more recently) in physics where it generalizes the notion of symmetry classes. Topology allows to identify distinct families or classes of structures which cannot be related by continuous deformations and which can be characterized by one or a set of integer numbers, called topological invariants due to their stability against a broad range of perturbations. This classification into topological classes has revealed particularly productive in mathematics. A well-known example from geometry is the Gauss classification of surfaces in three-dimensional space by their genus g (or integer Euler-Poincaré characteristics $\chi = 2 - 2g$), roughly equivalent to the number of holes piercing them (e.g. a torus, with $\chi = 0$, cannot be continuously deformed into a sphere, where $\chi = 2$, and so on). An early physical example where topological features became particularly fascinating is provided by quantum anomalies in field theory, i.e. to classical symmetries broken at the quantum level [GJ72], such as the chiral anomaly recently observed in condensed matter [XKL+15]. The resulting anomalous currents were shown to be generically related to topological quantities expressed by modern and sophisticated mathematical tools such as the Atiyah-Singer index theorem or Chern classes [AS84]. The relevance of topological descriptions in condensed matter physics became widely understood in the context of the integer quantum Hall effect, where the Hall conductance σ_H of two-dimensional semi-conductors in a strong magnetic field is quantized in integer multiples of a fundamental conductance σ_0 [KDP80]. The quantized behavior has been linked to the topological properties of the filled electronic bands in the presence of the applied magnetic field, characterized by a so-called Chern number \mathcal{C} such that the allowed conductance values are $\sigma_H = \mathcal{C}\sigma_0$ [TKNdN82, AOS03]. Chern numbers and other topological invariants are now recognized to be ubiquitous in many other systems, such as quantum anomalies [NN83], the classification of topological defects [Mer79], topological insulators and superconductors [HK10], band structures

with Dirac [CGP⁺09] or Weyl points [LWY⁺15, XBA⁺15], and also for quasicrystals.

Among the large variety of complex non-periodic structures, quasiperiodic distributions play a special role. These structures have some of their physical properties (e.g. dielectric coefficient, potential, reflectivity, ...) modulated according to a deterministic but non periodic pattern [Jan94, BG13]. One of the many reasons for the ongoing and continuous interest is that despite their lack of periodicity, quasiperiodic structures exhibit long-range order manifesting in sharp diffraction peaks [SBGC84, SÖ87], and display interesting similarities with random structures, e.g. localization of the modes, insulating behavior, highly structured spectra. Moreover, quasi-periodic 1D structures can be viewed as realizations of quasi-crystalline order and there are interesting candidates to study transport and thus understand the insulating behavior of these structures. A celebrated example in 1D is the Fibonacci chain (denoted as S_∞), i.e. a one-dimensional structure modulated according to the Fibonacci sequence [Fib]. Among the many nontrivial properties of the Fibonacci and other quasiperiodic chains, we may note that the study of wave (acoustic, optical, matter, ...) propagation in these quasiperiodic structures reveals a highly lacunar singular-continuous energy spectrum, with an infinite set of energy gaps arranged in a multifractal hierarchy for infinite chains [KSI87]. Moreover, quasicrystals and tiling spaces have long been recognized (by mathematical physicists) as being a natural playground for topological features including the existence of topological invariants [Shu79, Sim82]. These features were elaborately studied in 1D (where structural and transport properties are better known) [Bel82, Kun86, Bel92]. For instance, in the 1D case, the infinite set of spectral gaps corresponds to an infinite set of Bragg peaks in the diffraction spectrum of a Fibonacci quasicrystal. Each gap/peak is centered at a location $k_q = p + q/\tau$ in appropriate units. Here q and $p(q)$ are integers and $\tau \equiv (1 + \sqrt{5})/2$ is the golden mean. The integers q and $p(q)$, labeling of the infinite set of spectral gaps (Bragg peaks) are proven to be topological Chern numbers through another important approach. The gap labeling theorem [Bel82, Bel92] labels the normalized integrated density of states of the chain, $\mathcal{N}(\epsilon)$, at the spectral gap energies ($\epsilon = \epsilon_{gap}$) by the very same Chern integer numbers p, q through $N(\epsilon_{gap}) = p + q/\tau$. However, despite a recent interest in the subject [ZFJ99, EAE⁺06, MM12, KLR⁺12, KZ12, Sch13, TGB⁺14, VZL⁺15, BRS16], the underlying symmetry governing the relation of these properties to physical observables has not yet been identified, and a more physical understanding of the existence of Chern numbers in the quasiperiodic structures spectrum without external fields has not been given. This subject has been long considered as tangential by the mainstream topological physics community, or at least still enshrined in mystery.

The current work aims to fill this gap. Firstly we have identified a purely structural origin for the Chern numbers in the Fibonacci chain and have defined a real space torus and a corresponding reciprocal space torus giving these topological invariants their most basic explanation - the winding number around some curved

surface. These findings constitute a proposal for a direct and indirect (through a winding number) measurement of the Chern numbers in the Fibonacci spectrum. Secondly, we have structurally analyzed the Fibonacci potential problem to find an underlying spatial symmetry cycle relevant for a large family of finite structures. This cycle is the mechanism by which the purely structural winding maps into spectral properties, obtained from the response of the structure to incoming waves along the quasiperiodicity direction. Thirdly, we have analyzed the Fibonacci potential example by means of the scattering approach to find that its spectral topological features are related to the two independent phases of the scattering matrix. The first phase is the total phase shift, which describes the frequency spectrum, and encodes the Chern numbers in the gap labels. The second phase, is the (newly defined) chiral phase which is sensitive only to topological features through a winding number. This winding number corresponds to the Chern numbers of the gap labels. In addition, conveniently designed gap modes, sensitive to the chiral phase and equivalent to edge states are proposed to measure spectral properties directly related to the Chern numbers. An effective topological Fabry-Perot cavity model is presented to discuss these modes, shedding light on spatial symmetry issues. This analysis constitutes a proposal for various forms of indirect (through the gap modes winding number or spatial symmetry) measurement of the Chern numbers in the Fibonacci spectrum. An identical analysis have been performed in reciprocal space, obtained from the response of the structure to incoming waves perpendicular to the quasiperiodicity direction. A diffraction chiral phase has been identified, and also a reciprocal space counterpart for the gap mode winding. In addition, a new understanding emerged from the reciprocal space analysis, allowing to obtain all allowed Chern numbers for a finite chain in one diffraction measurement. Finally, we have experimentally measured Chern numbers in the Fibonacci spectrum using two different setups capitalizing on our theoretical predictions. Our main results are general and apply to a large class of quasiperiodic structures. We expect much of these current results to be generalizable to higher dimensional quasiperiodic systems.

1.2 Some chronology

The current work started at 2010 with a very simple idea - we wanted to enter the busy field of random lasers [LBS94, Cao05], which has been debating the subject of lasing mode formation and its correspondence to Anderson localization of light [And58]. We wished to contribute by using deterministic tools and keeping to 1D structure which are easier to analyze and fabricate. This led us to explore fractal and quasiperiodic chains, where the former is spatially fractal while the latter is spectrally fractal. Firstly, these chains possess a multi-gap spectrum with spatially localized prominent band-edge modes which may be considered as a deterministic

counterpart of the random lasing spatially localized modes. Secondly, the theory of Anderson localization prediction for a localization phase transition for $d > 2$, and a crossover to localization due to the finite size of the structure for $d < 2$ is interesting to explore using the non-integer fractal dimension. The methods we've chosen to address this problem were the scattering approach (as a computerizable general tool to understand non-periodic problem) [ADL13], and a rather low-budget experimental technique for fabricating organic dielectric multilayer structures (spin coating) and doping some layers with active material (organic dyes or core/clad quantum dots) [KIM+07, YLC+06].

During the process of perfecting the scattering approach computer code, and the building of a spin coating lab including the doping by active material, came a new idea (in 2012). A cavity QED prediction for nontrivial sub-lasing-threshold behavior of modes within the spectrum of a quasiperiodic chain has shifted our attention. For instance, spontaneous emission from a quantum emitter coupled (spectrally and structurally) to a resonant cavity mode occurs at a different rate than in free space quantified by a Purcell factor [GRGH83, GG99, GG01, TS09]. If the regular cavity is replaced by a quasiperiodic one (Fibonacci for example), possessing a fractal spectrum, an anomalous Purcell effect is expected which is a precursor of strong coupling regime due to the (Fibonacci) cavity. The spontaneous emission from within such a cavity is expected to decay following a power law rather than a single exponent with the power being related to the spectral fractal dimension of the Fibonacci spectrum. On top of that power law trend, log-periodic oscillations in emission intensity were expected, being the true fingerprint of fractality [AG13]. The methods remained the same, with an additional tool: the wavelet transform [GV89]. This route encountered some experimental difficulties, as the relevant timescales for the nontrivial phenomena could not be derived *'a priori'* at that stage.

During the ongoing process of perfecting the scattering approach computer code, and the building and testing of the spin coating lab, came another new idea (in 2014). A first experimental quantitative measurement of the Fibonacci spectrum fractality along with a hierarchical labeling of the dense set of spectral gaps related to topological Chern numbers [TGB+14], and a tight binding paper linking topological properties of quasicrystals to the winding of edge states [KZ12, KLR+12] made us realize we have the tools and methods to connect the gap labeling theorem to a winding of edge states. Our choice to consider finite structures with low value of contrast led to a successful analysis, predicting a factor 2 with respect to other outstanding results and relating it to a combination of reflected phase shifts, and also to a Fabry-Perot model [LBFA15] quickly led to a successful first experimental effort to spectrally measure these predictions in a cavity polariton setup through a collaboration [Bab16]. In parallel, a surprising proposal to measure these numbers in the diffraction profile of a Fibonacci Young's slit experiment as a function of ϕ , led to another fruitful collaboration to achieve a purely structural understanding of the

topological properties of quasiperiodic chains, lending more schemes to measure the Chern numbers [Dar16]. This experimental collaboration has proven to be a pivotal point in our understanding, as it was the first incidence of experimental observation driving us towards a better theoretical understanding.

The nature of this work is to connect the knowledge gained by several usually unrelated communities, in a meaningful way, helping all communities to benefit from the progress made in these seemingly tangential fields.

1.3 How to read this manuscript

In a pedagogical effort, the content of roughly 5 papers and one book chapter has been dissected into three technical chapters. As a result, each of these chapters contain some review, a methods section and many new results. Well known results are cited accordingly, and new findings or new notations usually cites our current preprints, or written without citations. Chapter 2 discusses purely structural properties of quasicrystals through the Fibonacci example, in both real and reciprocal space, focusing on the properties leading to the topological properties to be discussed in later chapters. Chapter 3 discusses the spectral properties of quasicrystals through the Fibonacci chain example, e.g. the density of states spectrum probed by the scattering of waves. This chapter also sets the ground for understanding the last technical chapter. Chapter 4 discusses the findings regarding the relations between the topological invariants of the Fibonacci spectrum obtained through the gap labeling theorem, to other, perhaps more natural measurable quantities. These quantities are the winding of scattering phases, and the winding of edge states, the winding of the diffraction pattern intensity and phase, and a full diffraction map of the available Chern numbers. Furthermore, this chapter discusses the origin of the gap labeling theorem topological invariants using purely structural properties of reciprocal space. This chapter contains a detailed theoretical understanding of the topological properties of quasicrystals, and also the results of two experimental realizations to measure these topological properties. Finally, chapter 5 summarizes and gives our prospect to short and long term further research.

Chapter 2

Structural analysis of quasiperiodic chains

In this chapter we review some known methods for generating quasiperiodic chains, and discuss their resultant structural properties. Among these properties we present a new symmetry cycle occurring in a large family of finite quasiperiodic chains, and also a discussion regarding the reciprocal lattice properties. We concentrate, for simplicity, on the Fibonacci chain example, and generalizations are given when possible.

2.1 Structural generation method

In this section we review relevant methods to generate the Fibonacci and other quasiperiodic chains, and discuss their equivalence and differences, attributes and generalizations. In addition we discuss some structural properties of the resultant Fibonacci and other chains, relevant to the current work (presented in Chapters 3 and 4).

2.1.1 The Fibonacci chain - methods for generation

The Fibonacci structure is generated using a two letter alphabet and a building rule which follows the Fibonacci sequence [Fib]. The letters may represent any physical property such as density, dielectric constant, reflectivity, potential and so on. We shall now describe five different building rules which yield the same structure.

2.1.2 Generation methods: Concatenation rule

The j th generation Fibonacci sequence, S_j , is generated from the alphabet $\mathcal{A} = \{A, B\}$, from the initial two generations $S_0 = B$, $S_1 = A$, and the concatenation rule [Jan94]

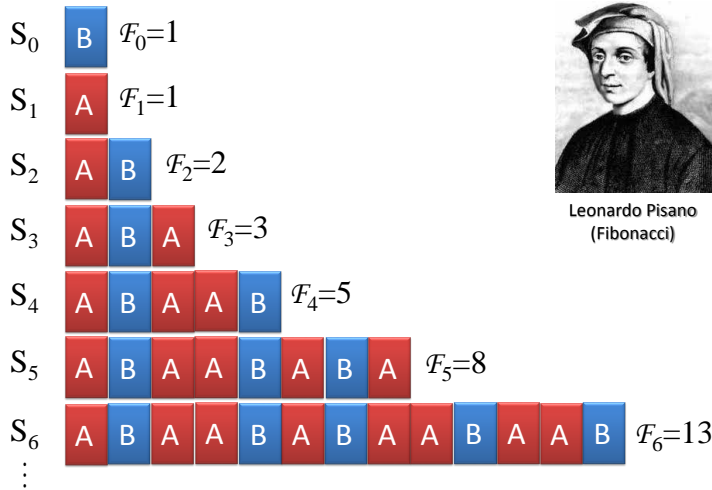


Figure 2.1: The first generations of the Fibonacci chain, S_j ; $j = 0, 1, 2, 3, 4, 5, 6$.

$$S_{j>1} = [S_{j-1}S_{j-2}],$$

where the square brackets symbolizes concatenation. Repetitive implementation of this rule yields the structures

$$A \rightarrow AB \rightarrow ABA \rightarrow ABAAB \rightarrow ABAABABA \rightarrow ABAABABAABAAB \dots, \tag{2.1}$$

where the lengths of the resultant chains, \mathcal{F}_j , are fixed by the same rule, $\mathcal{F}_{j>1} = \mathcal{F}_{j-1} + \mathcal{F}_{j-2}$, and correspond to the Fibonacci numbers

$$\mathcal{F}_j = 1, 1, 2, 3, 5, 8, 13, 21, 34, 55, 89, 144, 233, 377, 610, \dots, \tag{2.2}$$

The resultant structures are also illustrated in figure 2.1. The ratio $\mathcal{F}_{j+1}/\mathcal{F}_j$ tends to the golden mean $\tau = (1 + \sqrt{5})/2$ in the limit $j \rightarrow \infty$. The corresponding sequence S_∞ becomes rigorously quasiperiodic and invariant, i.e., self-similar under this iteration transformation. The concatenation method for building the Fibonacci sequence is very well known, but limited only to Fibonacci like quasiperiodic chains as it is not generalizable.

2.1.3 Generation methods: Substitution rules

A substitution is a rule that replaces letters with words, thus generating highly ordered, self-similar objects which are not necessarily periodic. As a graphic illustration, figure 2.2 depicts a 2D generalization for substitution rules, where 2D letters are replaced by 2D words. In our 1D case, this method considers an alpha-

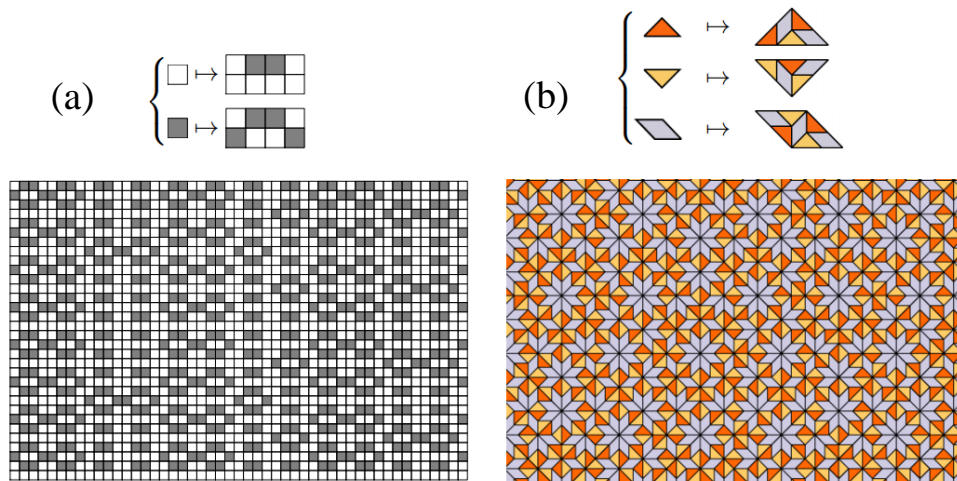


Figure 2.2: examples of 2D substitution quasiperiodic structures. (a) Rectangular substitution, and (b) Ammann-Beenker tilings generated using non-rectangular substitution. From [Jol13].

bet $\mathcal{A} = \{A, B, C, \dots\}$ composed of different letters, and a substitution rule $\xi(\mathcal{A})$ [SS86, Jan94], so that

$$\begin{aligned} \{\xi(\mathcal{A})\} &= \{\xi(A), \xi(B), \xi(C) \dots\} \\ \xi([\mathcal{A}_1 \mathcal{A}_2 \mathcal{A}_3 \dots]) &\equiv [\xi(\mathcal{A}_1) \xi(\mathcal{A}_2) \xi(\mathcal{A}_3) \dots], \end{aligned}$$

where the square brackets again symbolizes concatenation. Now, the j th generation of a structure, W_j , may be generated from an initial generation W_0 (composed of the legitimate alphabet) through $W_j \equiv \xi^j(W_0)$.

Specifically, the j th generation Fibonacci sequence, S_j is generated from the alphabet $\mathcal{A} \equiv \{A, B\}$, from the initial generation $S_0 \equiv B$, and the substitutions $\xi(A) \equiv AB$, $\xi(B) \equiv A$, through $S_j \equiv \xi^j(B)$. This process results in the same structures (see figure 2.1) with the same Fibonacci lengths as in (2.1) and (2.2) [Jan94]. The 1D substitution rules method describes a very large family of quasiperiodic chains, the largest variety compared to the other methods introduced here (see 2.1.7). This generation method is used to establish the gap labeling theorem [Bel82, Bel92] which assigns labels to spectral gaps (to be discussed in chapter 3), and is very relevant to the understanding of the topological properties of quasiperiodic chains (see 2.1.7 and 3.4).

2.1.4 Generation methods: Characteristic function

We define a discrete map χ_n taking, for each letter n , two possible values $\{-1, 1\}$ that we associate to the alphabet $\{B, A\}$ respectively. Among possible choices for such a function [Kes66, OP84, GO90, NLR08], we consider the form recently proposed in

[KLR⁺12],

$$\chi_n(\phi) \equiv \text{sign} [\cos (2\pi n \tau^{-1} + \phi + \phi_0) - \cos (\pi \tau^{-1})]. \quad (2.3)$$

The angular degree of freedom $\phi + \phi_0$ can be safely ignored for S_∞ , but not for any finite segment $\vec{F}_N \equiv [\chi_1 \chi_2 \cdots \chi_N]$ of S_∞ . As we shall see, this is because the phase ϕ represents the translational degree of freedom resulting from the finite size. The finite (concatenation or substitution based) chain S_j can be reproduced by setting $\phi + \phi_0 = \phi_F \equiv \pi \tau^{-1}$, and $N = \mathcal{F}_j$. Alternatively, we may set $\phi_0 = \phi_F$, and consider the modulation phase shift ϕ as a structural degree of freedom to be discussed.

The characteristic function (2.3), and its dependence on the value of the modulation phase ϕ will be shown to be very useful to the understanding of the topological properties of quasiperiodic chains (see 2.2). This generation method describes a large family of periodic and quasiperiodic chains by replacing τ^{-1} by other (rational and irrational) numbers. It is equivalent to the Cut and project method to be discussed in 2.1.5. Moreover, omitting the $\text{sign}[\#]$ function from (2.3) generalizes it to the Aubry-Andre-Harper potential [Har55, AA80]. Recently, a smooth transition between the two models, using a smoothing parameter β , has been proposed [KZ12].

2.1.5 Generation methods: Cut and Project (C&P) method

The Cut and Project (C&P) method has been used to investigate quasicrystals, tilings and dynamical systems [DK85, Jan94, BG13]. As depicted in figure 2.3, a C&P chain is obtained from the \mathbb{Z}^2 -lattice crossed by a line Δ defined (for the Fibonacci case) by $y = \tau^{-1}x + \text{const}$. We denote Δ_\perp the direction perpendicular to Δ and define an acceptance window by the band of width Ω (along Δ_\perp), centered at Δ , and discard all lattice points outside this window. This realizes the "cut" part of the algorithm. Note that this stage is enough to generate the chain: if we connect the C&P set dots using lattice upward and rightward steps, and label them as "B" and "A" respectively. A C&P set is obtained by projecting the remaining \mathbb{Z}^2 points on Δ and along Δ_\perp . If we analyze the distribution of distances along Δ between neighboring projections, we find it to be two valued. One value corresponds to the projection of a step upward, and the other represents the projection of a step rightward. The two possible distances along Δ between neighboring projections, are denoted $\{A, B\}$, and we thus generate S_∞ . We note that as the slope τ^{-1} is an irrational number, the line Δ intersects one and only one lattice point. In general, if a rational slope p/q is chosen, then the line Δ periodically intersects infinite lattice point creating a periodic chain, with a natural definition for the unit cell as the non-periodic segment between intersection points. From this viewpoint we may consider S_∞ as the infinite unit cell of a periodic structure.

For finite chains the situation is different, due to the translational degree of freedom. An origin has to be defined, which in turn determines the letter order. In order to reproduce the finite Fibonacci chain S_j (given by the substitution and

concatenation rules) the structure origin is chosen to be the intersection point of the line Δ with a \mathbb{Z}^2 point, and the number of elements (letters) to be taken is \mathcal{F}_j . Drawing from the two last points, we emphasize that the finite Fibonacci chain S_j may be perfectly reproduced by many rational approximants, p/q , of the irrational slope, τ^{-1} , as long as the number of letters in the unit cell of the resultant periodic chain, $p + q - 1$, remains larger than \mathcal{F}_j . For S_{10} (with $\mathcal{F}_{10} = 89$) this first irrational approximant is $55/89$. The rational approximants for τ^{-1} follow the Farey sequence :

$$\frac{1}{1} : \frac{1}{1} : \frac{1}{2} : \frac{2}{3} : \frac{3}{5} : \frac{5}{8} : \frac{8}{13} : \frac{13}{21} : \frac{21}{34} : \frac{34}{55} : \frac{55}{89} : \dots : \frac{\mathcal{F}_j}{\mathcal{F}_{j+1}} : \dots \quad (2.4)$$

Keeping to the S_{10} example, any successor approximant to $55/89$ will produce S_{10} , while any predecessor will produce a distorted chain (more than one unit cell). We note here that C&P method is equivalent to the characteristic function method through the constant term in the equation for Δ , namely, $y = \tau^{-1}x - \frac{\phi}{2\pi}$, where ϕ is the modulation phase shift in (2.3). Therefore, the C&P method spans the same quasiperiodic chain family as the characteristic function method.

2.1.6 Generation methods: Co-numbering method

The co-numbering method ([VM01] and refs. therein) is very similar to the C&P method, except that it allows for the construction of finite structures only - the unit cell of a periodic approximant. Figure 2.4 depicts the process which, as in the C&P, begins from the \mathbb{Z}^2 -lattice crossed by a line Δ defined (for the Fibonacci case) by $y = \frac{\mathcal{F}_j}{\mathcal{F}_{j+1}}x$ (with an approximant slope and with the origin set to reproduce the concatenation/substitution chain S_j). The mutually prime \mathcal{F}_j and \mathcal{F}_{j+1} (from the Farey sequence) describe a periodic C&P structure with a unit cell containing $\mathcal{F}_j + \mathcal{F}_{j+1}$ lattice points leading to $\mathcal{F}_j + \mathcal{F}_{j+1} - 1$ letters, produced as before by the projection of these in-band letters onto Δ . The co-numbering method defines a spatial generating vector g , connecting the origin (the intersection point the line Δ with a \mathbb{Z}^2 point) to the in-band lattice point with the smallest distance from the line Δ . It has been shown that all the in-band \mathbb{Z}^2 points may be obtained from each other by successive vectorial addition of g (a total of $p + q$ times), and a geometrical winding around the unit cell (see figure 2.4).

The generator g may be found using one of the two the predecessor approximants in (2.4), depending on the parity of j . This may be proven rather easily. Let the zero crossing line Δ be represented by $y = \mathcal{F}_j/\mathcal{F}_{j+1}x$. Let $(x_1, y_1) = (q, p)$, where $q, p \in \mathbb{Z}$ is a general \mathbb{Z}^2 lattice point. The expression for $\delta(q, p)$, the minimal distance of the point (q, p) from the line Δ is

$$\delta(q, p) = \frac{|\mathcal{F}_{j+1}p - \mathcal{F}_jq|}{\sqrt{\mathcal{F}_j^2 + \mathcal{F}_{j+1}^2}},$$

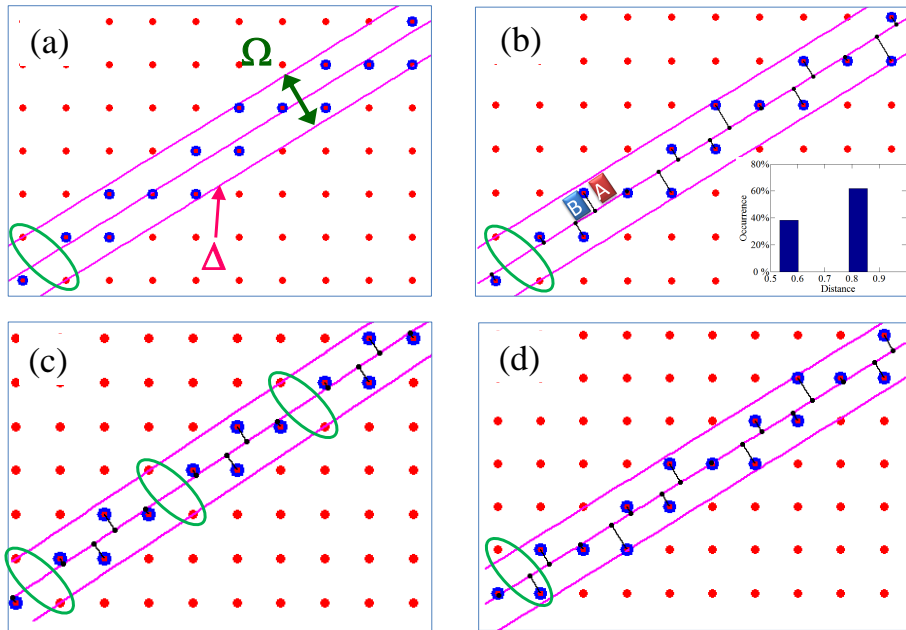


Figure 2.3: The Cut and Project (C&P) method. (a) The “cut”: a \mathbb{Z}^2 -lattice (red circles) is crossed by a line Δ defined by $y = \tau^{-1}x + const$ (magenta) and acceptance window Ω (green double arrow). Only points within Ω are selected. The origin is taken as the intersection point between the lattice and Δ (green ellipse). (b) The “project”: Selected points are projected onto Δ (black lines), and the projections are recorded (black dots). The distribution of nearest projection distances is two valued with uneven occurrence (inset). If the possible distances are termed “A” and “B”, and we record the first 13 letters, we obtain the chain $S_6 = ABAABABAABAAB$. (c) C&P process for the rational slope $2/3$. The line Δ crosses multiple lattice points, thus defining the unit cell of a periodic structure $ABAB ABAB ABAB\dots$. (d) C&P process for the Fibonacci slope with a slight change in ϕ , resulting in the structure $AABABAABABAAB \neq S_6$. The origin is still the green ellipse, but the intersection point with the lattice has shifted along Δ . This shows that scanning ϕ is equivalent to an origin shift along S_∞ .

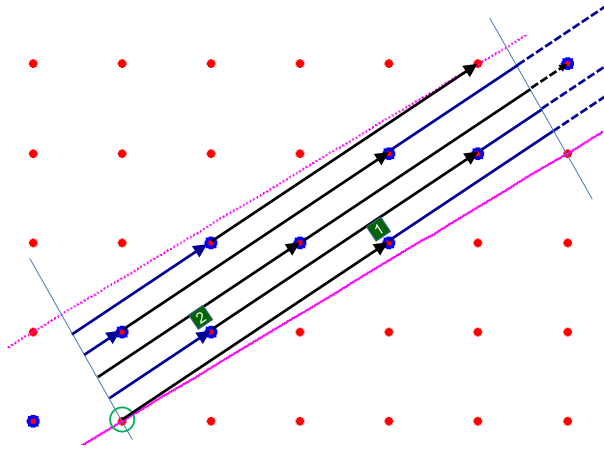


Figure 2.4: The co-numbering method (a simple example). The \mathbb{Z}^2 lattice is crossed by the line Δ (solid magenta line) defined by $y = \frac{3}{5}x$. The intersection point is marked by a green circle. The thin blue lines orthogonal to Δ mark the physical boundary of the unit cell, and the dotted magenta line notes the C&P allowance band Ω . The generator g is found as the first nonzero intersection of the line $y = \frac{2}{3}x$, and this lattice point is marked as "1". A sequential vectorial addition of g labels $p + q = 8$ times maps all $p + q - 1 = 7$ in-band lattice points with a co-numbering index. Alternating black and blue arrows account for the addition of the generator g , the winding around the unit cell boundaries is indicated by the dashed arrows, and the first two points are labeled to illustrate the method.

so the condition for the in-band lattice point with the smallest distance from the line Δ is

$$\mathcal{F}_{j+1}p - \mathcal{F}_jq = 1,$$

for which a solution is guaranteed as \mathcal{F}_j and \mathcal{F}_{j+1} are mutually prime. We now make use of the Vajda identity [Vaj07]

$$\mathcal{F}_{j+\mu}\mathcal{F}_{j+\nu} - \mathcal{F}_j\mathcal{F}_{j+\mu+\nu} = (-1)^j\mathcal{F}_\mu\mathcal{F}_\nu,$$

to show that by taking $(\mu, \nu) = (-1, 1)$, and using the generalization $\mathcal{F}_{-j} = (-1)^{j+1}\mathcal{F}_j$, the predecessor approximant in (2.4), $\mathcal{F}_{j-1}/\mathcal{F}_j$, fulfills

$$\mathcal{F}_{j-1}\mathcal{F}_{j+1} - \mathcal{F}_j^2 = (-1)^j.$$

This implies that for S_j with even j , taking $(p, q) = (\mathcal{F}_{j-1}, \mathcal{F}_j)$ defines the generator g . For odd j the predecessor approximant gives a point which is out of the band, and we need to go to the next predecessor (more primitive) approximant, $(p, q) = (\mathcal{F}_{j-2}, \mathcal{F}_{j-1})$. This is done by setting $j' = j + 1$, taking $(\mu, \nu) = (-1, -2)$, and noting that $\mathcal{F}_{-1} = 1$; $\mathcal{F}_{-2} = -1$, to yield $\mathcal{F}_{j'}\mathcal{F}_{j'-3} - \mathcal{F}_{j'-1}\mathcal{F}_{j'-2} = (-1)^{j'} = (-1)^{j+1}$.

This technique is used to label the in-band \mathbb{Z}^2 points in a way which is very generalizable to other sequences and higher dimensions. However, it does not possess

a translational degree of freedom, as an origin has to be set. We will use a similar reasoning in chapter 4.

Remark

In this work, we depart from concatenation and substitution rules conventions, as they always represent a single point in a wider structural map governed by the degree of freedom ϕ and at any desired length. We choose to work hereafter with the gauge phase ϕ , occasionally returning to the equivalent C&P picture. However, in most cases we will still limit ourselves to discuss only structures of length \mathcal{F}_j for reasons to be described in chapter 4.

2.1.7 Substitution rules structures properties

The substitution rules method is used for the generation of periodic and quasiperiodic structures. In the case of quasicrystals, the substitution rules approach lends a profound understanding regarding the occurrence of letters or super-letters, i.e. doublets, triplets and so on, as they may be used as inflation or deflation rules [Bel82, Bel92]. For instance, in the two letter alphabet, one can define the letter occurrence matrix \mathcal{M}_1 such that the matrix element \mathcal{M}_1^{ij} contains the occurrence of the i^{th} letter in the j^{th} substitution, namely

$$\begin{pmatrix} \xi(A) \\ \xi(B) \end{pmatrix} \equiv \mathcal{M}_1 \begin{pmatrix} A \\ B \end{pmatrix}, \quad (2.5)$$

such that for the Fibonacci sequence $\mathcal{M}_1 = \begin{pmatrix} 1 & 1 \\ 1 & 0 \end{pmatrix}$. Similarly we may define the super-letter occurrence matrix \mathcal{M}_2 , such that a matrix element \mathcal{M}_2^{ij} contains the occurrence of the i^{th} 2-letter combination (doublet) in the j^{th} 2-letter substitution. For the Fibonacci chain, the 3 doublets alphabet is $\{AA, AB, BA\}$, and the corresponding substitutions are $\{\xi(AA) = ABAB, \xi(AB) = ABA, \xi(BA) = AAB\}$. No BB doublets occur. The occurrences of the doublets in the 2-letter substitutions are obtained as follows [Bel82, Bel92]. The numbers of doublets to be deduced (by shifting a 2-letter acceptance window from left to right) is equal to the number of letters in the substitution for the single first letter of the doublet. For $\xi_2(AA)$ and $\xi_2(AB)$ we should deduce 2 doublets (as the length of $\xi(A) = AB$ is 2), and for $\xi_2(BA)$ we should deduce 1 doublet (as the length of $\xi(B) = A$ is 1). Finally,

$$\xi_2(AA) = \xi_2(AB) = (AB)(BA); \quad \xi_2(BA) = (AA),$$

which leads to the occurrence matrix

$$\mathcal{M}_2 = \begin{pmatrix} 0 & 0 & 1 \\ 1 & 1 & 0 \\ 1 & 1 & 0 \end{pmatrix}$$

$$\begin{pmatrix} \xi_2(BA) \\ \xi_2(AB) \\ \xi_2(AA) \end{pmatrix} \equiv \mathcal{M}_2 \begin{pmatrix} BA \\ AB \\ AA \end{pmatrix}, \quad (2.6)$$

and so on for \mathcal{M}_j . The occurrence matrices \mathcal{M}_1 and \mathcal{M}_2 may be diagonalized, and the eigenvectors corresponding to the highest mutual eigenvalue may be normalized, so that the sum of their elements is unity. In the Fibonacci case, the eigenvalues of \mathcal{M}_1 and \mathcal{M}_2 are $\{1-\tau, \tau\}$ and $\{1-\tau, \tau, 0\}$, respectively. Thus, τ is the highest mutual eigenvalue, and the corresponding normalized eigenvectors V_1, V_2 are

$$V_1 = \begin{pmatrix} \tau^{-1} \\ 1 - \tau^{-1} \end{pmatrix}; V_2 = \begin{pmatrix} 2\tau^{-1} - 1 \\ 1 - \tau^{-1} \\ 1 - \tau^{-1} \end{pmatrix}. \quad (2.7)$$

Using the identity $\tau^{-1} = \tau - 1$, equation 2.7 becomes

$$V_1 = \begin{pmatrix} \tau - 1 \\ 2 - \tau \end{pmatrix}; V_2 = \begin{pmatrix} 2\tau - 3 \\ 2 - \tau \\ 2 - \tau \end{pmatrix}.$$

The elements $V_1^{(i)}$ represent the occurrence of the i^{th} letter, and the elements $V_2^{(i)}$ represent the occurrence of the i^{th} doublet. For the Fibonacci case we may deduce from V_1 that the letter A occurs more than the letter B by approximately 61.8% : 38.2%. From V_2 we see that the AB , and BA doublets have an equal occurrence of $\sim 38.2\%$ each, and the AA doublet has $\sim 23.6\%$ occurrence.

The above derivation is the foundation of C-theory and the resulting gap labeling theorem for substitution quasiperiodic structures [Bel82, Bel92], which is a crucial element in understanding the topological properties of substitution quasiperiodic structures. This theorem for the Fibonacci chain is described in chapter 3 and the treatment of the resulting topological properties is discussed in chapter 4.

A final note on the family of substitution quasiperiodic structures. The eigenvalues of the occurrence matrix \mathcal{M}_1 (upon diagonalization) may be sorted by length. If the leading (largest) eigenvalue is greater than 1 (in modulus) and the others are smaller than 1 (in modulus), the substitution is called Pisot, and when all eigenvalues are greater than 1 (in modulus), the substitution is called non-Pisot [GL92]. The Fibonacci substitution is a Pisot one, as the modulus of the eigenvalues of \mathcal{M}_1 are $\{\sim 1.618, \sim 0.618\}$. Another example for a non-C&P Pisot substitution is the Thue-Morse quasiperiodic sequence, whose substitution is $\xi(A) = AB, \xi(B) = BA$,

and the letter occurrence matrix is $\mathcal{M}_1 = \begin{pmatrix} 1 & 1 \\ 1 & 1 \end{pmatrix}$. The corresponding modulus of the eigenvalues of \mathcal{M}_1 are $\{2, 0\}$. An example for a non-Pisot substitution is $\xi(A) = AAAB$, $\xi(B) = BBA$ which generates a quasiperiodic structure, for which the letter occurrence matrix is $\mathcal{M}_1 = \begin{pmatrix} 3 & 1 \\ 1 & 2 \end{pmatrix}$. In this case, the corresponding modulus of the eigenvalues of \mathcal{M}_1 are $\{\sim 3.618, \sim 1.382\}$, which is clearly non-Pisot. All characteristic function and C&P quasiperiodic structures have a substitution description which is strictly Pisot, and no characteristic function or C&P description exists for non-Pisot systems. The fundamental structural and spectral differences between Pisot and non-Pisot sequences are immense (see for instance the discussion in 2.1.9), but lies outside the scope of this thesis.

2.1.8 Characteristic function (and C&P) quasiperiodic structures properties

A quick look at the characteristic function and the equivalent C&P method, reveals a relation between the discrete nature of the chain and its quasiperiodicity. The characteristic function $\chi_n(\phi)$ is the sign of an under-sampled shifted cosine. Let us first consider the function $\chi(x) = \cos(2\pi x \tau^{-1} + \pi \tau^{-1})$ for the continuous variable x , and note that this is a regular cosine with frequency τ^{-1} . If we take the sign of the previous function, and relate it to the structure alphabet, it is still a periodic rectangular function spending the same “time” being negative or positive. Next, we consider a shift in the amplitude of the cosine to yield $\chi(x) = \text{sign}[\cos(2\pi x \tau^{-1} + \pi \tau^{-1}) - \cos(\pi \tau^{-1})] = \text{sign}[\cos(2\pi x \tau^{-1} + \pi \tau^{-1}) + 0.362 \dots]$. This function is still periodic, but now spends more “time” being positive than negative. The final step in this understanding of (2.3) is to under-sample this function so that instead of a continuous x , we have a discrete $x \in \mathbb{N}$. This under-sampling of the rectangular periodic function causes the resultant structure to depend on the irrationality or incommensurability of τ^{-1} with respect to the grid $x \in \mathbb{N}$ (see figure 2.5). For a rational approximant of the C&P slope τ^{-1} , a periodic sequence (with a non periodic unit cell) is obtained. As p/q , the rational approximant for τ^{-1} travels up the Farey sequence in (2.4), the quasiperiodic unit cell length becomes larger, until finally at the irrational limit, an infinite quasiperiodic sequence is obtained (infinite unit cell). This conforms to what we know from the C&P approach where any rational approximant for τ^{-1} results in a periodic structure with a unit cell of size $p + q - 1$. As before, for any finite size N chosen, there exist $\{p_i/q_i\}$ rational approximant set for τ^{-1} which will produce the very same structure compared to using the irrational itself (as long as $N < p_i + q_i - 1$). This property will be discussed in chapter 4 in detail.

In this quick look at (2.3), we may also notice that the modulation phase shift ϕ is equivalent to some shift of origin along the infinite chain S_∞ such that

$$\chi_n(\phi + \Delta\phi) = \chi_{n+\Delta n} \Rightarrow \Delta\phi = 2\pi \tau^{-1} \Delta n \quad (2.8)$$

which also corresponds to the C&P picture, where a scan of ϕ is equivalent to a continuous translation of the “cut” band along the y-axis which causes the origin of the resultant chain (the intersection of the line Δ with a \mathbb{Z}^2 lattice point) to translate with respect to the chosen structure. This implies that the relation between $\vec{F}_N(\phi)$ (generated through the characteristic function) to S_j (generated by substitution or concatenation rules) is that of translation along S_∞ . This property clarifies why ϕ , which represents a translational degree of freedom, is meaningful only for finite chains, and will be discussed in 2.2 in detail.

A unique property of the characteristic function (2.3), is the automatic occurrence of perfectly palindromic finite chains. If we examine (2.3), we notice that the under-sampled shifted cosine $\chi_n(\phi)$ is perfectly symmetric around the points where its argument is $2\pi n \tau^{-1} + \phi_0 + \phi = \pm 1$. If this condition is fulfilled for some letter index n , then any structure where n is the central letter will be perfectly palindromic. This property will be discussed in 2.2 in detail.

2.1.9 Structural properties of the Fibonacci chain and other C&P chains

Invariance under discrete translation

Any general finite Fibonacci segment $\vec{F}_N(\phi)$ (defined according to the characteristic function approach) occurs in an infinite but discrete number of locations along S_∞ (a numerical example is given in figure 2.6). This discrete invariance to translation is best understood using the concatenation method approach, by which every Fibonacci generation is forever embedded in all the following generations. This invariance is different than periodic structure case, as the recurrence of any string is discrete but not periodic. An instrumental method to be used in chapter 4 is to numerically verify whether a certain Fibonacci-like chain exists along S_∞ or not. Figure 2.6 shows, as an example, the inspection of the occurrence of $\vec{F}_N(\phi)$ and also of $\overleftarrow{F}_N(\phi)$, the mirror image of $\vec{F}_N(\phi)$ along S_∞ . The observed frequent occurrence of $\vec{F}_N(\phi)$ along S_∞ , is an indication for the long range order in quasiperiodic structures which is manifested in this discrete translation invariance. This is not a unique property of the Fibonacci chain, but a universal property of C&P structures (figure 2.7 shows two more examples). The frequent occurrence of $\overleftarrow{F}_N(\phi)$ along the infinite chain is also a universal property of C&P structures. As a curiosity, the Thue-Morse chain, which is a Pisot substitution structure carries the same properties as the C&P examples. In contrast to that, our non-Pisot substitution chain example (see 2.1.7) shows similar long range order, but the mirror image structure never occur along the infinite chain (see figure 2.8).

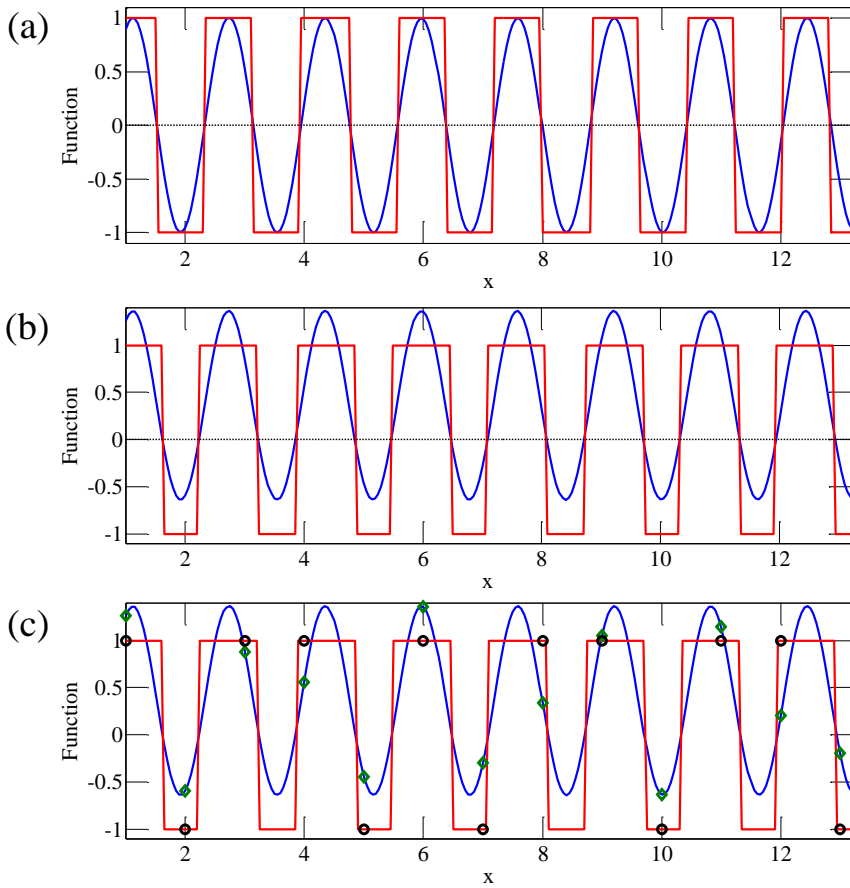


Figure 2.5: Components of the characteristic function. (a) The behavior of $\cos(2\pi\tau^{-1}x)$ in blue and of $\text{sign}[\cos(2\pi\tau^{-1}x)]$ in red, where $x \in \mathbb{Z}$. The resultant rectangular function in red is balanced between +1 (A) and -1 (B). (b) The behavior of $\cos(2\pi\tau^{-1}x) - \cos(\pi\tau^{-1})$ in blue and of $\text{sign}[\cos(2\pi\tau^{-1}x) - \cos(\pi\tau^{-1})]$ in red, where $x \in \mathbb{Z}$. Due to the positive offset, the resultant rectangular function in red favors +1 (A) over -1 (B). (c) The same functions as in (b), under-sampled such that $x \in \mathbb{N}$ (green diamonds for the full function and black circles for the sign function). The under-sampling makes the discrete structure to sometimes skip one oscillation. The positive offset makes sure that the -1 (B) half-cycle is never skipped (i.e. no BB doublet). The resulting structure is: ABAABABAABAAB which is identical to S_6 (generated through concatenation or substitution).

Occurrence of palindromes

A word is said to be a palindrome if it is invariant upon inversion. The Fibonacci chain is referred to as almost palindromic. It is well known that the infinite Fibonacci word, as all Sturmian words (see for instance [DP99]) hosts an infinite number of arbitrarily long palindromes. For the Fibonacci case it is possible to show that $S_j(1 : \mathcal{F}_j - 2)$, generated by discarding the last two letters of S_j , is always a palindrome for any value of j [Jan94]. From this statement and the concatenation rules approach, follows that arbitrarily long (lengths $< \mathcal{F}_j - 2$ for $j \rightarrow \infty$) palindromes exists throughout S_∞ , but as we will show in 2.2, these properties are not a necessary condition. Using our observation regarding the symmetry of the characteristic function, we will demonstrate new understanding of this phenomenon for all C&P finite structures using the properties of the characteristic function approach (see 2.2).

2.1.10 Generalization to 1D Aubry-Andre-Harper (AAH) model

The results given here for the C&P or the characteristic function approach are generalizable to Aubry-Andre-Harper (AAH) potential by simply dropping the sign[#] function in (2.3) (see [KZ12], and also the green diamonds in figure 2.5c). The AAH potential is still discrete, but it is composed of a continuous alphabet. For instance, AAH sequences also contain palindromes when the cosine in the characteristic function is ± 1 , but it does not share the discrete invariance to translation with the C&P structures.

2.2 The modulation phase ϕ for a finite size Fibonacci chain

In this section we present some important properties of the structural phase ϕ defined in 2.1. In chapters 3 and 4, we shall term it a phason and we will show how it drives topological phases and topological edge states, essentially playing an analogous role to the magnetic field in quantum Hall physics.

2.2.1 Structural effect of scanning ϕ on the Fibonacci chain

The 2π -periodic modulation phase ϕ is a structural degree of freedom (a.k.a a phason [AYP04]) of the C&P structures family. Scanning ϕ continuously through one period for a finite chain (of length N), generates a series of only and exactly N identical local structural changes until the structure returns to its initial composition (see figure 2.9). These local structural changes, which may be called phason-flips [AYP04], are equivalent to the inversion of a single 6-letters segment $BAABAB \leftrightarrow BABAAB$ within the structure and occur only one at a time (see figure 2.10). The N resultant structures are N different segments of S_∞ which correspond to only N values of

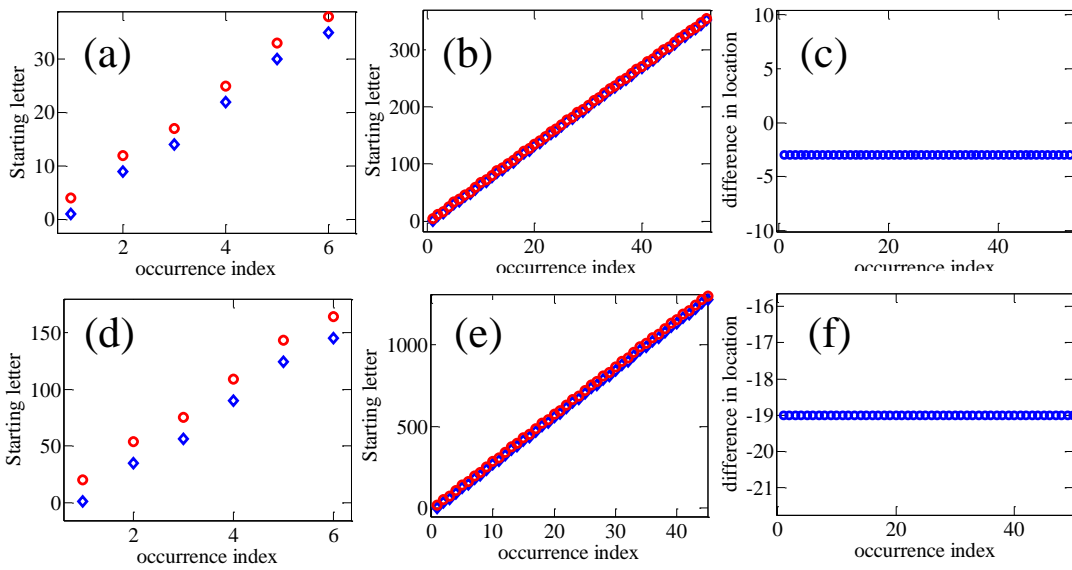


Figure 2.6: Occurrence of finite Fibonacci segments along S_∞ . (a)-(b) Occurrence of the segments $\vec{F}_8(\phi_F)$ and $\overleftarrow{F}_8(\phi_F)$ in blue and red respectively. These segments regularly occur (but not periodically) along S_∞ . The two segments occur at a constant distance from each other as depicted in (c), showing the difference between the occurrence coordinates of $\vec{F}_8(\phi_F)$ and $\overleftarrow{F}_8(\phi_F)$. (d)-(f) The same plots for $\vec{F}_{34}(\phi_F)$ and $\overleftarrow{F}_{34}(\phi_F)$.

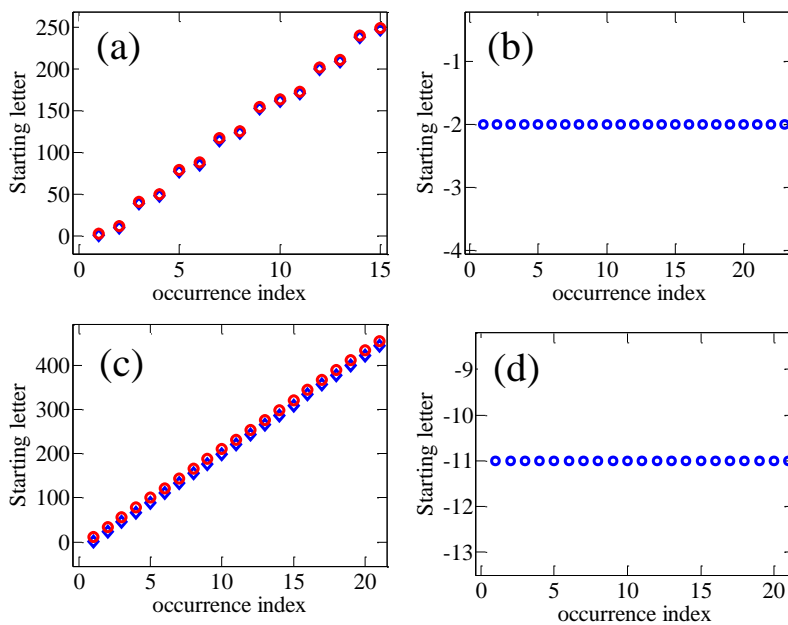


Figure 2.7: (a)-(b) The same as figure 2.6 for a 34 letter long C&P segments with slope $1/\sqrt{5}$. (c)-(d) The same plots for slope π^{-1} .

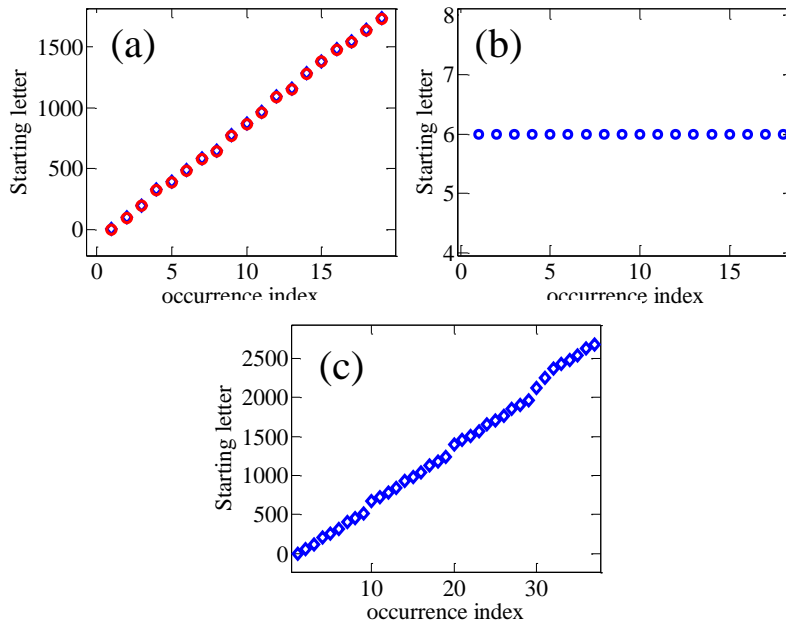


Figure 2.8: (a)-(b) The same as figures 2.6 and 2.7 for a 58 letter long segments of the Thue-Morse Pisot substitution. (c) The same plot for the non-Pisot substitution discussed previously. There are no occurrences of the mirrored segment.

translation (or origin shift) with respect to the original segment (2.8). The lack of change upon scanning ϕ between consecutive phason-flips is due to the fact that the $\text{sign}[\#]$ function in the characteristic function allows for some variation of ϕ before one of the N letters may change due to a change of sign in the argument. This allowance is also understandable from the C&P approach where the cut band may be shifted for some distance before an in-band points leaves the cut band (and another point enters, see figure 2.10).

The exact details of each phason-flip and the fact that only one change can happen at a time is also very understandable from the C&P approach. Firstly, examining figure 2.10, one may see how dragging the “cut” band upward may cause only one type of flip, and dragging the “cut” band downward will result in the exact opposite type of flip. Secondly, within a unit cell (up to the limit of an infinite unit cell when the slope is irrational) only one change may happen at a time because within the unit cell, the C&P line Δ may either intersect a single \mathbb{Z}^2 lattice site, or none. This discreteness of the ϕ -driven phason-flips is of utmost importance as it underlies the characteristic stepwise shapes in all of the spectral and topological ϕ dependent variables (as will be discussed in detail in chapter 4).

When the ϕ -scan N subsequent structures of length N are plotted on top of each other in a 2D map, one can see that the ϕ -driven phason-flips are distributed according to the geometrical pattern which may be easily traced to the original C&P \mathbb{Z}^2 lattice (see figures 2.11 and 2.12). Similar structure may be found for other C&P slopes (see figure 2.13). This N – by – N 2D map we term $\{\vec{F}_N(\phi)\}$ is of great

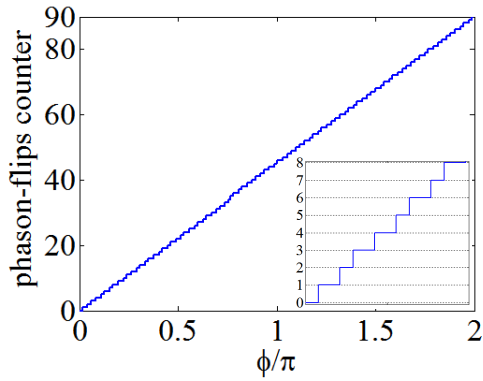


Figure 2.9: A continuous scan of ϕ in the characteristic function for the Fibonacci chain causes the structure to change. Here plotted the counter of these changes for \vec{F}_{89} as a function of ϕ . Inset: a closer look.

importance and will be discussed in detail in chapter 4.

Each phason-flip generates a valid segment of S_∞ and is therefore equivalent to a translation along S_∞ . Consequently we wish to explore these translations which are in general multi-valued. Figure 2.14 depicts the numerical study of the equivalent translations for the map $\{\vec{F}_N(\phi)\}$ with $N = 89$. It seems that the first appearance of the 89 segments in the infinite chain (figure 2.14a) is simply the translation by 1 to 89 letters arranged in a tilted lattice pattern as a function of ϕ (or the segment index in the map $\{\vec{F}_N(\phi)\}$). The next appearances of the 89 structures along S_∞ is just as ordered in terms of the angled lattice pattern, but not as ordered in terms of the translation values themselves (see figure 2.14b-d). Rechecking this behavior for two other C&P slopes reveals similar behavior (see figure 2.15).

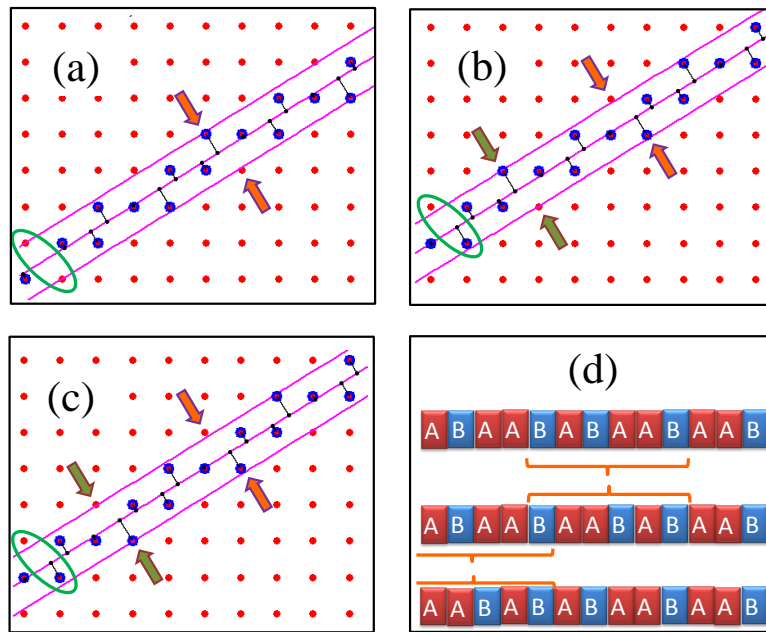


Figure 2.10: ϕ -driven phason-flips in the Fibonacci chain $\vec{F}_{13}(\phi)$: the C&P picture. The structure origin is indicated by a green ellipse. (a) The original chain $S_6 = \vec{F}_{13}(\phi_F)$. Orange arrows indicate the location of the first expected flip (for an increase in ϕ equivalent to dragging the “cut” band downwards). (b) The chain $\vec{F}_{13}(\phi_F + \Delta\phi)$ differing from S_6 by a single phason-flip. Orange and green arrows indicate the location of the previous and the next expected flip (for an additional increase in ϕ). (c) The chain $\vec{F}_{13}(\phi_F + 2\Delta\phi)$ differing from S_6 by a two phason-flips, marked with orange and green arrows. (d) Top to bottom, the resultant structures of (a), (b) and (c). The orange brackets indicated the identical phason flips equivalent to the inversion of a single 6-letters segment $BAABAB \leftrightarrow BABAAAB$.

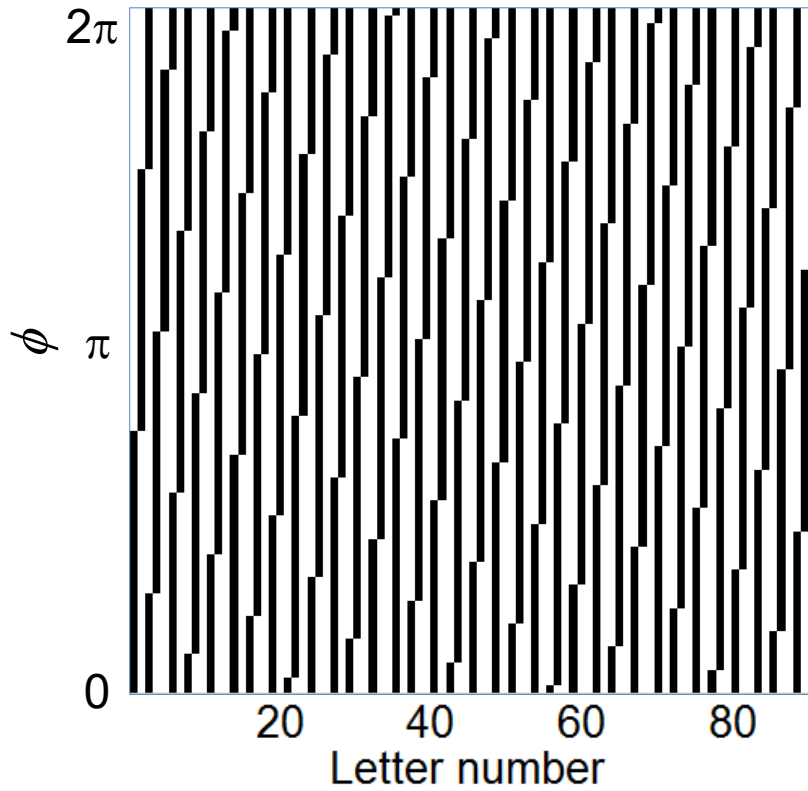


Figure 2.11: An x - ϕ colormap of $\{\vec{F}_N(\phi)\}$, with $N = 89$ for the Fibonacci chain as a function of ϕ . Black slabs stand for “B”, and white slabs stand for “A”.

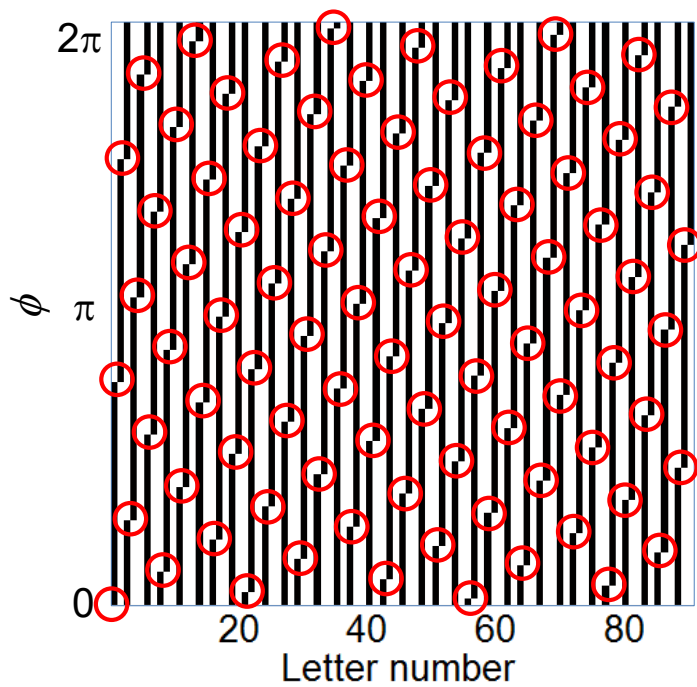


Figure 2.12: The same map as in figure 2.11. Red circles indicate the location of the 89 identical phason-flips.

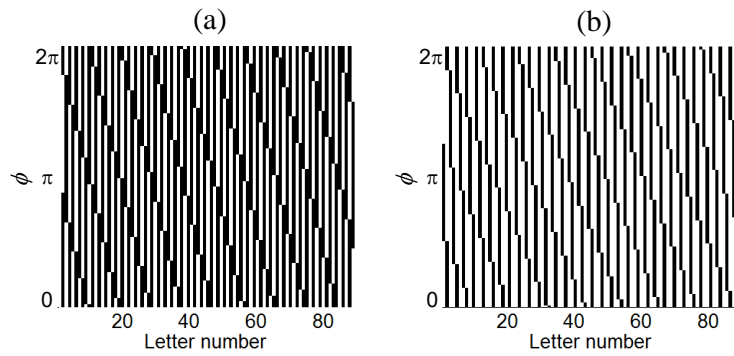


Figure 2.13: The same map as in figure 2.11 for other C&P slopes. (a) slope is $1/\sqrt{5}$. (b) slope is $2/\pi$.

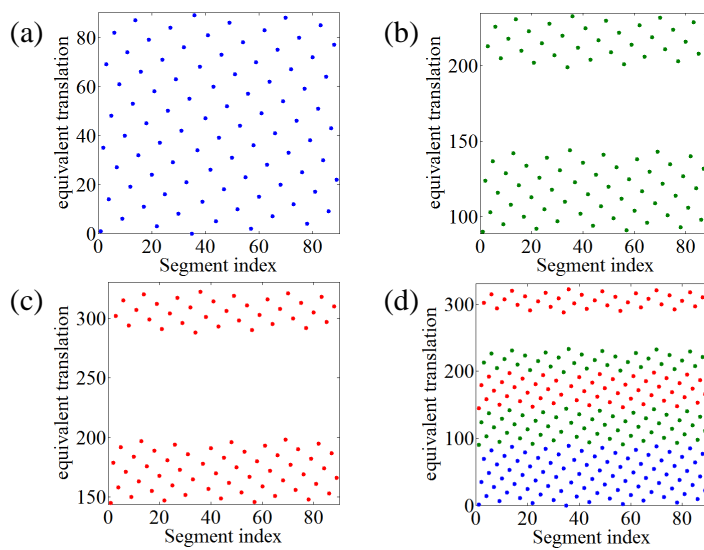


Figure 2.14: The Fibonacci chain as a function of ϕ . Equivalent translation for the $N = 89$ segments of the infinite chain chosen through scanning of ϕ (by the resultant segment index in $\{\vec{F}_N(\phi)\}$). (a) The equivalent translation for the first occurrence of each segment (in blue dots). (b) The same, for the second occurrence (in green). (c) The same, for the third occurrence (in red). (d). A superposition of (a)-(c).

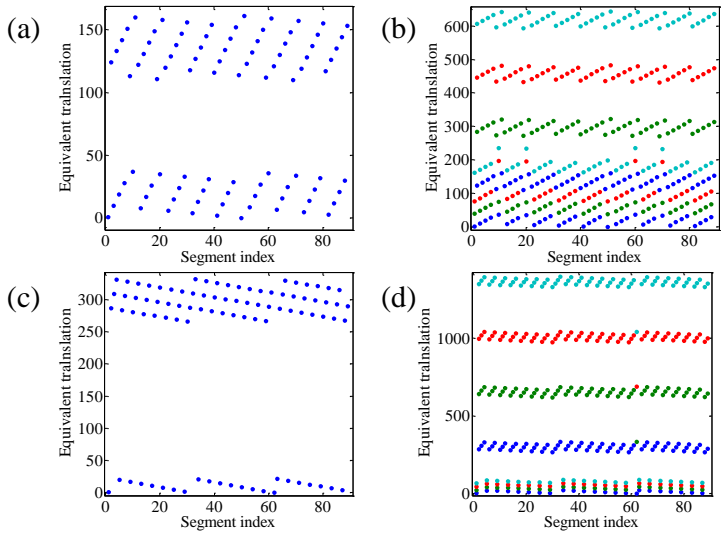


Figure 2.15: Other C&P chains as a function of ϕ . Equivalent translation for the $N = 89$ segments of the infinite chain chosen through scanning of ϕ for C&P slopes $1/\sqrt{5}$, and $1/\pi$. (a) C&P slope of $1/\sqrt{5}$. The equivalent translation for the first occurrence of each segment (in blue dots). (b) The same, for the four first occurrences (in blue, green, red and cyan, respectively). (c)-(d) The same as (a)-(b) for C&P slope of $1/\pi$.

The natural next step is to consider the chain $S_j = \vec{F}_{\mathcal{F}_j}(\phi_F)$ as an initial segment of S_∞ and then translate an acceptance window of length \mathcal{F}_j along S_∞ by $1, 2 \dots, N$ letters. We then calculate the equivalent $\Delta\phi$ value for each translation through equation 2.8. Figure 2.16 shows this analysis for C&P slopes τ^{-1} (Fibonacci), and also for the slopes $1/\sqrt{5}$, and $2/\pi$. It appears that these N chosen translations span the $[0, 2\pi)$ interval in $\Delta\phi$ (without repeating) is the same tilted lattice pattern. Moreover, this 2D pattern for the Fibonacci appear to be perfect torus (see figure 2.17), while for the two other slopes, the patterns are not perfect tori (the misfit occurs along the x-axis only). However, this is due to the fact that $N = 89 = \mathcal{F}_{10}$ is a “natural” length for Fibonacci chains but not necessarily for the other slopes. A simple “trial and error” approach leads to some values for the natural lengths for the non-Fibonacci slopes, upon which the $\Delta\phi - \Delta x$ patterns seem to become perfect tori (see figures 2.18 and 2.19). This subject is still open for analysis.

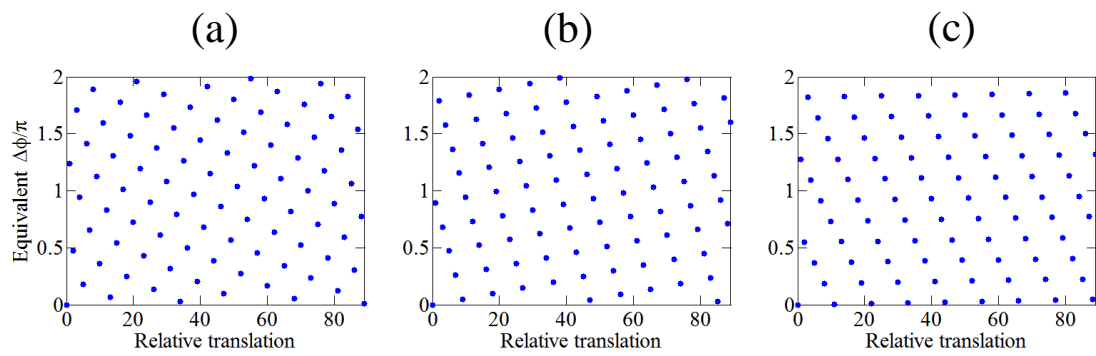


Figure 2.16: Equivalent value of ϕ for translations in the $N = 89$ segments of the infinite chain for C&P slopes: (a) τ^{-1} , (b) $1/\sqrt{5}$, and (c) $2/\pi$.

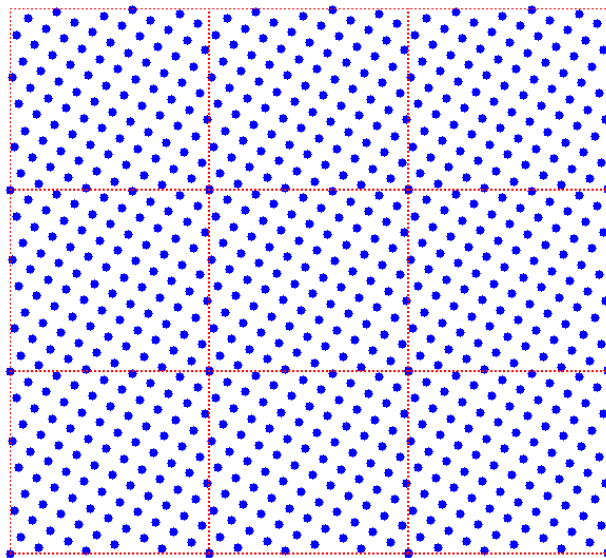


Figure 2.17: The 2D map of figure 2.16(a) is a perfect torus. Here it is used as the unit cell of a 3x3 periodic array to show the toroidal properties.

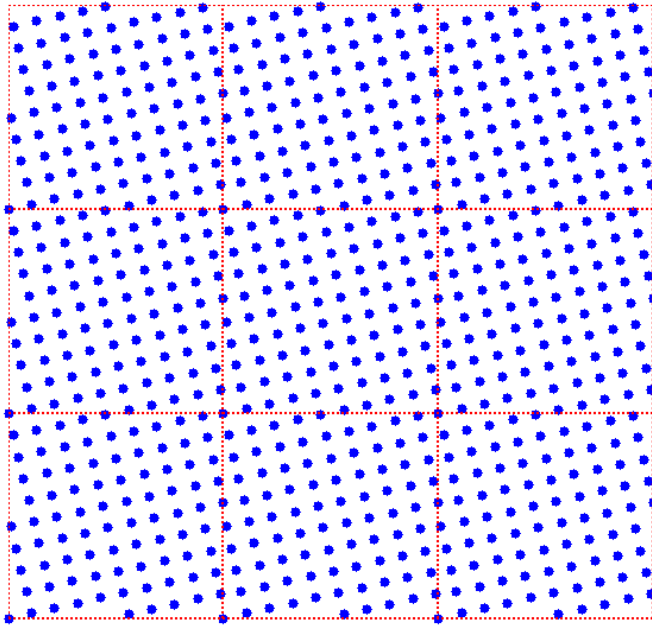


Figure 2.18: The 2D map of figure 2.16(b) is a perfect torus along the $\Delta\phi$ direction (y-axis), but not along the x-axis. If we shorten the segment to have $N = 84$, it becomes a torus. Here it is used as the unit cell of a 3x3 periodic array to show the toroidal properties.



Figure 2.19: The 2D map of figure 2.16c is a perfect torus along the $\Delta\phi$ direction (y-axis), but not along the x-axis. If we enlarge the segment to have $N = 354$, it becomes a torus. Here it is used as the unit cell of a 3x3 periodic array to show the toroidal properties.

2.2.2 ϕ -driven fractional translation

The ϕ -driven equivalent translation along S_∞ described above appears to be non-monotonic, while in fact a closer look at the map in figure 2.11, shows that a monotonic process of structural change occurs. If one follows the evolution of the structure through the ϕ -scan, they seem to be regularly drifting in one direction. From (2.8), we recall that the translation by 1 letter along S_∞ is accomplished for $\Delta\phi = 2\pi\tau^{-1} \cong 1.24\pi$. Assuming that the $N = \mathcal{F}_j$ identical phason-flips are evenly distributed, this translation by 1 letter is accomplished by $\mathcal{F}_j\Delta\phi/2\pi = \mathcal{F}_j\tau^{-1} \cong \mathcal{F}_{j-1}$ phason-flips. This gives rise to the notion of ϕ -driven fractional translation of $\frac{1}{\mathcal{F}_j\tau^{-1}}$ per phason-flip, completing after a full period in ϕ a fractional translation by $\tau \cong 1.62$ letters. This underlying monotonicity may be depicted by plotting the spatial correlation between the segment $\vec{F}_{\mathcal{F}_j}(\phi)$, and some target structure such as $\vec{F}_{\mathcal{F}_j}(\phi = \pi)$, given by $\vec{F}_{\mathcal{F}_j}(\phi)\vec{F}_{\mathcal{F}_j}(\phi = \pi)$ where the letters (A, B) are represented by $(0, 1)$ and taking values between 0 and 1 (see figure 2.20 for the Fibonacci case and another C&P slope example)

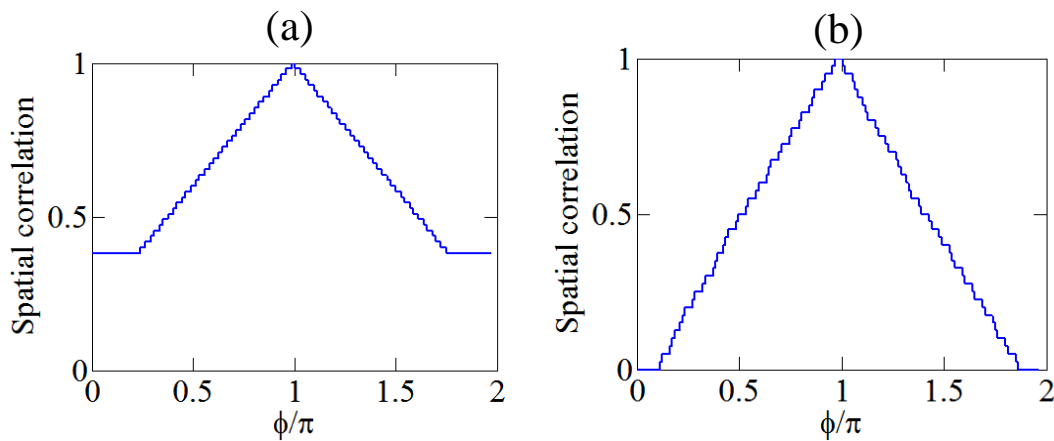


Figure 2.20: (a) The spatial correlation between the segment $\vec{F}_{89}(\phi)$, and some target structure such as $\vec{F}_{89}(\phi = \pi)$, as a function of ϕ . (b) the same plot for the C&P slope $1/\sqrt{5}$.

2.2.3 ϕ -driven fractional inversion

Following the same logic as the concept of fractional translation, the equivalence of each structural change to the inversion of an internal six-letter segment leads to the notion of fractional inversion. In order to define the fractional inversion, let us reuse the inverted chain $\overleftarrow{F}_N(\phi)$ defined in 2.1.9. The fractional inversion for the chain $\overrightarrow{F}_N(\phi)$ with respect to some initial chain $\overrightarrow{F}_N(\phi_i)$ is defined in $[0, 1]$ as

$$\xi(\phi, \phi_i) \equiv \frac{1}{2N} \sum_{j=0}^{N-1} |\chi_{j+1}(\phi_i) + \chi_{N-j}(\phi)|$$

where the letters (A, B) are now represented by $(-1, 1)$. $\xi(\phi, \phi_i) = 1$ means full inversion ($\overrightarrow{F}_N(\phi_i) = \overleftarrow{F}_N(\phi)$), and $\xi(\phi, \phi_i) = 0$ means no internal inversion ($\overrightarrow{F}_N(\phi_i) = -\overleftarrow{F}_N(\phi)$). It appears that for every value of ϕ_i , there exists a value of ϕ where $\overrightarrow{F}_N(\phi_i) = \overleftarrow{F}_N(\phi)$ (see figure 2.20 for the Fibonacci case and another C&P slope example). This understanding may lead us to the conjecture that the N Fibonacci segments of the set $\{\overrightarrow{F}_N(\phi)\}$ consist of $N/2$ different segments, and their fully inverted duplicates. This will be discussed in the following subsection. Moreover, the condition $\xi(\phi, \phi_i) = 0$ appears to be unreachable. In the Fibonacci case, this fixed plateau at 0.236 is very understandable through the substitution rules approach, as “BB” doublets never occur and the “AA” doublet occurrence is $2\tau^{-1} - 1 = 0.236$, see (2.7). For the other C&P slope example we used, the plateau is not fixed, and the correlation to occurrences is not that obvious at this stage.

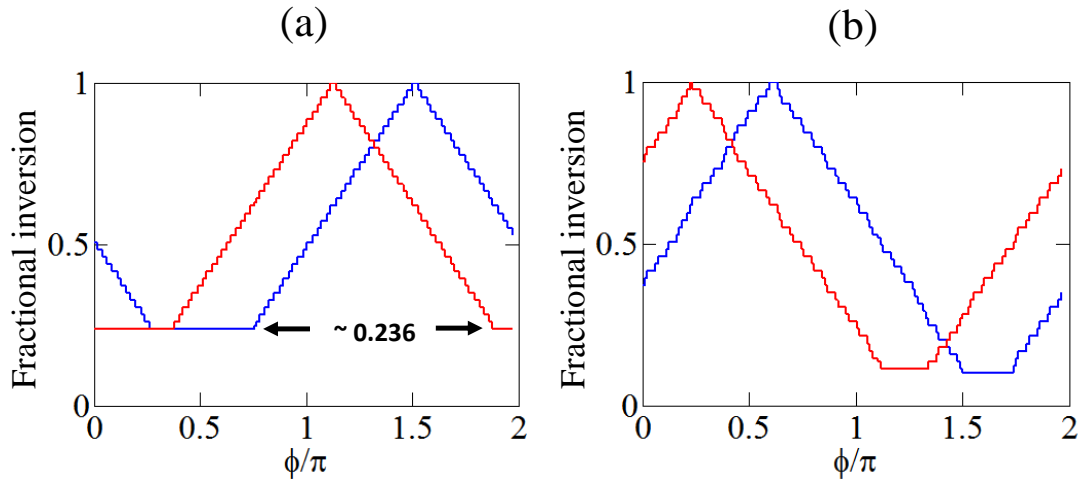


Figure 2.21: (a) The fractional inversion between the segment $\vec{F}_{89}(\phi)$, and some target structures such as $\vec{F}_{89}(\phi = \phi_F)$ in blue, and $\vec{F}_{89}(\phi = \phi_F + 0.4\pi)$ in red as a function of ϕ . The lowest fractional inversion plateaus at the value of $0.236 = 2\tau^{-1} - 1$. (b) the same plot for the C&P slope $1/\sqrt{5}$.

2.2.4 The ϕ -driven palindromicity cycle

The notion of fractional inversion, along with the combined description using the characteristic function ϕ and its associated C&P interpretation allows to unveil a structural symmetry cycle of quasiperiodic chains, namely their palindromic character (mirror symmetry). As noted in 2.1, sweeping ϕ over a period in (2.3), we observe that any chain of length N becomes perfectly symmetric for two specific values,

$$\phi_{pal}(N) = -(N + 2)\pi\tau^{-1} + m\pi, \quad (2.9)$$

where $m \in \mathbb{Z}$. We quantify deviations, or violation of this palindromic symmetry using a structural parameter $\eta(\phi)$, defined in $[0, 1]$ by

$$\eta(\phi) \equiv \frac{1}{N} \sum_{j=0}^{\lfloor \frac{N-1}{2} \rfloor} |\chi_{j+1}(\phi) - \chi_{N-j}(\phi)|, \quad (2.10)$$

where $\lfloor \frac{N-1}{2} \rfloor$ stands for the highest integer smaller than $\frac{N-1}{2}$, and the letters (A, B) are represented by $(-1, 1)$. For the two specific values where the chain becomes perfectly palindromic, we expect $\vec{F}_N(\phi_{pal}) = \overleftarrow{F}_N(\phi_{pal})$, which leads to $\eta(\phi_{pal}) = 0$, while the value $\eta(\phi_{ap}) = 1$ means the the segment is an anti-palindrome ($\vec{F}_N(\phi_{ap}) = -\overleftarrow{F}_N(\phi_{ap})$). Monitoring $\eta(\phi)$ through a full period of ϕ reveals a regular behavior of the deviation from a perfect palindrome between the two points of perfect palindromic symmetry. This palindromic cycle for $\eta(\phi)$ is displayed in figure 2.22a. It is therefore natural to set the origin of ϕ at the palindromic symmetry, i.e., to redefine ϕ as $\phi - \phi_{pal}(N)$ (see figure 2.22b). This cycle is a universal characteristic of C&P systems, quasiperiodic and periodic alike, as may be seen in figure 2.23. To conclude, starting from a naturally occurring palindromic Fibonacci segment, the ϕ -driven phason-flips shown in figure 2.12 also drives the structure away from palindromic symmetry, and than back towards a perfect palindrome in a π -periodic cycle. The observation of a ϕ -driven π -periodic palindromic cycle is one of the main result of this current work, and as we shall see in chapter 4, it underlies the topological properties of quasiperiodic structures.

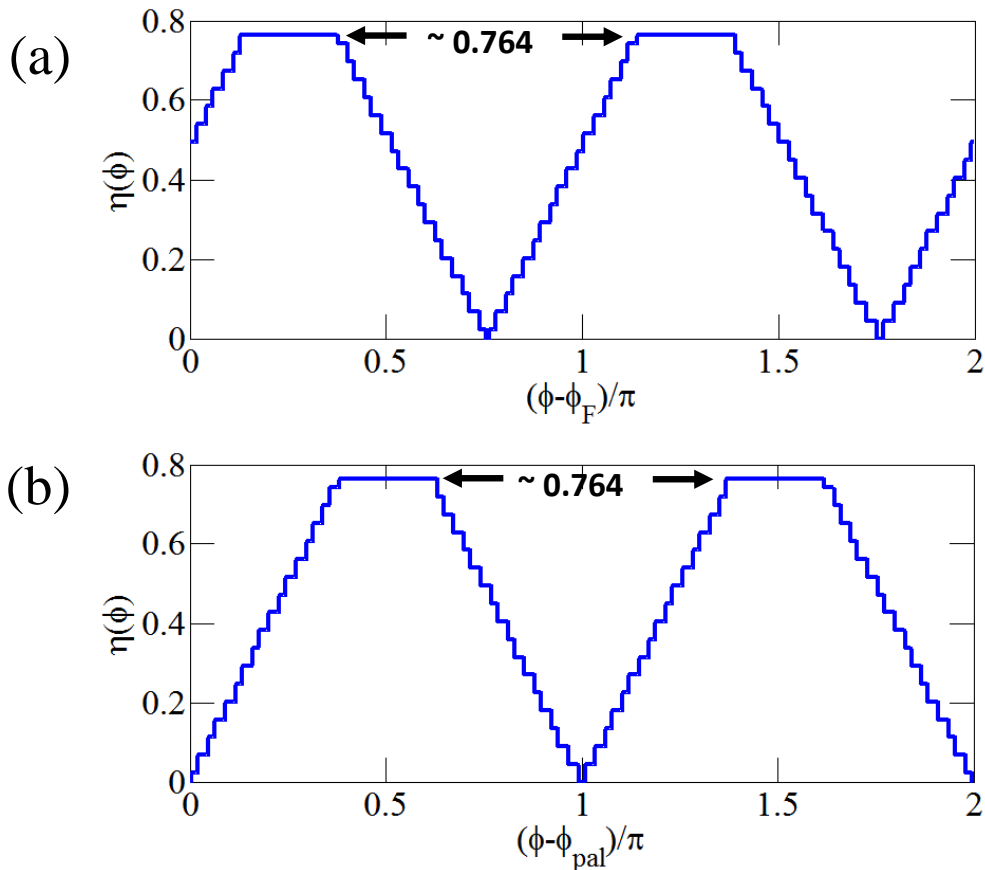


Figure 2.22: Behavior of $\eta(\phi)$ (for $N = 89$). The saturation at $\eta \simeq 0.76$ is specific to Fibonacci through the $[AA]$ doublet occurrence, $2\tau^{-1} - 1$. (a) Behavior of $\eta(\phi - \phi_F)$, where the value at $\phi - \phi_F = 0$ represent the deviation from a palindrome for S_{10} (b) The same plot for $\eta(\phi - \phi_{pal})$.

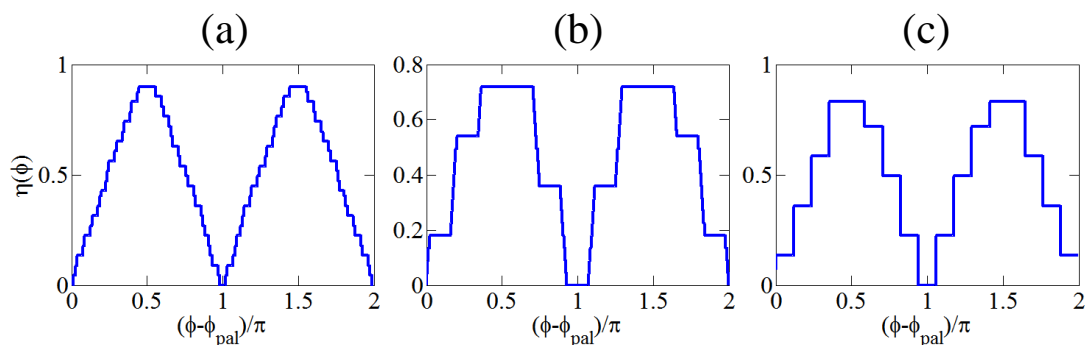


Figure 2.23: Behavior of $\eta(\phi)$ (for $N = 89$) for other C&P slopes. (a) $1/\sqrt{5}$, (b) $2/\pi$, and (c) $10/17$.

In the Fibonacci case, the fixed plateau at 0.764 is again understandable through the substitution rules approach, as “BB” doublets never occur and the “AA” doublet

occurrence is $2\tau^{-1} - 1 = 0.236$, see (2.7). For the other C&P slope example we used, the plateau is still fixed, but the correlation to occurrences is not that obvious at this stage.

A combination of the palindromic cycle and the existence of inverted structure pairs within one period of ϕ , leads to the understanding that the N structures described by $\vec{F}_N(\phi - \phi_{pal})$ contains all the structural information in the band $0 \leq \phi - \phi_{pal} \leq \pi$, while the structures corresponding to $\pi \leq \phi - \phi_{pal} \leq 2\pi$ may be generated from the previous set by taking $\vec{F}_N(\phi - \phi_{pal}) \rightarrow \overleftarrow{F}_N(2\pi - \phi + \phi_{pal})$.

We note here that although we have restricted ourselves to chains of length \mathcal{F}_j , the palindromic cycle defined and observed above persists even for structures of non-Fibonacci lengths. For instance, in figure 2.23, the deviation from a palindrome is calculated for the length $N = 89$, which is not a natural length for the chosen C&P slopes. However, there exists a fundamental difference between the palindromic cycle of the chain $\vec{F}_N(\phi)$ with $N = \mathcal{F}_j$, and with $N \neq \mathcal{F}_j$. To understand this, let's review the palindromic properties of (2.3). Discarding the previous choices for origin, the master characteristic function becomes

$$\chi_n(\phi) = \text{sign}\{\cos(2\pi n\tau^{-1} + \phi) - \cos \pi\tau^{-1}\}.$$

Examining the characteristic function for a given fixed ϕ , we will now show that a very long Fibonacci structure contains a series of palindromic symmetry poles corresponding to the Fibonacci numbers. The characteristic function itself is symmetric (palindromic) around sites/interfaces where $\cos(2\pi n\tau^{-1} + \phi) = \pm 1$, therefore,

$$\frac{2n_{pal}(\phi)}{\tau} + \frac{\phi}{\pi} = m; m \in \mathbb{Z}. \quad (2.11)$$

However, for palindromic symmetry to occur in a physical structure, $n_{pal}(\phi)$ may only take integer (mid-site) or half integer (interface) values. Moreover, as τ is irrational, the palindromic condition involves both the structure length (determining its center coordinate) and ϕ . If we take $\phi = 0$, we are left with

$$\frac{2n_{pal}(\phi = 0)}{\tau} = m; m \in \mathbb{Z}.$$

The approximate solutions for this equation are $n_{pal}(\phi = 0) \simeq \frac{\mathcal{F}_j}{2} = \frac{34,55,89\dots}{2} = 17, 27.5, 44.5\dots$, or $n_{pal}(\phi = 0) \simeq \mathcal{F}_j = 34, 55, 89\dots$. This approximations hold as a function of $\varepsilon(\mathcal{F}_j) = \text{mod}(\frac{\mathcal{F}_j}{\tau}, 1)$, with respect to the tolerance of the sign function of a shifted cosine. In other words, these symmetry poles are locally palindromic, until somewhere the symmetry breaks. This also means that the approximate separations between palindromic symmetry poles are $\{\mathcal{F}_j\}, \{\frac{\mathcal{F}_j}{2}\}, \{\mathcal{F}_j + \frac{\mathcal{F}_j}{2}\}$. For a nonzero value of ϕ , with the appropriate winding number, (2.8) gives $\Delta n(\phi) = \frac{\phi\tau}{2\pi}$. Therefore, the approximate solutions for (2.11) are $n_{pal}(\phi) \simeq n_{pal}(\phi = 0) + \Delta n(\phi)$.

Now if we take a finite size structure of a given length N , the picture is no longer

approximate. If we define $n_{cent} = \frac{N+1}{2}$, there will always be two values of $0 \leq \phi < 2\pi$ where the structure becomes a perfect palindrome

$$\cos(2\pi n_{cent}\tau^{-1} + \phi_{pal}) = \pm 1 \Rightarrow \frac{\phi_{pal}}{\pi} = -\frac{N+1}{\tau} + m; m \in \mathbb{Z}.$$

This can be interpreted as follows: for any structure length there are two values of ϕ which will translate it via (2.8) along S_∞ so that its geometrical center will coincide with a palindromic symmetry pole of a long enough palindrome. So, for a general structure length $N = \mathcal{F}_j + \Delta N$, the palindromic values of ϕ are

$$\frac{\phi_{pal}}{\pi} = -\frac{1}{\tau} - \frac{\Delta N}{\tau} - \frac{\mathcal{F}_j}{\tau} = -\frac{1}{\tau} - \frac{\Delta N}{\tau} + \varepsilon(\mathcal{F}_j); \varepsilon \ll 1, \quad (2.12)$$

which is equivalent to keeping $\phi = 0$ and translating the structure center along S_∞ by $\Delta n = -\frac{1}{2} - \frac{\Delta N}{2} + \frac{1}{2}\tau\varepsilon(\mathcal{F}_j)$. This result shows that the required value of ϕ makes the center of the structure coincide with a palindromic symmetry pole. It is here where chains of length \mathcal{F}_j differ from others. In the case $\Delta N = 0$, the structure edges (separated from the center by $\mathcal{F}_j/2$) are also located at palindromic symmetry poles. However, if we choose a structure with non-Fibonacci length, the center slab and the edge slabs are poles of different families. Therefore, a different value of ϕ is required to bring the structure to palindromic symmetry around the edges and around the middle slab.

2.2.5 Generalization to 1D Aubry-Andre-Harper (AAH) model

The results given here for the C&P or the characteristic function approach are generalizable to Aubry-Andre-Harper (AAH) potential by simply dropping the sign[#] function in (2.3) (see [KZ12], and also the green diamonds in figure 2.5c). The AAH potential is discrete, but it is composed of a continuous alphabet. Consequently, there are no ϕ -driven phason-flips, but a continuous change in the entire structure as a function of ϕ , and the discrete staircase dependence on ϕ shared by C&P structures is replaced by continuous dependence (see figure 2.24a). The absence of phason flips annuls the meaning of fractional inversion/translation. However, the deviation from a palindrome $\eta(\phi)$ may still be defined, and we observe that AAH structures also experienced a π -periodic palindromic cycle, with the same values of ϕ_{pal} . However, this time the cycle is without a plateau, as there is no meaning of words and occurrences (see figure 2.24b). In chapter 4, we shall see that this result verifies the topological equivalence between the Fibonacci and the AAH chains.

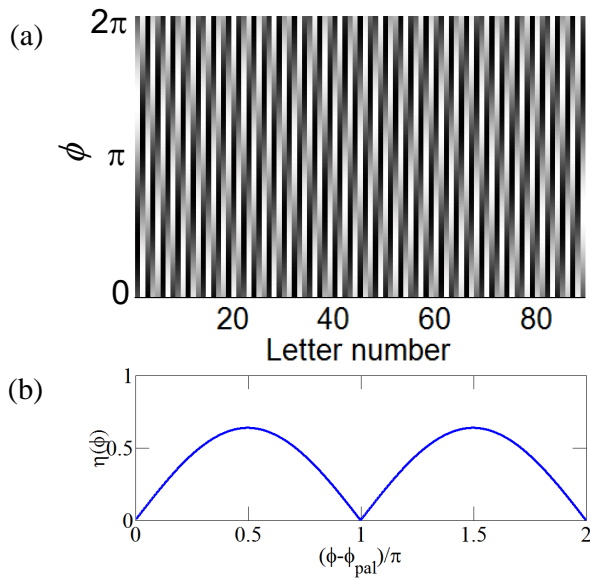


Figure 2.24: The Aubry-Andre-Harper structure dependence on ϕ . (a) An x - ϕ colormap of $\{\overrightarrow{AAH}_N(\phi)\}$, with $N = 89$ as a function of ϕ . This time the colormap is continuous in the interval $[-1, 1] - \cos(\pi\tau^{-1})$. (b) Behavior of $\eta(\phi - \phi_{pal})$.

2.3 Reciprocal space properties

Reciprocal space properties played a crucial historic role in the crystallography of quasicrystals. The electron diffraction measurement yielding a reciprocal space sharp diffraction pattern with a rotational symmetry which is irreconcilable with periodicity [SBGC84] has extended the formal definition of a crystal to include quasiperiodic structures. In this section we will describe the reciprocal space properties of C&P chains, and their connection to the spectral properties of the chains. These properties which are purely structural in origin will become instrumental in chapter 4 in the understanding of the topological properties of quasiperiodic chains.

2.3.1 Bragg peaks analysis of 1D structures

The diffraction pattern of infinite C&P quasiperiodic chains shows a dense set of Bragg peaks with their positions related by irrational numbers. In contrast to periodic crystals, where d integer indices are sufficient to characterize the diffraction of a d dimensional structure, n integer indices ($d < n$) are required to generate the diffraction vectors of quasiperiodic crystals [LS84, ZD85]. Except for the special case of non-Pisot quasicrystals that will not be discussed here, the relation between measurable diffraction peaks and theoretical Bragg peaks are quite similar between periodic and quasiperiodic structures. In 1D, the infinite chain (periodic or quasiperiodic) possess Bragg peaks, but for finite systems (as all experimental systems are) the diffraction spectrum contains sharp diffraction peaks which are

related to the Bragg peaks of the infinite chain. The main difference in that sense which sets quasiperiodic structures apart from periodic crystals is the large amount of peaks, the variable intensity of the peaks, and the fact that in general the spatial frequency of the diffraction peaks does not coincide with that of the infinite chain Bragg peaks.

The diffraction spectrum of the infinite Fibonacci chain is composed of sharp peaks, at the spatial frequencies given by

$$k_q = p + q\tau^{-1} \quad (2.13)$$

where $\tau \equiv (1 + \sqrt{5})/2$ is the golden mean, and $p, q \in \mathbb{Z}$. The locations and properties of the diffraction peaks may be analyzed using the C&P [ZD85] and the C&P based co-numbering [VM01] approach, after proper normalization. Figure 2.25 shows a numerical calculation of the diffraction pattern for Fibonacci chains of two lengths. The prediction of (2.13) in determining the resonant spatial frequencies k_q seem to be a very good fit, rapidly improving as a function of structure length.

The reciprocal space viewpoint is important to this work because the generalized Bloch theorem connects the Bragg peak spatial frequency and the spectral gaps obtained by the interrogation of the structure by the scattering of waves. In chapter 4 this relation will become very useful in explaining the topological properties of quasiperiodic structures, especially with regards to the question of their origin and the role of true irrationality.

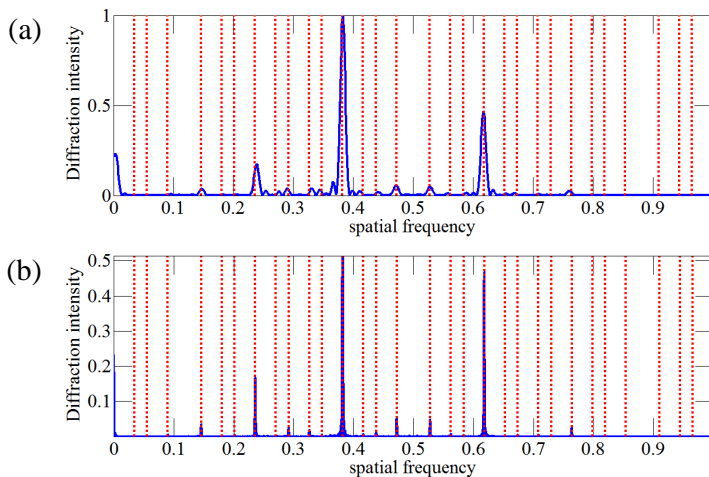


Figure 2.25: The Diffraction pattern of a Fibonacci chains (generated by substitution/concatenation) S_{10} (a) and S_{14} (b), in blue solid lines. The spatial frequency axis is normalized as described in chapter 4. Red dotted lines mark possible values for the diffraction peaks k_q predicted by (2.13).

2.3.2 The role of irrationality in reciprocal space

A repeating question regarding the topological and other properties of quasiperiodic structures is the following: if we are always dealing with a finite chain, then why do we need to use an irrational C&P slope, and how does the properties of the finite chain relate to those of the infinite chain.

From a purely structural point of view as developed here, we plot the diffraction spectrum of a C&P structure as a function of the C&P slope in a colormap (see figure 2.26). This plot is identical to that of Wannier [Wan78] for the case of Bloch electrons in magnetic field, where the spatial frequency is replaced by magnetic field, and the C&P slope is replaced by the electron density. Following the analysis by Wannier, we label the lines with the integers $[q, p]$ such that each line equation is $y = qx + p$ with (x, y) corresponding to C&P slope and spatial frequency respectively. Figure 2.27 depicts some of those labels. In the Fibonacci case these labels correspond to those of (2.13), as depicted in figure 2.28.

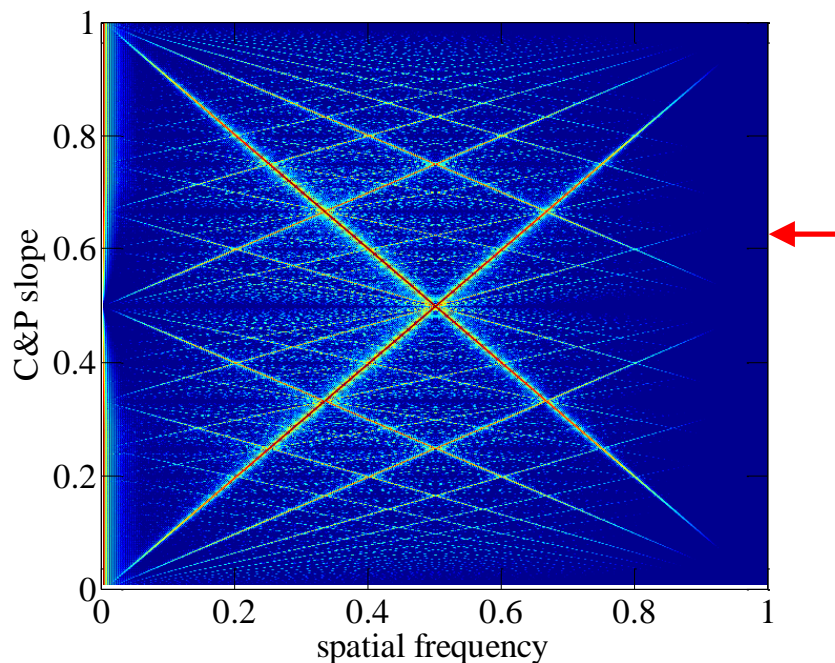


Figure 2.26: A colormap depicting the diffraction spectrum such as presented in figure 2.25 for multiple values of the C&P slope. The Fibonacci chain slope, τ^{-1} is indicated by a red arrow.

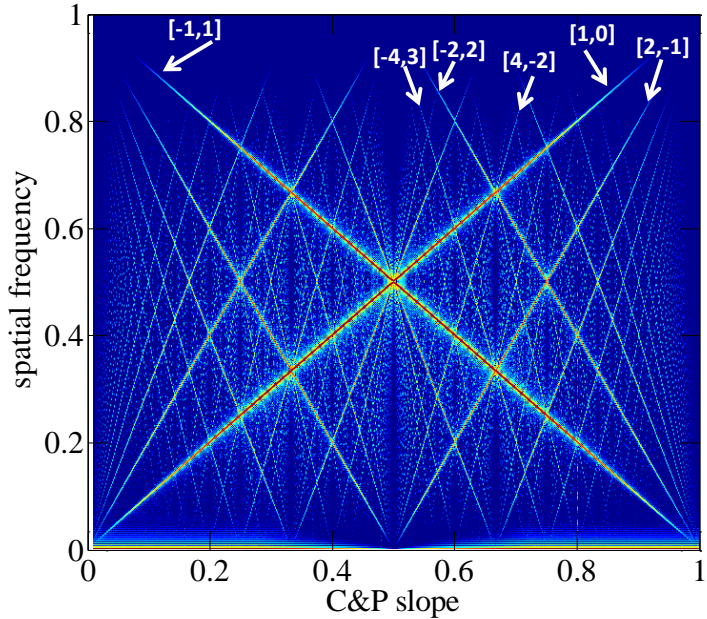


Figure 2.27: The same colormap as presented in figure 2.26, with inverted axes. The labels $[q, p]$ for several lines are indicated by white arrows.

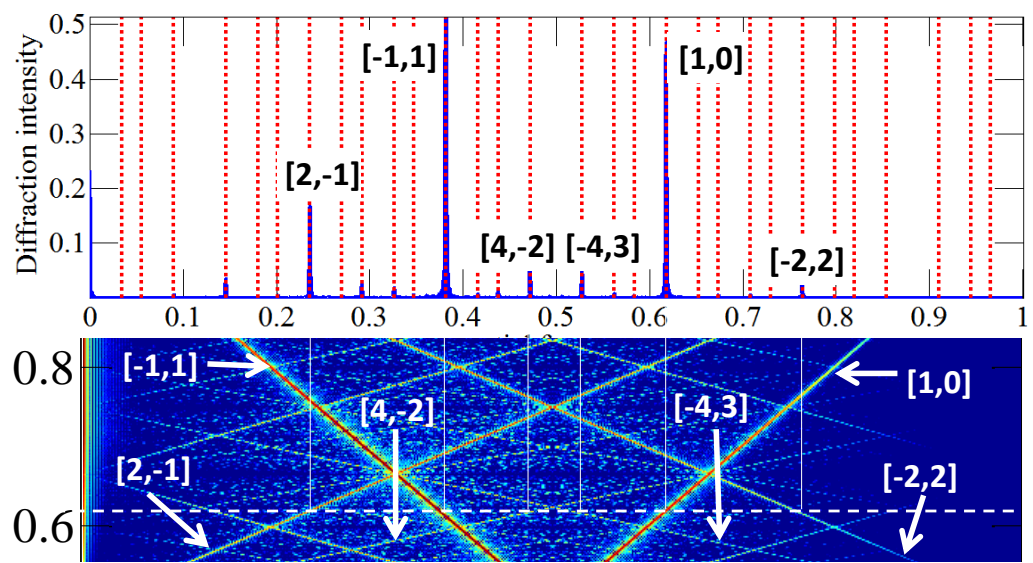


Figure 2.28: Top: the diffraction spectrum for the Fibonacci chain S_{14} from figure 2.25. Bottom: A section of the colormap from figure 2.26 around the Fibonacci slope $\tau^{-1} \cong 0.62$ and the corresponding line labels $[q, p]$ as presented in figure 2.27. These labels are now assigned to the diffraction peaks, and corroborate (2.13).

These relations and conclusions are deeply connected to the topological properties of quasiperiodic chains, and will be discussed in detail in chapter 4. For the time

being, just by analyzing this C&P Wannier diagram, we may say that the labels $[q, p]$ of (2.13) have a regular dependence on the C&P slope and nothing abrupt happens at irrational slopes. The parameter which strongly depends on the slope is the number of diffraction peaks. We define the degree of irrationality of the C&P slope p'/q' by the length of the resulting unit cell, equivalent to $p' + q' - 1$ (see 2.1.8). For such a slope, we find a maximum number of nonzero non-redundant values of diffraction peaks k_q to be $q' - 1$. As a trivial example, the simplest periodic structure “ABABAB...” corresponds to the C&P slope $p'/q' = 1/2$ yielding only one diffraction peak. A less trivial example is the Fibonacci chain S_{10} , for which we have $p'/q' = 55/89$, yielding 88 (at maximum) observable diffraction peaks. Therefore, C&P structures generated by slopes of stronger irrationality and having the corresponding structure lengths, will have a number of diffraction peaks which will grow as $q' - 1$, and in the limit of a truly irrational slope and an infinite chain we will have an infinite number of peaks. The other side of this argument is that for a finite system, the labels of the observable diffraction peaks are conserved as compared to the infinite chain, but their spatial frequencies deviate from their infinite chain position by $q \left(\tau^{-1} - \frac{p'}{q'} \right)$.

2.3.3 Generalization to the Aubry-Andre-Harper model

The results given in 2.3.2 for the C&P or the characteristic function approach are not strictly generalizable to Aubry-Andre-Harper (AAH) potential obtainable by simply dropping the $\text{sign}[\#]$ function in (2.3). The AAH potential is discrete and quasiperiodic when using an irrational argument, but it is composed of a continuous alphabet. In this case, the maximum number of diffraction peaks for this structure is 2 (corresponding to a periodic structure). This behavior is depicted in a Wannier-like diagram in figure 2.29a. However, using a recent proposal [KZ12] to smoothly modify the AAH model into its equivalent C&P model (using a smoothing parameter β), we see that the number of diffraction peaks gradually increases (shown in figure 2.29).

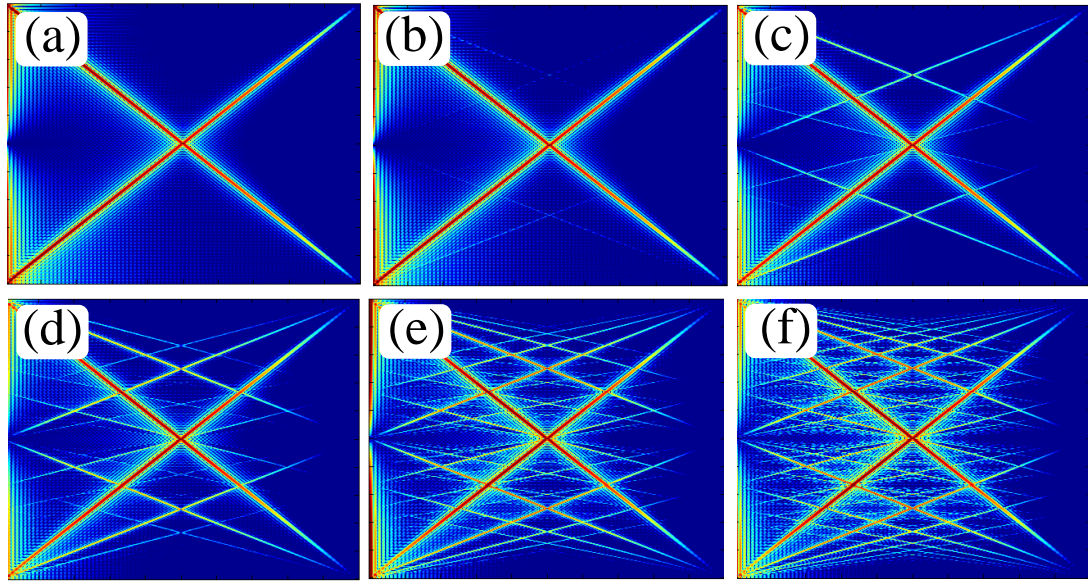


Figure 2.29: The diagram in figure 2.26 redone for the Aubry-Andre-Harper (AAH) model with the smooth transition parameter β (axes are omitted for clarity - they are identical to those in figure 2.26). Panel (a) is for the true AAH model. Panels (b)-(f) correspond to $\beta = 0.3, 1, 2, 5, 10$ respectively.

Chapter 3

Spectral analysis of quasiperiodic chains

In this chapter we develop methods, essential for the understanding of chapter 4. The well known scattering matrix approach [ADL13] will be revisited, and presented using specific notations which will become useful in chapter 4. The computerized version of our scattering matrix method will be demonstrated for various families of structures, finally focusing on the Fibonacci spectrum and its topological and other properties. Additionally, we revisit the gap labeling theorem which assigns integer topological labels to the spectral gaps. Finally, we discuss the concept of inducing defect gap modes in any structure with a gaped spectrum, and develop a Fabry-Perot cavity model to fully analyze such modes.

3.1 Tools and methods: Scattering analysis of 1D structures

3.1.1 Background

We now review the methods for studying wave propagation in one-dimensional complex structures. Examples are presented for transport through finite-sized layered dielectric systems with periodic, quasi-periodic, fractal, disordered, and random structure, to illustrate the effect of spatial structure upon the spectrum of modes as well as the local mode intensity.

Both classical and quantum waves are highly sensitive probes of the details of the physical and geometric structure of the medium in which they propagate. Periodic dielectric structures produce spectra with transmission bands, leading to the remarkable physics of photonic band gaps [JJWM11]. Other kinds of structures, such as quasi-periodic [AC03, Mac06, DG11, DB12], fractal, disordered or random structures [And58, AM07], lead to other distinct spectral features such as topological features. Important questions include the frequency distribution of modes, as well as their spatial localization and structure. We describe the density of states, the

counting function (the integrated density of states), the transmission probability, and also the local field amplitude and intensity, each of which has a direct physical meaning, and present a variety of results to illustrate the effect of the layered structure type on the aforementioned physical quantities. This summary is intended to highlight the adaptation performed to this very well known method [ADL13], and also to introduce the notations which will be helpful in the next chapters.

3.1.2 Wave equations

The general aspects of coherent propagation are common to a wide variety of waves which propagate in scattering media. This notwithstanding, each type of wave exhibits its own characteristic behavior. We now present several examples of wave equations, and we study two important classes in greater detail: the Helmholtz equation, which describes scalar wave propagation suited for electromagnetic TE or TM modes propagating in a dielectric, and the Schrödinger equation associated with a non interacting electron gas (weakly disordered metals or semiconductors).

Helmholtz equation

The case of electromagnetic waves is special, for several reasons. It is probably one of the earliest examples where changes in wave phase coherence due to passage through a random medium was examined. In the beginning of the twentieth century, very precise studies were carried out on electromagnetic wave propagation through diffusive media, specifically the atmosphere. From a conceptual viewpoint, this problem stimulated the community working in the theory of probability, who regarded it as a new field for the application of methods developed for the study of Brownian motion. For the atmosphere, the description in terms of a static disordered medium is not appropriate. For many other cases, however, the description in terms of static disorder described by a time-independent potential works well, and it is this case that we consider here.

For a TE mode propagating in the x direction along a medium with spatially varying dielectric function $\epsilon(x)$, Maxwell's equations for the electromagnetic field amplitudes, $E_z = \psi(x)e^{-i\omega t}$ and $H_y = \chi(x)e^{-i\omega t}$, become two coupled equations

$$\frac{d\psi}{dx} = ik_0 \chi \quad , \quad \frac{d\chi}{dx} = ik_0 \frac{\epsilon(x)}{\bar{\epsilon}} \psi,$$

where $k_0 = \bar{n}\omega/c$, namely for an average dielectric of refractive index $\bar{n} = \sqrt{\bar{\epsilon}/\epsilon_0}$ and average dielectric constant $\bar{\epsilon}$ (See for instance [AM07]). This reduces to a scalar Helmholtz equation for $\psi(x)$,

$$-\frac{d^2\psi}{dx^2} - k_0^2 v(x)\psi(x) = k_0^2 \psi(x),$$

where $v(x) \equiv \frac{\epsilon(x)}{\epsilon} - 1 \equiv n^2(x) - 1$, with refractive index $n(x)$.

Schrödinger equation

The Schrödinger wave equation for a particle of mass m in a one dimensional potential $V(x)$ also has a Helmholtz-like form

$$-\frac{\hbar^2}{2m} \frac{d^2\psi}{dx^2} + V(x)\psi = E\psi(x).$$

This can be formally written as $H\psi = k^2\psi$.

The two examples we have discussed are not the only ones to exhibit effects related to coherent propagation in complex media. In fact, these effects are common to all wave phenomena (quantum, optical, hydrodynamic, etc), independent of dispersion relation and space dimension, provided that there are no nonlinear effects. Indeed, these may hide complexity effects. Moreover, nonlinear equations often have special solutions (solitons, vortices,...) whose stability is ensured by a topological constraint which is very difficult to destabilize by means of a disordered potential. The competitive role of disorder and non-linearity is important but is still relatively poorly understood.

3.1.3 Scattering matrix formalism

Propagation through a one-dimensional structure can be described by a scattering matrix, or S-matrix, $S(k)$, relating incoming and outgoing amplitudes of propagating plane waves of wave vector $k = \omega/c$ (see figure 3.1a). Excellent pedagogical discussions, particularly for one-dimensional systems, can be found in [AB85, BV12]. The scattering S matrix is defined as

$$\begin{pmatrix} o_L \\ o_R \end{pmatrix} = \begin{pmatrix} \overrightarrow{r} & t \\ t & \overleftarrow{r} \end{pmatrix} \begin{pmatrix} i_L \\ i_R \end{pmatrix} \equiv S \begin{pmatrix} i_L \\ i_R \end{pmatrix}. \quad (3.1)$$

The transmission and reflection amplitudes, $t \equiv |t|e^{i\theta_t}$, $\overrightarrow{r} \equiv |r|e^{i\theta_r}$, and $\overleftarrow{r} \equiv |r|e^{i\theta_l}$ are marked by arrows corresponding to left or right incoming waves in the two experiments represented on figure 3.1b. We consider the system to be invariant under time reversal, so that the matrix S is symmetric. Furthermore, it is unitary ($S^{-1} = S^\dagger$) as a consequence of conservation of probability (for the Schrödinger equation), or of the intensity of the field (for the Helmholtz equation). This leads to the set of relations

$$\begin{aligned} |\overrightarrow{r}|^2 + |t|^2 &= 1 \\ |\overleftarrow{r}|^2 + |t|^2 &= 1 \\ t\overrightarrow{r}^* + \overleftarrow{r}t^* &= 0. \end{aligned} \quad (3.2)$$

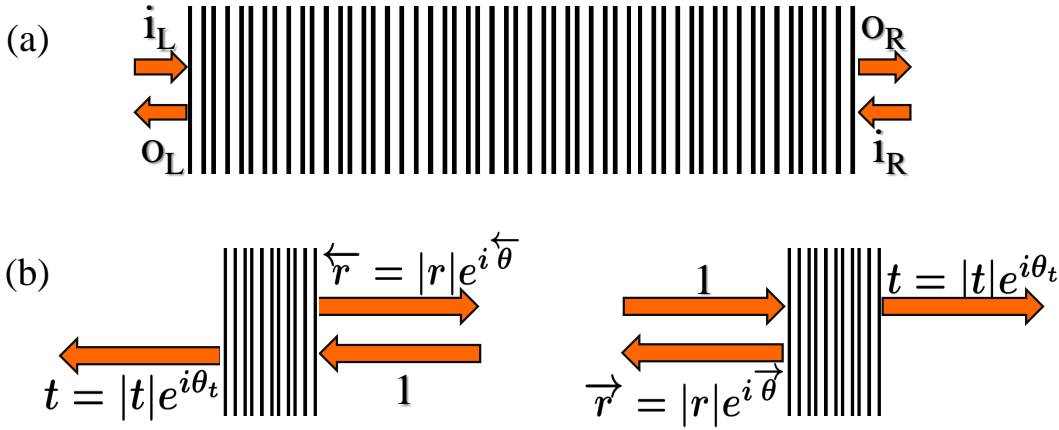


Figure 3.1: The scattering problem. (a) A sketch for the notations of incoming and outgoing waves. (b) The amplitude notations for two possible experiments: incoming waves from the right or from the left.

The scattering matrix, therefore, contain two magnitudes and three phases. Equation (3.2) implies that $\det S = \vec{r}\overleftarrow{r} - t^2 = -t/t^*$. Since S is unitary, it can be diagonalized by a unitary transformation into the diagonal form containing only two independent phases

$$\begin{pmatrix} e^{i\Phi_1} & 0 \\ 0 & e^{i\Phi_2} \end{pmatrix}. \quad (3.3)$$

Defining the total phase shift, $\delta(k) \equiv (\Phi_1(k) + \Phi_2(k))/2$, we then have

$$\det S(k) = e^{2i\delta(k)} = -\frac{t}{t^*}. \quad (3.4)$$

From the definition of the phase of the transmission amplitude, $t \equiv |t|e^{i\theta_t}$, and from (3.4), we obtain the relation $\delta(k) = \theta_t(k) + \pi/2$. A simple and elegant relation exists between the phase shift $\delta(k)$ and the change of density of states $\rho(k)$, such that

$$\rho(k) - \rho_0(k) = \frac{1}{2\pi} \text{Im} \frac{\partial}{\partial k} \ln \det S(k), \quad (3.5)$$

where $\rho_0(k)$ is the density of states for the free system, namely with zero potential for the Schrödinger equation, or $\epsilon(x) = \epsilon_0$ for the Helmholtz equation.

The source of scattering in either Schrödinger (or Helmholtz) equation is the varying potential $V(x)$ (or the varying refractive index $n(x)$). Should it vanish (the free space case), the S -matrix reduces to the identity. Now assume that the potential decreases fast enough so that we can enclose the scattering system inside a region of size L , much larger than the support of the scattering potential (as some sort of “black box”). We then apply periodic boundary conditions, $\psi(0) = \psi(L)$ and $\psi'(0) = \psi'(L)$, at the boundary of the large box, noting that for large enough L , the

physics is independent of the precise boundary conditions. For large enough L , we have

$$\begin{aligned}\psi(0) = \psi(L) &\Rightarrow i_L + o_L = o_R e^{ikL} + i_R e^{-ikL} \\ \psi'(0) = \psi'(L) &\Rightarrow ik(i_L - o_L) = ik(o_R e^{ikL} - i_R e^{-ikL}).\end{aligned}$$

These algebraic relations may be written as a spectral condition

$$\det \left(1 - e^{ikL} \begin{pmatrix} 0 & 1 \\ 1 & 0 \end{pmatrix} S(k) \right) = 0.$$

Solving for S , leads to the following relation between the total phase shift and the possible wave vectors

$$k_n(L) = \frac{\pi n}{L} - \frac{\delta(k_n)}{L}. \quad (3.6)$$

Noting that $k_n^{(0)}(L) = \pi n/2L$ are the eigenmodes in the absence of scattering potential, namely for $\delta(k) = 0$, we can rewrite (3.6) for two consecutive values of n under the form,

$$(k_{n+1} - k_n) \left(L + \frac{d\delta(k)}{dk} \right) = \pi.$$

Defining the density of states, or density of modes (DOM) as $\rho(k) = 1/(k_{n+1} - k_n)$ leads to (3.5)

$$\rho(k) - \rho_0(k) = \frac{1}{\pi L} \frac{d\delta(k)}{dk}.$$

For the integrated density of states (of modes), also known as the counting function, $\mathcal{N}(k) = \int^k \rho(k') dk'$, we obtain

$$\delta(k) = \pi L \Delta \mathcal{N}(k) = \pi L (\mathcal{N}(k) - \mathcal{N}_0(k)), \quad (3.7)$$

which relates the total phase shift of the S -matrix, and equivalently the transmitted phase shift, to an important spectral quantity. Both (3.5) and (3.7) are rather remarkable (and well-known) results since they express the fact that a measurement of the scattering data from a black box allows one to retrieve its spectral information provided it is coupled to the external environment. This is the strength of the scattering approach.

3.1.4 Transfer matrix formalism

In the previous paragraph, we have advocated the description of wave propagation in complex systems using the S -matrix. It relates outgoing to incoming amplitudes in a unitary way, and provides a number of elegant expressions for spectral and transport quantities. However, in certain situations, such as for transport in one-dimensional problems, the transfer matrix formalism offers computational advantages. For example, in layered systems it is useful to take advantage of the propagation of an incoming wave along a given fixed direction using the multiplicative property of the transfer matrix. To see how this works, we rewrite (3.1) in an equivalent form, now relating left-bound and right-bound amplitudes, instead of incoming and outgoing amplitudes (see figure 3.1)

$$\begin{pmatrix} i_R \\ o_R \end{pmatrix} = \begin{pmatrix} \frac{1}{t} & -\frac{\vec{r}}{t} \\ \frac{\vec{r}}{t} & \frac{1}{t^*} \end{pmatrix} \begin{pmatrix} o_L \\ i_L \end{pmatrix} \equiv M \begin{pmatrix} o_L \\ i_L \end{pmatrix}, \quad (3.8)$$

which defines the transfer matrix M . Note that $\det M = 1$.

Remark: A great asset of the S -matrix and M -matrix formulations is that they are very general and they do not require to specify a wave equation or any local properties such as group velocity, dispersion at least until some more specific calculations.

The main advantage of the transfer matrix description over the algebraically related S -matrix is that it allows to computerize the calculation of the total transfer M matrix for many complex structures such as the cases of a one-dimensional periodic, quasi-periodic, fractal-like and random. This results from the multiplication structure, i.e. a piecewise-constant stratified structure [BW00], although the method can serve as an approximation for any dielectric stratified medium with $\epsilon = \epsilon(z)$, $\mu = \mu(z)$. The transfer matrix can be viewed as a mapping transforming the wave after it passes through each scatterer (interface conditions) or layer (phase accumulation).

The implementation of the method in the case of the propagation of electromagnetic waves in one-dimensional (1D) waveguide structures built out of complex media is described as follows. We first reiterate the basic equations and then consider specific cases of layered dielectric media: free space, Fabry-Perot structure, periodic structures (photonic crystals), random systems and single impurity. Finally, we discuss in more detail the case of a Fibonacci potential. In all these cases, we obtain spectral quantities (transmission, counting function and density of modes) and the steady state (stationary) local structure of the electric field.

The use of the transfer matrix method for solving Maxwell equations in photonic systems essentially converts them into a set of finite difference equations in real space and then rearranges those equations into the form of a transfer matrix [BW00]. The

general solution for the transverse electric (TE) electric field E_x propagating along the z -direction in a 1D structure is obtained from the solution of the wave equation $c^2 \partial_z^2 E_x - \partial_t^2 E_x = 0$. It takes the form

$$E_x(z, t) = E_x^{(\rightarrow)}(z_0) e^{i(k_z(z)z - \omega t)} + E_x^{(\leftarrow)}(z_0) e^{i(-k_z(z)z - \omega t)},$$

where $E_x^{(\rightarrow)}(z_0)$ and $E_x^{(\leftarrow)}(z_0)$ denote right-bound (\rightarrow) and left-bound (\leftarrow) waves steady-state amplitudes evaluated at the origin z_0 of the structure. Setting $k(z) = n(z)k$, we can write for a monochromatic wave of frequency ω ,

$$E_x(z) = E_x^{(\rightarrow)}(z_0) e^{ik(z)z} + E_x^{(\leftarrow)}(z_0) e^{-ik(z)z}. \quad (3.9)$$

Using (3.8), we obtain

$$\begin{pmatrix} E_x^{(\rightarrow)} \\ E_x^{(\leftarrow)} \end{pmatrix}_{z_{end}} \equiv M \begin{pmatrix} E_x^{(\rightarrow)} \\ E_x^{(\leftarrow)} \end{pmatrix}_{z_0}, \quad (3.10)$$

where z_0 and z_{end} are the coordinates of the two outer boundaries of the structure. In non-absorbing dielectric structures considered here, conservation of energy implies that M is a unitary 2×2 complex valued matrix of unity determinant. In a layered structure $z_0 < z_1 < \dots < z_{end}$, and denoting $M_{z_i \rightarrow z_{i+1}}$ the transfer matrix associated to a layer, we have a general multiplication scheme

$$M_{z_0 \rightarrow z_{end}} = M_{z_{end-1} \rightarrow z_{end}} \cdots M_{z_1 \rightarrow z_2} M_{z_0 \rightarrow z_1}.$$

For practical purposes we use a scheme which is a bit more intricate. Namely, each $M_{z_i \rightarrow z_{i+1}}$ appears as a product of sub-matrices responsible either for the crossing of an interface between two adjacent dielectrics or for the free propagation through a homogeneous dielectric slab. Also, we will now restrict ourselves to the more specific case of a binary layered structure built out of N slabs of two types of dielectrics A and B , where $n_{A,B}$ are the respective refractive indices in type A and B slabs of respective corresponding thicknesses $d_{A,B}$. The dielectric contrast, describing the modulation strength and defined as $(n_{high} - n_{low})/n_{low}$. The notations for this case are given in figures 3.2 and 3.3. The solution for the electric field in a single slab of type A or B can be written as

$$E_{A,B} = E_{A,B}^{(\rightarrow)} e^{in_{A,B}kz} + E_{A,B}^{(\leftarrow)} e^{-in_{A,B}kz}, \quad (3.11)$$

where $E_{A,B}^{(\rightarrow)}$ and $E_{A,B}^{(\leftarrow)}$ are the right-bound and left-bound electric fields evaluated at the left boundary of slab A, B .

Remark: As stated in the before, the M (or S)-matrix formalism does not require precise knowledge of a local wave equation inside the structure and can be formulated without the input of a local group velocity (even when ill-defined in the

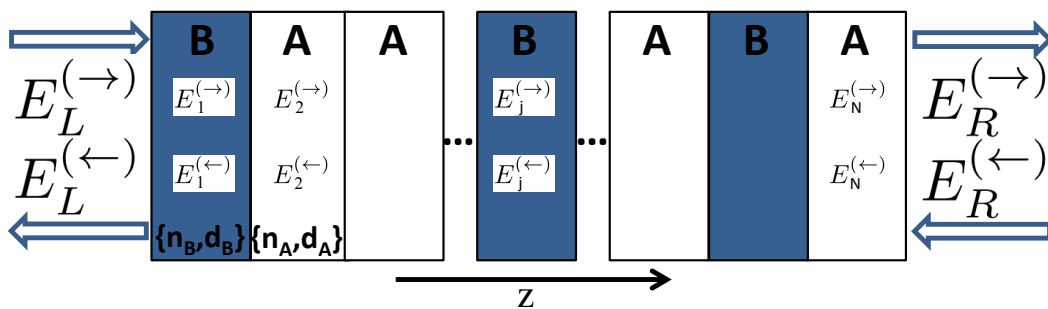


Figure 3.2: Setup and wave propagation notations for the dielectric scattering geometry problem. $\{i_L, o_L\} \equiv \{E_L^{(\rightarrow)}, E_L^{(\leftarrow)}\}$ denote the electric field amplitudes of incoming and outgoing waves at the left boundary, respectively. Similarly, $\{i_R, o_R\} \equiv \{E_R^{(\leftarrow)}, E_R^{(\rightarrow)}\}$ are defined outside the right structure boundary.

present case due to the discontinuity of the refractive index in the layered structure). But at some point the writing of relations (3.9) and (3.11) rely on the definition of a wave vector and a group velocity : here we assume free propagation in each individual slab.

An interface $I \equiv A \leftrightarrow B$ between adjacent slabs A and B is defined in figure 3.3. The boundary conditions at a dielectric interface are imposed through continuity relations

$$E_A^{(\rightarrow)} + E_A^{(\leftarrow)} \Big|_{I\pm} = E_B^{(\rightarrow)} + E_B^{(\leftarrow)} \Big|_{I\mp}, \quad (3.12)$$

and

$$n_A \left(E_A^{(\rightarrow)} + E_A^{(\leftarrow)} \right) \Big|_{I\pm} = n_B \left(E_B^{(\rightarrow)} + E_B^{(\leftarrow)} \right) \Big|_{I\mp}. \quad (3.13)$$

The phase accumulation which accounts for free propagation through a slab A or B is

$$\begin{cases} E_{A \rightarrow, B \rightarrow}^{(\rightarrow)} = E_{A \leftarrow, B \leftarrow}^{(\rightarrow)} e^{in_{A,B}d_{A,B}k} & \equiv E_{A \leftarrow, B \leftarrow}^{(\rightarrow)} e^{i\delta_{A,B}} \\ E_{A \rightarrow, B \rightarrow}^{(\leftarrow)} = E_{A \leftarrow, B \leftarrow}^{(\leftarrow)} e^{-in_{A,B}d_{A,B}k} & \equiv E_{A \leftarrow, B \leftarrow}^{(\leftarrow)} e^{-i\delta_{A,B}}, \end{cases}$$

where we have defined,

$$\delta_A \equiv n_A d_A k \quad , \quad \delta_B \equiv n_B d_B k. \quad (3.14)$$

It is convenient to set the layer thickness so that $n_A d_A = n_B d_B$ which leads to $\delta_A = \delta_B \equiv \delta$.

Remark: All scattering matrix based plots in this chapter and on have the same x -axis: $\delta/\pi = ndk = 2nd/\lambda$. For simplicity, the axis title is given as k .

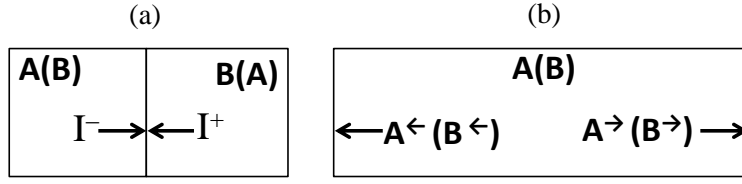


Figure 3.3: Setup of notations for the continuity relations at an interface BA or BA (a), and for the free propagation through a slab A or B (b).

The next step is the change of variables

$$\begin{cases} E_{A,B}^{(+)} & \equiv E_{A,B}^{(\leftarrow)} + E_{A,B}^{(\rightarrow)} \\ E_{A,B}^{(-)} & \equiv i \left(E_{A,B}^{(\leftarrow)} - E_{A,B}^{(\rightarrow)} \right), \end{cases} \quad (3.15)$$

The continuity equations (3.12) and (3.13) can then be rewritten as

$$\begin{cases} E_{A,B}^{(+)} \Big|_{I^{+,-}} & = E_{B,A}^{(+)} \Big|_{I^{+,-}} \\ E_{A,B}^{(-)} \Big|_{I^{+,-}} & = \frac{n_{B,A}}{n_{A,B}} E_{A,B}^{(-)} \Big|_{I^{+,-}}. \end{cases} \quad (3.16)$$

This leads to the definition of four sum transfer matrices defined by the two sets of relations,

$$\begin{aligned} \begin{pmatrix} E^{(+)} \\ E^{(-)} \end{pmatrix} \Big|_{A|I^+} & \equiv T_{AB} \begin{pmatrix} E^{(+)} \\ E^{(-)} \end{pmatrix} \Big|_{B|I^-} \\ \begin{pmatrix} E^{(+)} \\ E^{(-)} \end{pmatrix} \Big|_{B|I^+} & \equiv T_{BA} \begin{pmatrix} E^{(+)} \\ E^{(-)} \end{pmatrix} \Big|_{A|I^-}, \end{aligned}$$

and

$$\begin{aligned} \begin{pmatrix} E^{(+)} \\ E^{(-)} \end{pmatrix} \Big|_{A \rightarrow} & \equiv T_A \begin{pmatrix} E^{(+)} \\ E^{(-)} \end{pmatrix} \Big|_{A \leftarrow} \\ \begin{pmatrix} E^{(+)} \\ E^{(-)} \end{pmatrix} \Big|_{B \rightarrow} & \equiv T_B \begin{pmatrix} E^{(+)} \\ E^{(-)} \end{pmatrix} \Big|_{B \leftarrow}. \end{aligned}$$

Now, with the aid of (3.14) and (3.15), we obtain four real valued matrices

$$T_{AB} = \begin{pmatrix} 1 & 0 \\ 0 & \frac{n_B}{n_A} \end{pmatrix} = T_{BA}^{-1}, \quad T_{BA} = \begin{pmatrix} 1 & 0 \\ 0 & \frac{n_A}{n_B} \end{pmatrix} = T_{AB}^{-1},$$

and

$$T_{A(B)} = \begin{pmatrix} \cos \delta_{A(B)} & -\sin \delta_{A(B)} \\ \sin \delta_{A(B)} & \cos \delta_{A(B)} \end{pmatrix},$$

so that the total transfer matrix \widetilde{M}_N of N dielectric slabs is

$$\begin{pmatrix} E^{(+)} \\ E^{(-)} \end{pmatrix}_N \equiv \widetilde{M}_N \begin{pmatrix} E^{(+)} \\ E^{(-)} \end{pmatrix}_0. \quad (3.17)$$

To illustrate the efficiency of this systematic approach to the calculation of \widetilde{M}_N as a product of an appropriate sequence of the four sub-matrices, we consider the matrix \widetilde{M}_8 describing the Fibonacci chain S_5 inserted between infinite slabs of type A (to preserve unitarity) as

$$\widetilde{M}_8([A][ABAABABA][A]) = T_A T_{AB} T_B T_{BA} T_A T_{AB} T_B T_{BA} T_A T_A T_{AB} T_B T_{BA} T_A.$$

Once the transfer matrix is obtained, the next step is to find the scattering matrix. One way is to use the algebraic transformation between the matrices.

3.1.5 Scattering and transfer matrix calculations

The spectral numeric calculations in the current work begins by simply obtaining the S -matrix components, $\{t, \vec{r}, \overleftarrow{r}\}$, directly from the \widetilde{M} -matrix. We consider the two experiments schemes in figure 3.1b, and write the corresponding version of (3.17) such that

$$\begin{cases} E_0^{(\rightarrow)} = 1 \\ E_N^{(\rightarrow)} = t(k) \\ E_0^{(\leftarrow)} = \vec{r}(k) \\ E_N^{(\leftarrow)} = 0 \end{cases}, \quad \begin{pmatrix} t \\ -it \end{pmatrix} \equiv \widetilde{M}_{tot} \begin{pmatrix} \vec{r} + 1 \\ i(\vec{r} - 1) \end{pmatrix}, \quad (3.18)$$

and

$$\begin{cases} E_0^{(R)} = 1 \\ E_N^{(R)} = \overleftarrow{r}(k) \\ E_0^{(L)} = t(k) \\ E_N^{(L)} = 1 \end{cases}, \quad \begin{pmatrix} 1 + \overleftarrow{r} \\ i(1 - \overleftarrow{r}) \end{pmatrix} \equiv \widetilde{M}_{tot} \begin{pmatrix} t \\ it \end{pmatrix}. \quad (3.19)$$

From these expressions, we directly calculate the amplitudes $\{t, \vec{r}, \overleftarrow{r}\}$ (magnitude and phase), and from them, deduce the transmission and reflection coefficients $\mathcal{T}(k)$ and $\mathcal{R}(k)$, the density of modes $\rho(k)$ and the counting function $\mathcal{N}(k)$.

- Transmission and reflection spectra

The transmission and reflection spectra are calculated for the case in (3.18) or

(3.19), so that the spectra are normalized by the incoming plane wave electric field amplitude. The final expressions are

$$\begin{aligned} \mathcal{T}(k) &\equiv |t(k)|^2 = \frac{4}{\|\widetilde{M}_{tot}(k)\|_2^2 + 2} \\ \mathcal{R}(k) &\equiv |\vec{r}(k)|^2 = |\overleftarrow{r}(k)|^2 = \frac{\|\widetilde{M}_{tot}(k)\|_2^2 - 2}{\|\widetilde{M}_{tot}(k)\|_2^2 + 2} = 1 - \mathcal{T}(k), \end{aligned} \quad (3.20)$$

where $\|\widetilde{M}\|_2^2 \equiv \widetilde{M}_{11}^2 + \widetilde{M}_{12}^2 + \widetilde{M}_{21}^2 + \widetilde{M}_{22}^2$, and $\widetilde{M} = [\widetilde{M}_{ij}]$.

- Density of modes spectrum calculation

The density of modes (DOM), $\rho(k)$, can now be calculated from either the scattering or transfer matrix, utilizing the total phase shift $\delta(k)$ or the phase of the transmitted amplitude $\theta_t(k)$. For a 1D system of length L , the normalized DOM given by (3.5) is $\rho(k) \equiv \frac{1}{L} \frac{d\theta_t(k)}{dk} = \frac{1}{L} \frac{d\delta(k)}{dk}$. The normalization with the length L is convenient as it keeps the DOM of a free system equal to one, and simplifies the evaluation of the relative enhancement of $\rho(k)$ for a structured system compared to a free one. This normalization also allows, in the case of aperiodic inhomogeneous systems, to give a meaning to otherwise ill defined quantities such as the effective group velocity and wave vector. The calculation of $\rho(k)$ using either scattering or transfer matrices is thus based on,

$$\left\{ \begin{array}{l} \rho(k) = \frac{1}{L} \text{Im} \frac{\partial}{\partial k} \ln \det S(k) \\ \rho(k) = \frac{1}{L} \frac{d\theta_t(k)}{dk} = \frac{1}{L} \frac{y'(k)x(k) - x'(k)y(k)}{x^2(k) + y^2(k)} \\ t(k) = x(k) + iy(k) \end{array} \right. .$$

- Integrated density of modes (counting function) calculation

The integrated density of modes, also normalized by $1/L$, and following the very same relations may be calculated as

$$\left\{ \begin{array}{l} \mathcal{N}(k) = \frac{1}{\pi L} \text{Im} \ln \det S(k) \\ \mathcal{N}(k) = \frac{1}{\pi L} (\theta_t(k) + \pi/2) \end{array} \right. .$$

- Amplitude of the local electric field

The electric field amplitude and intensity $k - z$ maps are obtained by calculating $E^+(k)$ for each z coordinate inside the structure, using two transfer matrices instead of one: the total transfer matrix \widetilde{M}_{tot} , and the partial transfer matrix from the left end to the point of interest \widetilde{M}_j . We now describe the calculation for the case of incoming waves from the left and also for a combination. An equivalent process may be repeated for incoming waves from the right. Firstly, \vec{r} and t are calculated as before using \widetilde{M}_{tot} . Then, we can simply use \widetilde{M}_j to calculate the field and intensity in slab j using

$$\left\{ \begin{array}{l} \left(\begin{array}{c} E^{(+)} \\ E^{(-)} \end{array} \right)_j = \widetilde{M}_j \left(\begin{array}{c} \vec{r} + 1 \\ i(\vec{r} - 1) \end{array} \right) \\ E_j^{net} = \text{Re} [E_j^+] , E_j^{env} = |E_j^+| \\ I_j^{net} = |E_j^{net}|^2 , I_j^{env} = |E_j^{env}|^2 \end{array} \right. \quad (3.21)$$

The net electric amplitude at a point z , is the coherent amplitude sum of multiply reflected right-bound and left-bound waves, incorporating interference effects inside the system. This process is repeated for all j in order to create the full electric field $E^{net}(k, z)$ and intensity distribution $I^{net}(k, z)$ maps which depend on the incoming wave phase. The phase independent, or envelope spatial distribution is given by $E^{env}(\omega, z)$ and $I^{env}(k, z)$ maps.

3.1.6 Scattering computer code properties

A straightforward Matlab computer code has been developed in order to perform the numerical scattering calculations throughout this manuscript. Here we describe the general algorithm, and the few nontrivial points to concentrate upon.

The input to the code is any binary structure, generated by any method of choice, and the two refractive index values $\{n_A, n_B\}$ (which defines the contrast). The code then performs the following actions:

1. Calculates the real matrices T_{AB} and T_{BA} for later use.
2. Fits the proper slab thickness so that $n_A d_A = n_B d_B$.
3. Creates the z -axis describing the coordinate of interfaces along the structure.
4. Creates the wave-number sampling grid $0 \leq \delta(k) \equiv k n_A d_A = k n_B d_B < \pi$.
5. Calculates the real matrices $T_A(\delta) = T_B(\delta)$ for later use.
6. Calculates the real matrix $\widetilde{M}_{tot}(\delta)$ using the input structure and the appropriate multiplication of T_{AB}, T_{BA}, T_A, T_B .
7. Calculates the complex scattering amplitudes $t(\delta), r(\delta), r'(\delta)$.
8. Calculates the real matrix $\widetilde{M}_j(\delta)$ using the input structure (slabs 1 till j) and the appropriate multiplication of T_{AB}, T_{BA}, T_A, T_B .
9. Calculates the spatial behavior of the electric field amplitude and intensity within the structure.

Some nontrivial points important to realize such code:

1. In the calculation of the counting function, care should be taken when unwrapping the numerical data of the reflected phase shift to avoid artifacts.

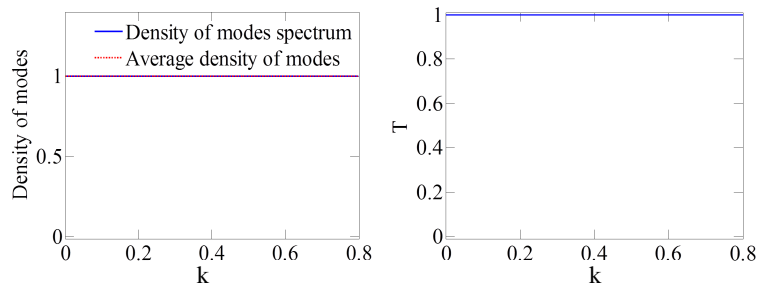


Figure 3.4: The normalized density of modes (left part) and the transmission spectrum (right part), for free space (no scattering structure).

2. The spectrum of many structures contains very sharp, high quality factor modes accompanied with an extremely large density of modes with a very narrow bandwidth. Examples are band edge modes in photonic crystals, defect/boundary modes in photonic crystals and quasicrystals, and Anderson localized modes in disordered structures (see figures 3.10, 3.11, 3.15, 3.18, 3.20, 3.25, and 3.26). This fact forces the user to make a very fine wave-number sampling grid to accommodate such modes which is very costly in terms of computational power. We advocate the use of an adaptive grid rather than a fixed one, which turns out to be crucial in some structural schemes.
3. In spectra which contain transmission band gaps, the calculation of the transmitted amplitude and of the electric field spatial behavior within a gap may suffer from numerical instability. In this case the transfer matrix elements become extremely large and prone to error as some calculation calls for the difference between two large numbers. Apart from standard floating point and normalization methods, we advocate the calculation of the inverse transfer matrix instead of the “straight” one, so now the electric field amplitude within the gaps are exponentially magnified through the transfer sub-matrices multiplication and then renormalized, in contrast to the exponential decay in the electric field amplitudes which is numerically unstable.
4. The spatial resolution in the calculation of the electric field spatial behavior can be greatly enhanced to account for intra-slab behavior by a simple numerical subdivisions (pixelization) of the slabs.
5. High resolution spatial data is costly in terms of memory. It is better to record only the electric amplitudes at the left interface of each slab, and redo the phase accumulation calculations on demand starting from this record.

3.1.7 Illustrative Examples of Layered Systems: Free space

In this illustration, the entire structure is composed of type A slabs. The transmission spectrum and the normalized density of modes are shown in figure 3.4. As expected,

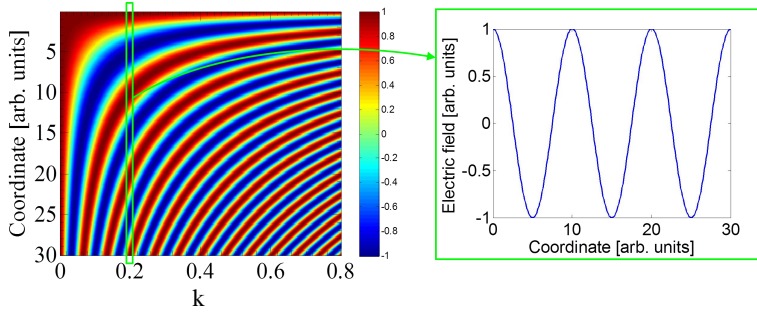


Figure 3.5: Left panel : the electric field amplitude $k - z$ map for free space. Right panel: a cross section of the map along the entire stack at a single frequency ($L/\lambda = 3$).

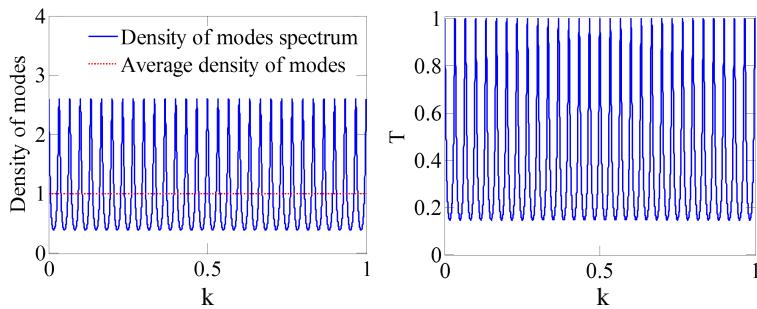


Figure 3.6: The normalized density of modes (left part) and the transmission spectrum (right part), for a Fabry-Perot resonator.

both quantities are equal to one and independent of k . The electric field amplitude map is displayed in figure 3.5. The map shows the fundamental sinusoidal oscillations of the traveling plane wave, as seen in the cross section of the map on the right part of the figure.

3.1.8 Illustrative Examples of Layered Systems: Fabry-Perot structure

The all dielectric Fabry-Perot resonator is realized here by placing two type B slabs separated by several type A slabs, and for illustration we have chosen the refractive index n_B to be three times larger than n_A . The transmission spectrum and the normalized density of modes are presented in figure 3.6.

Although this simple realization serves as a poor resonator, transmission peaks and dips are distributed according to the Fabry-Perot resonance condition $\frac{2L}{\lambda_N} = m$, where $m = 0, 1, 2, \dots$. The density of modes is enhanced above the free one at resonances and attenuated off-resonance. This is, of course, due to interference effects inside the resonator as displayed by the corresponding electric amplitude map in figure 3.7.

The electric field amplitude map is identical to the free space map with the additional “selection rules” for the Fabry-Perot cavity (“allowed” and “forbidden”

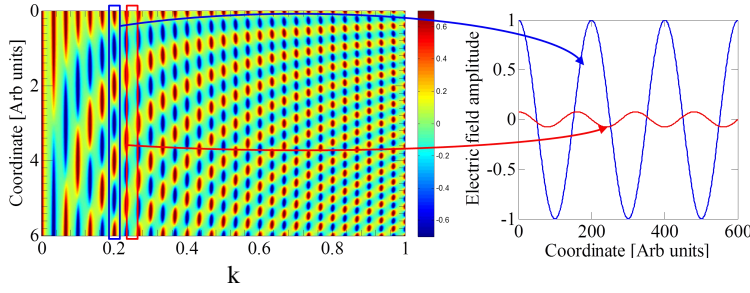


Figure 3.7: Left panel : the electric field amplitude map for a Fabry-Perot resonator. Right panel: a cross-section of the map along the entire stack at a frequency of an allowed mode ($2L = 6\lambda$) in blue and of a forbidden mode ($2L = 7.5\lambda$) in red.

modes). The two different cross sections of the map shown in the right part of figure 3.7 make clear the strong destructive interference effects taking place in off-resonance frequencies inside the structure.

3.1.9 Illustrative Examples of Layered Systems: Periodic structure - photonic crystal

In recent years, light propagation in periodic dielectric media such as photonic crystals has attracted attention due to their novel physics as well as light-guiding applications. Compared to homogeneous media, the new property of periodic media is the existence of band-gaps inside Bloch bands, where linear light propagation is forbidden due to interference (see [JJWM11]).

The transfer matrix formalism is particularly convenient to study the case of a periodic layered system. In this case, the calculation of the total transfer matrix $(M_{cell}(k))^N$ for a sequence of N slabs, simplifies considerably thanks to the Cayley-Hamilton theorem which states that for unimodular matrices,

$$M^2 - (\text{Tr}M)M + 1 = 0.$$

This allows to easily obtain in a recursive way, powers M^n of the transfer matrix

$$M^n(k) = U_{n-1}(\cos\theta)M(k) - U_{n-2}(\cos\theta), \quad (3.22)$$

where $U_n(\cos\theta) = \frac{\sin((n+1)\theta)}{\sin\theta}$ are the Chebychev polynomials of the second kind. A direct calculation shows that

$$\text{Tr}M^n = \cos n\theta(k) = T_n(\cos\theta),$$

where $T_n(\cos\theta)$ are the Chebychev polynomials of the first kind. It is also straightforward to obtain the expression of the transmission coefficient $T_N = |t_N|^2$ for a Bragg system made of N identical layers each described by the same transfer matrix M . From (3.22), we have the expression of M^N , which by definition is of the form

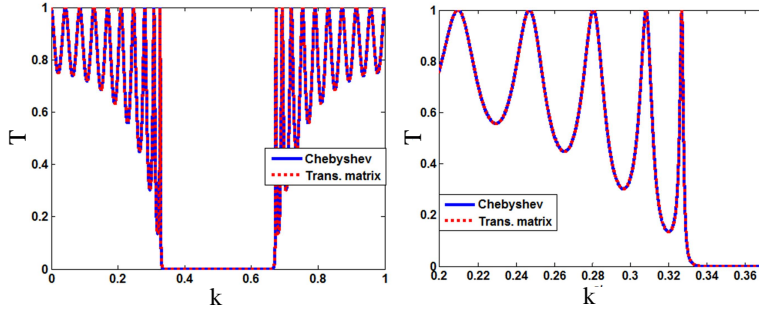


Figure 3.8: Periodic Bragg system of 10 unit cells. The band structure is calculated using both the Chebyshev polynomials (3.23) and via the transfer matrix numeric approach (3.18). Right part is a close up on the long wavelength band edge mode.

(3.8), namely,

$$\begin{aligned} \frac{1}{t_N} &= \frac{U_{N-1}}{t_1} - U_{N-2} \\ \frac{\vec{r}_N}{t_N} &= \frac{\vec{r}_1}{t_1} - U_{N-1}. \end{aligned}$$

Since $\det M^N = 1$, then $\left| \frac{1}{t_N} \right|^2 - \left| \frac{\vec{r}_N}{t_N} \right|^2 = 1$, so that

$$\mathcal{T}_N = |t_N|^2 = \frac{1}{1 + \left| \frac{\vec{r}_1}{t_1} \right|^2 \left(\frac{\sin N\theta}{\sin \theta} \right)^2}, \quad (3.23)$$

where the calculation for $\vec{r}_1 t_1$ can be performed using Fresnel equations. This analytic method, and also the straightforward numeric algorithm equivalently obtain the well known Bragg spectrum with transmission bands and band gaps (see figure 3.8 for a comparison).

Remark

Note that this analytic solution in (3.23) is specific to the periodic case and although some generalizations exist, it can hardly be generalized to other more complex structures which are our main interest, and for which the only the general relations must be used to obtain the spectrum.

The dielectric photonic crystal analyzed from here forth is composed of alternating type A and B slabs with 20 unit cells [AB]. The refractive index is chosen to be $n_B = \frac{3}{2}n_A$. The transmission spectrum for this 40 slab photonic crystal is shown in Figure 3.9. The periodicity gives rise to transmission bands and photonic band gaps centered at the $\frac{\lambda}{4}$ condition, as expected. A closer look at the transmission and the density of modes spectrum near the first stop band is depicted in figure 3.10 for transmission and figure 3.11 for the density of modes.

The sharp band edge modes with a 50-fold enhancement in the DOM compared

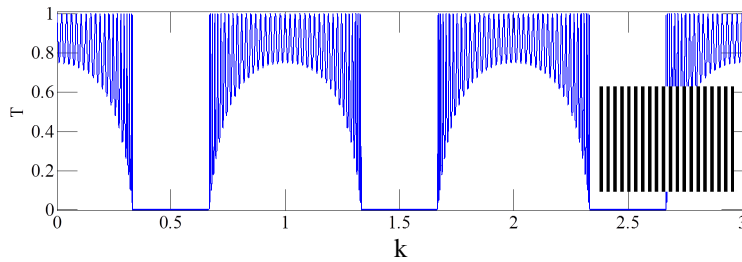


Figure 3.9: The transmission spectrum for a 40 slab long photonic crystal whose structure is illustrated in the inset.

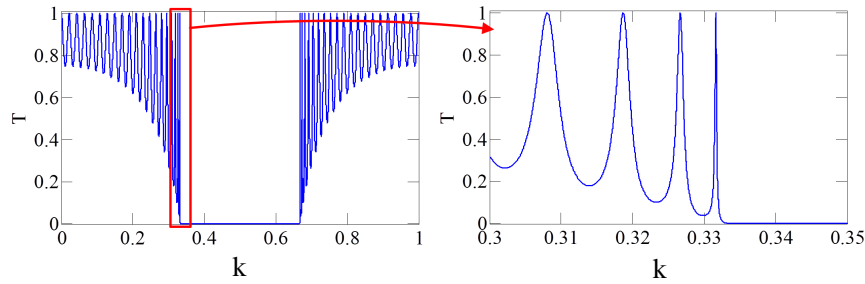


Figure 3.10: The transmission spectrum for a 40 slab photonic crystal. The figure on the right shows a close-up on the long wavelength band edge mode.

to a free system is observed. The number of resonant modes corresponds to the number of unit cells.

The electric field amplitude map corresponding to this photonic crystal is displayed in figure 3.12, as well as a close up look at the band edge modes. Figure 3.12 shows that the band edge modes also have an enhanced electric field distribution peaks - up to 12 times that of the incoming field, due to constructive interference effects and transient energy buildup. It is also visible that while the electric field "hot-spots" in the long wavelength band edge mode tends to be located in one type of slab, it tends to be located in the other type for the short wavelength band edge mode. This feature is presented more clearly in figure 3.13.

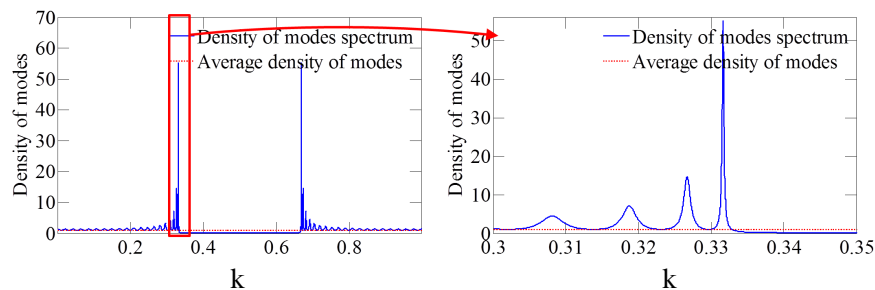


Figure 3.11: The normalized density of modes spectrum for a 40 slab photonic crystal. The figure on the right shows a close-up on the long wavelength band edge mode.

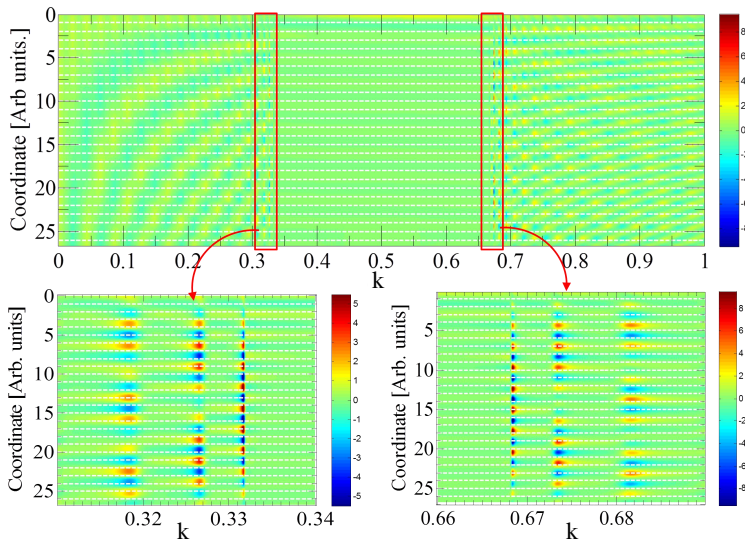


Figure 3.12: The electric field amplitude $k - z$ map for a 40 slab photonic crystal. Spatial boundaries of each slab are indicated by dashed gray lines. Bottom figures are a close-up on the long (bottom left figure) and short (bottom right figure) band edge modes.

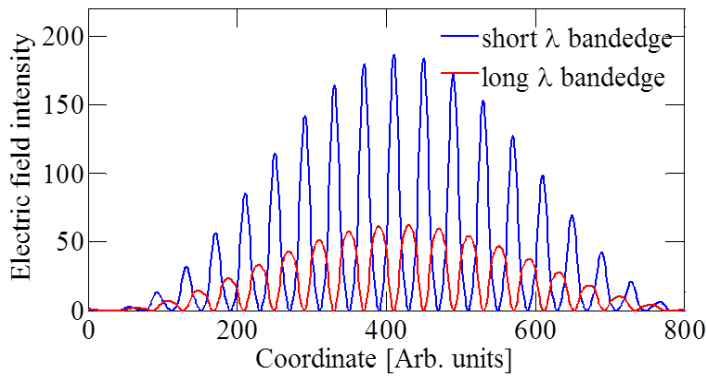


Figure 3.13: The electric field amplitude cross section for the long and short wavelength band edge modes in a 40 slabs photonic crystal. Electric field of the short and long wavelength modes concentrate on different slab types.

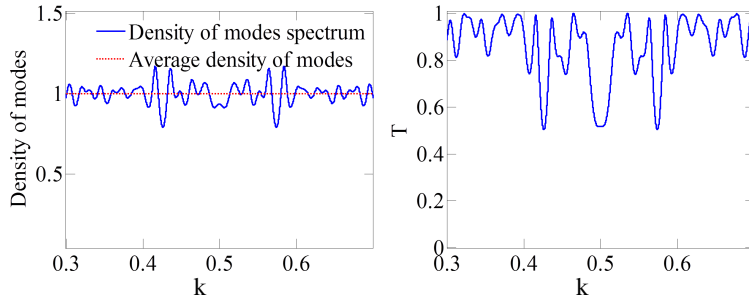


Figure 3.14: The normalized density of modes (left part) and the transmission spectrum (right part), for a weakly disordered structure.

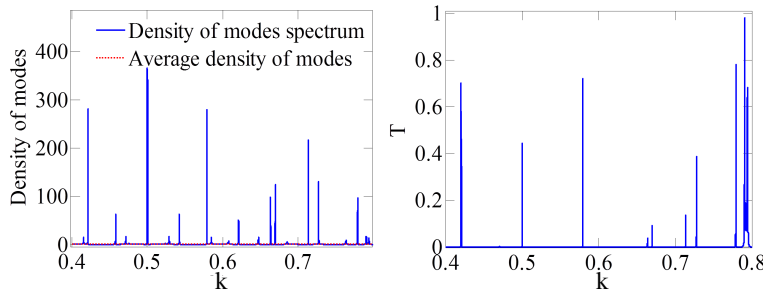


Figure 3.15: The normalized density of modes (left part) and the transmission spectrum (right part), for a strongly disordered structure.

3.1.10 Illustrative Examples of Layered Systems: Random structure

Disordered layered structures have been studied in very great details as a successful and easy to implement model for 1D realization of Anderson localization [And58, EH82, AM07] (and references therein) and other related complex systems. It would be a hopeless task to list all relevant works here.

In accordance with our binary layered structure model, the dielectric random system is generated here by a random "coin flip" sequence of type A and B slabs. This process can be easily done with any random number generator, and repeated to create an ensemble of disorder realizations of each structure in study. The strength of the disorder in 1D chains depends on the localization length as compared to the structure length. Calculating for a 55 slabs long structure, we have obtain a weakly disordered random chain by setting the refractive index n_B to be 10% higher than n_A . For a strongly disordered random system, the refractive index contrast was set to $n_B = 2n_A$. The transmission spectrum and the normalized density of modes for a weakly disordered structure is displayed in figure 3.14.

It can be seen in the right part of figure 3.14 that a weak disorder can attenuate the transmission spectrum significantly, but as seen in the left part of the figure, the density of modes is not much affected by this disorder. Figure 3.16a shows that in the case of weak disorder, the modes are smeared spatially and the spatial distribution of electric field extends to the edges of the stack, i.e. there are no

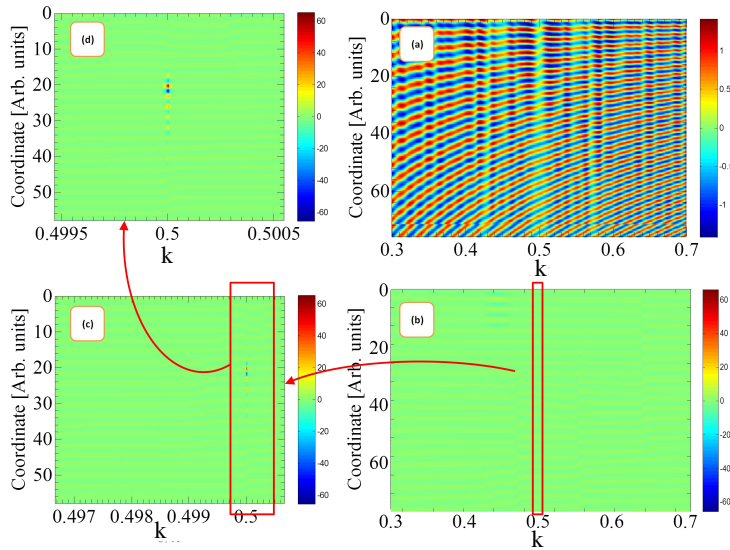


Figure 3.16: The electric amplitude map for disordered structures. (a) a weakly disordered structure. (b)-(d) a strongly disordered structure, with increasing close-up view of a resonant mode.

localized modes - the localization length in this case is greater than the total length of the structure. The transmission spectrum and the normalized density of modes for strong disorder is shown in figure 3.15. In contrast to the previous case of weak disorder, the transmission for strong disorder is inhibited for all frequencies except for a set of a realization dependent discretely distributed modes. The density of modes shows the same discrete resonant frequency pattern together with a significant enhancement of the DOM compared to a free system. The electric field amplitude map for strongly disordered structures in figures 3.16b-d shows that the electric field amplitude map displays vanishingly small values for all frequencies except for some high transmission, high DOM spectrally isolated modes. These modes are spatially localized with a localization length smaller than the structure length (localization length appears to be here about 5% of the structure length). The electric field amplitude is greatly enhanced in the resonant modes - about 70 times that of the incoming wave - also due to constructive interference and transient energy buildup.

3.1.11 Illustrative Examples of Layered Systems: Aperiodic structures - “Fractal” Cantor set structure

The triadic Cantor set is fractal structure, generated by the removal of the middle third of a finite interval, and then repeating this action on each remaining line *ad infinitum*. The meaning of the term fractal is related to the definition of self-similarity or discrete dilational (scaling) symmetry. If we write the general scaling law for the 1D “mass” within a given length, $m(\Delta x)$, namely



Figure 3.17: A schematic view of generations 0-5 of a triadic Cantor set.

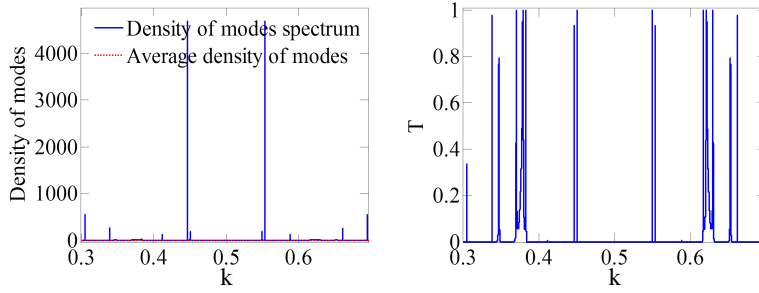


Figure 3.18: The normalized DOM (left part) and the transmission spectrum (right part), for the 4th generation triadic Cantor set structure with $n_B = 1.5n_A$.

$$m(b^p \Delta x) = a^p m(\Delta x), \quad (3.24)$$

we find this scaling is correct for the Cantor set only for $b = 3$ and $a = 2$, showing that this scaling symmetry is discrete and not continuous. The general solution in this case is

$$\begin{aligned} m(\Delta x) &= (\Delta x)^{\ln a / \ln b} \mathbb{F}(\ln \Delta x / \ln b) \\ \mathbb{F}(X + 1) &= \mathbb{F}(X), \end{aligned} \quad (3.25)$$

where \mathbb{F} is a periodic function of period 1. For the triadic Cantor set we expect the mass as a function of length to behave as a power law with a fractional power, $\ln a / \ln b = 0.631$, along with a log periodic oscillation which is the fractal fingerprint.

A finite iteration of the Cantor set structure is realized here by arranging type A and type B slabs according to the triadic Cantor sequence (see figure 3.17). The refractive indices are set here such that n_B to be 50% larger than n_A . The transmission spectrum and the normalized density of modes for a 4th generation Cantor set structure is shown in figure 3.18. Similar to the random structures, this structure exhibits a gaped energy spectrum with jagged discrete resonant modes accompanied by a DOM enhancement. A close up look at the transmission curve of one of these modes, and the electric field intensity map for the same mode is given in figure 3.19.

Figure 3.19 shows that as in the random structure spectrum, the resonant modes

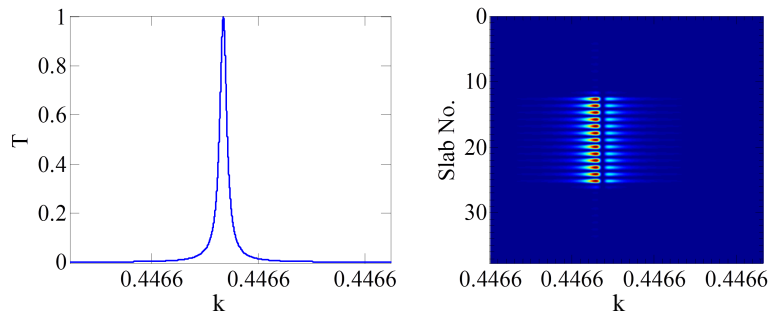


Figure 3.19: A close-up on the transmission curve (left) and electric field intensity map (right) for a resonant mode in figure 3.18.

in a Cantor set structure are isolated spectrally, and localized spatially. However, the spatial localization in the Cantor case is geometric in nature - the electric field spatial distribution is enclosed in the middle third of the structure, while the smaller Cantor motifs at both sides serve as dielectric mirrors (just like the Fabry-Perot resonances discussed above). This view of a Fabry-Perot resonances in a cavity delimited by aperiodic mirrors will be discussed in 3.3 as it is instrumental for some of the findings to be described in chapter 4.

3.1.12 Illustrative Examples of Layered Systems: Aperiodic structures - the Fibonacci quasiperiodic structure

The Fibonacci quasiperiodic structure has been defined and discussed at length in chapter 2. Following through with the scattering approach for the chain S_{10} , setting the refractive indices to be $n_B = 1.5n_A$, the transmission spectrum and the normalized density of modes spectrum are shown in figure 3.20. The spectrum shows two distinct band gaps, and some spectrally isolated band-edge modes with enhanced DOM, arranged according to a self-similar “fractal like” structure. Note that the DOM does not obey an exact self-similarity, but only an approximate one. However, it has been established [Sam94] that the energy spectrum of an infinitely long Fibonacci structure is multi-fractal from the Cantor set family (see figure 3.17). This type of spectrum is called singular-continuous, and the number of spectral gaps is infinite. To explore this self similarity in a finite chain, we consider the transmission spectrum for two different generations of the structure. The spectra are depicted in figure 3.21.

The similarity between the middle section of the transmission spectra for different Fibonacci structure can be seen in the close up figures (the middle spectral feature is the same for very different bandwidths). This result initially obtained in [KSI87] is reproduced here. Another way to observe the same property is the counting function, $\mathcal{N}(k)$, shown in figure 3.22. The gaps appear as plateaus and the modes contribute to the staircase. Zooming in on the spectrum results in a discrete self-

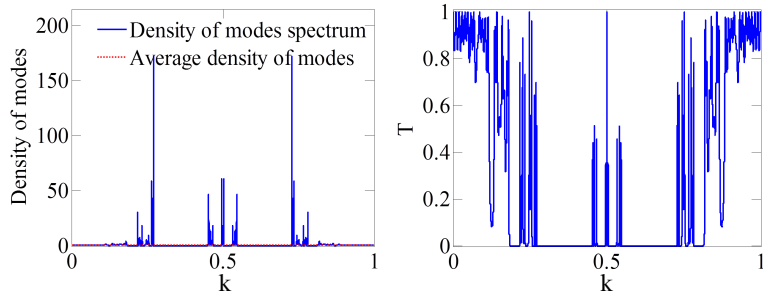


Figure 3.20: The normalized density of modes (left part) and the transmission spectrum (right part), for the Fibonacci chain S_{10} .

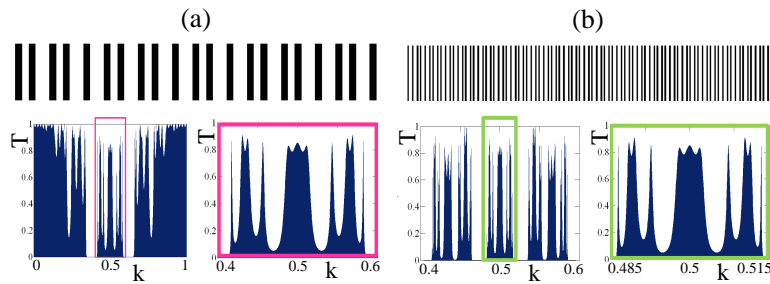


Figure 3.21: Transmission spectrum and stack structure for S_9 (a), and S_{12} . Structures are illustrated above the spectra. The self similarity of the spectra is evident in the close-up on the middle part of the two spectra.

similarity. However, in the previous paragraph regarding the spatially fractal Cantor set, a quantitative measure of self similarity and fractality has been demonstrated in (3.24) and (3.25). A similar argument applies here as well, with the counting function replacing mass, and wave-number k replacing the length, namely,

$$\mathcal{N}(b^p \Delta k) = a^p \mathcal{N}(\Delta k); \mathcal{N}(\Delta k) = \int_k^{k+\Delta k} \rho(k') dk', \quad (3.26)$$

which results in a scaling law with a corresponding power law behavior and log-periodic oscillation,

$$\begin{aligned} \mathcal{N}(\Delta k) &= (\Delta k)^{\ln a / \ln b} \mathbb{F}(\ln \Delta k / \ln b) \\ \mathbb{F}(X + 1) &= \mathbb{F}(X), \end{aligned} \quad (3.27)$$

where \mathbb{F} is a periodic function of period 1. Figure 3.23 shows a numerical calculation of $\mathcal{N}(\Delta k)$ [Gur], for a Fibonacci chain of ~ 2000 letters. This calculation has shown that even for a “finite iteration”, the fractal fingerprints are observable. However this lies outside the scope of this thesis.

The electric intensity map for the Fibonacci chain S_8 , and a close up look at

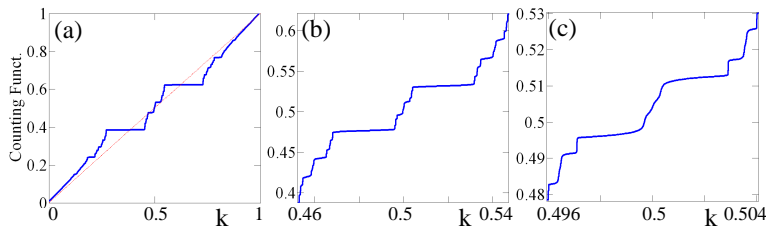


Figure 3.22: Self similarity in the counting function (a) The counting function $\mathcal{N}(k)$ for S_{12} . (b) A close-up on the middle part of panel (a). (c) A close-up on the middle part of panel (b).

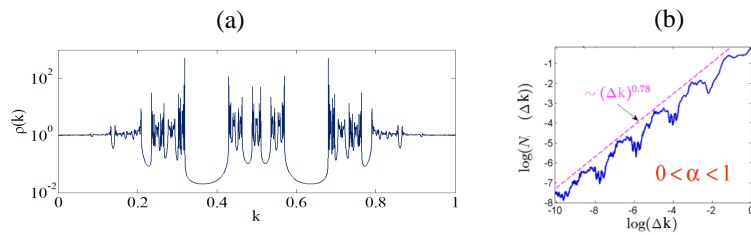


Figure 3.23: (a) Density of modes spectrum and stack structure for S_{16} . (b) A numerical of the quantity $\mathcal{N}(\Delta k)$ in (3.27) .

some interesting modes is shown in figure 3.24. The plots show that the electric field intensity is vanishingly small for almost all frequencies except for some discrete modes. For some of these modes the electric intensity spatial distribution is localized and (surprisingly) symmetric around the middle of the stack, and self similar and resembling the Cantor set structure. The reason for the symmetry is believed to be the almost palindromic nature of the Fibonacci sequence [DP99]. This somewhat odd electric field spatial structure is probed due to the enhanced intra-slab resolution of the calculation. Here too there is a strong enhancement of the electric field amplitude in the band edge modes - up to 60 times that of the incoming field.

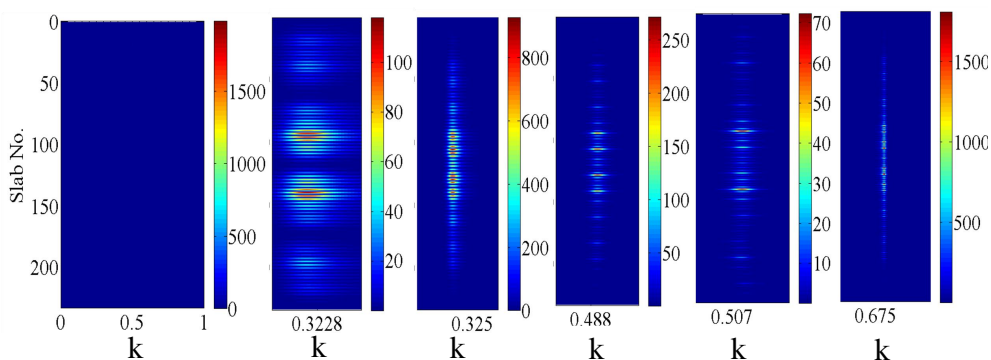


Figure 3.24: The electric field intensity map for the Fibonacci chain S_8 . Left- full spectrum. Other plots: close up zoom on some isolated modes. Spatial localization and spatial self-similarity are apparent.

3.2 Gap modes in quasiperiodic structures: A Fabry-Perot approach

It is well known that the energy spectra of periodic and quasiperiodic chains contain transmission pass bands and band gaps. Band gaps are characterized by a vanishingly small density-of-modes and transmittance values and a high reflectance. There are several methods to induce gap modes in structures with spectral gaps, the most familiar being defect modes. Gap modes are very useful due to their relatively high spectral isolation and spatial localization. Here they will prove as a tool to probe the topological properties of quasiperiodic structures (in chapter 4). In this section we will argue that the concept of “gap mode” bears a Fabry-Perot like meaning (see a short discussion in the Cantor set paragraph in 3.1.11), and that in that sense, many seemingly different gap modes are all the same. An even broader view may be developed using this notion to connect every spectrally isolated transmission mode (e.g. Anderson localized mode in random structures, band-edge modes) to an effective Fabry-Perot cavity, however this lies outside the scope of this current work.

3.2.1 An example: Defect modes in photonic crystal structure

We begin by discussing the best known example for a gap mode, which is the dielectric (photonic) crystal with a single structural defect. If we consider a local defect inserted into a dielectric periodic chain, a localized defect mode with perfect transmission arises inside the band-gap, where light is said to be “trapped” by the local defect and can thus propagate without loss. This is somewhat against intuition. For instance, one would expect light to be guided in a higher index region due to total internal reflections as occurs in a traditional optical fiber. Yet, light is better guided in a lower index region such as an air-hole in a photonic crystal fiber (due to the defect). Apart from low-loss fibers this “work horse” is utilized in lasers-on-chip (VCSELs), and for trapping light in very small volumes for Purcell effect or single photon device purposes [GG99, GG01, Gay01].

For our scattering analysis we take the simplest periodic chain “ABABABAB.....”, with a defect (say an [AA] segment) inserted to the center of the chain. This produces a mid gap mode, localized spatially inside the defect. The transmission spectrum and the normalized density of modes for a photonic crystal hosting a single impurity is shown in figure 3.25.

A close up look at the defect mode transmission and its electric field amplitude map, is depicted in figure 3.26. The defect mode is indeed isolated spectrally and localized spatially. However, if unintentional defects also exist, additional defect modes can exist and may “smear” each other spatially and spectrally.

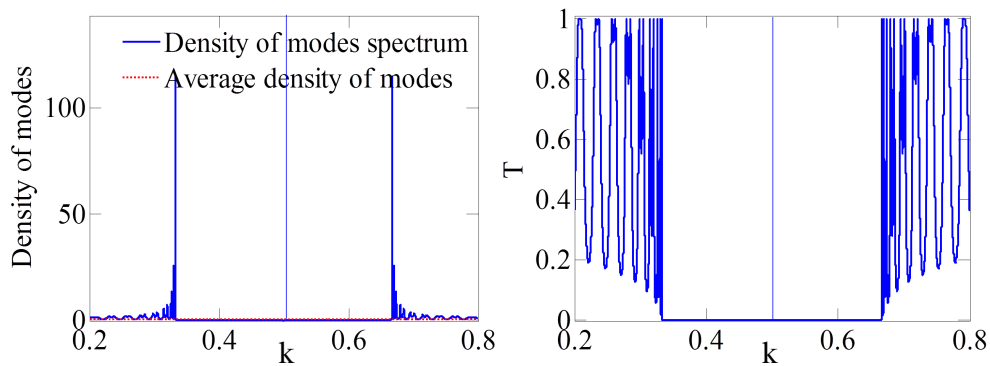


Figure 3.25: The normalized density of modes (left part) and the transmission spectrum (right part), for a photonic crystal hosting a single defect.

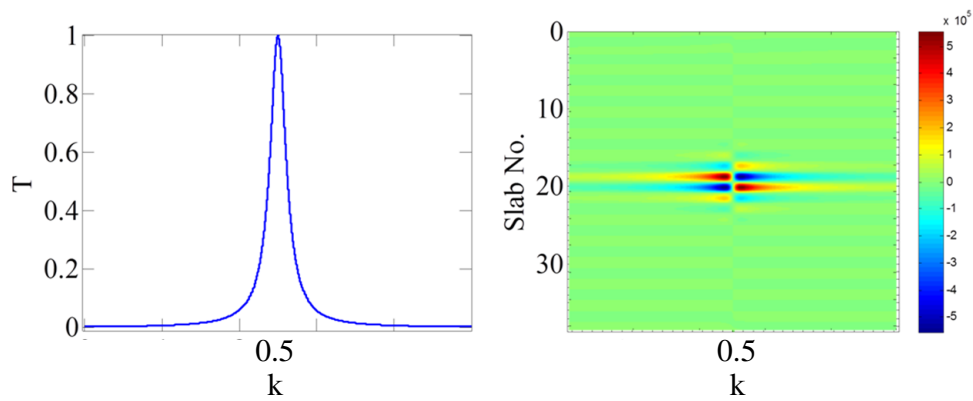


Figure 3.26: A close-up on the transmission curve (left part) and the electric field intensity map (right part) for the resonant defect mode in the photonic crystal structure.

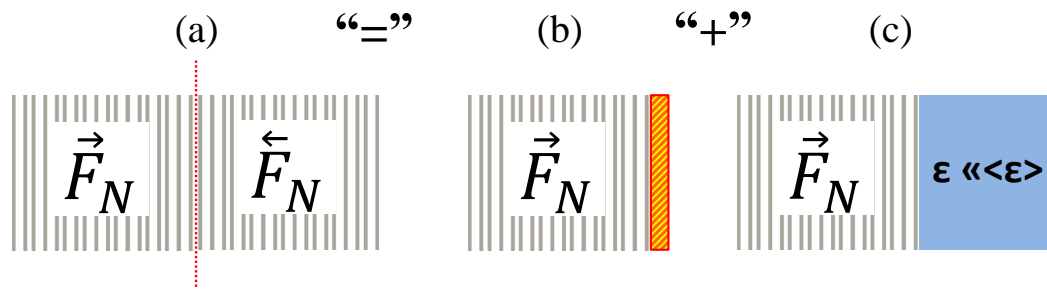


Figure 3.28: (a) The artificial palindrome for the Fibonacci segment \vec{F}_N , hosting gap modes in the interface indicated by the dotted line. (b) A Fibonacci segment \vec{F}_N bounded from the right with a metallic mirror, hosting gap modes at the edge. (c) A Fibonacci segment \vec{F}_N bounded from the right by a continuum with refractive index smaller than the chain's, hosting gap modes at the edge. The arithmetic operators symbolizes the fact that the artificial palindrome is a generalized mirror.

Although less known than the periodic case, gap modes may be easily induced in any structure with spectral gaps. Even in the case of the Fibonacci photonic quasiperiodic chain, gap modes of all kinds have been observed: defect modes [ARS09], Fibonacci hetero-structures [HG98, HWG99, HJPH01, PHQ⁺02, NTMDN09, MVA09, Zhu10, EGDMM11, KMP⁺13], and surface gap modes in the case of a closed structure [EAE⁺06, MM12, PDW10, ZFJ99]. The origin of such gap modes in structures lacking symmetry is not that obvious. As a result, these gap modes have been given various names, such as “defect mode”, “perfect transmission resonances”, and a multitude of explanations are given for their origin [HG98, PHQ⁺02, Zhu10, KMP⁺13, MSKD14].

Here, we suggest and demonstrate a more geometrical optics point of view, which explains and predicts the existence and frequency of all the cases discussed above. This effective Fabry-Perot model is described in 3.3.

3.2.3 The artificial palindrome structural scheme

One scheme to produce gap modes has proven to be extremely important for the topological analysis of quasiperiodic chains, given in chapter 4. We call it the artificial palindrome scheme, and it is the concatenation of a chain with its mirror image (see figure 3.28a for the Fibonacci artificial palindrome).

This composite structure falls into the category of a hetero-structure scheme, but it is closely related to a closed boundary condition scheme. Imagine a given chain bounded from one side by a perfect mirror (either metallic as in figure 3.28b or index mismatch based as in figure 3.28c). Waves traveling to the mirror plane are reflected back into the chain, traveling in a reverse direction, and sometimes with the opposite phase. If we discard of the mirror, and unfold the structure with respect to the mirror plane, we arrive at the artificial palindrome scheme. Note that from a symmetry

argument, the possible gap modes residing in the interface of the artificial palindrome are equivalent to the union of the possible edge modes in the metallic mirror case (with a node in the mirror plane/interface), and the possible edge modes in the mismatch mirror case (with an anti-node in the mirror plane/interface). Therefore, the artificial palindrome scheme is a generalized mirror (generalized edge), hosting a double number of gap modes compared to any mirror. In the Fibonacci case, the artificial palindrome, along with other hetero-structures has been used to induce the appearance of perfect transmission resonances [HG98, PHQ⁺02, Zhu10, KMP⁺13, MSKD14]. Here we show that the nature of these resonances is geometric.

Figure 3.36 depicts the transmission spectrum of the artificial palindrome $\mathcal{P} = [\vec{S}_9 \overleftarrow{S}_9]$, based on the Fibonacci chain S_9 . The artificial palindrome, which is readily applicable to scattering approach (requiring scattering boundary conditions), has become instrumental to the analysis of topological properties through the behavior of edge states as a function of the modulation phase ϕ in chapter 4.

3.3 The effective Fabry-Perot model

This section presents a simple but extremely versatile model which predicts the existence and frequency of gap modes in the interface of a hetero-structure composed of substructures with gaped spectrum. We are also able to show that it predicts the frequency of other perfect transmission resonances observed is [HG98, PHQ⁺02, Zhu10, KMP⁺13, MSKD14] within the transmission bands.

This model treats each substructure as a frequency specific, phase shifting mirror, and then calculates the Fabry-Perot resonances for the cavity thus defined. The substructure mirror is frequency specific as the reflectance depends on frequency, and is sufficiently high within the gaps. It is phase shifting because, unlike the more conventional mirrors which either conserve phase or flip it, a multilayer structure may contribute any phase due to multiple reflection and interference. As for the cavity length, we will show that a geometrical cavity between the multilayer mirrors may be included, but is not necessary.

3.3.1 Formulation, and Resonant mode conditions

In the standard description, a Fabry-Perot cavity is defined by two mirrors separated by the length L , and a discrete spectrum (of resonant wavelengths λ_m) obtained by the resonant condition $2L/\lambda_m = m \in \mathbb{Z}$. An alternative view is given by the winding of a (frequency dependent) cavity phase,

$$\vartheta_L(k) \equiv \frac{4\pi L}{\lambda(k)}, \quad (3.28)$$

where $\lambda(k) = 2\pi/k$ is the wavelength. This leads to a resonance condition $\vartheta_L(k_m) = 2\pi m$, with $m \in \mathbb{Z}$. The interface between the right and left part of a hetero-structure defines a zero length effective cavity between two frequency specific and phase shifting mirrors. The accumulated phase shift of this effective cavity is termed the cavity phase

$$\theta_{cav}(k) = \overrightarrow{\theta}_{right}(k) + \overleftarrow{\theta}_{left}(k) \quad (3.29)$$

(for notations see figure 3.1). This cavity phase is used to generalize (3.28) to arrive at

$$\vartheta_{L,\theta_{cav}}(k) \equiv \frac{4\pi L}{\lambda(k)} + \theta_{cav}(k), \quad (3.30)$$

for which the resonance condition, $\vartheta_{L,\theta_{cav}}(k_m) = 2\pi m$, holds even in the absence of a geometrical cavity (when the two substructures are concatenated with zero separation, $L = 0$).

Alternatively and equivalently, we define a generalized frequency-dependent effective cavity length, composed of the geometrical length, L , and a cavity phase dependent virtual length, namely

$$\mathcal{L}(k) \equiv L + \frac{\lambda(k)}{4} \frac{\theta_{cav}(k)}{\pi}, \quad (3.31)$$

which considers any additional cavity phase as an effective cavity length, and thus holds even in the absence of a geometrical cavity ($L = 0$). Resonant modes occur at gap frequencies satisfying the usual Fabry-Perot condition for the generalized length

$$2\mathcal{L}(k_m)/\lambda(k_m) = m \in \mathbb{Z}. \quad (3.32)$$

We note here that although (3.32) may hold for many values of k , only $\{k_m\}$ values within the spectral gaps (where the reflectance values are sufficiently high) produces gap modes. The figure of merit used to predict the existence of gap modes is the mutual reflectance

$$\mathfrak{R}(k) \equiv |r_{right}| |r_{left}|, \quad (3.33)$$

related to the finesse of a Fabry-Perot cavity through

$$\text{Finesse} = \frac{\pi\sqrt{\mathfrak{R}}}{1 - \mathfrak{R}}, \quad (3.34)$$

(see also the discussion in 3.3.4). We usually demand that the mutual reflectance exceeds 90% in order to predict a gap mode. However, we are able to show that the remaining values which fall within the transmission band will result in perfect transmission resonances, but this lies outside the scope of this thesis.

The effective cavity length dependence upon k implies that for nontrivial $\theta_{cav}(k)$, resonant modes are not equally spaced in frequency as in the traditional Fabry-Perot, and even that a single Fabry-Perot mode may manifest in more than one frequency (see for instance figure 3.36). Moreover, in the case that a genuine cavity of length L with a uniform refractive index inserted between the substructures, the increase in the effective cavity length reduces the resonant mode separation. Since the gap widths did not change, multi-resonant-modes will appear in the gaps (see an example in figure 3.38).

This model serves to unify all gap modes producing schemes. Through this geometrical understanding, defect and surface modes have the same physical origin. Additionally, any hetero-structure with overlap in the substructure spectral gap frequencies will give rise to gap modes of the exact same origin. Moreover, we believe that this model may help to better understand the mechanism for strongly localized and spectrally isolated modes in undisturbed structures. However, this lies outside the scope of this thesis.

3.3.2 Fabry-Perot cavities with wavelength dependent effective length

We will start by stating that the important notion of a k dependent cavity length due to the phase shift in the mirrors is only seemingly strange. In fact, the use of a k dependent cavity length defined in (3.31) is required even in Fabry-Perot cavities of regular mirrors. In order to clarify this last statement, let us discuss two standard cases for a Fabry-Perot cavity. The first is of length L and two dielectric constant mismatch type mirrors which conserve phase. The second is of the same length with two metallic mirrors, where each mirror contributes a 1π reflected phase shift which is frequency independent (up to the plasma frequency). The Fabry-Perot resonant frequencies for both cases are well predicted without the use of any phase shifts, by the standard formula $2L/\lambda_m = m \in \mathbb{Z}$, with the lowest order nontrivial mode at $\lambda_1 = 2L$. However, metallic and dielectric mirrors provides different boundary conditions forcing nodes and anti-nodes in the electric field envelope, respectively (see figures 3.29a-b). Therefore, in the dielectric index mismatch phase conserving mirrors case, odd modes are anti-symmetric and even modes are symmetric (with respect to the mid-cavity coordinate) as usual. However, in the metallic mirrors case, the relation between spatial symmetry and the parity of m is the other way around. Moreover, if we now consider a non-standard Fabry-Perot cavity of size L with a dielectric mirror at one side and a metallic mirror on the other represented in figure 3.29c, we see that resonant modes are now asymmetric, and the lowest order mode occurs at $\lambda = 4L$, unaccounted for by the traditional formula by $2L/\lambda_m = m \in \mathbb{Z}$.

These deviations from the standard view are well understood when using the effective Fabry-Perot cavity length assigning an additional $\frac{\lambda}{4}$ virtual length for each metallic mirror following (3.31), and the resonant condition given by (3.32). In the

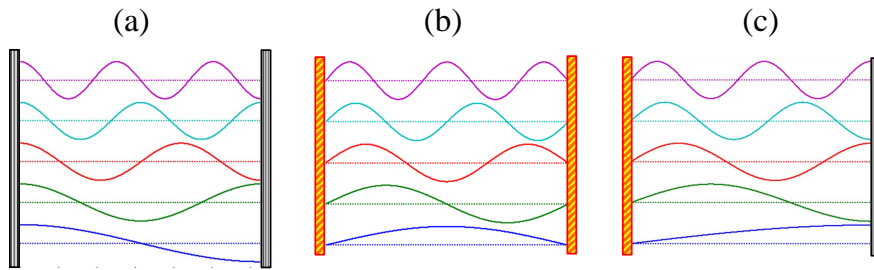


Figure 3.29: The first 5 Fabry-Perot resonant mode (and symmetry) for various mirror schemes. (a) The case with two index mismatch phase conserving mirrors (gray vertical strips represent the mirrors). (b) The case with two metallic phase flipping mirrors (golden diagonal stripes represent the mirrors). (c) The hybrid case with a metallic mirror on one side, and an index mismatch mirror on the other.

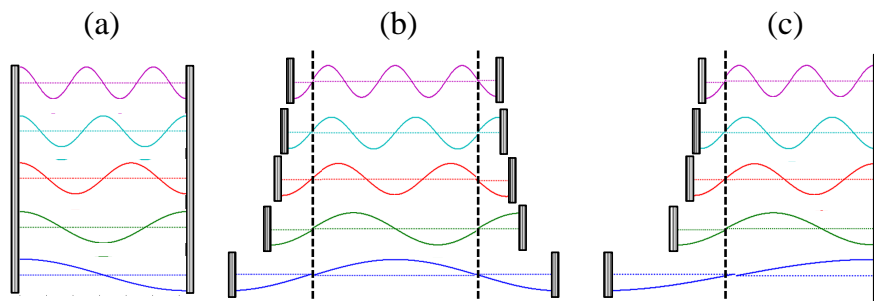


Figure 3.30: A sketch of the same cases as in figure 3.29 explained by replacing metallic mirrors by a phase conserving mirror, retracted by a quarter wavelength, i.e. explained by a frequency dependent cavity length.

all dielectric cavity, the cavity phase shift is zero, i.e. $\mathcal{L}(\lambda) \equiv L$, and resonant modes occur at $\lambda_m = \frac{2L}{m}$, with electric field anti-nodes at the boundaries, and with anti-symmetric (symmetric) odd (even) modes with respect to the mid-cavity coordinate (figure 3.30a). In the all metal cavity case, we have $\mathcal{L}(\lambda) \equiv L + \frac{\lambda}{2}$, as each metallic mirror effectively extends the cavity by $\frac{\lambda}{4}$ (figure 3.30b). The resonant modes are retrieved by solving $\lambda_m = 2\mathcal{L}(\lambda_m)/m$ self consistently to arrive at $\lambda_m = \frac{2L}{m-1}$ which gives identical frequencies to the all dielectric case but for the opposite parity. This result, along with the fact that the effective and the geometrical cavity center coordinates coincide, fully explains the spatial properties of resonant modes in an all metal Fabry-Perot cavity. In the hybrid cavity case, we have $\mathcal{L}(\lambda) \equiv L + \frac{\lambda}{4}$, as only one (metallic) mirror effectively extends the cavity by $\frac{\lambda}{4}$ (figure 3.30c). Solving $\lambda_m = 2\mathcal{L}(\lambda_m)/m$ self consistently gives $\lambda_m = 2L/(m - 1/2)$ yielding a different set of resonant frequencies than previous cases, including $\lambda_1 = 4L$. As the effective cavity center coordinate is shifted by $\frac{\lambda}{8}$ from the geometrical cavity center coordinate, symmetric and anti-symmetric modes for the effective cavity appear asymmetric with respect to the geometrical cavity center coordinate.

We proceed with the case studied in 3.2.1. The effective Fabry-Perot model perfectly predicts the existence and describes some spatial properties of the gap mode in photonic crystal with a central defect. Figure 3.31 shows a comparison between scattering matrix calculations and the generalized Fabry-Perot model predictions for the case of a 55 layers long 1D photonic crystal composites with an optical contrast 1 : 2, with a perfect fit (for $m = 2$). Figure 3.32 depicts the spatial distribution of the electric field in the gap mode frequency, showing that the electric field is localized within the defect, and also that the electric field spatial distribution is symmetric with respect to the cavity center (understandable for an even m - see figure 3.29a). The calculated gap modes are indeed Fabry-Perot modes. Figures 3.33 and 3.34 shows the same calculation for a photonic crystal with a large defect leading to the appearance of multi-gap modes with a perfect fit. The spatial symmetry of the gap modes indeed alternate between symmetric and anti-symmetric corresponding to the parity of the Fabry-Perot integer m .

We proceed with the Fibonacci case. We are easily able to induce a defect in a single Fibonacci chain (figure 3.35), simulate a reflective edge of the two possible kinds, or create an artificial palindrome (figures 3.36, 3.37, 3.38, and 3.39), with all frequencies and spatial symmetries perfectly predictable by the Effective Fabry-Perot model.

3.3.3 Spatial symmetry prediction

A property which is identical to the traditional Fabry-Perot is the spatial symmetry of resonant modes. Resonant modes in the spectral gaps of a hetero-structure possess the Fabry-Perot alternating symmetric/anti-symmetric spatial electromagnetic field

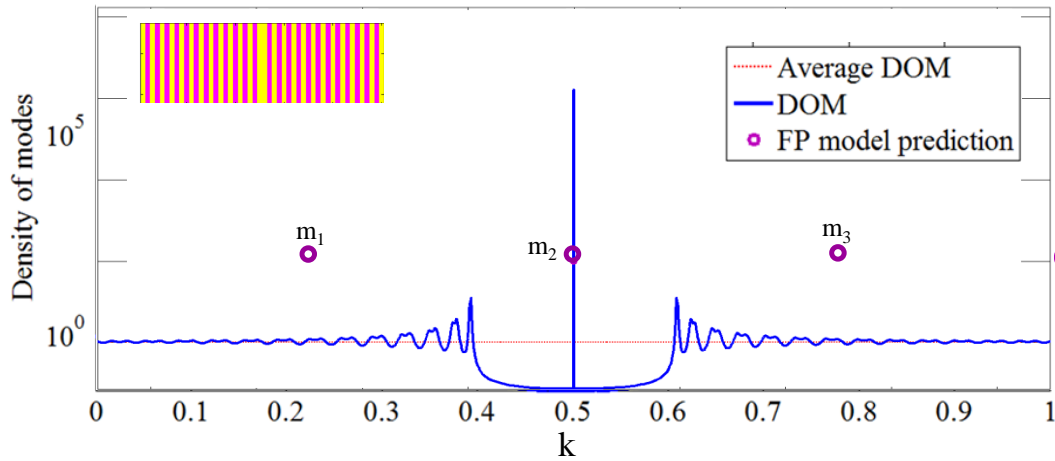


Figure 3.31: Density of modes (in blue) for a 55 letter periodic chain with a central defect (inset). The Effective Fabry-Perot model finds a solution within the spectral gap: $k_2 = 0.5$ fitting the scattering method calculated spectrum.

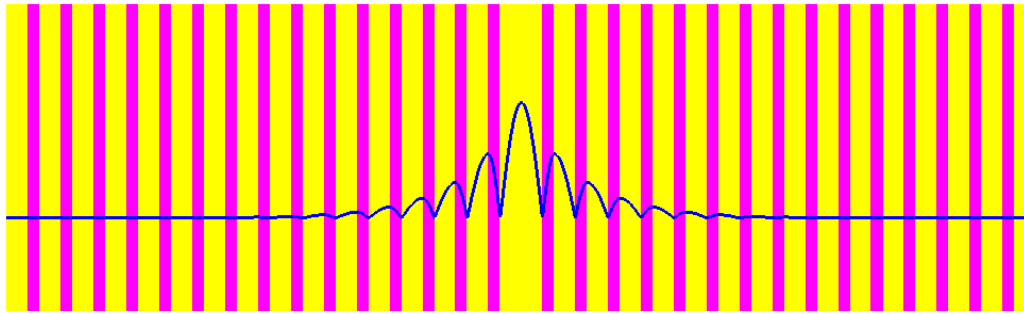


Figure 3.32: The Electric field strength of the gap mode presented in figure 3.31 (in blue) on top of the structural detail.

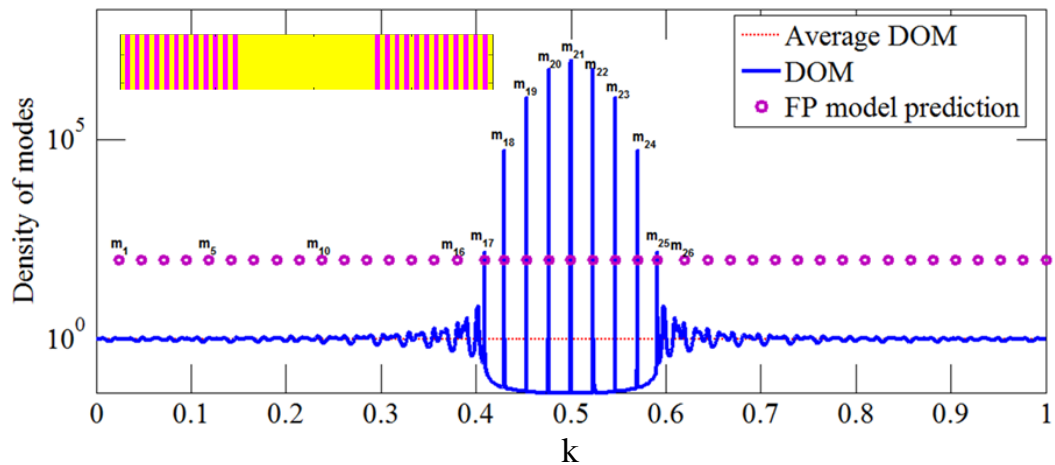


Figure 3.33: Density of modes (in blue) for a 55 letter periodic chain with a 30 letter long central defect (inset). The Effective Fabry-Perot model finds 9 solutions within the spectral gap $\{k_m\}$ $m = 17, 18, \dots, 25$ fitting the scattering method calculated spectrum.

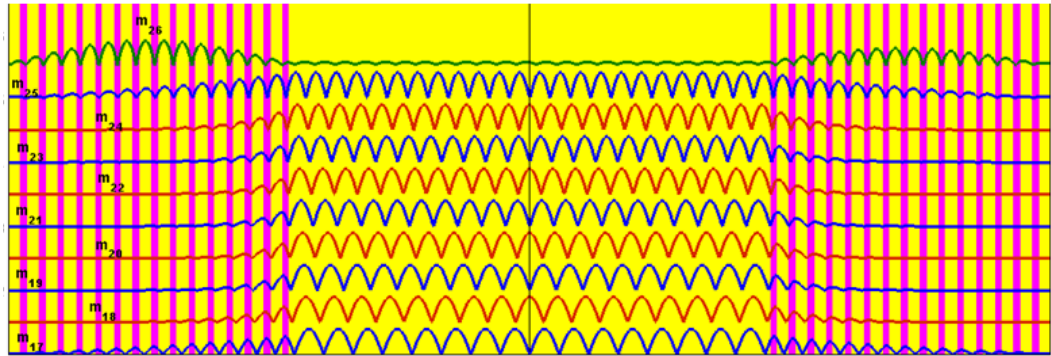


Figure 3.34: The Electric field strength of the gap mode presented in figure 3.33 (in blue) on top of the structural detail.

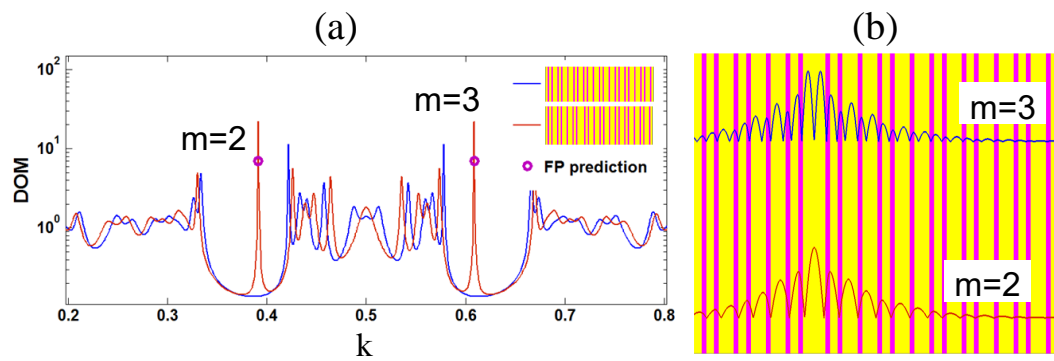


Figure 3.35: The Fibonacci chain S_9 with a non central single letter defect. (a) Density of modes for the undisturbed structure (in blue) compared to the same structure with single non central defect (in red). The 2 effective Fabry-Perot model intra-gap solutions with $\{k_m\}$ $m = 2, 3$ is in purple circles. (b) The Electric field strength of the defect gap modes $m = 2$ (in red) and $m = 3$ (in blue) on top of the structural detail.

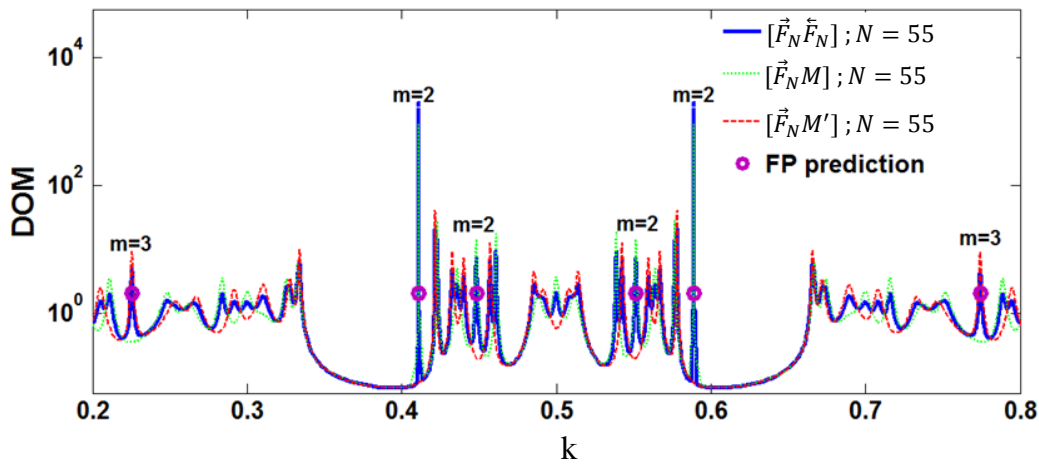


Figure 3.36: The Fibonacci chain S_9 with a reflective boundary conditions, and in the artificial palindrome scheme. Density of modes for S_9 based artificial palindrome (in blue), for S_9 with a reflective boundary condition (index mismatch $n_{\text{continuum}} \ll n_B$) (in dashed green), and for S_9 with a reflective boundary condition (index mismatch $n_{\text{continuum}} \gg n_B$) (in dashed red). The effective Fabry-Perot model intra-gap solutions $\{k_m\}$ is in purple circles.

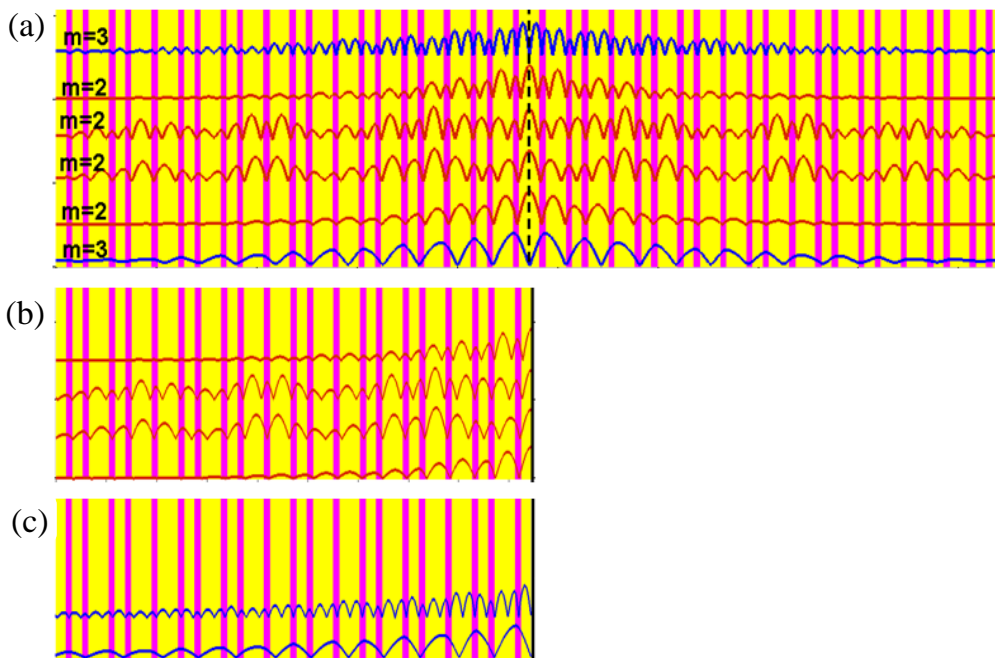


Figure 3.37: The Electric field intensity profile and spatial symmetry for selected gap modes of the structures of figure 3.36. (a) S_9 based artificial palindrome. (b) The S_9 chain with a reflective boundary condition (index mismatch $n_{\text{continuum}} \ll n_B$). (c) The same as (b) for a metallic reflective boundary, $n_{\text{continuum}} \gg n_B$.

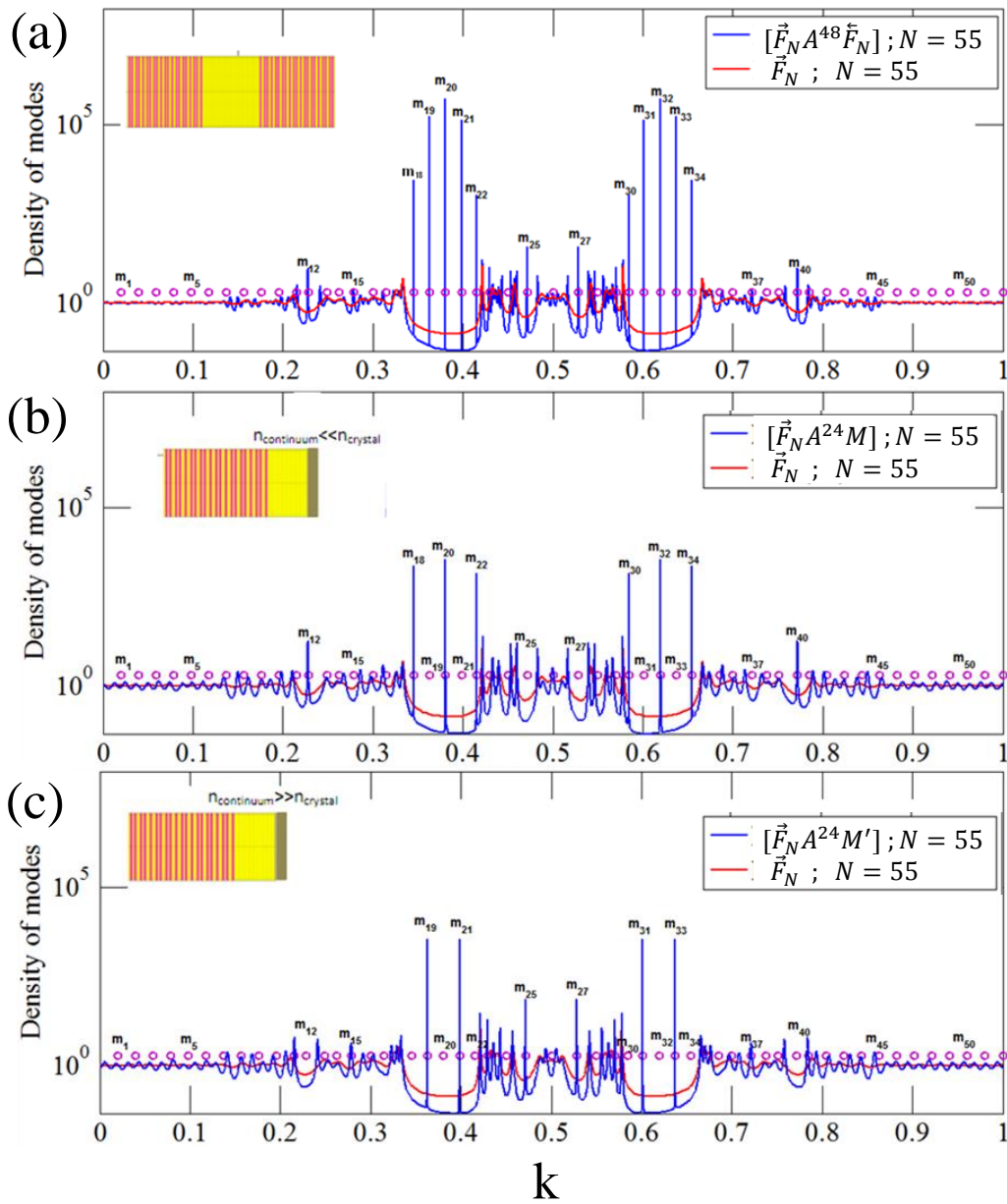


Figure 3.38: The Fibonacci chain S_9 with a reflective boundary conditions, and in the artificial palindrome scheme with a geometrical cavity length. (a) Density of modes for artificial palindrome with a 48 letter geometrical cavity (in blue), compared to the undisturbed structure (in red). The effective Fabry-Perot model intra-gap solutions $\{k_m\}$ is in purple circles. (b) Density of modes for the chain S_9 with a reflective boundary condition (index mismatch $n_{\text{continuum}} \ll n_B$) with a 24 letter stand-off (in blue), compared to the undisturbed structure (in red). The effective Fabry-Perot model intra-gap solutions $\{k_m\}$ is in purple circles. (c) The same as (b) for a metallic reflective boundary, $n_{\text{continuum}} \gg n_B$.

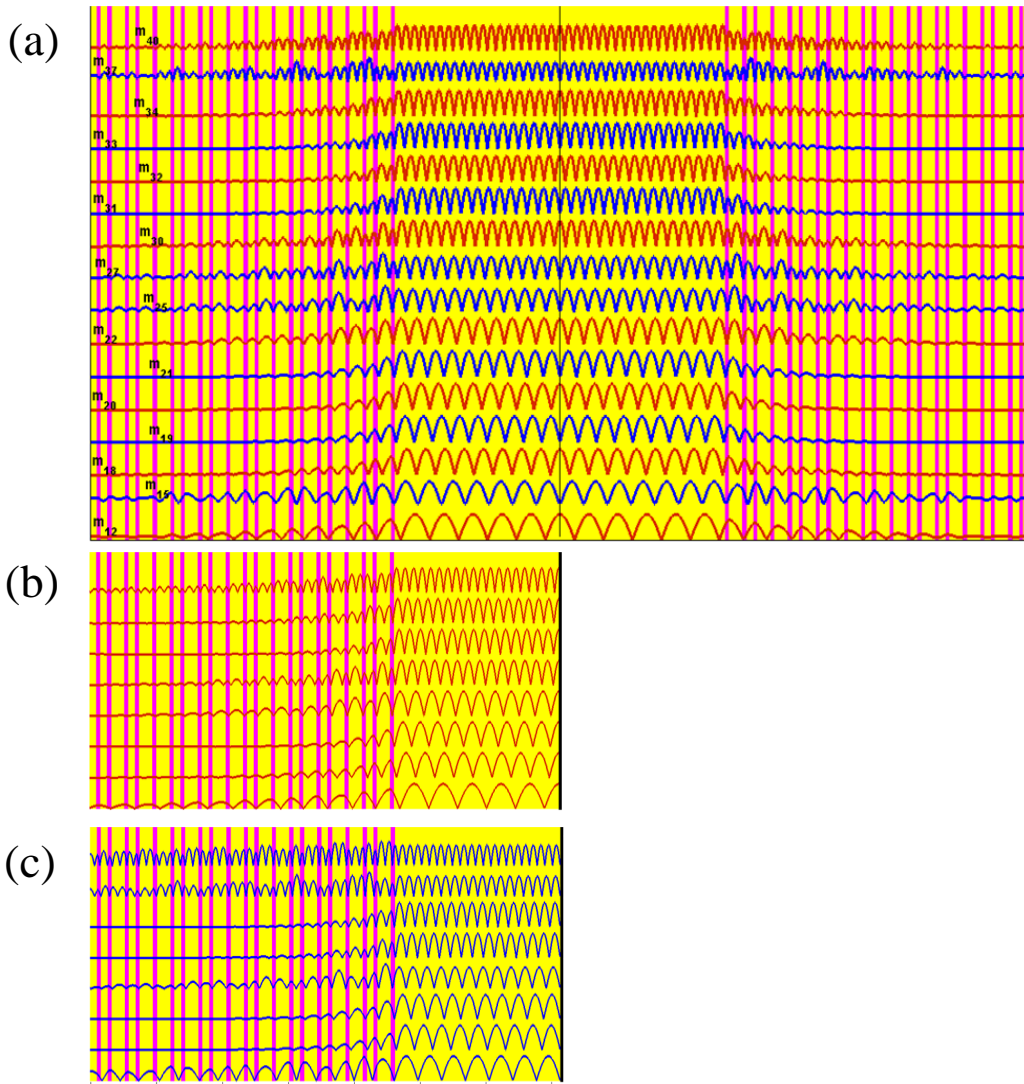


Figure 3.39: The Electric field intensity profile and spatial symmetry for selected gap modes of the structures of figure 3.38. (a) S_9 based artificial palindrome with a 48 letter geometrical cavity. (b) The S_9 chain with a reflective boundary condition (index mismatch $n_{\text{continuum}} \ll n_B$) with a 24 letter stand-off. (c) The same as (b) for a metallic reflective boundary, $n_{\text{continuum}} \gg n_B$.

distribution (with respect to the mid-cavity coordinate) as a function of the parity of m . Odd (even) modes are anti-symmetric (symmetric) with respect to the geometric center, all having electromagnetic field anti-nodes (nodes) at the effective cavity boundaries (see figures 3.29a, 3.34). When the structure is delimited by a reflective boundary, only half of the possible modes show up, due to spatial symmetry selection rules (see for instance figures 3.35, 3.37, and 3.39). This spatial attribute, which holds only within the virtual cavity length, will come in handy in the analysis of the topological properties of quasiperiodic structures in chapter 4.

3.3.4 Calculation of gap modes for a hetero-structure

The artificial palindrome discussed in 3.2.3 is used throughout chapter 4 to monitor the topological properties of the quasiperiodic chain spectrum (see also 3.4). This is accomplished through monitoring the properties of the gap modes as a function of the modulation phase ϕ defined in 2.1, and discussed in 2.2. We shall now derive the conditions for the existence and frequency of a gap mode in the spectrum of a hetero-structure through the scattering approach.

We consider a hetero-structure $[J_1 J_2]$ with no geometrical cavity. This hetero-structure can be described using its scattering matrix $\mathcal{S}_{12}(k)$. We will now obtain a relation between $\mathcal{S}_{12}(k)$ and the scattering matrices $\mathcal{S}_1(k)$, $\mathcal{S}_2(k)$ of the respective substructures J_1, J_2 using the definition for a general scattering matrix given in 3.1, namely

$$\begin{pmatrix} E_L^{(\leftarrow)} \\ E_R^{(\rightarrow)} \end{pmatrix} = \mathcal{S} \begin{pmatrix} E_L^{(\rightarrow)} \\ E_R^{(\leftarrow)} \end{pmatrix},$$

and the following matrices

$$\mathcal{S}_{1(2)} = \begin{pmatrix} \vec{r}_{1(2)} & t_{1(2)} \\ t_{1(2)} & \overleftarrow{r}_{1(2)} \end{pmatrix}; \mathcal{S}_{12} = \begin{pmatrix} \vec{R} & T \\ T & \overleftarrow{R} \end{pmatrix}.$$

The same description is available through the complex valued transfer matrix generally defined by (3.10), namely

$$\begin{pmatrix} E_R^{(\rightarrow)} \\ E_R^{(\leftarrow)} \end{pmatrix} = M \begin{pmatrix} E_L^{(\rightarrow)} \\ E_L^{(\leftarrow)} \end{pmatrix},$$

such that

$$M_{1(2)} = \begin{pmatrix} 1/t_{1(2)}^* & \overleftarrow{r}_{1(2)}/t_{1(2)} \\ -\vec{r}_{1(2)}/t_{1(2)} & 1/t_{1(2)} \end{pmatrix}; M_{12} = \begin{pmatrix} 1/T^* & \overleftarrow{R}/T \\ -\vec{R}/T & 1/T \end{pmatrix}.$$

We now define the chiral phase $\alpha(k)$, relating the two reflected wave amplitudes of the scattering matrix, $\vec{r} = |\vec{r}| e^{i\vec{\theta}}$, and $\overleftarrow{r} = |\overleftarrow{r}| e^{i\overleftarrow{\theta}}$. As $|\vec{r}| = |\overleftarrow{r}|$, we may write

$$\alpha \equiv \overleftarrow{\theta} - \overrightarrow{\theta} ; \overleftarrow{r} = \overrightarrow{r} e^{i\alpha}. \quad (3.35)$$

The chiral phase $\alpha(k)$ probes the asymmetry of a given structure, vanishing identically for palindromic structures. In 3.6, we will discuss the important role of the chiral phase, along with the total phase shift $\delta(k)$ in the scattering matrix, and in the analysis of topological properties.

The total phase shifts $\delta_1, \delta_2, \delta_{12}$ of the respective scattering matrices $\mathcal{S}_1, \mathcal{S}_2, \mathcal{S}_{12}$ are defined as follows.

$$e^{2i\delta_{1(2)}} = \det \mathcal{S}_{1(2)} = -\frac{t_{1(2)}}{t_{1(2)}^*} = \frac{\overleftarrow{r}_{1(2)}}{\overrightarrow{r}_{1(2)}^*} ; e^{2i\delta_{12}} = \det \mathcal{S}_{12} = -\frac{T}{T^*} = \frac{\overleftarrow{R}}{\overrightarrow{R}^*}, \quad (3.36)$$

while through (3.7) we have

$$\frac{\delta_{1(2)}(k)}{\pi} = \Delta \mathcal{N}_{1(2)}(k) ; \frac{\delta_{12}(k)}{\pi} = \Delta \mathcal{N}_{12}(k).$$

Rewriting the definition for the chiral phase, we yield

$$\overrightarrow{\theta}_{1(2)} = \delta_{1(2)} - \frac{1}{2}\alpha_{1(2)} ; \overleftarrow{\theta}_{1(2)} = \delta_{1(2)} + \frac{1}{2}\alpha_{1(2)}.$$

As in the regular scattering calculations, we again make use of the multiplicative properties of the algebraically related transfer matrix, namely $M_{12} = M_1 M_2$. We get

$$M_{12} = \begin{pmatrix} 1/t_2^* & \overleftarrow{r}_{2/t_2} \\ -\overrightarrow{r}_{2/t_2} & 1/t_2 \end{pmatrix} \begin{pmatrix} 1/t_1^* & \overleftarrow{r}_{1/t_1} \\ -\overrightarrow{r}_{1/t_1} & 1/t_1 \end{pmatrix} = \begin{pmatrix} 1/T^* & \overleftarrow{R}/T \\ -\overrightarrow{R}/T & 1/T \end{pmatrix}. \quad (3.37)$$

Using (3.36), it is possible to extract from (3.37) the hetero-structure scattering total phase shift δ_{12} . After some algebra, we arrive at a relation between the hetero-structure scattering total phase shift δ_{12} , to the substructures scattering total phase shift δ_1 and δ_2 .

$$e^{2i\delta_{12}} = e^{2i(\delta_1 + \delta_2)} \frac{1 - (\overrightarrow{r}_2 \overleftarrow{r}_1)^*}{\overrightarrow{r}_2 \overleftarrow{r}_1 - 1}. \quad (3.38)$$

Expression (3.38) may be rewritten under the definition

$$e^{i\varphi} = \frac{1 - (\overrightarrow{r}_2 \overleftarrow{r}_1)^*}{\overrightarrow{r}_2 \overleftarrow{r}_1 - 1} = \frac{1 - \zeta^*}{\zeta - 1} ; \zeta \equiv \overrightarrow{r}_2 \overleftarrow{r}_1, \quad (3.39)$$

to arrive at a simple expression

$$\delta_{12} - (\delta_1 + \delta_2) = \frac{\varphi}{2}. \quad (3.40)$$

Through ζ , two Fabry-Perot parameters are naturally introduced into the formalism. From the definition (3.39), we have $\zeta = |r_1| |r_2| e^{i(\vec{\theta}_1 + \vec{\theta}_2)} \equiv \Re e^{i\theta_{cav}}$, where θ_{cav} is defined in (3.29) and $\Re(k) \equiv |r_1| |r_2|$ is the mutual reflectance of the substructures, related to the finesse of the Fabry-Perot cavity by (3.34), and used in the effective Fabry-Perot model in order to predict the existence of gap modes (see 3.3).

Thus, we write the relation between the hetero-structure and substructures total phase shifts δ_{12} , δ_1 , δ_2 to the cavity parameters \Re , θ_{cav} represented by φ , namely

$$\Re \cos(\theta_{cav} + \frac{\varphi}{2}) = \cos(\frac{\varphi}{2}), \quad (3.41)$$

Equation (3.41) can be rewritten as:

$$\frac{\varphi}{2} = \begin{cases} \frac{\pi}{2} + m\pi & \Re = 0 \text{ (open system)} \\ \arctan\left(\frac{\Re \cos(\theta_{cav}) - 1}{\Re \sin(\theta_{cav})}\right) & \Re > 0 \text{ (closed system)} \end{cases}. \quad (3.42)$$

We shall also rewrite (3.42) for nonzero \Re as

$$\tan \frac{\varphi(k)}{2} = \frac{\Re(k) \cos(\theta_{cav}(k)) - 1}{\Re(k) \sin(\theta_{cav}(k))}. \quad (3.43)$$

The condition for the appearance of a single gap mode k_m in a perfect gap ($\Re = 1$) of the spectrum of $[J_1 J_2]$ is

$$\delta_{12}(k_m) - [\delta_1(k_m) + \delta_2(k_m)] = \pi + 2\pi m, \quad (3.44)$$

where $m \in \mathbb{Z}$. Using (3.40), we equivalently write the condition as $\varphi = 2\pi m$. This condition may be viewed as a resonance condition of the Levinson theorem [Ma06]. We may rephrase the condition as: a new gap mode will arise at a frequency where φ completes a full winding and the mutual reflectance is perfect. However, this relation is only approximate for the more realistic case of $\Re < 1$. From (3.41), one can see that for this perfect mutual reflectance case, $\varphi(\theta_{cav}, |\Re = 1) = -\theta_{cav}$, which yields an alternative condition for the appearance of a new mode, $\theta_{cav}(k_m) = 2\pi m$. Analyzing (3.43) for perfect and also imperfect mutual reflectance, we observe that although any deviation from perfect mutual reflectance smears the winding of φ , the winding of θ_{cav} remains intact (see figure 3.40). It seems that θ_{cav} captures the emergence of new modes through its winding despite the imperfect mutual reflectance, and it is more suitable than φ for identifying new modes in spectral gaps. However, this should not come as a big surprise, as we already argued that any gap mode is nothing but a Fabry-Perot resonant mode predictable by the condition $\theta_{cav}(k_m) = 2\pi m$ which was already derived in 3.3.

A comparison of the behaviors of $\theta_{cav} = 2\vec{\theta}_{\overleftarrow{S}_{10}}$, and $\varphi = 2\delta_{\overleftarrow{S}_{10}} - 4\delta_{\overleftarrow{S}_{10}}$ for the artificial palindrome hetero-structure based on the Fibonacci chain S_{10} , is given

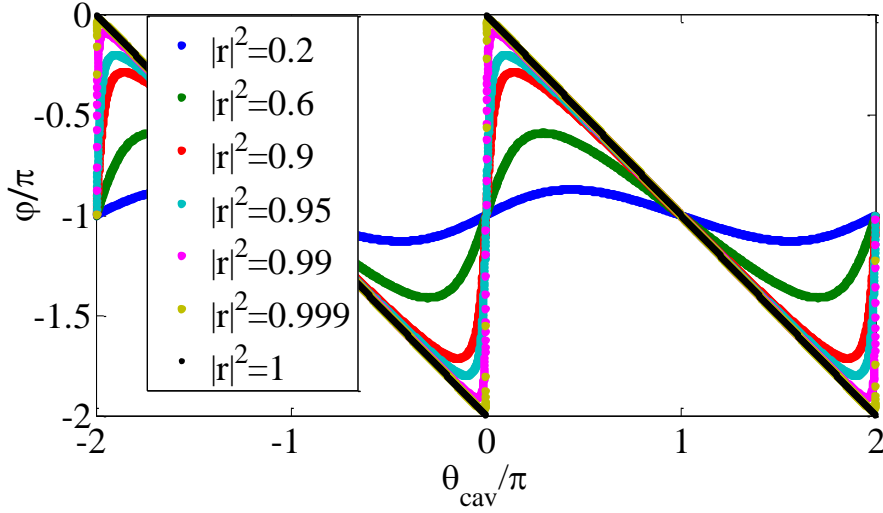


Figure 3.40: $\varphi(\theta_{cav}, \Re)$ as calculated from (3.41). The relation $\varphi = -\theta_{cav}$ holds only for perfect reflectance..

in figure 3.41, examined at two different spectral gaps, characterized by different values of $\Re = |r|^2$. Indeed, the winding of θ_{cav} is unaffected by $|r|^2$, while φ ceases to cover the interval $[0, 2\pi]$ (even for $|r|^2 = 0.98$). Thus, for any value of $|r|^2$, the condition $\theta_{cav}(k_m) = 2\pi m$ can be used to calculate the gap mode frequencies for the artificial palindrome.

3.4 The topological spectrum of substitution chains

The dense distribution of gaps in substitution based infinite quasiperiodic chains can be characterized by the gap labeling theorem [Shu79, Bel82, Kun86, Bel92]. It provides a precise expression of the (normalized to unity) integrated density of states (IDOS) $\mathcal{N}(k_{gap})$ at k values residing inside the gaps. For the case of the Fibonacci infinite chain, gaps are labeled by means of two integers (p, q) such that,

$$\mathcal{N}(\varepsilon_{gap}) = p + q\tau^{-1}, \quad (3.45)$$

where $\tau = (1 + \sqrt{5})/2$ is the golden mean. and $p(q)$ keeps $\mathcal{N}(k_{gap})$ within $[0, 1]$. The purely spectral expression (3.45) is derived from the purely structural substitution rules for the Fibonacci chain as follows. We start from the occurrence matrices \mathcal{M}_1 and \mathcal{M}_2 , defined by (2.5) and (2.6), the highest mutual eigenvalue τ , and the normalized eigenvectors V_1 and V_2 , given by (2.7). Then, the normalized IDOS in the gaps can be calculated as follows [Bel82, Bel92]. Let $\mathbb{Z}[x]$ be the set of finite polynomials of degree N with integer coefficients,

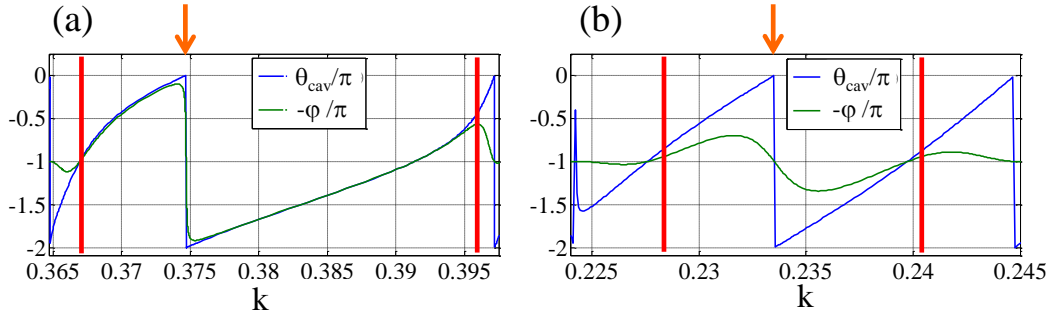


Figure 3.41: The behavior of the phases $\varphi(\theta_{cav}(k), \mathfrak{R})$ and $\theta_{cav}(k)$ as a function of k for the artificial palindrome $[\vec{S}_{10} \overleftarrow{S}_{10}]$ with a dielectric contrast of 25%, at different spectral gaps (gap edges are indicated by red bars, and the gap mode frequency is indicated by orange arrows). (a) Gap at $k \approx 1 - \tau^{-1}$ given by (2.13), with $\mathfrak{R} = |r|^2 \approx 0.98$. (b) Gap at $k \approx 2\tau^{-1} - 1$, with $|r|^2 \approx 0.25$.

$$\mathbb{Z}[x] = \left\{ \sum_{n=1}^N q_n x^n \mid q \in \mathbb{Z}, N \in \mathbb{N} \right\}. \quad (3.46)$$

Now, \mathcal{N}_{gap} , the IDOS at possible gaps is equal to [Bel82, Bel92]

$$\mathcal{N}_{gap} = \{ a\mathbf{P}(\vartheta^{-1}) \mid \mathbf{P}(\vartheta^{-1}) \in \mathbb{Z}[\vartheta^{-1}] \} \text{ mod. } 1, \quad (3.47)$$

where $a \in \{V_1, V_2\}$, and ϑ is the highest common eigenvalue of the occurrence matrices (i.e. $\vartheta = \tau$ for the Fibonacci chain). Using (2.7), the set appearing in (3.47) for the Fibonacci chain is reduced to

$$\mathcal{N}_{gap} = \left\{ q_1 \frac{\tau^{-1}}{\tau^{n_1}}; q_2 \frac{(1-\tau^{-1})}{\tau^{n_2}}; q_3 \frac{(2\tau^{-1}-1)}{\tau^{n_3}} \right\} \text{ mod. } 1, \quad (3.48)$$

where $n_{1,2,3} \in \mathbb{N}$, and $q_{1,2,3} \in \mathbb{Z}$. Since $\tau^{-2} = 1 - \tau^{-1}$, the set can be further compacted into

$$\mathcal{N}_{gap} = \{ q\tau^{-1}, q \in \mathbb{Z} \} \text{ mod. } 1, \quad (3.49)$$

where $q \in \mathbb{Z}$, leading to (3.45). These features which have been widely studied [Shu79, Sim82, Kun86, KSI87, DG11] and recently measured in a finite system using cavity polaritons [TGB⁺14], are shown in figure 3.42.

The integers q and $p(q)$ belong to the Chern class, i.e. Chern numbers were shown to appear as integer labels to the spectral gaps [Bel82, Bel92]. Chern numbers [Sim82, Shu79], are topological invariants known to play a role in problems where an underlying topology exists. Examples are provided by the quantum Hall effect, anomalies in Dirac systems and topological insulators. For each case, the origin of topological features is identified, e.g. magnetic field, chirality or nontrivial

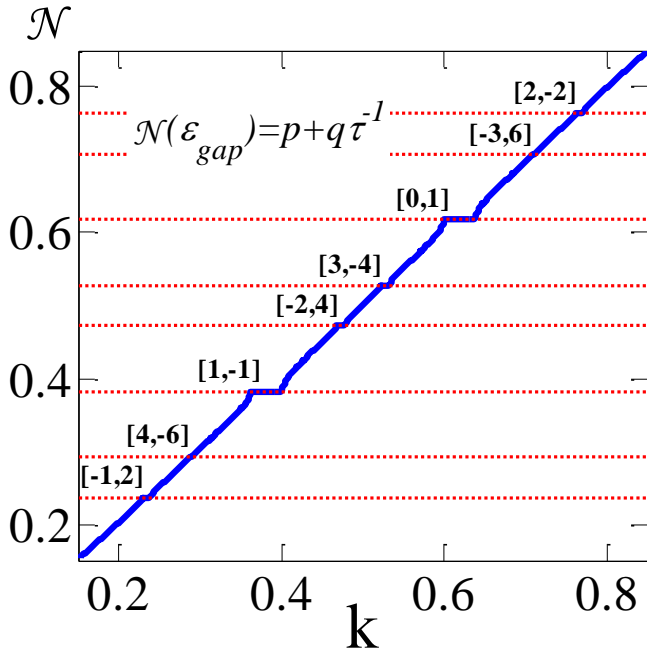


Figure 3.42: Normalized IDOS for the Fibonacci chain S_{10} , with a dielectric contrast of $(n_{high} - n_{low})/n_{low} = 15\%$. The location of 8 selected gaps using their topological numbers $[p, q]$ are indicated in accordance to (3.45).

band structures. The appearance of such numbers in the spectrum of quasiperiodic structures such as the Fibonacci chain, marks the quasiperiodic structure spectrum as topological. The quasiperiodic structure is topological with no further manipulation (such as external fields) required, as it originates from a purely structural property. However, this statement still lacks an understanding regarding the underlying symmetry, relating Chern numbers in gap labels to other known topological problems. The purpose of chapter 4 is to address this point and to propose new expressions and possible measurements of Chern numbers in their most fundamental definition—a winding of a phase driven by some gauge field.

The gap labeling theorem is defined for any substitution quasicrystal, although the amount of integers required to label each spectral gap is usually larger than 2.

3.5 Spectral gaps and Bragg peaks

Here we use the opposite argument to that given in 2.3. The fact that the quasiperiodic chain scattering spectrum is topological (through the integer labels of the spectral gaps) extends to its reciprocal space properties, discussed in 2.3, through the generalized Bloch theorem. The spatial frequency of the infinite number of Bragg peaks of the infinite quasiperiodic chain is directly related to the infinite number of spectral gaps in the scattering (or transmission) spectrum. Figure 3.43 shows this equivalence holds for the Fibonacci chain S_{10} example.

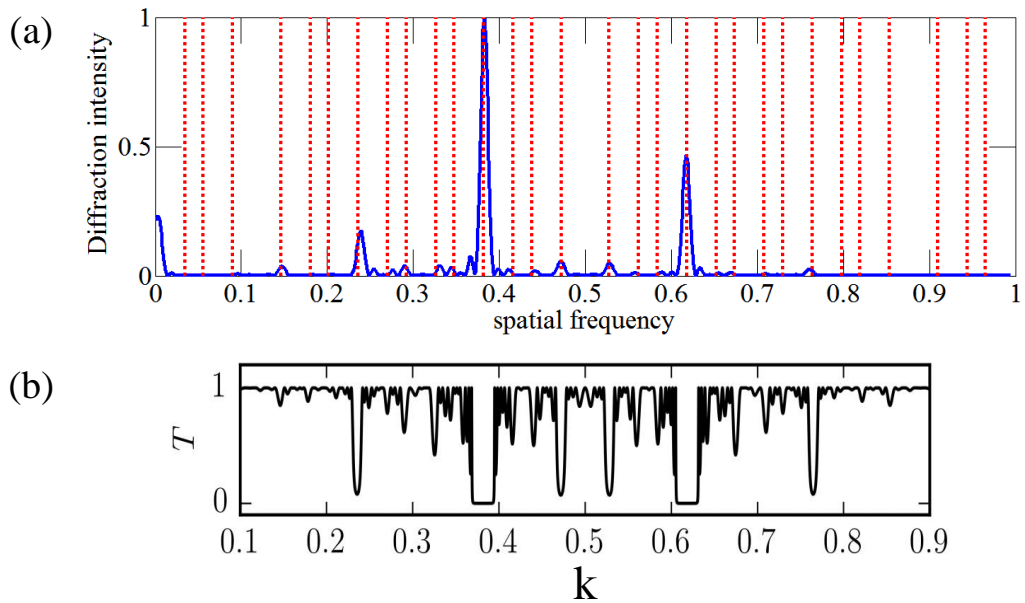


Figure 3.43: A reciprocal space and scattering analysis of the Fibonacci chain S_{10} . The relations between the spatial frequency of observable diffraction peaks (a), and the frequency of the spectral gaps in the transmission spectrum (b), where the contrast is 100%.

Regarding this equivalence, we note that the diffraction spectrum arises from purely structural properties, while the scattering of waves involves parameters such as dielectric contrast, controlling the width of the gaps. In chapter 4 this relation will become very useful in explaining the topological properties of quasiperiodic structures, especially with regards to the question of their origin and the role of true irrationality.

Furthermore, through the gap labeling theorem given in (3.45), lends topological meaning to p, q in expression (2.13).

3.6 Independent phases of the scattering matrix

In this section we reiterate some understandings regarding the properties of the scattering matrix in order to provide a new language considering the independent phases of the scattering matrix and their relations to observable properties. This new definition will bear meaning in the analysis of topological properties of quasiperiodic chains (to be discussed in chapter 4), but we believe this definition is universal, i.e. it is applicable to other scattering problems.

3.6.1 Two independent phases

The scattering matrix S of any chain (3.1) contains four elements. These four elements consists of only two (related) amplitudes, $|t|$ and $|r|$ where

$$|r| = |\vec{r}| = |\overleftarrow{r}|$$

$$|r|^2 + |t|^2 = 1,$$

but three phases, namely θ_t , $\vec{\theta}$ and $\overleftarrow{\theta}$ (see 3.1). However, being unitary and thus diagonalizable, the diagonal form of S (3.3) contains only two independent phases $\Phi_1(k)$, and $\Phi_2(k)$. The next textbook step is the definition of the total phase shift, $\delta(k) \equiv (\Phi_1(k) + \Phi_2(k))/2$. The total phase shift is obviously the first independent phase of the scattering matrix. This phase leads to the density of modes spectrum $\rho(k)$ and counting function $\mathcal{N}(k)$ for any chain. For quasiperiodic chains, it is this phase that takes the singular continuous fractal properties, and even topological properties in substitution based structures. We note here that through (3.2), the total phase shift may be expressed using the transmitted phase shift, or using the average of the two reflected phase shifts, namely

$$\begin{aligned} \delta(k) &= \theta_t(k) + \pi/2 \\ &= \frac{1}{2} \left(\vec{\theta} + \overleftarrow{\theta} \right). \end{aligned} \quad (3.50)$$

The transmitted phase shift is independent on the direction of the transmission experiment (see figure 3.1b). Therefore, $\rho(k)$ and $\mathcal{N}(k)$ for any chain are indifferent to a full inversion of the chain, and do not differentiate between symmetric or asymmetric chains. The second independent phase of the scattering matrix is not consensual.

This second independent phase of the scattering matrix has to involve a different combination of $\vec{\theta}$, and $\overleftarrow{\theta}$. Our proposition here, is to consider the chiral phase $\alpha = \overleftarrow{\theta} - \vec{\theta}$ as the second independent phase of the scattering matrix for various reasons. One very natural reason is the fact that unlike δ , the chiral phase α is sensitive to the symmetry of the chain (for example it vanishes identically for inversion symmetric chains). The second reason is not that obvious, and involves the fact α is the scattering phase which is sensitive to the gauge phase ϕ , through the palindromic symmetry cycle discussed in 2.2. This will become clearer in chapter 4.

A questions to be asked is what observables may depend on the phase α , as the entire spectral properties are encapsulated in the total phase shift δ . The obvious answer is non scattering observables due to a non scattering boundary conditions. For instance, the conditions for the existence of new gap modes in a hetero-structure such as the artificial palindrome are related to the chiral phase α (see 3.6.2).

3.6.2 Scattering analysis of a hetero-structure

This problem has already been analyzed using two different methods in 3.3.1 and 3.3.4. Here we note that the cavity phase shift θ_{cav} shown by the two approaches to govern the condition for new resonant gap modes may be written as:

$$\theta_{cav}(k_m) = 2\delta(k_m) + \alpha(k_m) = 2\pi m, \quad (3.51)$$

essentially dependent on both phases of the scattering matrix (including a direct dependence upon α). This formula will prove to be very important in understanding the relations between these phases in terms of topological properties.

Chapter 4

Topological properties of quasiperiodic chains: theory and experiment

This chapter presents our main findings regarding the existence of Chern topological invariants in quasiperiodic chains, their properties and their physical origin. We will propose 6 new schemes to measure these Chern numbers, and demonstrate the experimental measurement in 4 of those schemes. When relevant, the differences from outstanding results will be discussed. This chapter is ordered in a more chronological rather than pedagogical manner. Section 4.1 gives further introduction regarding topological invariants and their properties. Section 4.2 conveys the theoretical analysis of the topological properties of quasiperiodic chains using the scattering approach. Section 4.3 describes a first experimental measurement of Chern numbers in the spectrum of the Fibonacci chain using the theoretical proposal given in section 4.2. Section 4.4 describes a first experimental measurement of Chern numbers in the diffraction pattern of the Fibonacci chain. Finally, Section 4.5 gives a theoretical description of Chern numbers in quasiperiodic chains from a purely structural point of view, clarifying the results given in section 4.4, and also shedding light over the existence of Chern numbers in quasiperiodic chains without any external fields.

4.1 Topological invariants: Further introduction

This section reviews and reiterates important subjects regarding topological invariants for various systems including C&P quasicrystals.

4.1.1 topological invariants in physical problems

Topological features of physical systems, thoroughly investigated in condensed matter physics during the last decades, provide a general classification of a wide range

of physical phenomena in terms of a small number of integer topological invariants. A common example is provided by the topological classification of geometrical surfaces by means of the integer Euler-Poincaré characteristics. For instance (see chapter 1, and figure 4.1), a sphere cannot be continuously deformed into a torus. A comprehensive approach to the above ideas is given in terms of Chern numbers. These numbers play an important role in modern physics and particularly in condensed matter. They have been used to classify possible stable defects (e.g. vortices, dislocations) of ordered phases of matter. Chern numbers are also instrumental to understand, from a topological perspective, the quantization of the Hall conductance in quantum Hall effects and have motivated several topological models of quantum condensed matter, e.g. topological insulators and graphene. In the wake of the quantum Hall effect discovery, relations have been established between topological properties and quasiperiodic order.

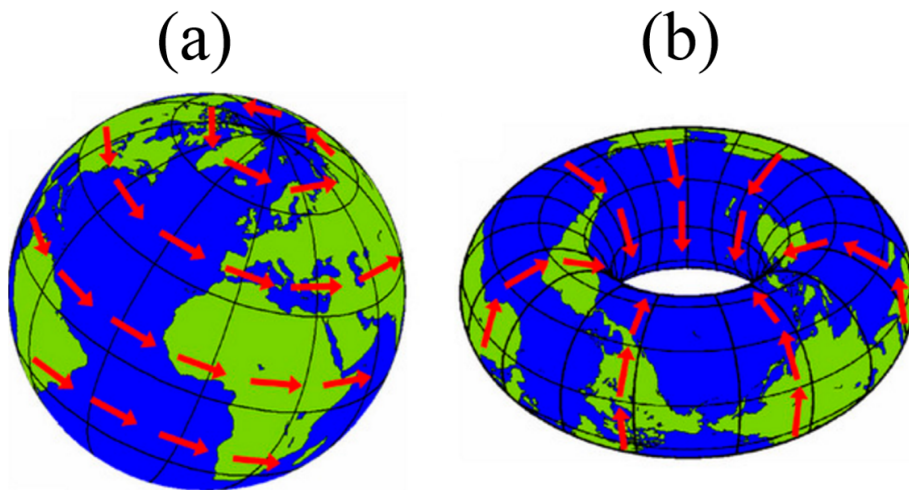


Figure 4.1: A sketch of the topological properties of a sphere (a) and a torus (b)

Since the discovery of the integer quantum Hall effect [KDP80] and its explanation in terms of topological invariants (see for instance [AOS03]), much attention has been devoted to the physics of topological phases. A topological phase, and its transport properties such as the quantum Hall conductance depends mostly on the bulk spectrum topology and not on the bulk structural details, thus being robust against imperfections. The current carrying states in such systems are topological edge states localized at the system boundaries and with energies inside the bulk band gap between Landau levels, obeying certain chirality rules. Understanding the classification of electronic states according to topological invariants in many body systems with bulk spectral gaps becomes an important problem no longer confined to solid-state physics but expanding into neighboring domains. For instance, cold atoms

systems can be tailored to possess large synthetic analogous magnetic fields and spin-orbit coupling controlling the topological phases [DGJÖ11]. Another example which is non-magnetic are photonic systems have been used to mimic condensed matter physics [LRG11, RZP⁺13, Haf14, PPH15].

4.1.2 The physics of topological edge states

Much of the recent interest in topological phases involves the existence and properties of edge-states [Hat93b, Hat93a, Sch13]. For us it is important to stress here two points. The first point is that the edge states themselves are not topological. In $2D$ systems such as the integer quantum Hall effect, they are the current carrying states due to the insulating properties of the bulk. Therefore, the measurement of edge-states *per se* is not the most fundamental measurement of the topological properties, but a rather convenient indirect measurement. The second point is that in the case of quasiperiodic chains, since the edge is zero-dimensional, and no external fields are at play, the existence of edge states is not required to obtain the topological properties. In the case they do exist, their properties carry topological information. Therefore, in this chapter we will see that one needs to be careful in how to produce and constrain edge states in order to reveal the entire quasiperiodic topological “story”.

4.1.3 Topological properties of quasicrystals

For quasiperiodic chains such as the Fibonacci chain, the scattering and diffraction spectrum has been shown to carry topological information [Bel82, Kun86]. However, the fundamental physical interpretation of the existence of Chern numbers with no further manipulation or underlying symmetry has been enshrined in mystery. Recently, a relation between quasiperiodic order and topological properties has been theoretically and experimentally addressed in tight binding Aubry-Andre-Harper model and Fibonacci systems using edge states [KLR⁺12, VZL⁺15]. A traverse of topological edge states has been predicted as a function of an internal degree of freedom, the modulation phase, and a derivation of corresponding Chern numbers through a Chern density defined from projection operators. An effect of this traverse has been measured experimentally for an Aubry-Andre chain in the adiabatic pumping of light from one edge of the chain to the other. Another work has connected the band Chern numbers in Cut&Project crystals to the winding of the reflected phase shift as a function of the modulation phase [KLR⁺12, Haf14, Dan14, PPH15].

In the past years, we have investigated the spectral and topological aspects of $1D$ Fibonacci and other quasicrystals [ADL13, TGB⁺14]. Here, we report of the progress made regarding this link between quasiperiodic order and topological phases. Analyzing the structural effect of the 2π -periodic modulation phase ϕ on a given structure, we have found an overall structural cycle of deviation from palindromic sym-

metry which is π -periodic with respect to the modulation phase. Using a scattering approach, we have identified the scattering chiral phase α as a fundamental probe of topological information. This result contains a factor 2 with respect to other results [KLR⁺12, Haf14, Dan14, PPH15], due to the factor 2 between the modulation phase periodicity and the spatial palindromic symmetry cycle. Using this understanding, we have constructed an edge state producing scheme where the edge state intra-gap frequency is sensitive to α . In this proposed experiment, Chern numbers may be obtained using a simple spectral measurement of the edge state frequency, and the account for the winding number of the edge state upon a scan of the modulation phase along a full period. Using a scattering analysis, we exactly predict the topological edge state existence and frequency for every open gap as a function of the modulation phase through an effective Fabry-Perot geometrical model. This model generalizes our approach even further, and also yields a Fabry-Perot rule for the spatial symmetry of the edge state. We have pursued this proposal, and performed such a measurement in a cavity polariton setup, and demonstrate this indirect measurement of Chern numbers in two open gaps using the edge state winding number and also the spatial symmetry changes as a function of the modulation phase.

From the previous discussion, it may seem that the existence of Chern numbers is a characteristic of the energy spectrum only. Surprisingly, we have also shown that gap Chern numbers also exist in purely structural aspects of the quasiperiodic chain and may be directly measured using nothing but the diffraction pattern of the structure. In addition to being complementary to the spectral one, this new approach allows to measure in a simple setup, extremely high values of Chern numbers for rather short structures. We have pursued this proposal, and recently performed such a measurement using a programmable diffraction grating.

4.2 Topological properties of Fibonacci quasicrystals: A scattering analysis of Chern numbers

This section consists of a scattering based study of topological properties of Fibonacci quasicrystals [LBFA15]. Chern numbers which label the dense set of spectral gaps, are shown to be related to the underlying palindromic symmetry. Topological and spectral features are related to the two independent phases of the scattering matrix: the total phase shift describing the frequency spectrum and the chiral phase sensitive to topological features. Conveniently designed gap modes with spectral properties directly related to the Chern numbers allow to scan these phases. An effective topological Fabry-Perot cavity is presented.

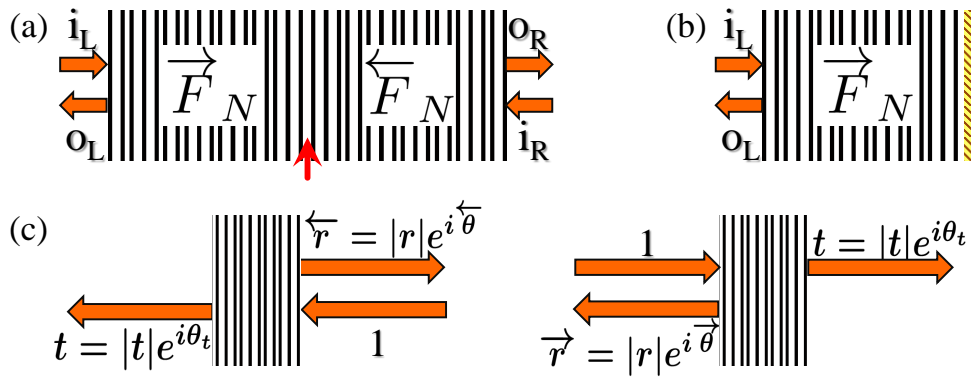


Figure 4.2: (a) The scattering setup. A finite chain is inserted in between perfect dielectric media supporting incoming (i_L, i_R) and outgoing waves (o_L, o_R). Displayed case: $\mathcal{P} \equiv \vec{F}_N \overleftarrow{F}_N$ (\uparrow indicates the interface) (b) The chain \vec{F}_N with a reflecting boundary condition (golden bar), is equivalent to the unfolded open structure \mathcal{P} in (a). (c) Complex amplitudes corresponding to a wave incident respectively on the right or left side of the chain.

4.2.1 Preface

Topological features of quasiperiodic structures have been studied under various guises (see 4.1). Chern integers label the dense set of gaps in the energy (frequency) spectrum [Bel82, Kun86, Bel92]. More generally, Chern numbers are known to play a role in problems where the underlying topology has been identified e.g., magnetic field, chirality or nontrivial band structures. However, in quasiperiodic structures like the Fibonacci chain, the physical origin underlying the existence of Chern numbers has not yet been identified. We consider finite Fibonacci chains and study the behavior of some spectral quantities driven by the modulation phase ϕ (defined in chapter 2) accounting for the important but not yet studied palindromic or mirror symmetry of Cut and Project (C&P) quasiperiodic chains. We then propose new expressions and possible measurements of Chern numbers using the analysis results. We shall discuss the specific case of Fibonacci chains, but we expect our results to apply to a larger class of similar quasiperiodic chains, and also for higher dimensions.

Quasiperiodic systems share similar spectral properties, e.g. their singular continuous frequency spectrum has a fractal structure, with a dense distribution of gaps characterized by the gap labeling theorem (discussed in chapter 3). It provides a precise expression of the normalized counting function $\mathcal{N}(\varepsilon_{gap})$ at energies ε_{gap} inside the gaps. For the Fibonacci chain, gaps are labeled by means of two integers (p, q) such that, $\mathcal{N}(\varepsilon_{gap}) = p + q\tau^{-1}$, where $\tau = (1 + \sqrt{5})/2$ is the golden mean. The integers q are known to be Chern numbers and $p(q)$ keeps $\mathcal{N}(\varepsilon_{gap})$ within $[0, 1]$ (see figure 3.42). We stress that although self-similarity and gap labeling are spectral properties of the infinite S_∞ (where ϕ is irrelevant), they hold very well in finite

chains.

Our analysis of the Fibonacci chain makes use of three of the generation methods described in 2.1. The first is substitutions which justifies the gap labeling theorem and the appearance of Chern numbers in gap labels. The second is the characteristic function which defines ϕ , predicts the existence of perfect palindromes, and gives equivalent result to the C&P method which are more computerizable. The third is C&P which allows for a useful interpretation of ϕ , as the rearrangement of letters equivalent to translation (see figure 2.3), in a series of identical local phason-flips $BAABAB \leftrightarrow BABAAB$ arranged in a C&P-like geometrical pattern (see figure 2.12). This inherent discreteness underlies the characteristic stepwise behavior of spectral and structural properties as a function of ϕ (depicted in many figures throughout this chapter).

The main analysis method is the scattering approach discussed at detail in 3.1. Figure 4.2a reiterates notations to be used in this section. We recall that any quantum or wave system with a potential defined with respect to a free part can be probed using scattering waves of wave vector k , thus our results may be generalizable to many other systems.

Another essential ingredient in this analysis is the ϕ -driven palindromic symmetry cycle, $\eta(\phi)$ (described in 2.2 and depicted for the Fibonacci case in figure 2.22), as we shall see. This cycle, is underlying the existence the spectral manifestation of Chern numbers in C&P quasiperiodic chains, and in the corresponding Aubry-Andre-Harper tight binding model (described in 2.2). The structural phase ϕ driven symmetry cycle, thus plays a role analogous to the magnetic field in the 2D quantum Hall effect, and we wish to express the Chern numbers labeling spectral gaps as the winding of some phase with respect to the gauge phase ϕ . In accordance to that, the origin of ϕ is set in this section to a palindromic symmetry value.

4.2.2 Semi-quantitative numeric description

We start by restating that the scattering total phase shift $\delta(k)$ do not discriminate between the sequence $\vec{F}_N \equiv [\chi_1 \chi_2 \cdots \chi_N]$ and its reversed $\overleftarrow{F}_N \equiv [\chi_N \chi_{N-1} \cdots \chi_1]$, and therefore it is not sensitive to the symmetry of the sequence (palindromic or not). This insensitivity, in addition to the fact that shifts in ϕ are equivalent to translations (shifts in origin) along S_∞ , clarifies why bulk spectral properties (e.g. transmittance, density of modes, counting function), derived from $\delta(k)$, are independent of ϕ (see figure 4.13a). Specifically, the independence of the counting function $\mathcal{N}(k)$ upon ϕ implies that the Chern numbers appearing as the integer labels of the gaps are also ϕ -independent. This agrees with the fact that the gap labeling theorem is used for S_∞ , for which ϕ is undefined, and based on substitution rules for which ϕ is unimportant. This is not the case for the reflection amplitudes, related by $\overleftarrow{r} = \overrightarrow{r} e^{i\alpha}$, where α is the chiral phase (defined in 3.3) which is, by definition, sensitive to the symmetry of the

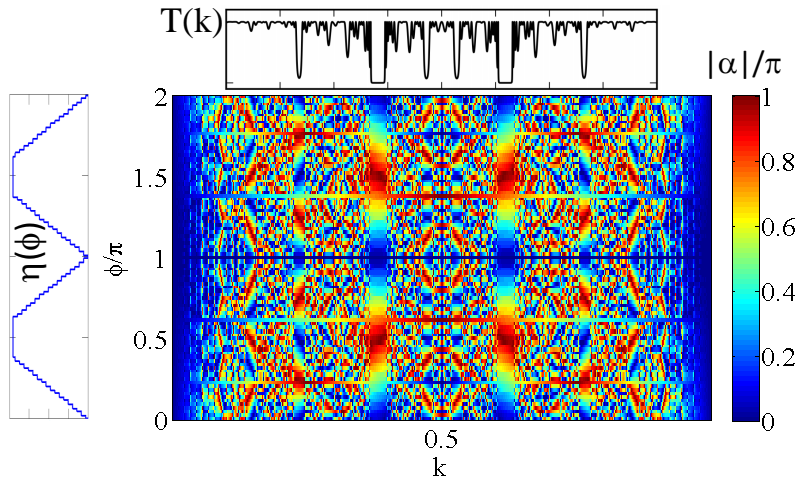


Figure 4.3: Colormap: $|\alpha(\phi, k)|$ for \vec{F}_N ; $N = 89$. On top: The transmittance spectrum for the structure. On the left: the structural palindromic symmetry cycle.

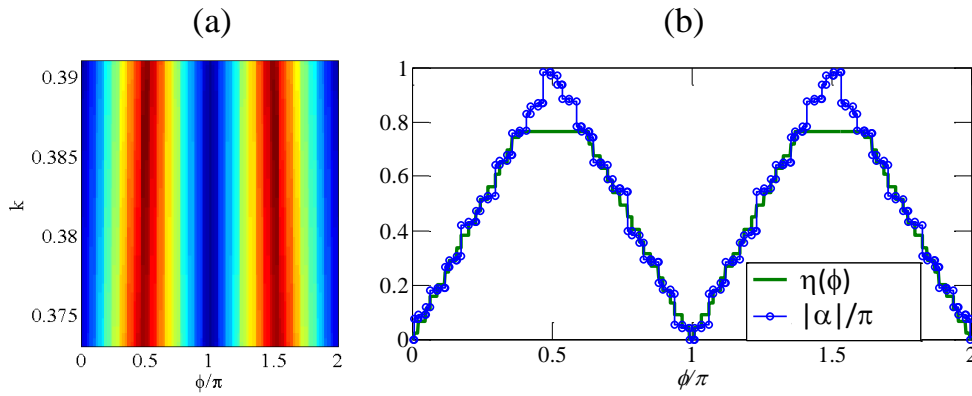


Figure 4.4: (a) The colormap of figure 4.3, at k values inside the gap $q = -1$. (b) A cut through the colormap in (a) at mid-gap (blue circles), compared the structural palindromic symmetry cycle (green line).

structure as measured in the difference between the two experiments in figure 4.2c. The vanishing of α (identically) for palindromic values of ϕ makes it a candidate for a spectral counterpart of the structural deviation from palindromic symmetry $\eta(\phi)$.

A numerical calculation of the chiral phase $0 \leq |\alpha(\phi, k)| \leq \pi$ for the set $\{\vec{F}_{89}(\phi)\}$ defined in 2.2.1 yields a beautiful butterfly-like map with a strong dependence upon ϕ as well as upon k (see figure 4.3). A closer look reveals that within each of the gaps, $|\alpha(\phi, k)|$ is a very regular function of ϕ , essentially insensitive to k (see close-ups in figures 4.4a, 4.5a and 4.6). The purely structural staircase of phason-flips aided dependence on ϕ , is equivalent to multivalued translation, but also drives various structural properties such as fractional translation, fractional inversion, and the deviation from a perfect palindrome, through a regular dependence upon ϕ (see 2.2). Here, we show that it is mapped to a regular winding of the scattering chiral phase as a function of ϕ .

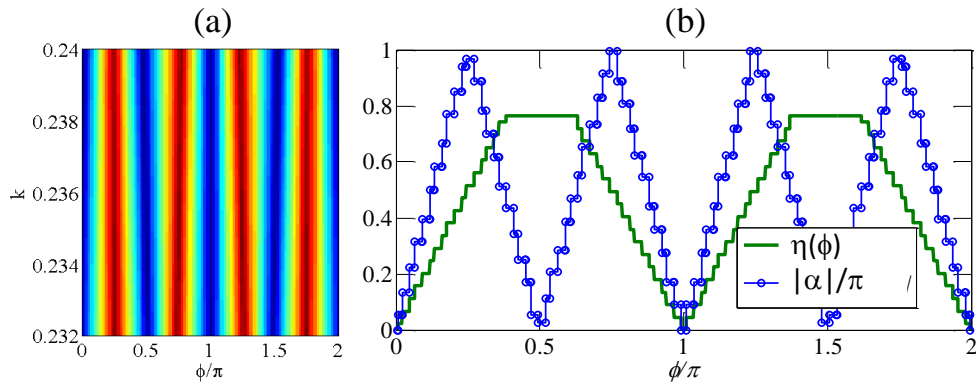


Figure 4.5: (a) The colormap of figure 4.3, at k values inside the gap $q = 2$. (b) A cut through the colormap in (a) at mid-gap (blue circles), compared the structural palindromic symmetry cycle (green line).

Furthermore, within a 2π -period of the phason ϕ , the chiral phase $\alpha_q(\phi)$, where q is the Chern number of the gap label, is strongly correlated to the palindromic symmetry cycle and consequently completes an integer amount of windings (figures 4.4b, 4.5b). The winding number, including the sign, is related to the gap Chern number q by

$$\mathcal{W}(\alpha_q) = \frac{1}{2\pi} \int_0^{2\pi} d\phi \frac{d\alpha_q(\phi)}{d\phi} = 2q$$

where the integration is defined in a piecewise manner, and $\alpha_q(\phi)$ is properly unwrapped. The winding corresponds to a π/q period, with the zeroes coinciding with the zeroes of the structural deviation from palindromic symmetry $\eta(\phi)$, as depicted in figures 4.7, 4.8, and 4.9. We may say that $\alpha_q(\phi)$ behaves numerically as the q^{th} harmonic of the palindromic symmetry cycle. This constitutes a novel method to measure the Chern numbers labeling the gaps in quasiperiodic chains through the winding of the phase α_q as a function of the gauge field ϕ . This method, together with the gap labeling theorem forms some complete topological scattering formulation. Both independent phases of the scattering matrix carry the same topological information. The total phase shift is independent on the phason ϕ , but the topological invariants appear as integers labeling the spectral gaps. The chiral scattering phase is independent of k within the gaps, and carries the information of the gap's topological invariant in the integer winding as a function of the phason ϕ .

The measurement of the gap labeling Chern numbers through the winding of $\alpha_q(\phi)$, proves to be a much more sensitive method than the gap labeling itself. Firstly, the condition (3.45) is proven for S_∞ and holds for finite systems (within experimental/numerical resolution), while such arguments are not needed in the case of the perfectly integer winding of $\alpha_q(\phi)$. Secondly, for a finite chain, this

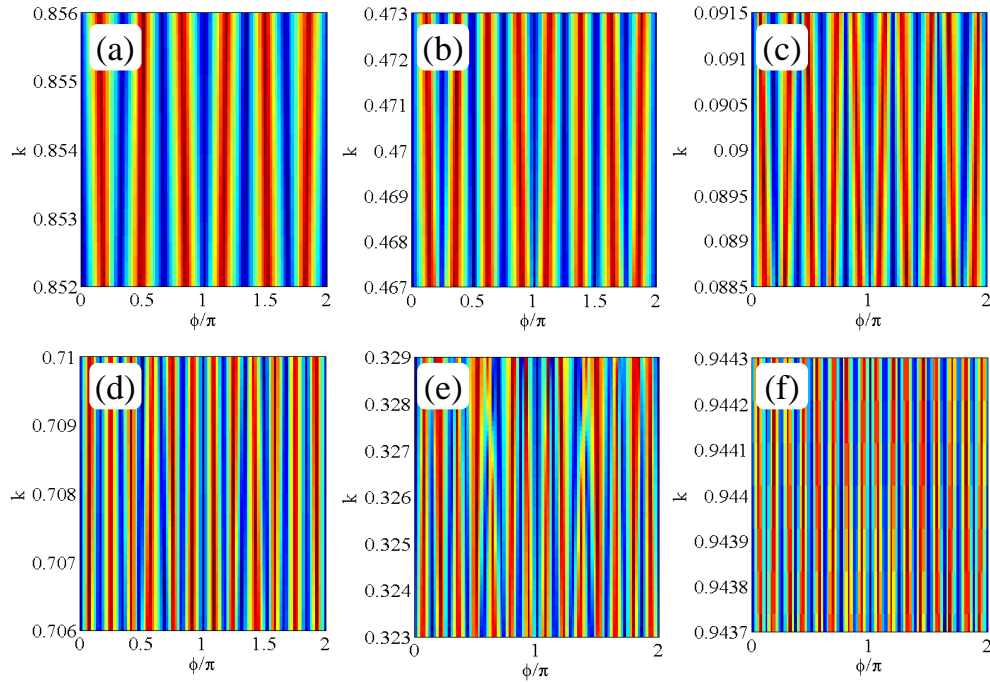


Figure 4.6: (a)-(f) The colormap of figure 4.3, at k values inside the gaps $q = 3, 4, 5, 6, 7, 8$, respectively.

method seem to obtain many more Chern numbers than accessible (open) gaps in the integrated density of states spectrum (figure 4.6f, for instance, monitors 16 windings corresponding to $q = 8$ which is unobservable in the integrated density of states spectrum of the same structure). It seems that the limitation for this measurement comes from the finite number N of phason flips within a period of ϕ which will eventually cause an under-sampling of the winding. If $N = 89$, and we take a minimal value of 3 sampling point per winding, we should be able to capture 30 windings which corresponds to a gap labeling Chern number of $q = 15$. Figure 4.10 shows a numerical measurement of Chern number $q = 13$ under the conditions discussed here.

In this context, we note here that the two ingredients of $\alpha_q(\phi)$, namely $\vec{\theta}_{\vec{F}}(\phi, k)$ and $\overleftarrow{\theta}_{\vec{F}}(\phi, k)$, also experiences an integer winding as a function of ϕ within spectral gaps. This winding is equal to q , but it is not decoupled from the spectrum, as the phase (or origin) of the winding has a significant dependence on k (see the right panel in figure 4.17). That been said, the reduced number of windings compared to $\alpha_q(\phi)$ may be used to measure a Chern number twice as high. Figure 4.12 shows a numerical measurement of Chern number $q = 25$ under the conditions discussed above.

We note that schemes for such measurement of Chern numbers by using the reflected phase shift have already been proposed [MMB11, FHA12, Haf14, PPH15].

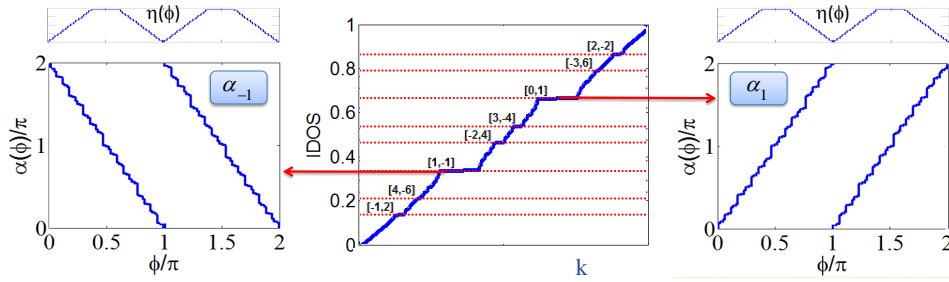


Figure 4.7: In the center: The integrated density of states (IDOS) of \vec{F}_N ; $N = 89$, with gap labels $[p, q]$ using (3.45). On both sides: $\alpha(\phi, k)$, at k values within the gaps $q = \pm 1$ (compared to the palindromic symmetry cycle).

Although not strictly quasiperiodic, the structures considered by this body of work may be generalized to quasiperiodic chains. The main differences with respect to the current work are given in figure 4.11. The winding of the reflected phase shift over the 2π -period of ϕ is indeed integer which is equal to q . However, there is no explicit explanation given to this winding of the phase except for a connection to the existence of topological edge states. Moreover, no method is given to derive or understand the zeros of this winding (which also depend on k), and also, the zeros of this winding is not correlated to the palindromic symmetry cycle, neither to the zeros of the gap mode crossover discussed ahead. Finally, up to this current work, the reflected phase shift method has not been tested against a theoretical prediction for the values of gap Chern numbers. Here we have a combination of reflected phase shifts which is by definition a probe for the structural symmetry cycle driven by ϕ in C&P chains. This combination is k -independent within the gaps, and has natural zeroes at the palindromic values of ϕ , which are π -periodic in clear correlation to the palindromic symmetry cycle, and to the zeros of the gap mode crossover discussed ahead. Accordingly, the longest period possible for α is π (for $|q| = 1$), and for higher values of q more zeroes occur (i.e. the period of the structural palindromic cycle is always π , whilst the period of the spectral palindromic symmetry cycle is gap dependent and equals π/q). Finally, the current work has tested its prediction against the theoretical Chern numbers derived from the substitution rules.

As stated in 3.6, the phase $\alpha_q(\phi)$ is most conveniently investigated using states other than ϕ -independent scattering states. We thus consider distinct choices of boundary conditions and study the resulting gap boundary states whose spectral locations depend on these choices, e.g. closed (mirror) boundary condition, interface or local defect (see 3.2). Since each choice leads to edge states of the same origin (see 3.3), without loss of generality, we consider a finite Fibonacci chain (of length $N = \mathcal{F}_j$, to properly fix the origin of ϕ) with reflective boundary condition at one end (figure 4.2b). To adapt this setup to the scattering approach, we unfold it as displayed in figure 4.2a, to arrive at the artificial palindrome $\mathcal{P} \equiv \vec{F}_N \overleftarrow{F}_N$ which is an

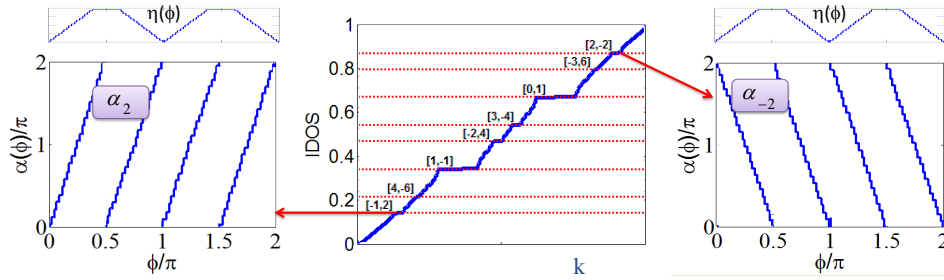


Figure 4.8: In the center: The integrated density of states (IDOS) of \vec{F}_N ; $N = 89$, with gap labels $[p, q]$ using (3.45). On both sides: $\alpha(\phi, k)$, at k values within the gaps $q = \pm 2$ (compared to the palindromic symmetry cycle).

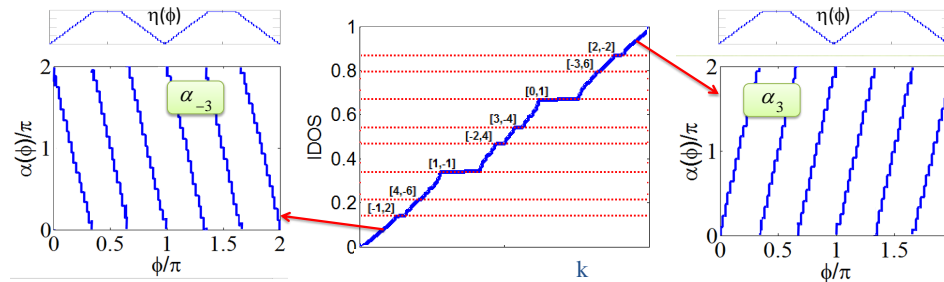


Figure 4.9: In the center: The integrated density of states (IDOS) of \vec{F}_N ; $N = 89$, with gap labels $[p, q]$ using (3.45). On both sides: $\alpha(\phi, k)$, at k values within the gaps $q = \pm 3$ (compared to the palindromic symmetry cycle).

open scattering system of length $2N$ which may be regarded as a generalized edge (see 3.2.3). Since \mathcal{P} is not a *bona fide* Fibonacci chain, additional interface modes appear in the gaps of \vec{F}_N at values $k_m(\phi)$. A numerical calculation of the artificial palindrome spectrum as a function of ϕ reveals that the gap modes frequencies $k_m(\phi)$ behavior as a function of ϕ essentially depends only on the Chern number q of each gap as assigned by relation (3.45). Modes cross the gaps in a direction set by $\text{sign}(q)$ and a crossing period of $\pi/|q|$, in perfect accordance with the winding of α , and with the palindromic symmetry cycle, as shown in figures 4.13, 4.14, 4.15. When \vec{F}_N is palindromic ($\vec{F}_N = \overleftarrow{F}_N$), and α vanishes, \mathcal{P} reduces to \vec{F}_N with periodic boundary conditions instead of a mirror. It is also possible to show numerically that $\mathcal{P}(\phi) = \vec{F}_{2N}(\phi)$ in the spirit of 2.1.9. Naturally, no gap modes exist as depicted in figure 4.15. This constitutes a novel method to measure the Chern numbers labeling the gaps in quasiperiodic chains through the spectral winding of conveniently designed boundary states as a function of the gauge field ϕ using a simple spectroscopic setup.

Using the fact that taking $\mathcal{P} \equiv \overleftarrow{F}_N \vec{F}_N$ instead of $\mathcal{P} \equiv \vec{F}_N \overleftarrow{F}_N$ is equivalent to taking $\alpha \rightarrow -\alpha$, we have also been able to mimic the behavior of a closed system (with reflective boundary conditions at both ends) using the structure $\vec{F}_N \overleftarrow{F}_N \vec{F}_N$, now having topological gap modes localized at the two interfaces (mimicking the

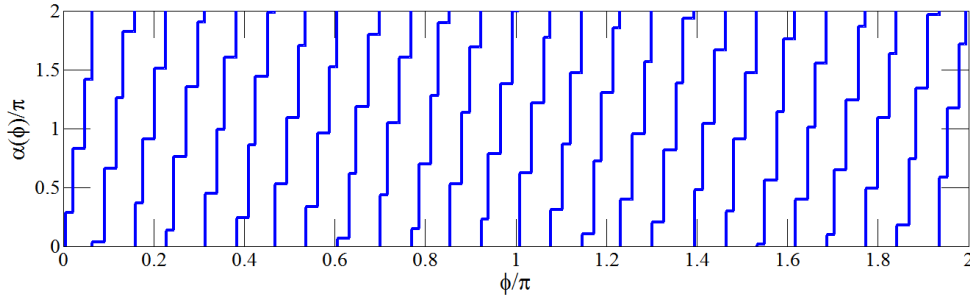


Figure 4.10: $\alpha(\phi, k)$, at $k = 13\tau^{-1} - 8$, labeled by $q = 13$.

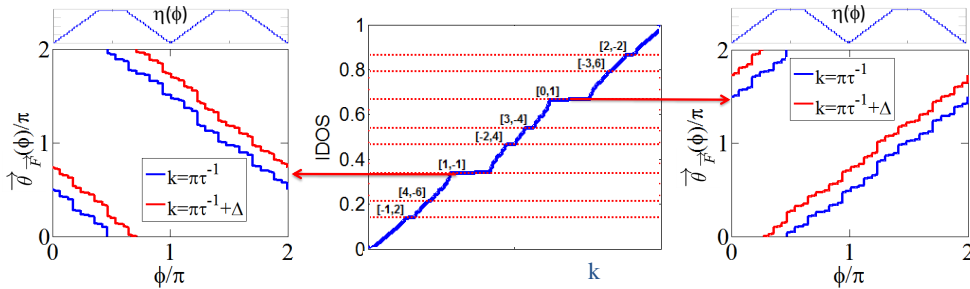


Figure 4.11: In the center: The integrated density of states (IDOS) of \vec{F}_N ; $N = 89$, with gap labels $[p, q]$ using (3.45). On both sides: $\vec{\theta}_{\vec{F}}(\phi, k)$, at two different k values within the gaps $q = \pm 1$ (compared to the palindromic symmetry cycle).

two edges of a closed system), and traveling in opposite directions. This is depicted in figure 4.16.

Once again, we note here that other schemes for such measurement of Chern numbers using the properties of edge states have been proposed, demonstrated and analyzed [KLR⁺12, Dan14]. Although the proposed Aubry-Andre-Harper structures are not describable by C&P neither by substitutions, the structures considered by that body of work can be generalized as such [KZ12]. The main differences from the current work are as follows. Firstly, the edge states in those demonstration are excited due to the $\Psi = 0$ boundary condition at the edges. However, the experimental paper [KLR⁺12] does not gives this explanation. Secondly, the Chern numbers are not measured through the winding number of the edge state, but using a Chern density argument, without testing it against a theoretical prediction. The winding number was added later in a theoretical paper [Dan14]. Thirdly, this body of work only counts the winding, but gives no explanation to the mechanism of the winding or information regarding the zeros of the windings. Finally, the calculated winding of the edge states seem to pause after every winding and then to restart another winding. The authors were aware of this problem and attempted to explain it. Here we have a correspondence of the gap mode winding to the structural palindromic symmetry cycle driven by ϕ in C&P chains. This correspondence has natural zeroes (with a periodic boundary condition argument) at the zeros of $\eta(\phi)$, which is π -

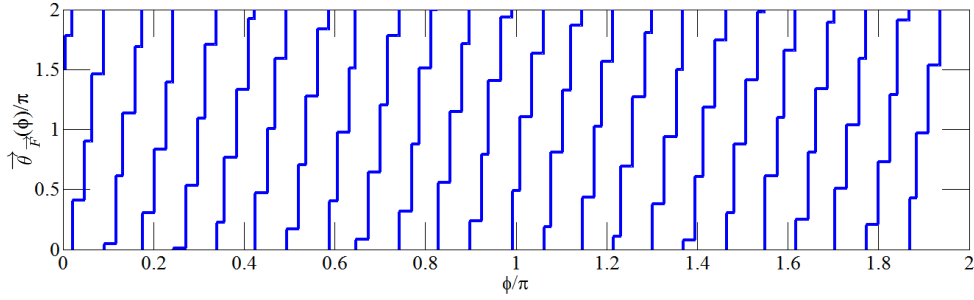


Figure 4.12: $\vec{\theta}_{\vec{F}}(\phi, k)$, at $k/\pi = 25\tau^{-1} - 15$, labeled by $q = 25$.

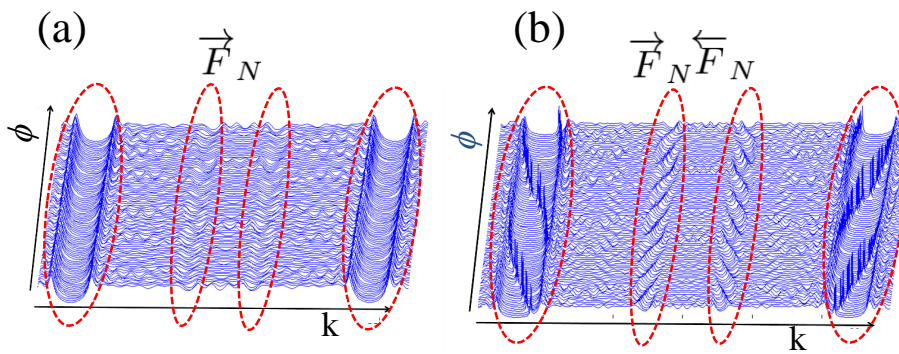


Figure 4.13: Topological gap modes in the spectrum of the artificial palindrome $\mathcal{P} \equiv \vec{F}_N \overleftarrow{F}_N$; $N = 89$. (a) A semi 3D plot of the density of states as a function of ϕ and k for the structure \vec{F}_N ; $N = 89$. The ϕ -independent gaps with $q = \pm 1, \pm 4$ are marked with dashed red ellipse. (b) The same as (a), for the structure $\mathcal{P} \equiv \vec{F}_N \overleftarrow{F}_N$; $N = 89$. Gap modes and their traverse as a function of ϕ is observable.

periodic, and topological zeroes at the other zeroes of $\alpha(\phi)$. Accordingly, the longest period possible for the winding is π (for $|q| = 1$), and for higher values of q more zeroes occur (i.e. the period of the structural palindromic cycle is always π , whilst the period of the gap mode winding is gap dependent and equals π/q). Our Fabry-Perot understanding of the problem suggests that if the authors of [KLR⁺12] were to use a phase conserving boundary conditions, than instead of the observed traverse they would have a pause, and instead of the pause they would have a traverse. The fact that spatial symmetry constraints forbids half of the possible gap modes is visible in figures 3.36, 3.37, 3.38, and 3.39. Additionally, the current work has tested its prediction against the theoretical Chern numbers derived from the substitution rules. Finally, a quantitative description for the existence of topological gap modes including an explanation to the disagreement regarding the winding number is given in 4.2.3.

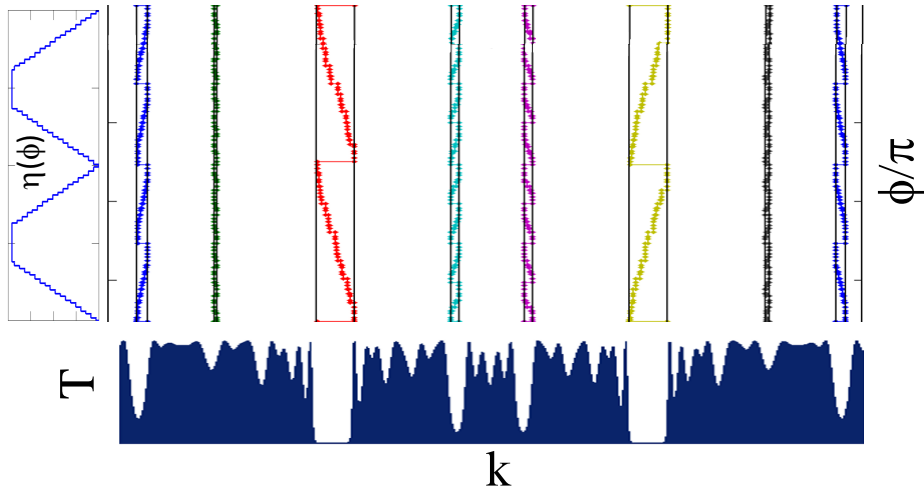


Figure 4.14: Topological gap modes in the spectrum of the artificial palindrome $\mathcal{P} \equiv \vec{F}_N \overleftarrow{F}_N$; $N = 89$. Eight selected gap modes frequencies as a function of ϕ is in colored markers, compared to the transmission spectrum below, and the palindromic symmetry cycle on the left.

4.2.3 Quantitative description

The observations in 4.2.2 become more quantitative by recalling the expressions developed for the emergence of gap modes in a hetero-structure developed in 3.3.4. The condition for the appearance of a gap mode k_m in the spectrum of \mathcal{P} was found to be

$$\theta_{cav}(\phi, k_m) = 2\pi m. \quad (4.1)$$

This condition has been exactly obtained using two points of view: A full scattering calculation with a Levinson theorem-like resonance condition, and an effective Fabry-Perot model. Since θ_{cav} for the artificial palindrome $\mathcal{P} \equiv \vec{F}_N \overleftarrow{F}_N$ is obtainable from the scattering analysis of \vec{F}_N through (3.51), gap modes $k_m(\phi)$ of \vec{F}_N bounded by any type mirror at one end, can be obtained from the scattering data of the corresponding open chain. Using a mutual reflectance condition (3.33), we define k_i^q, k_f^q as the low and high frequency edges of the gap labeled by q , and define k_q such that $k_i^q < k_q < k_f^q$. Now, if for a value of ϕ , there exists $k_m(q, \phi) \in k_q$ such that the condition 4.1 is fulfilled, then it represents the (spectral) location of a gap mode of the gap q , allowing to characterize their crossing direction and periodicity in correspondence to the gap Chern number q (see figure 4.18). As observed in 4.2.2, at $\phi = 0$ set to be a palindromic value for \vec{F}_N , this condition is not fulfilled for any gap, and also at $\phi = \pi$, and $\phi = 2\pi$. Counting the number of crossovers in the gap q yields $2q$ complete crossovers. The counting may be performed by normalizing the k -axis so that $k_m(q, \phi) \rightarrow k'_m(q, \phi) \equiv 2\pi(k_m(q, \phi) - k_i^q) / (k_f^q - k_i^q)$, properly unwrapping $k'_m(q, \phi)$ and calculating

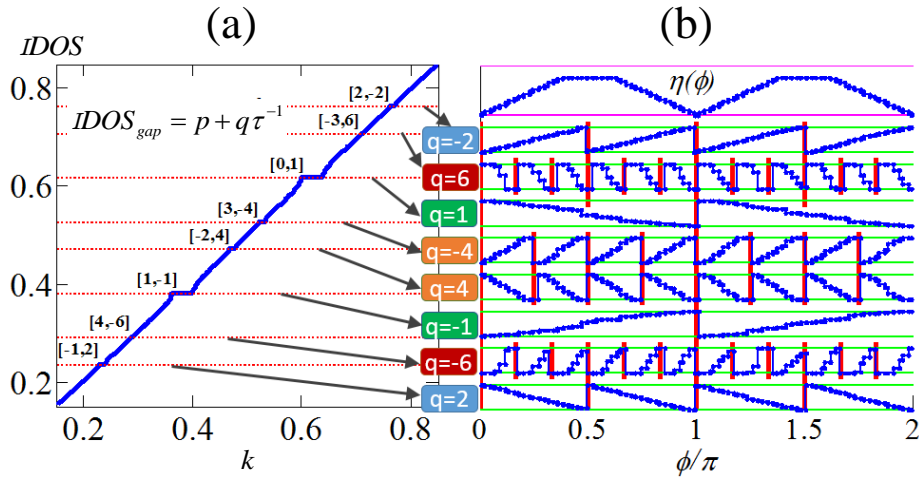


Figure 4.15: Topological gap modes in the spectrum of the artificial palindrome $\mathcal{P} \equiv \overrightarrow{F}_N \overleftarrow{F}_N$; $N = 89$. (a) The integrated density of states (IDOS) of \overrightarrow{F}_N ; $N = 89$, with gap labels $[p, q]$ using (3.45). (b) Eight selected gap modes relative in band frequencies as a function of ϕ is in blue (gap edges are in light green), compared to the palindromic symmetry cycle on top and to the gap Chern number q . Red bars split the ϕ axis to guide the eye in estimating the Harmonic.

$$\mathcal{W}(k'_m(q, \phi)) = \frac{1}{2\pi} \int_0^{2\pi} d\phi \frac{dk'_m(q, \phi)}{d\phi} = 2q$$

defined in a piecewise manner, to yield a another determination method of the corresponding Chern number q .

This quantitative description is the basis of the more qualitative analysis of 4.2.2. Using (3.51) allows to disentangles θ_{cav} into $\delta(k)$, insensitive to ϕ , and a k -independent $\alpha_q(\phi)$, both displaying the topological properties in different ways (see figure 4.17). As a straightforward consequence of this definition of θ_{cav} , its winding number for any $k \in k_q$ within a gap q is

$$\mathcal{W}(\theta_{cav}) = \frac{1}{2\pi} \int_0^{2\pi} d\phi \frac{d\theta_{cav}(q, \phi, \mathbf{k} \in k_q)}{d\phi} = 2q \quad (4.2)$$

defined in a piecewise manner, provides another direct determination of the corresponding Chern number q . These expressions quantify the methods to measure the gap Chern number proposed in 4.2.2, by presenting an exact mechanism which determines the existence and frequency of topological gap modes, and a correspondence to a ϕ -driven scattering chiral phase and a ϕ -driven structural symmetry cycle. These results are especially interesting since they relate the Chern numbers labeling the spectral gaps of the infinite chain S_∞ to the scattering matrix of finite chains without any need for approximations. In other words, the gap labeling prediction

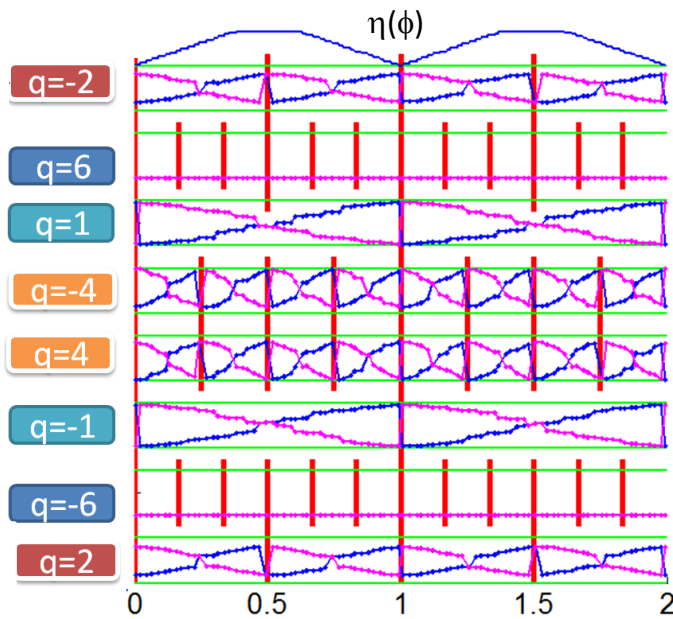


Figure 4.16: Topological gap modes in the spectrum of the structure $\vec{F}_N \overleftarrow{F}_N \vec{F}_N$; $N = 89$. The eight selected gap modes (see figure 4.15) relative in band frequencies as a function of ϕ is in blue for the first interface, and magenta for the second (gap edges are in light green), compared to the palindromic symmetry cycle on top and to the gap Chern number q . Red bars split the ϕ axis to guide the eye in estimating the Harmonic.

for Chern numbers in the integrated density of states are given for S_∞ and may hold only approximately for finite chains, while the winding of edge states occurs only in a finite chain carries exact information regarding the Chern number of S_∞ . It is thus possible to directly deduce Chern numbers from a scattering experiment.

The Fabry-Perot interpretation leading to (4.2) which is described in 3.3 lends an understanding regarding the spatial symmetry of the topological gap modes. As a gap mode traverses the gap, it keeps the parity of m in (4.1) and therefore its spatial symmetry with respect to the interface. When this mode is merged into one band edge, and another gap mode bifurcates from the other, the parity of m is changed. This means that the traversing modes spatial symmetry flips between traverses. This flipping may be understood if we consider the Fabry-Perot description for the case with a geometrical cavity allowing for a multi-valued Fabry-Perot resonant frequency comb to be observed (see figures 3.38 and 3.39). In this case it is clear that the resonant modes alternate in the parity of m , and that scan of ϕ will cause all of them to regularly traverse the gap. Here we observe the same behavior, through a spectral window which is the same width of the gap mode separation. This is another method to count the number of traverses, i.e. to measure the gap Chern number.

These topological properties presented here do not depend on the structural mod-

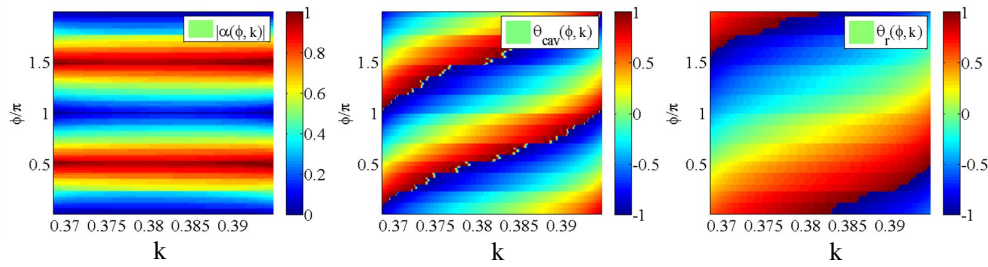


Figure 4.17: Left to right: a comparison between the colormaps for $\alpha_q(\phi)$, $\theta_{cav}(\phi, k)$, and $\theta_{\vec{F}}(\phi, k)$ for the structure $\mathcal{P} \equiv \vec{F}_N \overleftarrow{F}_N$; $N = 89$ within the gap $q = -1$.

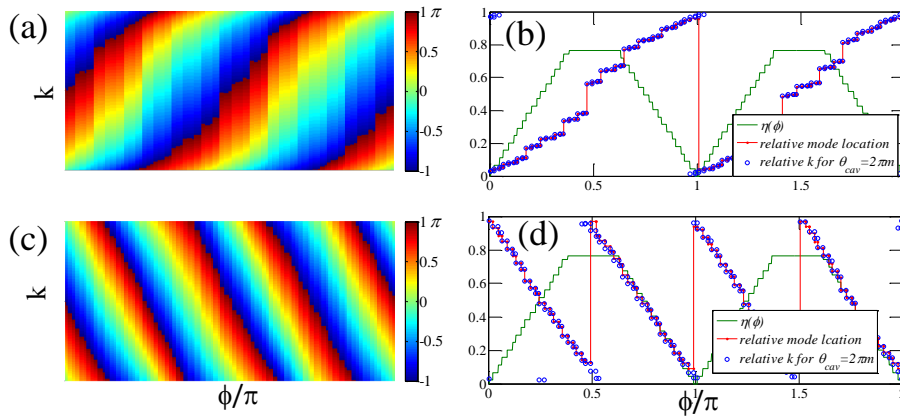


Figure 4.18: Topological gap modes in the spectrum of the artificial palindrome $\mathcal{P} \equiv \vec{F}_N \overleftarrow{F}_N$; $N = 89$. (a) Colormap of $\theta_{cav}(\phi, k)$ within the gap $q = -1$. Light green areas correspond to the resonance condition (4.1). (b) Crossover of the gap mode $k_m(\phi)$. Relative spectral location (red) is compared to the resonance condition (4.1) in blue, and to the palindromic symmetry cycle (green). (c)-(d) The same as (a)-(b) for $q = 2$.

ulation strength (or dielectric contrast). However, the value of contrast affects the number of spectral gaps open for analysis, which is higher when the contrast is increased. Also, the value of contrast affects the details of the staircase behavior of the scattering chiral phase and of the gap mode crossover. For any value of contrast the staircase jumps are not even as some are larger than other. This is understandable since within spectral gap frequencies, the interface (as any other slab) is exponentially coupled to its neighbors (as discussed in 3.2.2). Phason-flips occurring close by to the interface will promote the phase winding and mode crossover more than phason-flips occurring further away. Increasing the contrast strengthens the exponential decay, making the large staircase jumps even higher at the expense of the smaller jumps. In the limit of very high contrast, one staircase jump is responsible to the entire winding/traverse making it harder to observe the phenomenon. This is depicted in figures 4.19, and 4.20.

In summary, we have shown in this section that topological properties of quasiperi-

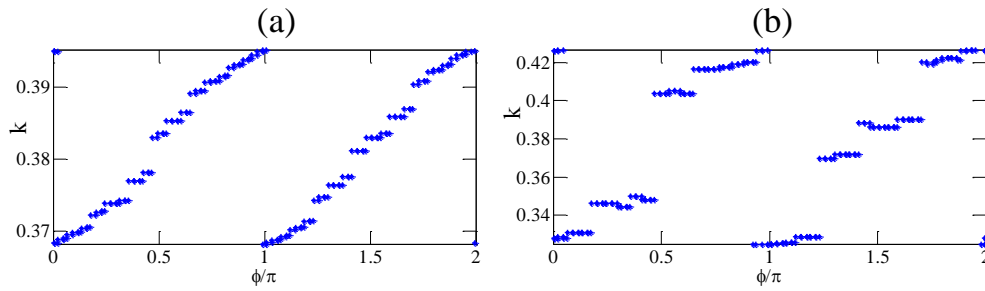


Figure 4.19: Contrast dependence of the topological gap modes trajectory as a function of ϕ for the structure $\mathcal{P} \equiv \overrightarrow{F}_N \overleftarrow{F}_N$; $N = 89$. (a) The spectral location of gap modes $k_m(\phi)$ as for the $q = -1$ gap with a 15% dielectric contrast and (b) The same as (a) for a 80% dielectric contrast.

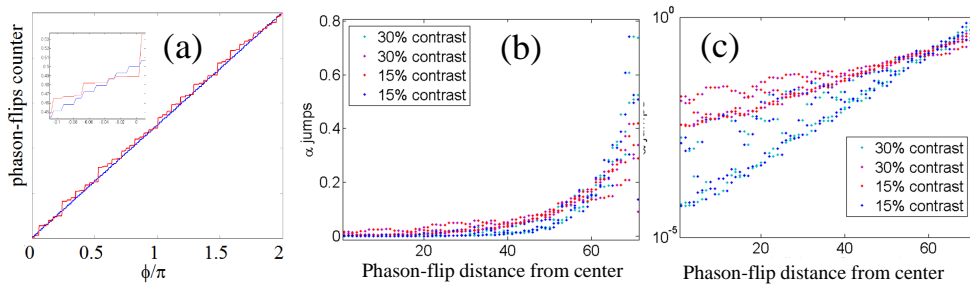


Figure 4.20: The effect of a single phason-flip on the scattering chiral phase $\alpha_q(\phi)$, for the structure $\mathcal{P} \equiv \overrightarrow{F}_N \overleftarrow{F}_N$; $N = 144$, and $q = -1$. (a) The phason flip counter compared to a properly unwrapped $\alpha_q(\phi)$ as a function of ϕ (inset: a close-up view). (b) The effect of a single phason-flip on the scattering chiral phase $\alpha_q(\phi)$ as a function of its distance from the center for two values of dielectric contrast (15% and 80%) in Linear scale (c) The same as (b) in logarithmic y -scale.

odic Fibonacci chains encoded in Chern numbers labeling the dense set of spectral gaps, are related to the existence of an underlying palindromic symmetry driven by a structural gauge phase ϕ . Using a scattering approach, we have shown that these Chern numbers can be obtained either by following the behavior of conveniently generated gap modes or by measuring scattering phases. Equivalently, finite length quasiperiodic Fibonacci chains act as topological mirrors so that cavities defined by two such mirrors enclose modes whose properties are determined by topological features. These results are readily applicable to all C&P quasiperiodic chains, and the corresponding Aubry-Andre-Harper model.

4.2.4 Generalizations to other C&P slopes and the Aubry-Andre-Harper model (artificial palindrome scattering)

Our results are readily generalizable to any C&P slope, and also to the Aubry-Andre-Harper scattering potential. Calculations have been performed for several C&P slopes, to arrive at the same conclusions as in 4.5.3. Figures were left out for the sake of compactness. The Aubry-Andre-Harper scattering potential was out of reach for our binary structures computer code (see 3.1). We will suffice in comparing tight binding calculations from [KLR⁺12] to our own and conclude that they fit perfectly. In fact, we can reset the origin in the original plots by knowing the palindromic value of ϕ , and also explain the factor 2 in the number of traverses between both calculations by mere boundary conditions constraints. In that note, we reiterate our opinion that the artificial palindrome is a generalized edge, which is the most natural scheme to observe edge states and their correspondence to the structural palindromic symmetry cycle.

4.3 Experimental measurement of Chern numbers using the edge states of Fibonacci polaritonic quasicrystals

The work described in this section is the fruit of a collaboration with the polariton measurement team in LPN, CNRS, Marcoussis, France [Bab16].

In this section we investigate the topological properties of cavity polaritons confined in quasiperiodic potentials following the Fibonacci structures $\mathcal{P} \equiv \overleftarrow{F}_N \overrightarrow{F}_N$ (described in 4.2.2). Edge states forming in the gaps of a fractal energy spectrum are imaged in both real and momentum space. These edge states traverse the gaps periodically the gaps as a function of the phason ϕ . The period and direction of the traverses provide a direct determination of the gap Chern numbers. Additionally, we show that the Chern numbers can also be retrieved from the spatial symmetry of the edge states.

To fabricate these Fibonacci structures, we process a planar microcavity (of nominal Q factor 70000) grown by molecular beam epitaxy. The cavity consists in a $\lambda/2$ Ga_{0.05}Al_{0.95}As layer surrounded by two Ga_{0.2}Al_{0.8}As/Ga_{0.05}Al_{0.95}As Bragg mirrors with 28 and 40 pairs in the top and bottom mirrors respectively. Twelve GaAs quantum wells of width 7 nm are inserted in the structure, resulting in a 15 meV Rabi splitting. Fibonacci structures are designed using electron beam lithography and dry etching. Each structure consists in a quasi-1D cavity (wire), whose lateral width is modulated quasi-periodically, as shown in the SEM image of figure 4.21c (top view).

The modulation consists in two wire sections A and B of same length $a = 1\mu m$, but different widths $w_A = 3.5\mu m$ and $w_B = 2.2\mu m$. The width modulation induces an effective 1D potential for the longitudinal motion of polaritons (figure 4.21b),

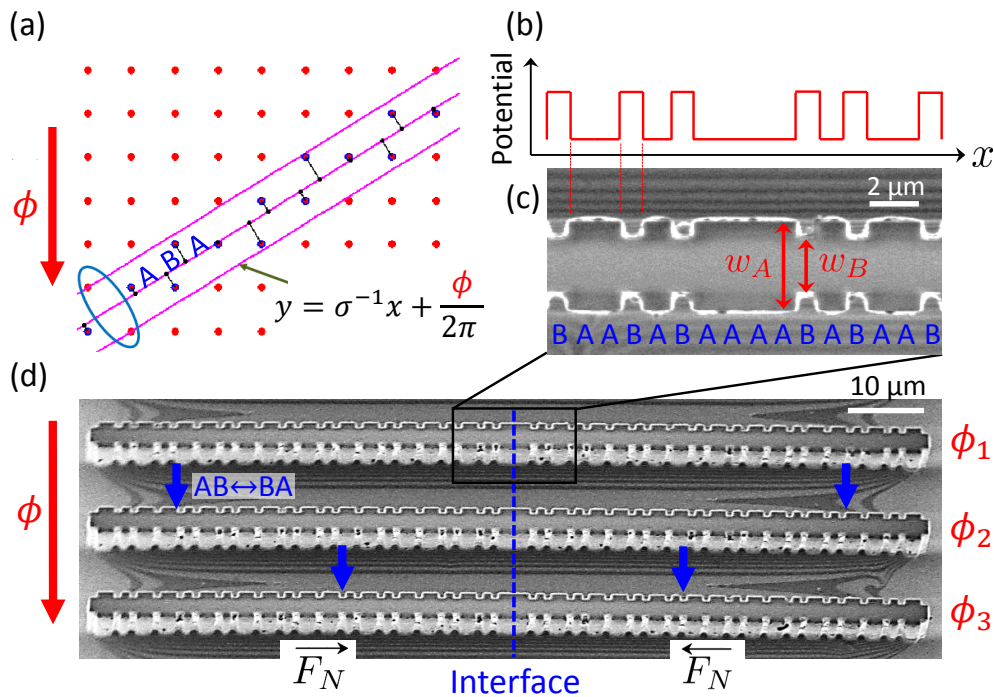


Figure 4.21: (a) Illustration of the C&P method dependence on the phason ϕ . (b) Nominal energy potential corresponding to a laterally modulated 1D cavity. (c) Scanning electron microscopy (SEM) image of a portion of a 1D cavity reproducing the Fibonacci based sequence $\mathcal{P} \equiv \overleftarrow{F}_N \overrightarrow{F}_N$. The letters A and B correspond to two different widths of the cavity. (d) SEM image showing the full view of 3 fabricated Fibonacci structures, corresponding to 3 different values of the phason. Vertical blue arrows indicate the position of phason-flips in the sequences.

that follows the desired Fibonacci sequence. The SEM image of three exemplary structures, with $N = 55$, is shown in figure 4.21d. The position of the interface between the substructures is indicated by a vertical line. These structures correspond to three different values of the phason ϕ . The exciton-photon detuning is of the order of -20meV for all experiments.

To study the polariton modes in these quasi-periodic structures, we perform low temperature (10K) micro-photo-luminescence experiments. Each structure $\mathcal{P}(\phi)$ is excited non-resonantly at low power, using a CW single mode laser at 740nm . The excitation spot covers a $80\mu\text{m}$ -long region centered on the interface. The emission is collected with a 0.5 numerical aperture microscope objective and focused on the entrance slit of a spectrometer coupled to a CCD camera. Imaging the sample surface or the Fourier plane of the collection objective allows studying the polariton modes either in real or momentum space.

Figure 4.22 shows the real (a) and momentum space (b) photo-luminescence of $\mathcal{P}(\phi)$ with $\phi = 0.6\pi$. An intricate energy spectrum is observed, with the alternating state bands and band gaps. The emission in real space allows identifying two types of modes in the spectrum: modes extending over the whole structure, and modes

(encircled) localized at the central interface. The extended modes aggregate into bands, as can be seen in the momentum space emission: these modes are bulk modes forming a fractal energy spectrum characteristic of the Fibonacci quasi-crystal, as previously evidenced in similar structures [TGB⁺14]. The states that are localized at the interface lie in the gaps of the fractal energy spectrum: these are the topological edge states proposed to correspond to the gap Chern numbers q . Two such edge states are visible in figure 4.22 within the highest amplitude gaps.

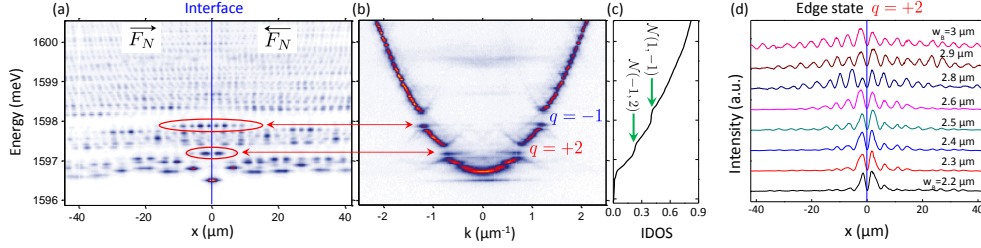


Figure 4.22: (a)-(b) Energy-resolved emission from $\mathcal{P}(\phi)$ with $\phi = 0.6\pi$ in real space (a) and in momentum space (b). Edge states are visible in the two lowest energy gaps, characterized by $q = +2$ and $q = -1$. These states are localized at the central interface ($x = 0$). (c) Integrated density of states (IDOS) obtained by wave-vector integration of the spectrum of panel (b). (d) Spatial profile of the edge state of gap $q = +2$ measured in a series of structures of same width $w_A = 3.5\mu\text{m}$ of letters A, but various widths w_B of letters B, yielding different contrasts for the Fibonacci potential.

We monitor the evolution of interface states as the phason is varied over a period 2π with the origin of ϕ is set, as before, at a palindromic value. To test the predictions in 4.2, we have designed on a single panel the $N = 55$ required realizations of $\mathcal{P}(\phi)$, with $w_B = 2.4\mu\text{m}$. For each structure, we perform spectroscopic measurements similar to that in figure 4.21a-b, and extract the energy of the two edge states relative to the lowest bulk energy mode (bottom of the parabola, energy E_0). The process results are plotted in figure 4.23, where the gap boundaries are indicated by the horizontal lines. We observe that, as the phason is scanned, the states perform a spectral traverse inside the gaps. The direction and periodicity of this traverse is different for the two edge states: the lower energy state traverses 4 times upwards (winding number $\mathcal{W} = +4$), while the higher energy state traverses 2 times downwards ($\mathcal{W} = -2$), when ϕ spans $[0, 2\pi)$. This winding of the edge states allows for a direct extraction of the Chern numbers (see 4.2). Indeed, the measured winding number is $\mathcal{W} = 2q$. The Chern numbers here extracted from the winding of the edge states are thus fully consistent with those previously determined from the bulk band structure (wave-vector position and IDOS in the gaps), illustrating the application of the bulk-edge topological correspondence in our quasi-periodic system.

We note that the spectral traverses of the edge states deviate from a simple linear-like traverse. Apart from the intrinsic staircase driven by the discrete occurrence

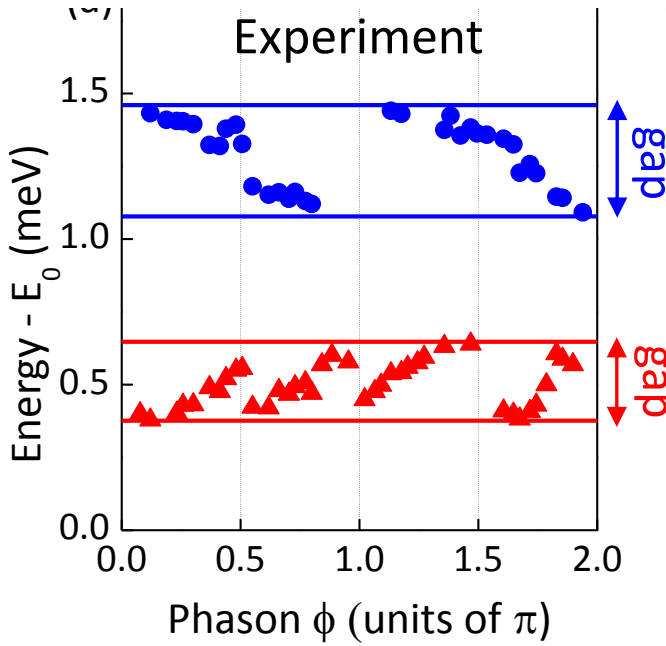


Figure 4.23: Measured energy of the edge states of gaps $q = +2$ and $q = -1$ as a function of the phason ϕ . The energy of the lowest bulk mode is denoted as E_0 , and the solid lines indicate the gap boundaries.

of phason flips (also dependent upon contrast) this deviation is also due to some disorder in the sample affecting the energy of edge states. The exact energy of edge states is not a topologically protected quantity, while their existence and winding number is. We estimate the fluctuations around the nominal spectral trajectory of the modes, of the order of $50 \mu\text{eV}$. Figure 4.22d shows the measured spatial profile of the edge state $q = +2$ in a series of structures of increasing potential contrast (from top to bottom). Contrast enhances the localization of the edge state. Hence, we expect the spectral traverse to be smooth in the limit of small contrast, and to evolve towards a more abrupt profile as the contrast is increased. To verify this prediction, we have performed experiments on two additional sets of structures, having a higher and a lower contrast than the sample studied in figure 4.23. The results, shown in figure 4.24, confirm the above prediction and also illustrate the reproducibility of our experimental results.

Finally, we show that Chern numbers are not only encoded in the spectral properties of the edge states, but also in their spatial structure (as discussed in 4.2). Figure 4.25 shows the measured spatial profile of the $q = +2$ and $q = -1$ edge states for values of ϕ taken in the 4 successive quadrants: $[0, \pi/2]$, $[\pi/2, \pi]$, $[\pi, 3\pi/2]$ and $[3\pi/2, 2\pi]$. The states either show either a node or an anti-node at the interface ($x = 0$). We refer to these two spatial structures as symmetric (S) and anti-symmetric (AS), respectively. We observe that the $q = +2$ state (red) switches symmetry in each quadrant, while the $q = -1$ state (blue) keeps the same symmetry in the first two quadrants before switching to the opposite symmetry in the last two

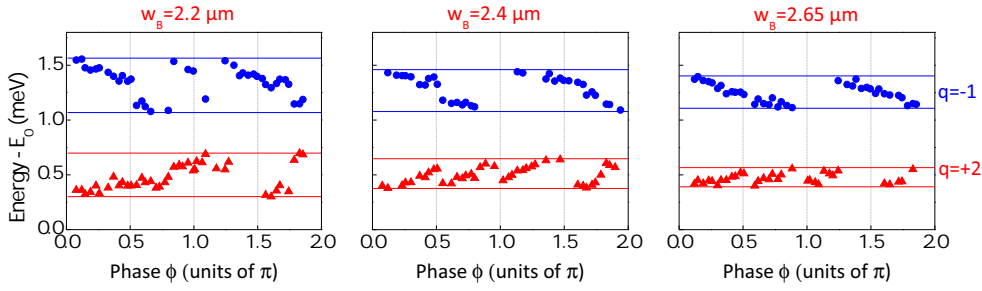


Figure 4.24: Measured energy of the edge states of gaps $q = +2$ and $q = -1$ as a function of the phason ϕ for three values of contrast (determined by w_B). The energy of the lowest bulk mode is denoted as E_0 , and the solid lines indicate the gap boundaries.

quadrants. Comparing this behavior with the spectral features, we observe that symmetry flips are indeed exactly synchronized with the spectral traverse of the states: they occur in between two successive traverses. Hence, the $q = -1$ state changes symmetry only once within a full scan of the phason, while the $q = +2$ state changes symmetry twice. These features demonstrate an alternative method for determining Chern numbers in quasi-crystals, that could prove useful in physical systems where the spectral degree of freedom is inaccessible.

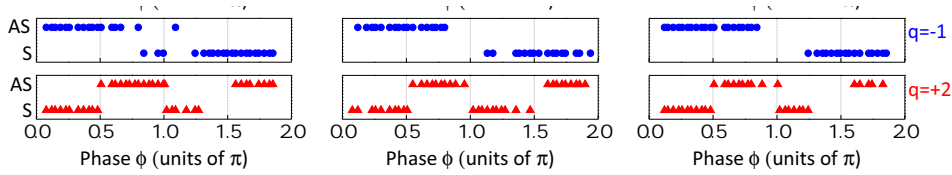


Figure 4.25: Measured spatial symmetry of the edge states of gaps $q = +2$ and $q = -1$ as a function of the phason ϕ . The spatial symmetry flips between alternating gap mode traverses.

In summary, in this section we have investigated the topological properties of $1D$ Fibonacci polaritonic quasi-crystals. We have evidenced the spectral and spatial properties of edge states created in the gaps of the fractal energy spectrum of the quasi-crystal. These edge states spectrally traverse inside the gaps upon varying the phason. The periodicity and direction of this traverses allow a direct determination of the Chern number assigned to each gap by the gap-labeling theorem. Moreover, the spatial symmetry of the edge states provide an alternative and widely applicable method to determine the underlying Chern numbers.

4.4 Direct measurement of Chern numbers in the diffraction pattern of a Fibonacci chain

The work described in this section is the fruit of a collaboration with the cold atom team in LKB, College de-France, Paris, France [Dar16].

Chern numbers are usually related to transport or spectral measurements (see 4.2, 4.3, and also [KLR⁺12, VZL⁺15]). In this section we report on an experiment where the Chern numbers of quasiperiodic structures are directly determined by the traditional crystallographic approach. We demonstrate that all the possible Chern numbers for a finite-length Fibonacci chain can be observed directly in their diffraction pattern, using a quasiperiodic diffraction grating equivalent to a quasiperiodic multi-slit Young's experiment. Finally, we also demonstrate quantitatively the stability of these topological invariants with respect to structural disorder. We realized a simple optical setup which allows us to generate any finite-length Fibonacci chain. The corresponding Chern numbers q in 3.45 appear as winding clearly visible in the diffraction patterns. Moreover this new approach allowed us to obtain a "topological map" of these chains and to measure, in a simple setup, all available Chern numbers. We measured high Chern numbers up to $|q| = 44$ for a structure of $N = 89$ elements. Our method provides a new and original experimental approach to study topological properties of matter, different from transport or spectral body of work. The results in this section imply that Chern numbers also characterize a fundamental, purely structural aspect of quasiperiodic structures. These implications will be discussed at detail in 4.5

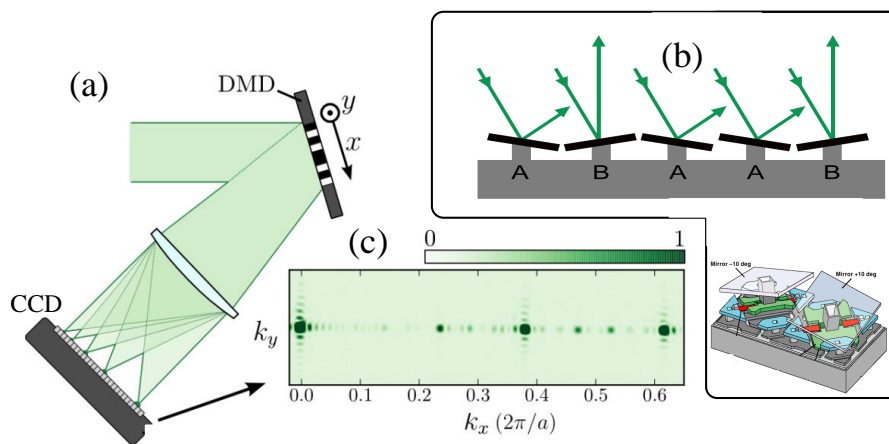


Figure 4.26: Experimental setup. (a) A sketch of the optical setup. A collimated laser beam at a wavelength of $532nm$ diffracts off a grating programmed on a Digital Mirror Device (DMD). The far-field diffraction pattern is measured on a CCD camera. (b) A sketch of the DMD mirrors. (c) When the grating is structured following a Fibonacci sequence along the horizontal x direction (and uniform along the vertical y direction), we observe diffraction peaks characteristic of the quasi-periodic structure of the chain.

In our experiment, we realized Fibonacci chains using a Digital Micromirror Device (DMD), i.e. an array of about one million micron-sized mirrors ("pixels") of size $a \times a$. Each mirror can be independently switched between a reflective (B) and a non-reflective (A) state (see figure 4.26b). We illuminated the grating with monochromatic light source, and observed the far-field diffraction pattern on a CCD

camera (see figure 4.26 and also 4.4.1).

As a preliminary experiment, we programmed along the x -axis a Fibonacci grating \vec{F}_N ; $N = \mathcal{F}_{10} = 89$ of length $L = \mathcal{F}_{10} \times a$. We displayed one-pixel-large vertical lines either in reflective (B) or non-reflective (A) state according to the structure (semi-1D due to the 2D slab symmetry). We show in figure 4.26c the measured diffraction pattern. Within our experimental resolution, we cannot distinguish the positions of the peaks from those expected from (2.13) for the infinite chain, namely $k_q = p + q/\tau$, in units of $2\pi/a$ (see 4.5).

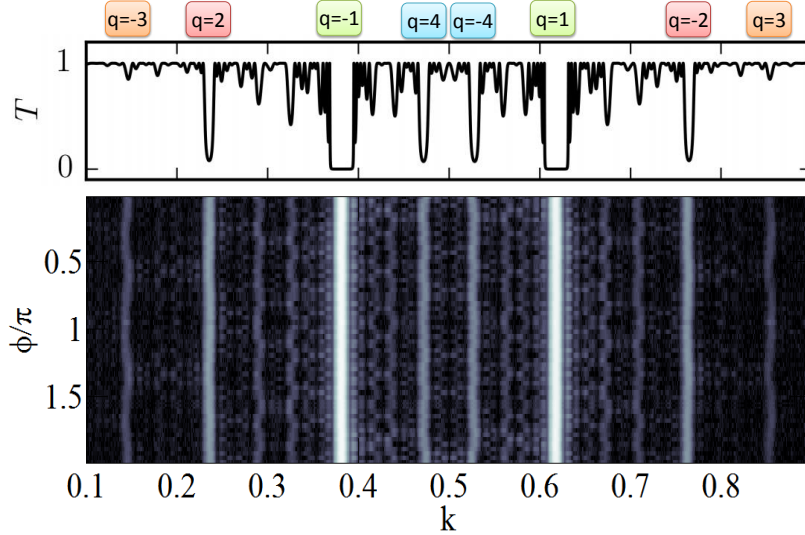


Figure 4.27: Grayscale map: measured diffraction pattern for the structure $\vec{F}_N \vec{F}_N$; $N = 89$. Each ϕ value corresponds to a different diffraction experiment. The global pattern, which is almost independent of ϕ , is compared to the transmission of an \vec{F}_N dielectric structure (above) calculated using scattering analysis of chapter 3. Chern numbers labeling the transmission gaps (and diffraction peaks) through (3.45) are indicated above.

To reveal the topological features hidden in this pattern, we studied the effect of the phason degree of freedom by scanning over all chains corresponding to the N distinct and relevant values of ϕ , setting the origin of the ϕ -axis at a palindromic value of ϕ (in equivalence to the practice in 4.2).

In a first experiment, we measured the diffraction pattern of a grating consisting of the Fibonacci composite $\vec{F}_N \vec{F}_N$. All the results are consolidated to form the graph shown in figure 4.27, where each ϕ value corresponds to a single diffraction measurement (shown in figure 4.26). We observe vertical stripes located at a value k_q corresponding to gaps in the transmission spectrum. These stripes appear independent of ϕ .

In a second experiment, following the ideas in 4.2, we used a grating consisting of a Fibonacci artificial palindrome $\mathcal{P} \equiv \vec{F}_N \overleftarrow{F}_N$ (see figure 3.37a). The resulting diffraction pattern as a function of ϕ is strikingly different (see figure 4.28). The

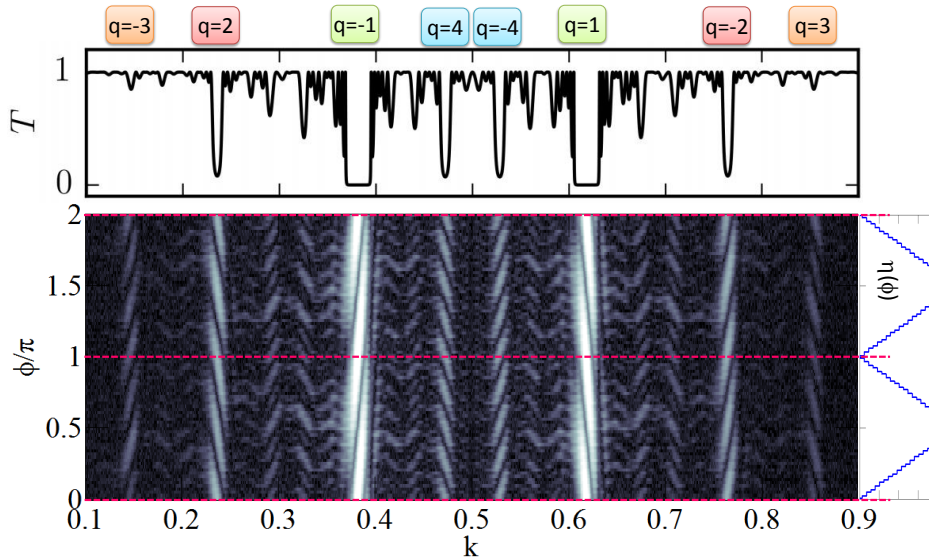


Figure 4.28: Grayscale map: measured diffraction pattern for the structure $\mathcal{P} \equiv \vec{F}_N \overleftarrow{F}_N$; $N = 89$. Each ϕ value corresponds to a different diffraction experiment. The global pattern, showing a dependence on ϕ , is compared to the transmission of an \vec{F}_N dielectric structure (above) calculated using scattering analysis of chapter 3, and to the purely structural palindromic symmetry cycle of chapter 2 (on the right). Chern numbers labeling the transmission gaps (and diffraction peaks) through (3.45) are indicated above.

vertical stripes are now striated to form a regular and well-structured pattern which is completely synchronized with the purely structural palindromic symmetry cycle associated with the scanning of the phason (see 2.2). The direction of the striation (which appears as a traverse of a single dark spot splitting the diffraction peak in two) is determined by the sign of q (figures 4.29 and 4.30). For palindromic values of ϕ , namely $\phi = 0, \pi, 2\pi$, no diffraction peak is split, which is understandable because the relevant structures are equivalent to the structure $\vec{F}_N \vec{F}_N$.

Specifically, the intensities measured at the original location of the diffraction peaks k_q , vary sinusoidally with ϕ , with a period that we identify as $\pi/|q|$ as the q -harmonic of the palindromic symmetry cycle.

This behavior is in complete equivalence to the theoretical and experimental results in the completely different system of the topological edge states in Fibonacci scattering dielectric, discussed in 4.2 and 4.3. This constitutes a novel method to measure the Chern numbers labeling the spectral gaps and diffraction peaks in quasiperiodic chains through the winding of the split in the diffraction peak k_q as a function of the gauge field ϕ . This method gives a purely structural meaning to the gap labeling Chern numbers.

In a third experiment, following a proposal in 4.2 shown in figure 4.16, we repeated the experiment with the structure $\vec{F}_N \overleftarrow{F}_N \vec{F}_N$. In a complete analogy to the spectral calculations, the measured diffraction pattern now shows a double

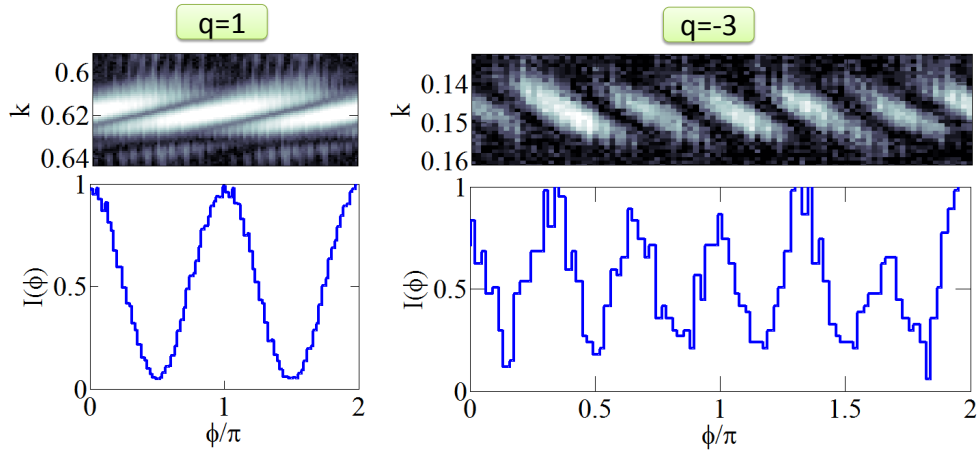


Figure 4.29: A close-up view on the diffraction pattern of figure 4.28 for peaks labeled with $q = 1, -3$. The oscillatory behavior of the diffraction intensity at the original peak frequency as a function of ϕ is shown.

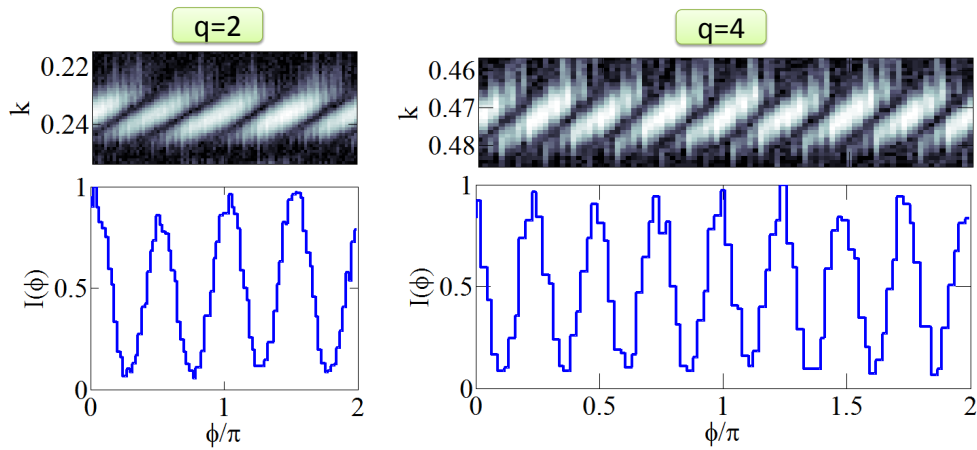


Figure 4.30: A close-up view on the diffraction pattern of figure 4.28 for the peak labeled with $q = 2, 4$. The oscillatory behavior of the diffraction intensity at the original peak frequency as a function of ϕ is shown.

striation with opposite directions (see figure 4.31).

In a forth experiment, we used the entire 2D map $\{\vec{F}_N(\phi)\}$ (defined in 2.2, and depicted in figure 2.11) to obtain a single-shot measurement of all available Chern numbers q . We programmed $\{\vec{F}_N(\phi)\}$ forming an $N \times N$ array of pixels where the x direction is the quasiperiodicity direction, and the y direction is the phason direction. The measured diffraction pattern in the (k_x, k_y) plane is associated to a pattern in the (k_x, k_ϕ) plane.

The resultant diffraction pattern of $\{\vec{F}_N(\phi)\}$, which came as some surprise, is shown in figure 4.32. It displays a set of discrete peaks at well-defined positions in the (k_x, k_ϕ) plane. These discrete peaks are all located at the values k_q obtained from (2.13) exhibiting two main differences with respect to the previously obtained data

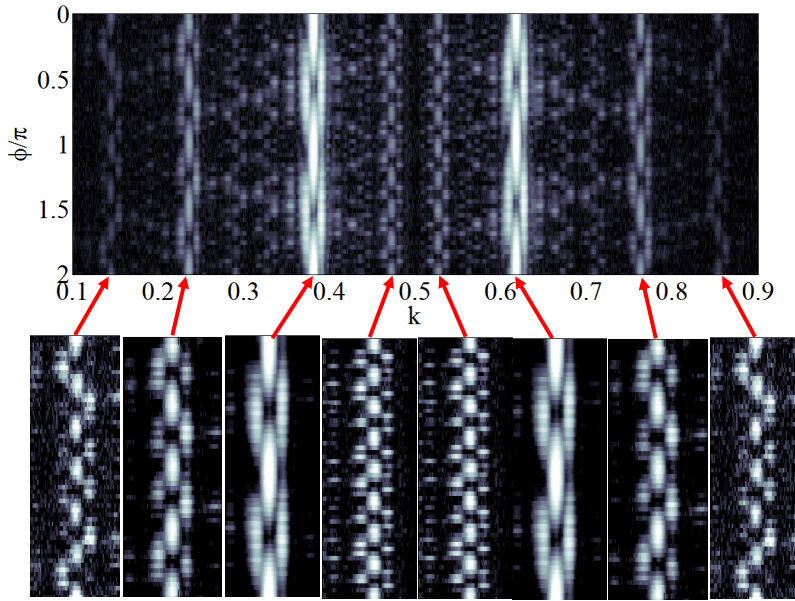


Figure 4.31: Grayscale map: measured diffraction pattern for the structure $\vec{F}_N \overleftarrow{F}_N \vec{F}_N$; $N = 89$. Each ϕ value corresponds to a different diffraction experiment. A close-up view for the vertical stripes of Chern numbers $q = -3, 2, -1, 4, -4, 1, -2, 3$ (from left to right).

for single chains (figure 4.26). Firstly, there are many more observable diffraction peaks than the single chain case, even though the same amount of emitting pixels are involved. Secondly and importantly, the peaks do not form a horizontal line, but appear shifted along k_ϕ by a quantity equal to the Chern number q of (2.13), following a simple normalization of the k_ϕ -axis. This direct measurement of Chern numbers in a single-shot experiment thereby provides a “topological map” of the Fibonacci chain. For a finite chain of length $N = \mathcal{F}_j$, peaks with N different Chern numbers are expected (see 4.5). In our experiment having $F_{10} = 89$, we indeed observe all the possible Chern numbers. This map bears a surprising equivalence to the gap labeling theorem (which also originates from the structural building rule) in the completely different system of the Fibonacci scattering dielectric problem discussed in 4.2 and 4.3. This constitutes a novel method to measure all the Chern numbers labeling the spectral gaps and diffraction peaks in quasiperiodic chains in one diffraction topological map. The theoretical analysis of the properties of the diffraction topological map (see 4.5) gives a structural meaning to the existence of Chern numbers in quasiperiodic structures.

Finally, in a fifth experiment, we explored the robustness of the diffraction pattern and of its topological features (depicted in figures 4.28, 4.29, and 4.30) against structural noise. We studied a similar configuration as in the second experiment, $\mathcal{P} \equiv \vec{F}_N \overleftarrow{F}_N$ but introduced noise by randomly selecting a fraction μ of the vertical

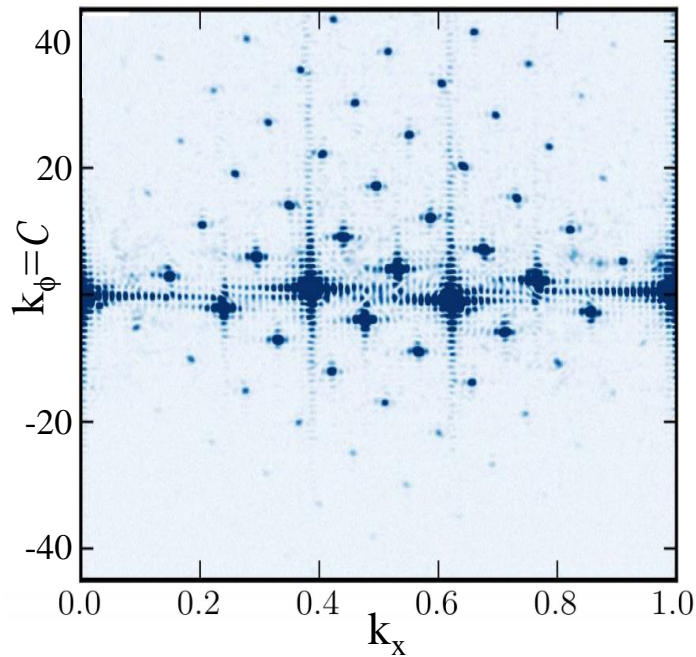


Figure 4.32: Grayscale map: measured 2D diffraction pattern (in a single measurement) for $\{\vec{F}_N(\phi)\}$; $N = 89$. The axes are calibrated to directly display the diffraction pattern as a function of k_x and $k_y = k_\phi$. We observe peaks at the k_x values obeying (2.13) but shifted along the vertical axis to $k_\phi = q \times 2\pi/aN$. The asymmetry between the intensity of the diffraction peaks for positive and negative k_ϕ values is due to the envelope of the diffracted intensity from the DMD, originates from the form factor of the micromirrors.

lines ($0 \leq \mu \leq 1$) whose states (reflective or non-reflective) are also chosen at random. Thus, $\mu = 0$ corresponds to a non-perturbed Fibonacci pattern and $\mu = 1$ to a random chain (see also 4.4.2). The resulting diffraction pattern was averaged over many realizations of the noise.

In figure 4.34, we show how the diffraction pattern evolves with increasing μ . As expected, peaks are washed out when increasing the fraction μ . We select three specific values of μ and show the evolution of the diffraction pattern when scanning the phason. Even for very weak peak signals, the modulation of the peak amplitude is always present and keeps the same frequency and direction. This demonstrates explicitly the expected robustness of the topological properties of the Fibonacci chains captured by the winding (and the winding number) of the diffraction peak amplitude as a function of ϕ .

To summarize, in this section we have demonstrated a simple way to measure topological invariants associated with quasiperiodic structures. The theoretical analysis of these results (see 4.5) had greatly clarified the structural origin of Chern numbers in quasiperiodic structures. Although we have worked with the simplest example, the Fibonacci chain, our method is not limited to it and could be applied

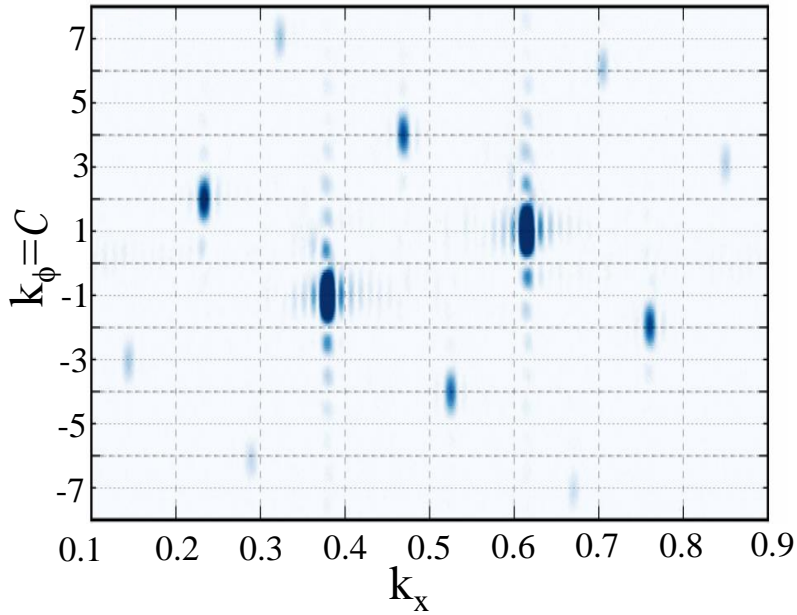


Figure 4.33: A close-up view of figure 4.32 .

to many other chains.

4.4.1 Optical setup

We use a 532nm laser source to illuminate our Digital Micromirror Device (DMD). The laser output is coupled into an optical fiber used as a spatial mode filter. The fiber output is expanded to obtain a Gaussian beam with $1/e^2$ radius of about 5mm , truncated using an aperture to give a roughly uniform illumination spot with a diameter of about 2.5mm . This size was chosen empirically to obtain the sharpest observable diffraction peaks. For larger beams, the imperfections (in particular, lack of flatness) of the DMD surface become more important and limit the achievable spot sizes. The DMD (model DLP7000 from Texas Instruments) consists of a matrix of 1024×768 square micromirrors with a size $a = 14\mu\text{m}$. The angle of incidence of the laser on the DMD surface is on the order of 22° (see figure 4.26). Depending on the mirror state the light is reflected almost perpendicularly to the DMD plane (state “B”) or to a large angle which is blocked (state “A”). The diffracted light is focused on a CCD camera using a 2” diameter aspherical lens with $f = 100\text{mm}$. The axes of the CCD camera – corresponding to the reciprocal space from the DMD plane – are calibrated by imprinting a periodic lattice of period $2a$ on the DMD, which gives a square lattice of peaks separated from the zeroth order by π/a . The manual reorientation of this directionality, and the fact that the CCD records the intensity using discrete spatial pixels, are the main source of error in deriving the sinusoidal dependence of the diffraction peak amplitude upon ϕ (misalignment error).

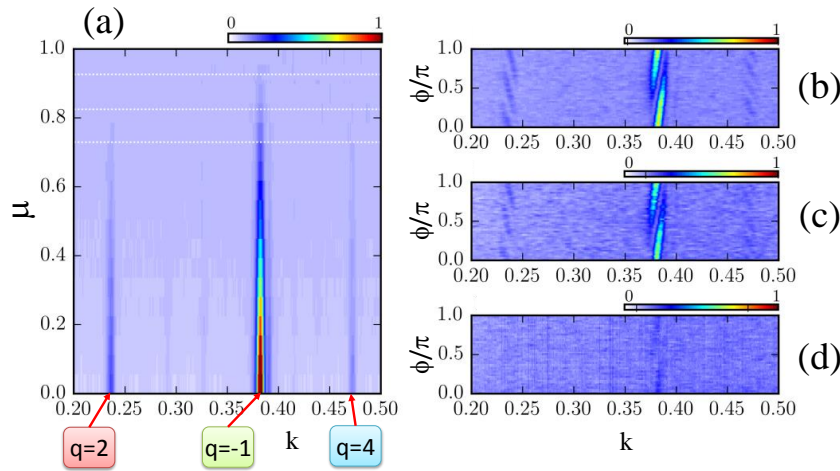


Figure 4.34: Colormap: robustness of the topological features against structural disorder. (a) Diffraction pattern of the structure $\mathcal{P} \equiv \vec{F}_N \overleftarrow{F}_N$ at $\phi = 0$ for different levels of noise μ . Each value of μ corresponds to a different diffraction experiment. The three white dotted lines correspond to three specific values of μ , namely $\mu = 0.73, 0.83, 0.93$ chosen as examples. (b)-(d) Evolution of the diffraction pattern when varying ϕ for three different noise levels, respectively. Note that only the $[0, \pi]$ interval of the period of ϕ is scanned.

4.4.2 Noise generation

We introduce noise in our DMD pattern in the following way. The initial signal is $\mathcal{P} \equiv \vec{F}_N \overleftarrow{F}_N$. Noting (we used $N = 89$ in our experiments), the total signal has a length of $2N$. We randomly choose N_{noise} mirrors out of the $2N$ mirrors of the chain. The state of the selected mirrors is then randomly chosen between reflective and non-reflective with a equal probability. This new, disturbed chain is then replicated as usual on each line of the DMD (semi-1D due to the 2D slab symmetry). This constitutes a single realization of a noisy pattern with a level of noise of $\mu = N_{\text{noise}}/(2N)$. Note that this algorithm a priori generates independent noise for the two parts of the chain (\vec{F}_N and \overleftarrow{F}_N). To average over several realizations of the noise pattern, we reproduce the procedure by randomly choosing a new set of mirrors and randomly flipping them. Each line from the figures 4.34a to 4.34d is obtained by averaging the measured diffraction signal over 200 independent realizations of the noise. In order to speed up the data acquisition process, we dynamically control the DMD so that it scans over all the noise realizations during the CCD camera exposure time, and the average is made by the CCD device.

4.5 The structural origin of Chern numbers in quasiperiodic chains

This section intends to clarify the somewhat surprising experimental results demonstrated in 4.4. By doing so, it sheds light over the purely structural origin of Chern numbers (some of these points are to be published as supplemental material for [Dar16]).

4.5.1 Diffraction amplitudes for various structural schemes

The Fibonacci chain is defined by $\vec{F}_N(\phi) \equiv [\chi_1 \chi_2 \cdots \chi_N]$; $N = \mathcal{F}_j$ with

$$\chi_n(\phi) = \text{sign} [\cos(2\pi n \tau^{-1} + \phi + \phi_0) - \cos(\pi \tau^{-1})]. \quad (4.3)$$

The reflectance R_n of a vertical line of pixels at position $x = na$ is given by $R_n(\phi) = [\frac{1-\chi_1(\phi)}{2} \frac{1-\chi_2(\phi)}{2} \cdots \frac{1-\chi_{F_n}(\phi)}{2}]$ which is either 0 for $\chi = 1$ (pixels A) or 1 (pixels B) for $\chi = -1$. The diffracted amplitude is thus the sum over all the active pixels B , namely,

$$A(k_x) = \sum_B e^{ik_x x_B(\phi)} \quad (4.4)$$

For a specific value of k_x , taken to be k_q , and a finite Fibonacci segment \vec{F}_N , this complex valued amplitude reads (with obvious notations):

$$A_q^{\vec{F}_N}(\phi) = \sum_B e^{ik_q x_B(\phi)} \equiv \mathcal{A}_q^{\vec{F}_N} e^{i\theta_q(\phi)} \quad (4.5)$$

where $\mathcal{A}_q^{\vec{F}_N}$ is the norm and $\theta_q(\phi)$ is the total phase. The inverted structure \overleftarrow{F}_N is obtained by replacing x by $-x + aN$ (a being the pixel size), we obtain,

$$A_q^{\overleftarrow{F}_N}(\phi) = \sum_B e^{ik_q(aN - x_B(\phi))} = \mathcal{A}_q^{\vec{F}_N} e^{-i\theta_q(\phi)} e^{ik_q aN} \quad (4.6)$$

We now take advantage of two known results. The first is that the diffraction intensities at $k = k_q$ for the two structures \vec{F}_N and \overleftarrow{F}_N are the same (i.e. have the same Chern numbers), and they have no ϕ -dependence, namely, $|A_q^{\vec{F}_N}(\phi)|^2 = |A_q^{\overleftarrow{F}_N}(\phi)|^2 = (\mathcal{A}_q^{\vec{F}_N})^2$, a result we already used in (4.6). The second result is that for the specific ϕ values, namely $\{\phi_{pal}\}$, for which the Fibonacci sequence is palindromic, i.e. $\vec{F}_N = \overleftarrow{F}_N$, we have $A_q^{\vec{F}_N}(\phi_{pal}) = A_q^{\overleftarrow{F}_N}(\phi_{pal})$ leading to $k_q aN = 2\theta_q(\phi_{pal})$.

We now proceed with the experiment using the structure $\vec{F}_N \overleftarrow{F}_N$ (or equivalently $\overleftarrow{F}_N \vec{F}_N$), defining the spatial origin at the center, to obtain

$$\begin{aligned} A_q^{\vec{F}_N \overleftarrow{F}_N}(\phi) &= \mathcal{A}_q^{\vec{F}_N} e^{i\theta_q(\phi)} (e^{-2i\theta_q(\phi_{pal})} + 1) \\ A_q^{\overleftarrow{F}_N \vec{F}_N}(\phi) &= \mathcal{A}_q^{\vec{F}_N} e^{-i\theta_q(\phi)} (1 + e^{2i\theta_q(\phi_{pal})}). \end{aligned} \quad (4.7)$$

As in the experimental results, the resultant diffraction intensities are identical and ϕ -independent,

$$|A_q^{\vec{F}_N \vec{F}_N}(\phi)|^2 = |A_q^{\overleftarrow{F}_N \overleftarrow{F}_N}(\phi)|^2 = 2(\mathcal{A}_q^{\vec{F}_N})^2(1 + \cos(2\theta_q(\phi_{pal}))). \quad (4.8)$$

Finally, we consider the topological experiment using the structure $\mathcal{P} \equiv \vec{F}_N \overleftarrow{F}_N$ or alternatively the structure $\mathcal{P}' \equiv \overleftarrow{F}_N \vec{F}_N$, defining the spatial origin at the center, to obtain

$$\begin{aligned} A_q^{\mathcal{P}}(\phi) &= \mathcal{A}_q^{\vec{F}_N} \left(e^{i[\theta_q(\phi) - 2\theta_q(\phi_{pal})]} + e^{-i[\theta_q(\phi) - 2\theta_q(\phi_{pal})]} \right) \\ &= 2\mathcal{A}_q^{S_N} \cos(\theta_q(\phi) - 2\theta_q(\phi_{pal})) \end{aligned} \quad (4.9)$$

and

$$A_q^{\mathcal{P}'}(\phi) = \mathcal{A}_q^{\vec{F}_N} (e^{-i\theta_q(\phi)} + e^{i\theta_q(\phi)}) = 2\mathcal{A}_q^{\vec{F}_N} \cos \theta_q(\phi) \quad (4.10)$$

where, unlike (4.7), the diffraction intensity is now ϕ -dependent. The results (4.9), and (4.10) still require an understanding of the phase $\theta_q(\phi)$. Note that these results are for any choice of origin, while in 4.4 we employ the choice $\phi_{pal} = 0$.

4.5.2 The phase term $\theta_q(\phi)$

Here, we wish to show that the phase term $\theta_q(\phi)$ in the diffraction amplitude (4.5) is linear with ϕ , with a slope equal to the Chern number q . A thorough proof is still an open ended subject.

This linear dependence can be understood from a simple calculation. From the characteristic function χ in (4.3), we note that changing ϕ from an initial value ϕ_i by an amount $\Delta\phi$ is equivalent to a spatial translation (or origin shift) along the chain (see 2.2.1). Specifically, for $\Delta\phi = 2\pi/\tau$, the resultant structure is translated by one pixel only, and therefore the diffraction amplitude $A_q^{\vec{F}_N}(\phi_i + 2\pi/\tau)$ carries an additional (translational) phase, $\theta_q(\phi_i + 2\pi/\tau) = \theta_q(\phi_i) + ak_q$. Using the approximation $k_q = (2\pi/a)(p + q\tau^{-1})$, leads to $\theta_q(\phi_i + 2\pi/\tau) = \theta_q(\phi_i) + 2\pi q\tau^{-1}$. This phase shift is achieved after $(2\pi/\tau)(N/2\pi)$ phason-flips out of the N total number of phason-flips in a single period of ϕ . Since each phason-flip involves a single active “B” pixel translation by one pixel, each phason-flip contributes on average $2\pi q/F_N$ to the additional phase, completing q periods in one period of ϕ (see 2.2.1). We thus write the general phase term as a linear function of the modulation phase change $\Delta\phi$:

$$\theta_q(\phi_i + \Delta\phi) = \theta_q(\phi_i) + q\Delta\phi. \quad (4.11)$$

This linear dependence is depicted in figure 4.35, which shows a numerical plot of the diffraction amplitude phase term $\theta_q(\phi)$ as a function of ϕ for different values of q , i.e. of k_q , comparing \vec{F}_N and \overleftarrow{F}_N . Choosing $\phi_{pal} = 0$ as the origin, three features are easily observable :

1. For a given value of q (i.e. of k_q), the two phases of \vec{F}_N and \overleftarrow{F}_N are deduced one from the other by changing ϕ into $-\phi$.
2. The total diffraction phase $\theta_q(\phi)$ is linear with ϕ with a slope q .
3. Changing k_q into k_{-q} is equivalent to changing ϕ into $-\phi$.

These results seem to be a rather general feature of the diffraction pattern of both periodic and quasi-periodic structures, and not restricted to 1D (see for instance [KM97, KM00, PTAV13]).

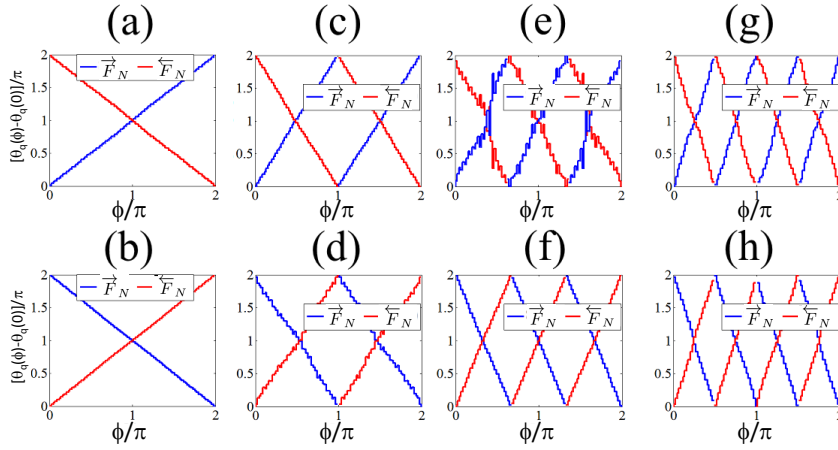


Figure 4.35: A numerical plot of the phase $\theta_q(\phi)$ of the diffraction amplitude $A_q^{\vec{F}_N}(\phi)$, as a function of ϕ for the structures \vec{F}_N (in blue) and \overleftarrow{F}_N (in red) and for the diffraction peaks k_q for various q values. (a)-(b) $q = \pm 1$, respectively. (c)-(d) $q = \pm 2$, respectively. (e)-(f) $q = \pm 3$, respectively. (g)-(h) $q = \pm 4$, respectively.

The phases of the diffraction peaks (in figure 4.35) are in complete agreement with the spectral gaps scattering reflected phase shifts discussed in 4.2. We have also succeeded to extend this analogy to all values of k , and to show that just as the winding of the scattering phases underlies the more convenient method to observe spectral winding (e.g. of gap modes in the artificial palindrome), so do the diffraction amplitude phases. Figure 4.36 shows the diffraction pattern phase analogue to the scattering chiral phase α discussed in 4.2. This diffraction chiral phase $\gamma(k, \phi)$, given by

$$\gamma(k, \phi) \equiv \text{phase} \left[A^{\overleftarrow{F}_N}(k, \phi) \right] - \text{phase} \left[A^{\vec{F}_N}(k, \phi) \right],$$

and depicted in figure 4.36, is completely analogous to the pattern depicted in figure 4.3. The main difference between $\gamma(k, \phi)$ and $\alpha(k, \phi)$, is that $\gamma(k, \phi)$ assigns the same widths to the “gaps” (i.e. regions where it is essentially $\gamma(\phi)$), while $\alpha(k, \phi)$ assigns a contrast dependent gap width hierarchy. Similar to the case of $\alpha(k, \phi)$, the diffraction chiral phase allows to many more Chern numbers in its winding compared to the intensity spectrum winding for the artificial palindrome case. This constitutes a novel method to measure the Chern numbers labeling the spectral gaps

and diffraction peaks in quasiperiodic chains through the winding of the phase of the diffraction peak k_q as a function of the gauge field ϕ . This method gives a purely structural meaning to the gap labeling Chern numbers.

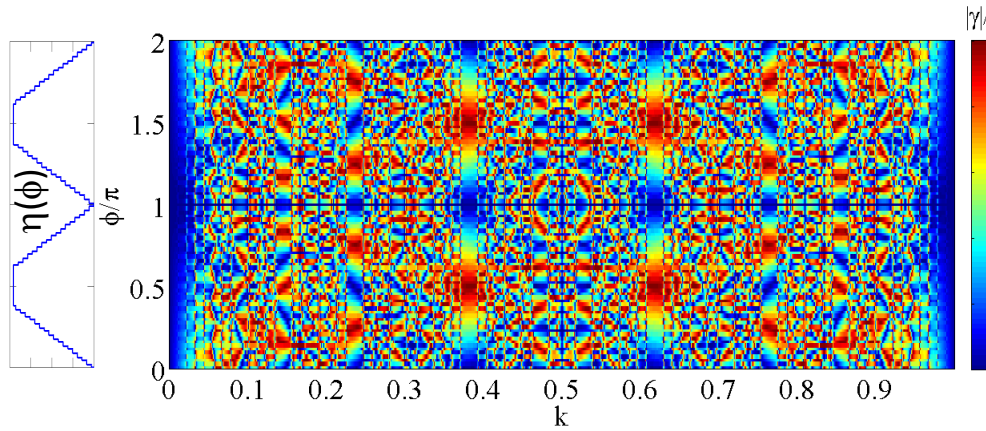


Figure 4.36: Colormap: $|\gamma(\phi, k)|$ for \vec{F}_N ; $N = 89$. Completely analogous to $|\alpha(\phi, k)|$ of figure 4.3, including the complete synchronization with the diffraction peaks in the k -axis, and to the structural palindromic symmetry cycle on the ϕ -axis.

4.5.3 Generalizations to other C&P slopes and the Aubry-Andre-Harper model (artificial palindrome diffraction)

The diffraction method presented in 4.4 is not limited to the Fibonacci sequence. It is readily generalizable to any C&P structure. Figure 4.37 shows a numerical calculation of the same methods applied to a C&P structure of slope $5^{-1/2}$. The behavior appears in full correspondence to the Fibonacci results, apart of two differences. The first difference is that that we do not have the gap labeling theorem to aid us with a prediction for Chern number values (as we do not know the substitution for this structure, see 3.4). However, it appears that all the diffraction peaks and windings are to be derived by the same formulation done for Fibonacci by replacing τ^{-1} with $5^{-1/2}$. For instance, there is a peak at $k = 1 \cdot 5^{-1/2}$ with 2 windings, a peak at $k = 2 \cdot 5^{-1/2}$ with 4 windings, a peak at $k = 3 \cdot 5^{-1/2}$; *modulo* 1 with 6 windings and so on. The second difference is that although the diffraction chiral phase still corresponds to the structural palindromic symmetry cycle, the striations in the diffraction peaks do not. The winding is conserved, but the origin of the striation is shifted (this is indicated by the blue line in figure 4.37b which is where all diffraction peaks are unsplit). This results from the fact that $N = 89$ is not a natural length for this C&P slope (it was chosen due to the lack of other generating rules). This problem was mentioned from structural considerations in 2.2.1, and will be discussed in 4.6.

Remark: more C&P slopes, such as $\pi^{-1/2}$, have been calculated to yield similar results.

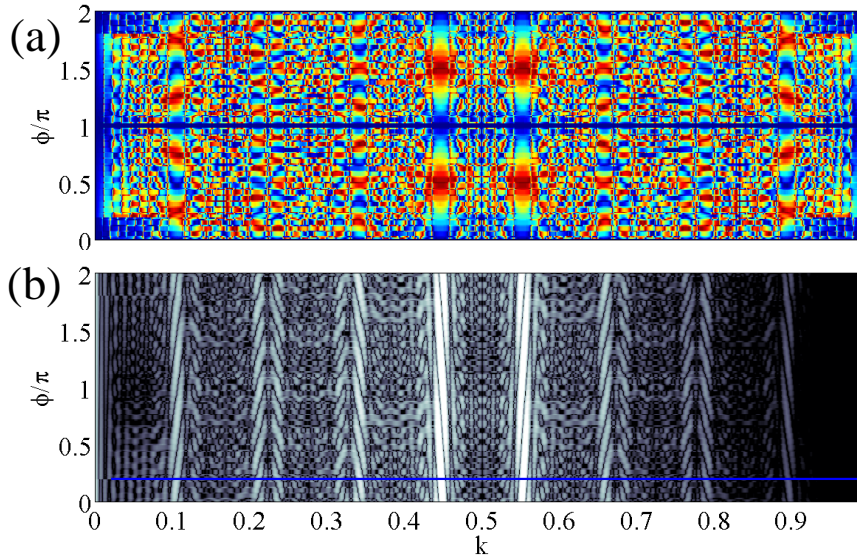


Figure 4.37: (a) Colormap: $|\gamma(\phi, k)|$ for a C&P structure with $N = 89$ and a slope $5^{-1/2}$ (with k and ϕ axes as before). Regions with a regular behavior of $|\gamma(\phi, k)|$ with integer windings, correlated to the palindromic symmetry cycle are easily observable. (b) Grayscale map: calculated diffraction pattern for two structure the artificial palindrome based on the structure describes in (a). Each ϕ value corresponds to a different diffraction spectrum. The global pattern, showing an integer winding in agreement with (a). Blue line indicates the ϕ value where no diffraction split exists.

Figure 4.38 shows the application of the same methods for the continuous alphabet Aubry-Andre-Harper (AAH) model. It has been noted from purely structural considerations in 2.3.3 that a maximum number of 2 diffraction peaks appear for this structure, but using a recent proposal [KZ12] to smoothly modify the AAH model into its equivalent C&P model (using a parameter β), more diffraction peaks may be excited. The results are indeed equivalent to those of the Fibonacci artificial palindrome, except for a new upper limit to the number of observable Chern numbers and diffraction peaks. This limitation depends on the smoothing parameter β . For $\beta \rightarrow 0$ which is the pure AAH case, only two peaks appear, with winding numbers ± 2 equivalent to Chern numbers ± 1 , while for higher values of β more diffraction peaks and the corresponding windings appear. This is in full accordance to the analysis presented in 2.3.3. The absence of diffraction peak splitting in ϕ values corresponding to structural palindromic symmetry is also evident and equivalent to the C&P counterpart structure. The full correspondence of the AAH structure topological properties to the palindromic symmetry cycle verifies the topological equivalence between the AAH structures and their C&P counterparts.

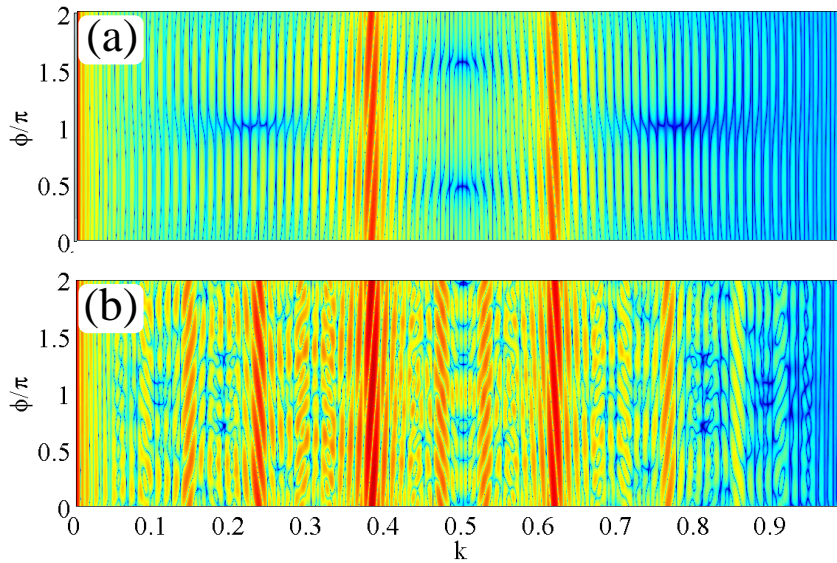


Figure 4.38: Colormap: calculated diffraction pattern for an artificial palindrome based on the Aubry-Andre-Harper (AAH) structure with $N = 89$ and a slope τ^{-1} (with k and ϕ axes as before). (a) Pure AAH structure (b) A modified AAH with $\beta = 3$. The global pattern appears to be a limited version of the Fibonacci case (and the limitation is a function of β).

4.5.4 Diffraction peak splitting - an Intuitive explanation

As much as the analysis of the oscillatory behavior of the diffraction peak amplitude serves as a Chern number measurement, we wish to better understand the fundamental effect of diffraction peak splitting and its correspondence to gap modes in the scattering spectrum of the dielectric system considered in 4.2. We do so using the notion discussed in 4.2 that the phason ϕ acts as a modulation of an effective cavity length between the substructure of the artificial palindrome. We define a “toy model” consisting of two identical periodic gratings with a variable separation between them which is analogous to the case of a photonic crystals based Fabry-Perot cavity with resonant modes.

Figure 4.39a depicts the diffraction pattern for the case with zero separation (undisturbed periodic structure). The single diffraction peak describing the periodicity of the structure is equivalent to the single spectral gap in the dielectric case. Figure 4.39a depicts the diffraction pattern for the case with a single slab which is equivalent to the dielectric photonic crystal with a single defect discussed in 3.2.1. In the dielectric case a single gap mode is excited at mid-gap, effectively splitting the gap in two. The diffraction pattern shows still a single peak, but split in two (through the middle). This is understandable upon calculation of the Fourier coherent sum of amplitudes we will not give here. We’ll suffice to say that in the undisturbed case, the diffraction intensity is the absolute value of a sum of cosines with many frequencies, all having an anti-node at $k = 0.5$. In the single slab separa-

tion the same sum exists, now all cosines have a node at $k = 0.5$ which manifests as a split in the diffraction peak. A more intuitive mental image is that the split in the diffraction peak carries information regarding the gap mode in the dielectric system.

If we monitor this analogy over more separation values we realize that at intermediate separations, the split still exists, but now the peak is unbalanced with respect to the split (see figure 4.40). In the Fourier sum viewpoint, we have a sum of cosines with an anti-node around $k = 0.5$ but not exactly there. The gap mode analogy still holds, and the location of the split in the diffraction peak carries information regarding the gap mode in the dielectric case.

Finally, if we completely free the separation parameter, we manage to mimic the topological winding of diffraction peaks measured in 4.4, with a winding number completely dependent on the rate of separation change which functions as the toy model " ϕ " (see figure 4.41).

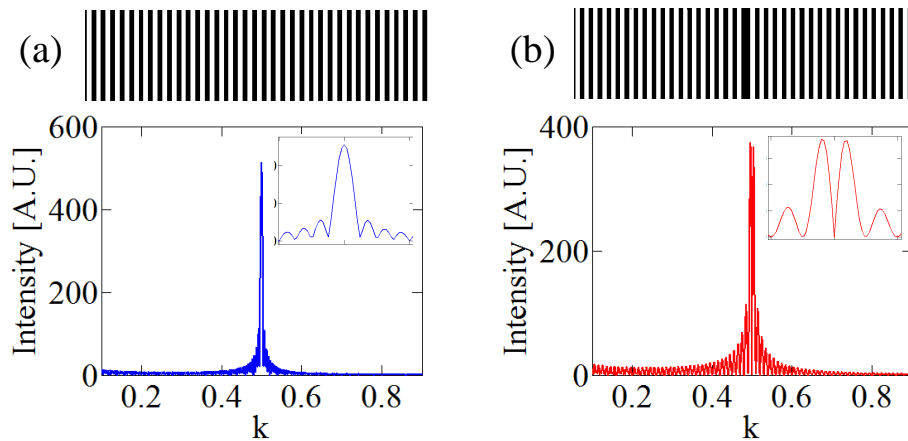


Figure 4.39: (a) Calculated diffraction pattern (in blue) for an undisturbed periodic structure (given above in a grayscale map). The inset gives a close up view of the single diffraction peak. (b) The same as (a) for a periodic structure with a single slab separation.

To summarize this part, an instructive way to understand the topological winding of diffraction peaks splitting in the Fibonacci artificial palindrome is the following. Each of the many diffraction peaks (or spectral band gap) of a single quasiperiodic segment carries the information of some partial periodicity in the structure. Therefore, for each peak, the artificial palindrome scheme is equivalent (in the dielectric case) to an effective Fabry-Perot cavity. We also know from the discussion in 4.2 that scanning ϕ is a nothing but a modulation of the effective cavity length. If we translate this to the diffraction language, we have for each diffraction peak (separately) an identical case to our toy model. The difference between peaks is the proportionality constant between ϕ and the Fabry-Perot effective cavity length.

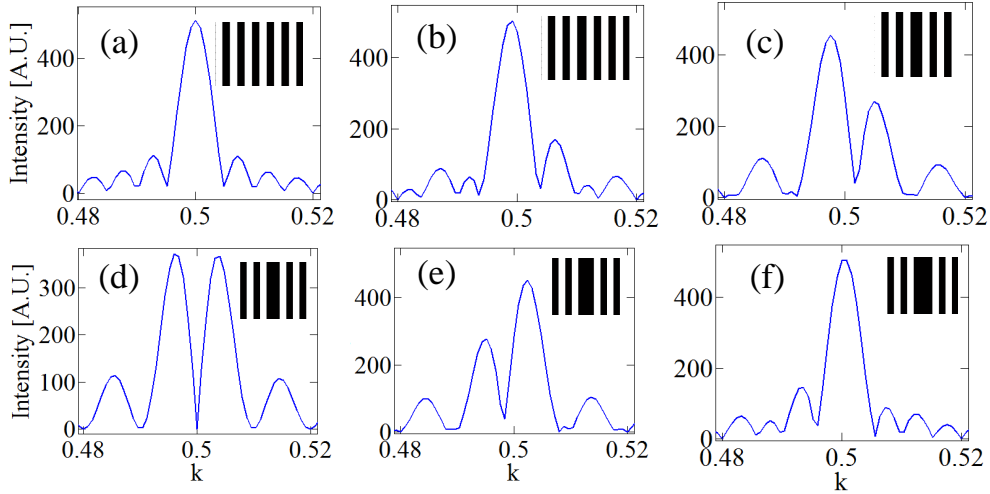


Figure 4.40: (a)-(f) A close up view of the single diffraction peak (in blue) for an increasing amount of separation (shown in the inset). The imbalance of the split is periodic in the amount of separation.

4.5.5 Chern numbers - structural origin

Here we aim to provide a theoretical description of the forth experiment presented in 4.4, i.e. to obtain the (k_x, k_Φ) map. The starting point is based on the Cut and Project (C&P) method, discussed in 2.1.5, and 2.1.8, which allows to obtain the Bragg peak structure of S_∞ [dB81, ZD85, Els86]. In the case of a finite segment \vec{F}_N , we have shown that there still exist diffraction peaks, located at approximate values of the exact Bragg peaks spatial frequencies, and also were able to probe their topological properties by scanning through the N possible realizations. Here, we extend this approach and apply it to $\{\vec{F}_N(\phi)\}$, the entire 2D structure composed of all possible N realizations (and defined in the rotated coordinate system (x, Φ)), to obtain both the (approximate) k values of the Bragg peaks and the corresponding observable (exact) Chern numbers.

We recall that the infinite Fibonacci chain S_∞ and any of its finite segments are generated through C&P by choosing the angle θ between the C&P line Δ and the basic \mathbb{Z}^2 -lattice such that $\tan \theta = \tau^{-1}$, τ being the golden mean (see 2.1.5). The first and most important step is to realize that $\{\vec{F}_N(\phi)\}$ depicted in figure 2.11, may be described as a 2D unit cell \mathbb{Z}^2 -lattice with a rotated with an angle φ with respect to the (x, ϕ) axes (see Fig.4.42a). Disregarding the form factor of the 2D unit cell of this lattice, the remaining square lattice of points is represented by the function,

$$Q(x, \phi) = \frac{1}{4\pi^2} \sum_{k,l} \delta(x - k \cos \varphi - l \sin \varphi) \delta(\phi + k \sin \varphi - l \cos \varphi), \quad (4.12)$$

where the sum is over a finite set of integers (k, l) . The Fourier transform of the rotated (x, ϕ) \mathbb{Z}^2 - lattice is also a \mathbb{Z}^2 -lattice rotated with the angle φ with respect to

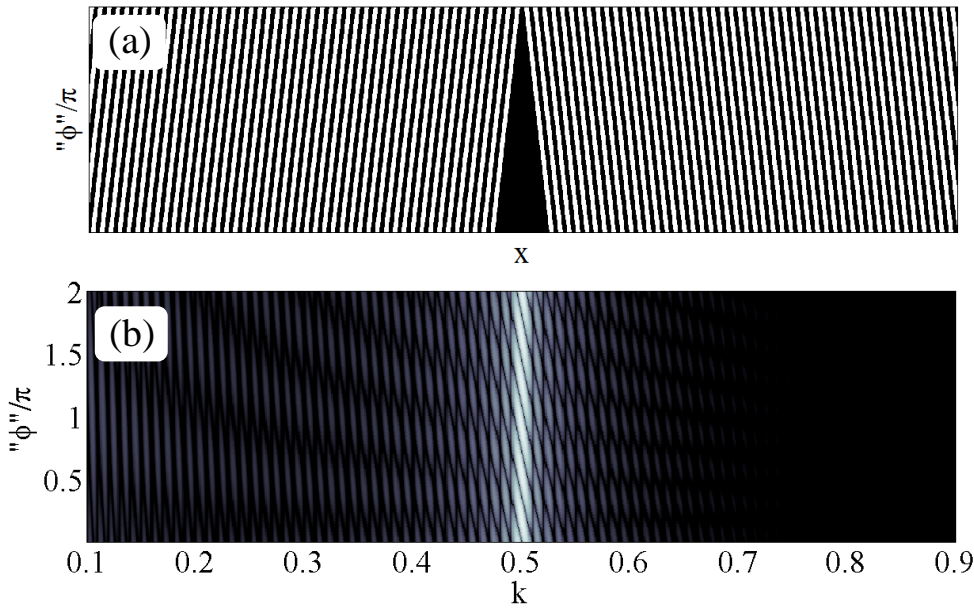


Figure 4.41: (a) Grayscale map: the periodic grating with a semi-continuously increasing separation. (b) Grayscale map: the calculated diffraction pattern for the structure set given in (a). Each "φ" value corresponds to a different diffraction calculation .

the reciprocal space (k_x, k_ϕ) , and represented by,

$$F(k_x, k_\phi) = \sum_{n,m} \delta(k_x - m \cos \varphi + n \sin \varphi) \delta(k_\phi - m \sin \varphi - n \cos \varphi), \quad (4.13)$$

where the sum is over an infinite set of integers (m, n) .

We now discuss the rotation angles θ and φ . In the case of S_∞ these angles are such that $\tan \theta = \tan \varphi = \tau^{-1}$, while for a finite segment they are different. To generate a finite chain \vec{F}_N of N letters, the slope of the cut Δ defined by $\tan \theta$ must not necessarily be taken as an irrational but may be given by a rational approximant p/q (as long as the unit cell of the resultant periodic chain $p + q - 2$ remains larger than N). For S_{10} this approximant is $34/55$. Similarly, to generate the complete set of N finite chains, $\{\vec{F}_N(\phi)\}$, the slope can again be taken as another rational approximant p/q (this time the needed unit cell $p + q - 2$ has to be larger than $2N + 1$). For S_{10} this approximant is $89/144$. The rotation angle φ is quite different. For the set $\{\vec{F}_N(\phi)\}$ with $N = \mathcal{F}_j$ generated using any of the allowed values of θ , the rotation angle φ determining the tiling angle of the new \mathbb{Z}^2 - lattice has always a fixed rational slope no matter how accurate is the approximation used for the irrational τ , namely,

$$\tan \varphi = \frac{q_l}{p_l}, \quad (4.14)$$

where the two mutually prime integers (p_l, q_l) depend only on $N = \mathcal{F}_j$ (see 4.5.7).

For S_{10} , we have $p_l = 5$ and $q_l = 8$.

The 2π -periodicity of the set $\{\vec{F}_N(\phi)\}$ in the phason direction ϕ , together with the fixed rational angle of rotation φ , means that the set may be folded to form a perfect 2D torus (see Fig.4.42). From 2.2 we know that this finite size map encloses exactly N unit cells (due to exactly N phason-flips). Therefore, the infinite reciprocal space of the finite set $\{\vec{F}_N(\phi)\}$ with $N = \mathcal{F}_j$ may be characterized by a finite quasi-Brillouin zone, QBZ $_N$, (also a 2D torus) which generalizes the usual notion of Brillouin zone. We use the fact that the rotation angle of the $\{\vec{F}_N(\phi)\}$ reciprocal lattice with respect to the (k_x, k_ϕ) axes is still described by $\tan \varphi$. To build the torus QBZ $_N$ in the (k_x, k_ϕ) reciprocal space, we follow the same guidelines as the structural co-numbering approach (see 2.1). We set an origin $(k_x, k_\phi) = (0, 0)$ at some point and label them with the lattice coordinates $[m = 0, n = 0]$. The next step is to identify the three other corners of the QBZ $_N$, using (4.14), to be $[m = q_l, n = -p_l]$ where $(k_x, k_\phi) = (q_l \cos \varphi + p_l \sin \varphi, 0)$, $[m = p_l, n = q_l]$ where $(k_x, k_\phi) = (0, p_l \sin \varphi + q_l \cos \varphi)$, and $[m = q_l + p_l, n = q_l - p_l]$ where $(k_x, k_\phi) = (p_l \sin \varphi + q_l \cos \varphi, p_l \sin \varphi + q_l \cos \varphi)$. These 4 points define the torus QBZ $_N$ as represented on Fig.4.43. It exactly encloses N points.

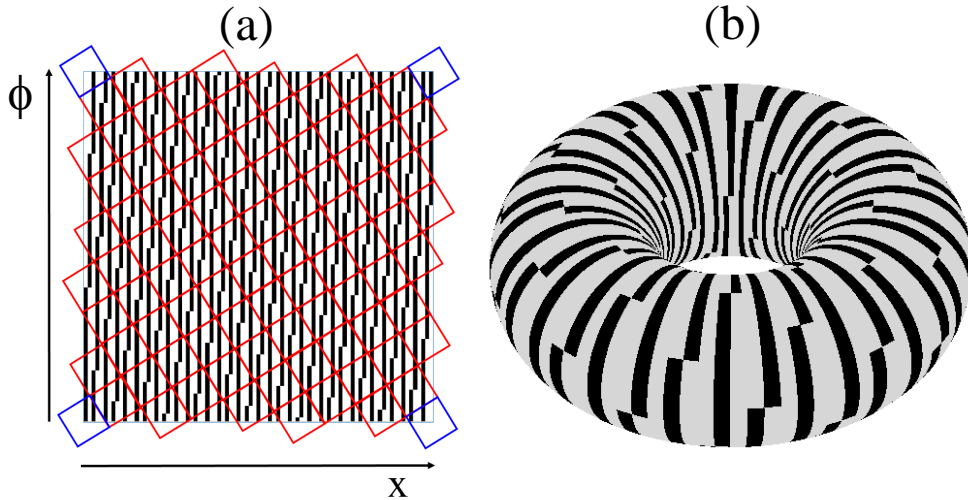


Figure 4.42: Structural properties of the 2D set $\{\vec{F}_N(\phi)\}$ for $N = 89$. (a) The structural $x - \phi$ map created through the Cut & Project method forms a tilted 2D crystal with a 2D unit cell indicated by red and blue squares. The fact that $p_l : q_l = 5 : 8$ is easy to deduce. This map is a torus obtained by wrapping the map along both axes, so that the four blue squares coincide. (b) An illustration of the resulting torus.

We now discuss the normalization of the reciprocal space torus coordinates. The k_x coordinates may be normalized by $(p_l \sin \varphi + q_l \cos \varphi)^{-1} = 1/\sqrt{p_l^2 + q_l^2}$ so that $k_x \in [0, 1]$. After this normalization, the N points at which $F(k_x, k_\phi) \neq 0$ correspond to all N possible (approximate) Bragg peaks values k_q . As for normalization along the ϕ -axis, it is obtained from the reciprocal lattice point with $k_\phi = \delta k_\phi$, the smallest

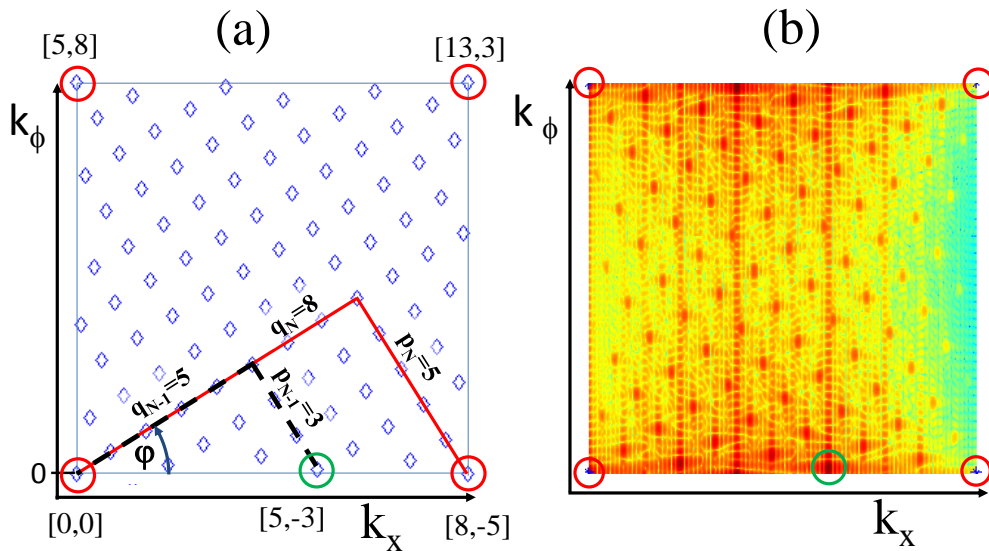


Figure 4.43: Construction of the torus QBZ_N for $N = \mathcal{F}_{j=10} = 89$ with the corresponding values $p_l = 5$ and $q_l = 8$. The red circles define the corners of the torus QBZ_N which encloses $\mathcal{F}_{10} = 89$ points (lattice coordinates $[m, n]$ are given). The fundamental k_ϕ value, δk_ϕ , corresponding to Chern number equal to 1, is represented by the green circle (along with the lattice coordinates $[m, n]$). This lowest non zero value of k_ϕ in this case is obtained using the predecessor approximant (p_{l-1}, q_{l-1}) in the Farey series. (a) An emulated lattice angled at φ (to set notations). (b) Colormap: the actual 2D Fourier transform of $\{\vec{F}_N(\phi)\}$ for $N = 89$.

nonzero value of k_ϕ . The (toroidal) vector between the origin and this lattice point, $(\delta k_x, \delta k_\phi)$, is instrumental to find all points within the QBZ_N torus according to the co-numbering algorithm (see 2.1). The N points are found through the recurrent vectorial addition (and winding) of this vector similar to the co-numbering generator (see Fig.4.43). This single fundamental lattice point is obtained using one of the two the predecessor approximants of the slope $\tan \varphi = p_l/q_l$ in (2.4), depending on the parity of l . This point has been proven in 2.1 using the Vajda identity [Vaj07]. It is given by the point $[m = q_{l-1}, n = -p_{l-1}]$ for even l , or the point $[m = q_{l-2}, n = -p_{l-2}]$ for odd l . In our example ($j = 10 ; l = 4$) this vector in reciprocal lattice coordinates gives

$$(\delta k_x, \delta k_\phi) = \left(\frac{q_{l-1} \cos \varphi + p_{l-1} \sin \varphi}{\sqrt{p_l^2 + q_l^2}}, q_{l-1} \sin \varphi - p_{l-1} \cos \varphi \right) \quad (4.15)$$

The expression for $(\delta k_x, \delta k_\phi)$ along with the co-numbering method sets the k_ϕ -scales in the reciprocal lattice, thus leading to the integer (Chern) numbers \mathcal{C}

$$\mathcal{C}(n, m) \equiv \frac{k_\phi}{\delta k_\phi} = \frac{m \sin \varphi + n \cos \varphi}{q_{l-1} \sin \varphi - p_{l-1} \cos \varphi} = mp_l + nq_l \quad (4.16)$$

where the last equality is obtained by noting that successive approximants in the Farey series (2.4) fulfill $|p_{l-1}q_l - q_{l-1}p_l| = 1$. We note here that (4.16) holds for odd values of l also as $|p_{l-2}q_l - q_{l-2}p_l| = 1$.

Additionally, a change of origin has to be performed in the k_ϕ toroidal dimension, such that all reciprocal lattice points with $\mathcal{F}_j/2 \leq k_\phi/\delta\phi$ are wrapped around the torus to have $k_\phi/\delta\phi \rightarrow \mathcal{F}_j/2 - k_\phi/\delta\phi$. The \mathcal{F}_j values of k_ϕ now come in pairs of equal magnitude and opposite sign. (see Fig.4.44).

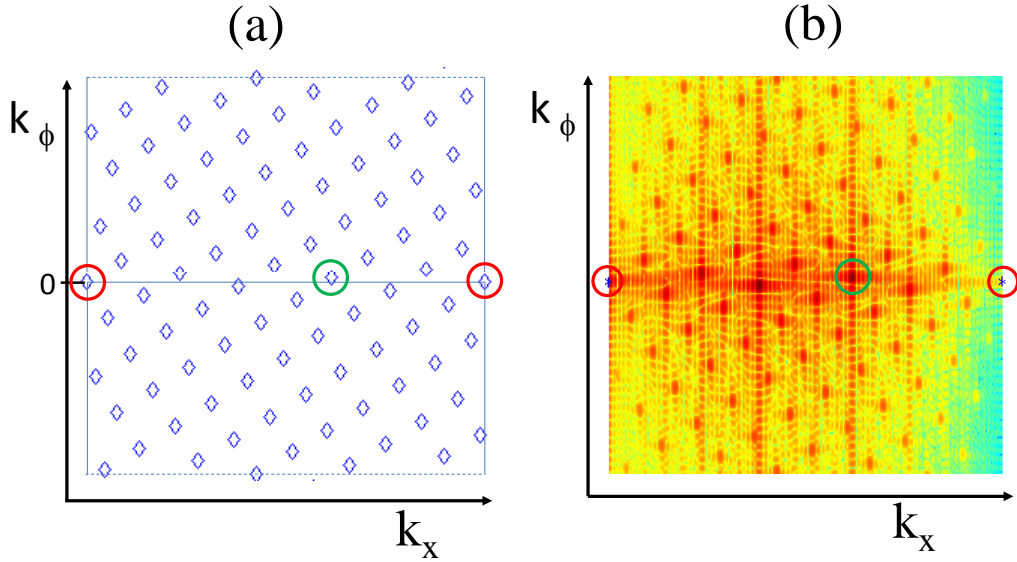


Figure 4.44: A properly unwrapped torus QBZ_N for $N = \mathcal{F}_{j=10} = 89$. The red circles define the 4 corners of the torus QBZ_N of figure 4.43. The fundamental k_ϕ value, δk_ϕ , corresponding to Chern number equal to 1, is represented by the green circle. k_ϕ values now come in pairs of equal magnitude and opposite sign. (a) An emulated lattice angled at φ . (b) Colormap: the actual 2D Fourier transform of $\{\vec{F}_N(\phi)\}$ for $N = 89$.

Finally, the Fourier transform (4.13) of $\{\vec{F}_N(\phi)\}$ can be rewritten in terms of the Chern numbers C and of the (approximate) Bragg peak values k_x as,

$$F(k_x, C) = \sum_{n,m} \delta \left(k_x - \frac{m \cos \varphi - n \sin \varphi}{\sqrt{p_l^2 + q_l^2}} \right) \delta(C - mp_l - nq_l) \quad (4.17)$$

where the integers (n, m) run over the 2D torus QBZ_N now entirely defined by

$$\begin{aligned} k_x(m, n) &= (mq_l - np_l) / (p_l^2 + q_l^2) \\ C(m, n) &= mp_l + nq_l \end{aligned} \quad (4.18)$$

The total number of points in the 2D torus QBZ_N is the number of Chern integers available, which is exactly $N = \mathcal{F}_j$. It is bounded from above by $\mathcal{F}_j/2$, namely $|C(m, n)| \leq \mathcal{F}_j/2$. Finally, we note that Chern numbers always appear in pairs of

opposite sign associated to the structure length N and its minimal Farey approximate $\tan(\theta) = p/q$, namely for the lowest approximant (periodic system), the values $\mathcal{C} = \pm 1$ will show up first, followed by higher paired values while increasing the ratio p/q . It is worth noting again that while the Chern numbers $\mathcal{C}(m, n)$ are always integers, the (approximate) Bragg vectors $k_x(m, n)$ depend on the chain length but they rapidly converge to the exact Bragg value obtained for $N \rightarrow \infty$. This last claim is demonstrated in figure 4.45.

This purely structural limitation to the observable number of Chern numbers, and to the accuracy of the k_q values for a finite chain may be used to give a formal meaning to the gap labeling theorem of finite chains. The Integrated density of states (IDOS) for a finite chain of length $N = \mathcal{F}_j$, may possess exactly N non-recurring gaps located at $k_{\mathcal{C}}$ values fulfilling

$$k_{\mathcal{C}} = \frac{q_{l-1} \cos \varphi + p_{l-1} \sin \varphi}{\sqrt{p_l^2 + q_l^2}} \cdot \mathcal{C} \text{ modulo } 1; \quad \varphi = \arctan \frac{p_l}{q_l}; \quad -\mathcal{F}_j/2 \leq \mathcal{C} \in \mathbb{Z} \leq \mathcal{F}_j/2,$$

to yield exactly N corresponding IDOS values

$$\mathcal{N}_{\mathcal{C}} = \frac{q_{l-1} \cos \varphi + p_{l-1} \sin \varphi}{\sqrt{p_l^2 + q_l^2}} \cdot \mathcal{C} \text{ modulo } 1; \quad \varphi = \arctan \frac{p_l}{q_l}; \quad -\mathcal{F}_j/2 \leq \mathcal{C} \in \mathbb{Z} \leq \mathcal{F}_j/2. \quad (4.19)$$

Now, for the infinite chain ($l \rightarrow \infty$) we have $\cos \varphi = 1/\sqrt{1 + \tau^{-2}}$; $\sin \varphi = \tau^{-1}/\sqrt{1 + \tau^{-2}}$, and $\sqrt{p_l^2 + q_l^2} = \sqrt{1 + \tau^{-2}}$. Using the identities (for $l \rightarrow \infty$): $q_{l-1}/q_l = \tau^{-1}$ and $p_{l-1}/q_l = \tau^{-2}$, the expression for the finite size gap labeling theorem (4.19) becomes:

$$\mathcal{N}_{\mathcal{C}} = \mathcal{C} \cdot \tau^{-1} \text{ modulo } 1,$$

which is identical to (3.45).

4.5.6 Generalizations to other C&P slopes and the Aubry-Andre-Harper model (topological map)

Performing the topological map method corroborate the conclusions in 4.5.3, and in 2.3.3. Figures 4.46 and 4.47 summarize the results.

4.5.7 Derivation of p_l and q_l for a structure of length $N = \mathcal{F}_j$

The $x - \phi$ map we use for the Fourier transform of $\{\vec{F}_N(\phi)\}$ is N by N (N letters and N phason flips). In order that each phason flip becomes the center of the $2D$ unit cell described above, we assign an area N for each tile (unit cell). The tile

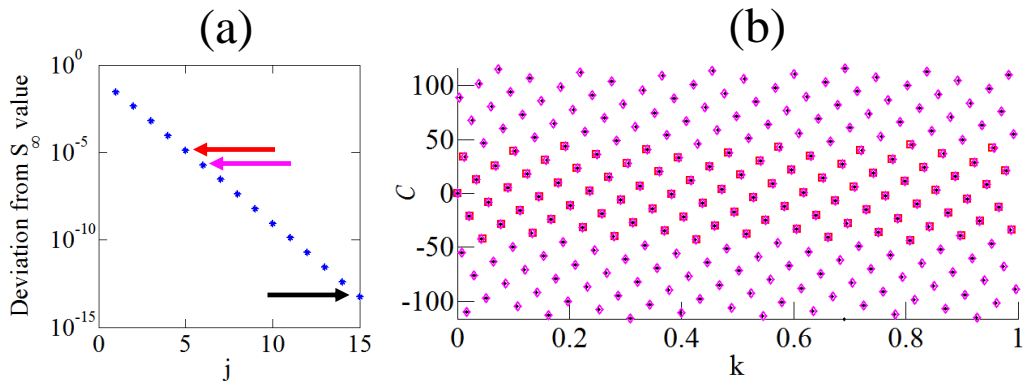


Figure 4.45: (a) The convergence of δk_x in the Fourier transform of $\{\vec{F}_N(\phi)\}$ as a function of structure length (as expressed by the Farey generation describing the reciprocal lattice) to τ^{-1} (represented by the 15th Farey approximant). (b) In black dots the reciprocal lattice of the 15th Farey approximant (representing the true quasiperiodic structure). In red squares the 89 reciprocal lattice points of the 4th Farey approximant. In magenta diamonds the 233 reciprocal lattice points of the 5th Farey approximant. The level of convergence in the k -axis is indicated in the colored arrows in (a)

is generally a parallelogram, and sometimes it is square. Two classes of Fibonacci lengths exist:

- 1) $N = \mathcal{F}_j$; even j , e.g.: $N = 2, 5, 13, 34, 89, 233, 610...$

For this class there exists the rule: $N = \mathcal{F}_j = \mathcal{F}_{j/2}^2 + \mathcal{F}_{j/2-1}^2$. This means that the tile is square, and that both real space tiling angles can be assigned the same Farey approximant $p_l : q_l = \mathcal{F}_{j/2} : \mathcal{F}_{j/2-1}$.

Examples:

$$N = 13 = \mathcal{F}_6 = \mathcal{F}_2^2 + \mathcal{F}_3^2 = 2^2 + 3^2 \rightarrow \text{the tiling is } 2 : 3 \text{ (tile area is } 13).$$

$$N = 34 = \mathcal{F}_8 = \mathcal{F}_3^2 + \mathcal{F}_4^2 = 3^2 + 5^2 \rightarrow \text{the tiling is } 3 : 5 \text{ (tile area is } 34).$$

$$N = 89 = \mathcal{F}_{10} = \mathcal{F}_4^2 + \mathcal{F}_5^2 = 5^2 + 8^2 \rightarrow \text{the tiling is } 5 : 8 \text{ (tile area is } 89).$$

The 100% tiling is the true proof that the $x - \phi$ map is in fact a torus.

- 2) $N = \mathcal{F}_j$; odd j , e.g.: $N = 21, 55, 144, 377...$

For this class there exists the rule: $N = \mathcal{F}_j = \sqrt{[\mathcal{F}_{(j-1)/2}^2 + \mathcal{F}_{(j-1)/2-1}^2][\mathcal{F}_{(j+1)/2}^2 + \mathcal{F}_{(j+1)/2-1}^2]}$. This means that the tile is not square.

Examples:

$N = 21 = \mathcal{F}_7 \approx \sqrt{[\mathcal{F}_3^2 + \mathcal{F}_2^2][\mathcal{F}_3^2 + \mathcal{F}_4^2]} = \sqrt{[2^2 + 3^2][3^2 + 5^2]} \rightarrow$ the tile constants are $x : y = 3 : 3$ and $x : y = 2 : 5$. The single tile coordinates $[x, y]$ are $[0, 0], [5, -2], [8, 1], [3, 3]$ (tile area is 21). Therefore the non-square tiling is $2 : 3$ for the x -axis ($2 \cdot 3 + 3 \cdot 5 = 21$) and $5 : 3$ for the y -axis ($5 \cdot 3 + 3 \cdot 2 = 21$). This can be fixed by deforming the y -axis, but there is no need because we already manipulate this axis to be in units of \mathcal{C} . The 100% tiling shows that the $x - \phi$ map is in fact a torus.

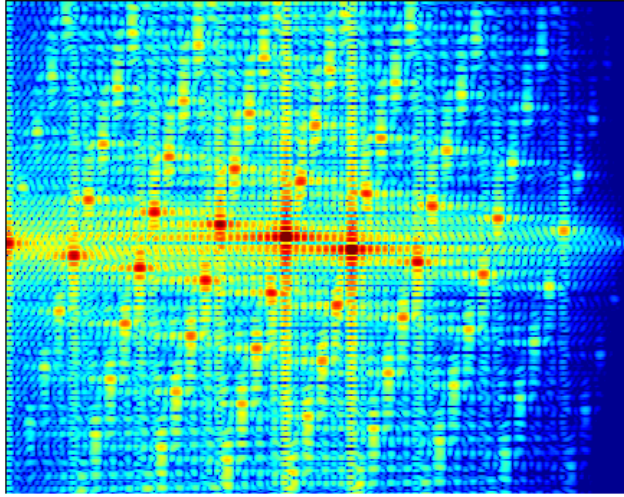


Figure 4.46: Colormap: topological map for the C&P structure with $N = 89$ and a slope $5^{-1/2}$ (with k and ϕ axes as before). Axes were discarded for clarity

4.6 The importance of keeping $N = \mathcal{F}_j$

In 2.1, we discussed the fact that characteristic function or C&P structures, apart for having a structural degree of freedom ϕ , are not limited in length as the substitution or concatenation generated structures. We then argued that in spite of this freedom, we restrict ourselves to the natural lengths $N = \mathcal{F}_j$. This section will shortly describe why.

Firstly, from the Gap labeling theorem point of view, stated for the infinite chain there is no length dependence and we have found it valid for structures with non-Fibonacci lengths. Secondly, we have shown that the structural palindromic cycle is universal to the C&P chain family, and its origin is a function of only slope and length. However, when performing spectral calculation to monitor gap modes in the artificial palindrome scheme, an origin shift is observed between the structural palindromic symmetry cycle and the gap mode traverse, while keeping the winding numbers intact (see figure 4.48). Following the quantitative approach using the effective Fabry-Perot resonance condition (3.30) yields the very same origin shift (see figure 4.49).

The shift in origin is found to be exactly $-\Delta N \tau^{-1}$, where ΔN is the difference between the structure length and the closest Fibonacci number \mathcal{F}_j . This is due to the expression 2.12 requiring that a palindromic symmetry pole will occur at the edge where the gap modes are localized. Due to (3.51) we may deduce that the quantity that changes as a function of ΔN is the total phase shift at the gaps $\delta(k)$.

This problem was mentioned from structural considerations in 2.2.1, and has been encountered in the diffraction setup when calculating for other C&P slopes (see 4.5.3). Although the diffraction chiral phase still corresponds to the structural

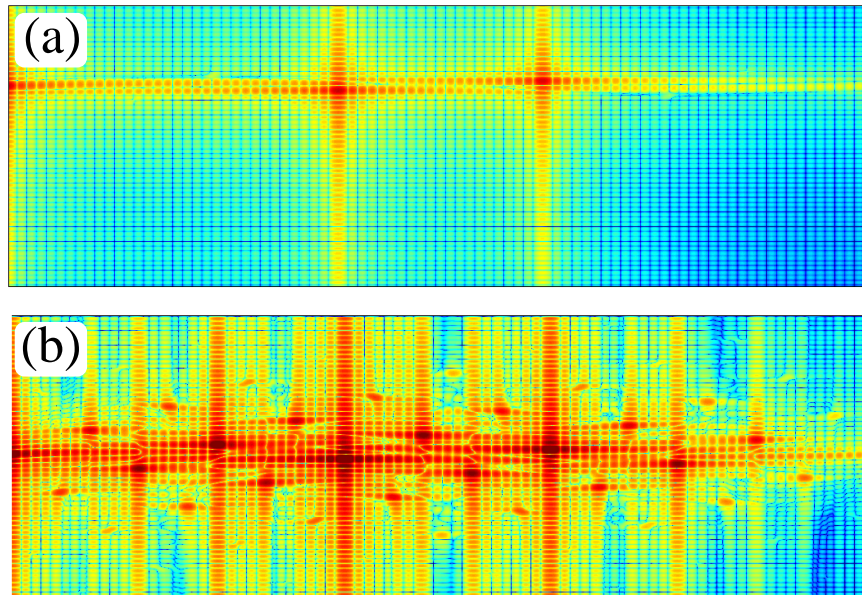


Figure 4.47: Colormap: topological map for the Aubry-Andre-Harper structure with $N = 89$ and a slope τ^{-1} (with k and ϕ axes as before). Axes were discarded for clarity. (a) Pure AAH structure (b) A modified AAH with $\beta = 3$. The global pattern appears to be a limited version of the Fibonacci case (and the limitation is a function of β).

palindromic symmetry cycle, the striations in the diffraction peaks do not. The winding is conserved, but the origin of the striation is shifted (this is indicated by the blue line in figure 4.37b which is where all diffraction peaks are unsplit). Perhaps this may be used to find a set of natural lengths for non Fibonacci C&P slopes (find lengths where both cycles are again synchronized). This Issue may also be viewed from a completely structural point of view. In 4.5.5 we argue that the structure set $\{\vec{F}_N(\phi)\}$ is a perfect torus. It is easy to see that if we change the structure length along the quasiperiodicity direction then the torus is not closed and we have a residual stub.

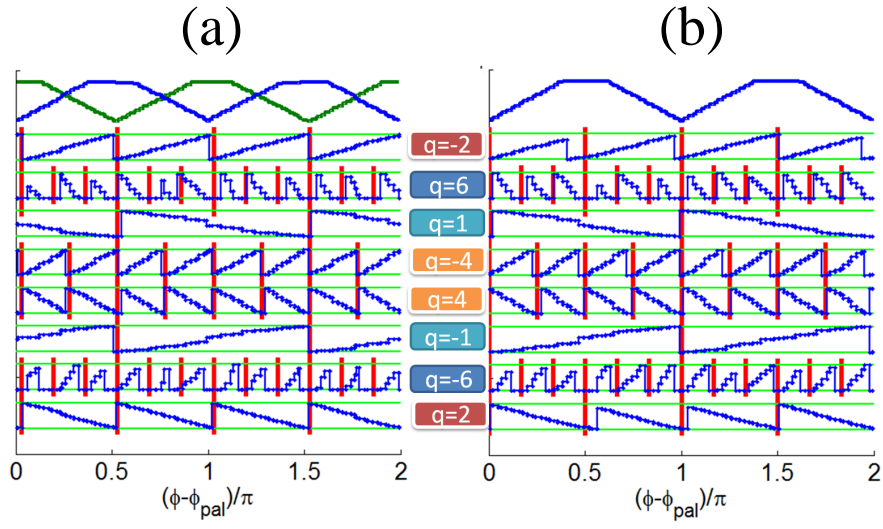


Figure 4.48: Topological gap modes in the spectrum of the artificial palindrome $\mathcal{P} \equiv \vec{F}_N \overleftarrow{F}_N$. Eight selected gap modes relative in band frequency as a function of ϕ is in blue (gap edges are in light green), compared to the palindromic symmetry cycle on top and to the gap Chern number q . Red bars split the ϕ axis to guide the eye in estimating the Harmonic. (a) $N = 93$. (b) $N = 89$.

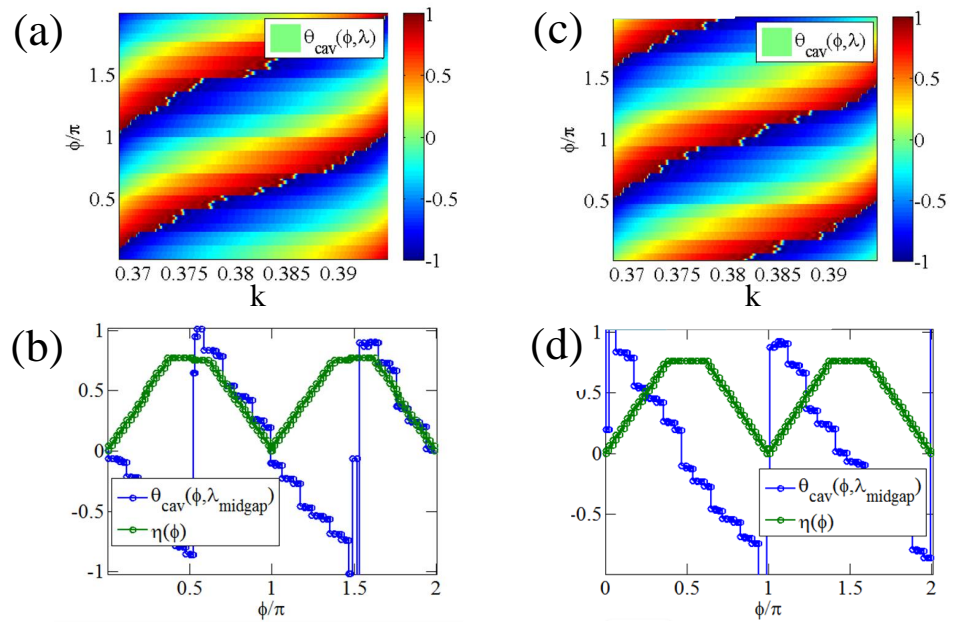


Figure 4.49: Topological gap modes in the spectrum of the artificial palindrome $\mathcal{P} \equiv \vec{F}_N \overleftarrow{F}_N$ as predicted by the scattering phase θ_{cav} . The gap with $q = -1$ is investigated for the existence and frequency of gap modes using θ_{cav} (colormaps) and specifically the condition $\theta_{cav} = 0$ (blue lines with circles), and compared to the structural palindromic symmetry cycle (green lines with circles). (a)-(b) $N = 93$. (c)-(d) $N = 93$.

Chapter 5

Summary and outlook

In the last 3 technical chapters we have reviewed much of the knowledge base in the fields of structural, spectral and topological properties of quasiperiodic chains in the aim to connect them in a meaningful way. The essence of the current work is this connection to form a highly interdisciplinary field of mathematical physics, scattering matrix approach, crystallography and cavity physics. Along the way we have uncovered many pieces of physics for the first time, to our knowledge. Some of which are still “open ended” at this stage and requires additional research. In this chapter, we will attempt to browse through the plot of the last 3 technical chapters in context, listing our contribution to this field, and finally mention the medium and long range outlook for this line of research.

5.1 The story

Quasiperiodic chains have been long known to have rich topological properties. Mathematical physics based analysis of the scattering and diffraction spectral properties of infinite quasiperiodic chains has well known outstanding results since the 1980's. True quasiperiodicity or irrationality is not a matter of question for these structures, and is crucial to produce a true multifractal spectrum with an infinite number of spectral gaps (or diffraction peaks) ordered in a hierarchical manner and labeled using integers which are Chern numbers. This mathematical classification of quasiperiodicity is written in the same language as more familiar physical examples of topological classification, such as quantum anomalies in field theory, the quantization of the Hall conductance in quantum Hall effects, where the Hall conductance σ_H of two-dimensional semi-conductors in a strong magnetic field is quantized in integer multiples of a fundamental conductance σ_0 , and topological models of quantum condensed matter such as topological insulators, graphene, and the classification of topological defects. For all these physical examples of topological classes, there exists an underlying symmetry or a gauge field, governing the relation of these properties to physical observables. For quasiperiodic chains, these driving forces have

not yet been identified or agreed upon, and a more physical understanding of the existence of Chern numbers in such structures with no further manipulation (e.g. field) has not been given.

The first step forward was to consider finite size quasiperiodic structures. If we take the quantum Hall effect as an example, then without this step there would have been no edge, no current carrying edge states and no Hall conductance. After the experimental observation of quantized Hall conductance (in a finite system), a successful theoretical effort has been focusing in the understanding of the manifestation or the mapping of the topological properties due to infinite structures to that of real life finite systems. A very similar path has been taken also in all the other examples discussed above. In the case of quasiperiodic structures it has not been this simple. Quasiperiodicity is an infinite concept in essence, a fact which has been a cause of a great reluctance to consider finite quasiperiodic systems without classifying them as periodic approximants of the quasiperiodic structure. However, a recent first attempt has been made in Aubry-Andre type tight binding model, acknowledging that when considering a finite segment of an infinite quasiperiodic chain you immediately gain a structural degree of freedom which is, in essence, the choice of the location of the segment along the infinite chain, or in other words, translational degree of freedom given by the modulation phase ϕ . Using this degree of freedom in a closed quasiperiodic segment with edge states excited through some closed boundary conditions, results in the freezing of the original (bulk) spectrum, and a regular traverse of the edge states frequency which was analyzed to conclude that it carries topological information, specifically in their winding number as a function of scanning the structural degree of freedom ϕ . In an effort to connect this phenomenon to the subject of topological current carriers and topological pumping, such pumping has been predicted and measured in Aubry-Andre type tight binding model systems. Questions have been raised regarding the role of true incommensurability to the results which have been obtained. In fact it has been shown that the same exact results may be obtained by using the same model without true incommensurability.

The next step forward was to change from tight-binding approximation to the scattering approach, and analyze discrete quasiperiodic chains, such as the (pure) Fibonacci chain, which are generated by the well established methods such as substitution and C&P. The properties of substitution rules structures give access to the gap labeling theorem's prediction for the existence of Chern numbers, and the C&P approach reveals the structural effect of the modulation phase ϕ . In order to treat an edge in the scattering approach, a generalized edge was designed, namely the artificial palindrome scheme. These building blocks led to the finding of the phason-flip driven structural palindromic symmetry cycle which has a double frequency compared to ϕ . Spectrally, this led to the understanding that for low enough contrast, the edge states of the generalized edge traverse the gaps in a way describable by an integer winding number. There were two major differences from the Aubry-Andre

tight-binding approach. The first difference was that instead of the previous \mathcal{C} windings within one period of ϕ , the winding numbers were now found to be $2\mathcal{C}$. The second difference was that instead of an edge state winding with pauses (i.e. with many values of ϕ where no edge states exist), we now have a gap mode inhabiting each gap at all times, except for the windings zeros which is in perfect synchronization with the structural palindromic symmetry cycle. A quantitative effective Fabry-Perot model has been used to easily explain the missing windings in the Aubry-Andre tight-binding results by means of boundary conditions constraints. The synchronization of the spectral phenomenon of edge states winding to a violation parameter of a structural symmetry of the C&P structure with respect to the same structural degree of freedom ϕ tells us that the generalized edge scheme is the one to tell the whole story. This was complemented by another important ingredient is using the scattering approach to find a combination of reflected phase shifts which is the spectral counterpart of the spatial degree (or violation) of palindromic symmetry. The very same mechanisms were also found in the diffraction amplitude phase of a single C&P chain, which translates to an intensity spectrum winding of the diffraction pattern in the artificial palindrome scheme.

The final step came from backtracking to the purely structural properties of C&P structures and the structural effect of the phason-flips. Noticing that the $2D$ map of phason flips for a finite chain forms a perfect structural torus, brought tremendous insight. A single segment of the C&P chain without any external periodic boundary conditions whatsoever forms its own internal periodic boundary conditions with respect to the translational degree of freedom (when controlled by the modulation phase ϕ). This quickly led to the definition of a quasi-Brillouin zone and to a quantitative formulation for the allowed number of Chern numbers, and the deviation of the spectral gaps/diffraction peaks/integrated density of modes at the gaps from the infinite chain values. This last progress sheds light on the recurring questions regarding the necessity of true irrationality, and of natural lengths to the properties we observe. Moreover, to our opinion it depicts the most fundamental description of the quasiperiodic Chern topological invariants: that of a winding around a torus.

5.2 Our contribution

1. We have performed a structural analysis of finite (discrete) C&P chains as a function of the translational degree of freedom ϕ . We have found, among other properties, the existence of a structural (violation of) palindromic symmetry cycle as a function of ϕ , with a double frequency compared to ϕ , and a natural origin where the structure is a perfect palindrome, dependent upon only length and C&P slope.
2. We have performed a non-tight-binding spectral scattering analysis of finite

(discrete) C&P chains as a function of the translational degree of freedom.

3. We have designed the artificial palindrome scheme as a generalized edge in order to monitor the winding of topological edge states. We have found that for low enough contrast, an integer winding occurs, with winding numbers for each gap of $2\mathcal{C}$. For the Fibonacci case, each Chern number \mathcal{C} was verified against the prediction of the gap labeling theorem. We have measured these predictions in a cavity polariton system.
4. We have shown that the mechanism of the spectral winding of edge states in the generalized edge scheme is perfectly synchronized with the violation of palindromic symmetry cycle (the \mathcal{C} -harmonic of the cycle). Specifically, at ϕ values where the structure is a palindrome no edge states occur for all gaps.
5. We have formulated an effective Fabry-Perot model using the scattering approach. When employed to the artificial palindrome scheme, this model constitutes an exact description of the existence and frequency of topological edge states as a function of ϕ . Through this model we were able to equate seemingly different situations such as different boundary conditions, a geometrical cavity, defect systems and hetero-structures.
6. We have uncovered a scattering phase shift (α) sensitive to the symmetry of a single chain. This phase has an integer winding as a function of ϕ within spectral gaps and no dependence on k . The winding numbers of this phase for each gap is $2\mathcal{C}$. For the Fibonacci case, each Chern number \mathcal{C} was verified against the prediction of the gap labeling theorem. We have shown that this winding is a much more sensitive probe of the Chern numbers than the edge state method.
7. We have shown that the mechanism of the spectral winding of the phase α is perfectly synchronized with the violation of palindromic symmetry cycle (the \mathcal{C} -harmonic of the cycle). Specifically, α vanishes at ϕ values where the structure is a palindrome.
8. We have performed a diffraction analysis for C&P chains and explored the role of true quasiperiodicity. A winding phenomenon has been discovered in the diffraction pattern of the artificial palindrome structure, with an integer winding numbers for each diffraction peak of $2\mathcal{C}$. For the Fibonacci case, each Chern number \mathcal{C} was verified against the prediction of the gap labeling theorem. We have measured these predictions in a programmable grating optical setup.
9. We have shown that the mechanism of the winding in the diffraction pattern in the artificial palindrome scheme is perfectly synchronized with the violation of palindromic symmetry cycle (the \mathcal{C} -harmonic of the cycle). Specifically, at

ϕ values where the structure is a palindrome the diffraction pattern is identical to that of a single chain.

10. We have uncovered a combination of diffraction amplitude phases sensitive to the symmetry of the chain. This combined phase has an integer winding as a function of ϕ for the spatial frequency values of the diffraction peaks. The winding numbers of this phase for each peak is $2\mathcal{C}$. For the Fibonacci case, each Chern number \mathcal{C} was verified against the prediction of the gap labeling theorem. This winding is a much more sensitive probe of the Chern numbers than the diffraction pattern method. We have shown that the mechanism of the winding of this diffraction amplitude phase combination is perfectly synchronized with the violation of palindromic symmetry cycle (the \mathcal{C} -harmonic of the cycle).
11. We have discovered a way to describe the quasiperiodic Fibonacci chain as a function of its translational degree of freedom (controlled by ϕ) so that it forms a perfect torus, leading to a toroidal reciprocal space, namely the quasi-Brillouin zone.
12. Using the quasi-Brillouin zone for a finite chain, we provide new expressions for the amount of available Chern numbers (which are exact), and the deviation of the spectral gaps/diffraction peaks/integrated density of modes at the gaps from the infinite chain values.
13. We then demonstrate a single-shot measurement recording the entire quasi-Brillouin zone with all available Chern numbers in a programmable grating optical setup.
14. We present an explanation and new expressions for the relevance of the natural Fibonacci lengths to our results.
15. We have shown the staircase by which topological boundary modes traverse the gaps is governed by the phason-flips. The distribution of heights of the stairs is contrast dependent. A contrast dependent exponential relation exists between the distance of the structural event from the relevant boundary and the height of the relevant step. This means that in the fully closed structure, a phason flip with strong effect on the right edge state, will have a minimal effect on the left one.

5.3 Outlook

5.3.1 Structural and spectral understanding of aperiodic order.

The current work has set up many new tools to analyze quasiperiodic chains. Some tools rely on substitution rules, and some require a C&P or characteristic degree of

freedom. However there are many C&P structures where no corresponding substitution description is known. Perhaps some of the tools described here may help to find the Chern numbers in another way, such as windings of measurable quantities. On the other hand, there is a large family of quasiperiodic substitutions for which a C&P description does not exist, and maybe a new translational degree of freedom is required. Furthermore, the spectra of quasiperiodic chains have a rich topology concerning the infinite number of spectral gaps on one hand and is a multifractal on the other. Effort should be focused in understanding of the relation between fractality and topology.

The role of potential or dielectric contrast in the exponential coupling modes should be formulated in the most general form.

5.3.2 The effective Fabry-Perot model

Being do generic, our model constituted a new bridge between the cavity community and the topological edge state community. Effort should be focused on projecting the knowledge base in one community to the other. A promising such projection may be topological Casimir physics.

5.3.3 Generalizations

In the current work, many generalizations have been presented, but the generalization effort is far from complete. The entire field of possible generalizations is to be explored, including generalization to higher dimension quasiperiodic structures. In the same sense, a more formal treatment is required regarding the smooth transition between the limited Aubry-Andre-Harper model and the rich behavior of the corresponding C&P structure.

5.3.4 What about p ?

In the Fibonacci example, we have shown the integer q to be the important Chern number which manifests as a winding of phases/edge states/diffraction peak intensity. $p(q)$ was given a more co-numbering-like meaning, determining only the winding in the k direction. Is there another scheme for which p is the important Chern number? Or to generalize the question, in the case of a gap labeling expression with many integers, which if they control the winding?

5.3.5 Is the palindromic cycle necessary?

Chern numbers exist in the labels of spectral gaps or diffraction peaks for any substitution structure. No translational degree of freedom is required, along with the resulting palindromic symmetry cycle. Even in the cases where the modulation phase ϕ is defined, the “topological map” method does not require any knowledge

of palindromic symmetry as a function of ϕ . On the other hand, it seems that in all cases where an actual winding measurement of a Chern number is to be obtained, the palindromic values serve as a natural origin “resetting” all windings. Secondly, it seems that the π -periodicity of the palindromic cycle governs the relation between winding and Chern number by adding a factor of 2. These aspects should be more carefully analyzed.

Bibliography

- [AA80] Serge Aubry and Gilles André. Analyticity breaking and Anderson localization in incommensurate lattices. *Ann. Israel Phys. Soc.*, 3(133):37, 1980.
- [AB85] Y Avishai and Y B Band. One-dimensional density of states and the phase of the transmission amplitude. *Phys. Rev. B*, 32(4):2674–2676, 1985.
- [AC03] Eudenilson L Albuquerque and Michael G Cottam. Theory of elementary excitations in quasiperiodic structures. *Physics Reports*, 376(4):225–337, 2003.
- [ADL13] E Akkermans, G Dunne, and E Levy. Wave propagation in one-dimension: Methods and applications to complex and fractal structures. In Luca Dal Negro, editor, *Optics of Aperiodic Structures: Fundamentals and Device Applications*, chapter 10. Pan Stanford, 2013.
- [AG13] Eric Akkermans and Evgeni Gurevich. Spontaneous emission from a fractal vacuum. *EPL (Europhysics Letters)*, 103(3):30009, 2013.
- [AM07] E Akkermans and G Montambaux. *Mesoscopic Physics of Electrons and Photons*. Cambridge University Press, 2007.
- [And58] P W Anderson. Absence of Diffusion in Certain Random Lattices. *Phys. Rev.*, 109(5):1492–1505, 1958.
- [AOS03] Joseph E. Avron, Daniel Osadchy, and Ruedi Seiler. A topological look at the Quantum Hall effect. *Physics Today*, 56(8):38–42, aug 2003.
- [ARS09] Ehab Abdel-Rahman and Amr Shaarawi. Defect mode in periodic and quasiperiodic one-dimensional photonic structures. *Journal of Materials Science: Materials in Electronics*, 20(1):153–158, 2009.
- [AS84] M F Atiyah and I M Singer. Dirac operators coupled to vector potentials. *Proceedings of the National Academy of Sciences*, 81(8):2597–2600, 1984.

- [AYP04] Eiji Abe, Yanfa Yan, and Stephen J Pennycook. Quasicrystals as cluster aggregates. *Nat Mater*, 3(11):759–767, nov 2004.
- [Bab16] Akkermans E. Baboux F. , Levy E., Bloch J. (in preparation). 2016.
- [Bel82] Jean Bellissard. Schrödinger operators with almost periodic potential: An overview. In *Mathematical problems in theoretical physics*, pages 356–363. Springer, 1982.
- [Bel92] Jean Bellissard. Gap labelling theorems for Schrödinger operators. In *From number theory to physics*, pages 538–630. Springer, 1992.
- [BG13] Michael Baake and Uwe Grimm. *Aperiodic order*, volume 1. Cambridge University Press, 2013.
- [BRS16] Miguel A Bandres, Mikael C Rechtsman, and Mordechai Segev. Topological Photonic Quasicrystals: Fractal Topological Spectrum and Protected Transport. *Phys. Rev. X*, 6(1):11016, 2016.
- [BV12] Petarpa Boonserm and Matt Visser. One dimensional scattering problems: A pedagogical presentation of the relationship between reflection and transmission amplitudes. *Thai Journal of Mathematics*, 8(4):83–97, 2012.
- [BW00] Max Born and Emil Wolf. *Principles of optics: electromagnetic theory of propagation, interference and diffraction of light*. CUP Archive, 2000.
- [Cao05] Hui Cao. Review on latest developments in random lasers with coherent feedback. *Journal of Physics A: Mathematical and General*, 38(49):10497–10535, dec 2005.
- [CGP⁺09] A H Castro Neto, F Guinea, N M R Peres, K S Novoselov, and A K Geim. The electronic properties of graphene. *Rev. Mod. Phys.*, 81(1):109–162, 2009.
- [Dan14] Itzhack Dana. Topologically universal spectral hierarchies of quasiperiodic systems. *Phys. Rev. B*, 89(20):205111, 2014.
- [Dar16] Beugnon J. Dureau A., Levy E., Akkermans E., Gerbier F. (submitted to *Science*). 2016.
- [dB81] N.G. de Bruijn. Sequences of zeros and ones generated by special production rules. *Indagationes Mathematicae (Proceedings)*, 84(1):27–37, 1981.
- [DB12] L. Dal Negro and S.V. Boriskina. Deterministic aperiodic nanostructures for photonics and plasmonics applications. *Laser & Photonics Reviews*, 6(2):178–218, apr 2012.

- [DG11] David Damanik and Anton Gorodetski. Spectral and Quantum Dynamical Properties of the Weakly Coupled Fibonacci Hamiltonian. *Communications in Mathematical Physics*, 305(1):221–277, 2011.
- [DGJÖ11] Jean Dalibard, Fabrice Gerbier, Gediminas Juzeliunas, and Patrik Öhberg. Colloquium : Artificial gauge potentials for neutral atoms. *Rev. Mod. Phys.*, 83(4):1523–1543, 2011.
- [DK85] Michel Duneau and Andre André Katz. Quasiperiodic patterns. *Physical Review Letters*, 54(25):2688, 1985.
- [DP99] Xavier Droubay and Giuseppe Pirillo. Palindromes and Sturmian words. *Theoretical Computer Science*, 223(1–2):73–85, 1999.
- [EAE⁺06] Y. El Hassouani, H. Aynaou, E. El Boudouti, B. Djafari-Rouhani, A. Akjouj, and V. Velasco. Surface electromagnetic waves in Fibonacci superlattices: Theoretical and experimental results. *Physical Review B*, 74(3):035314, jul 2006.
- [EGDMR11] J. Escorcia-García, C.a. Duque, and M.E. Mora-Ramos. Optical properties of hybrid periodic/quasiregular dielectric multilayers. *Superlattices and Microstructures*, 49(3):203–208, mar 2011.
- [EH82] Paul Erdős and R C Herndon. Theories of electrons in one-dimensional disordered systems. *Advances in Physics*, 31(2):65–163, 1982.
- [Els86] Veit Elser. The diffraction pattern of projected structures. *Acta Crystallographica Section A: Foundations of Crystallography*, 42(1):36–43, 1986.
- [EPB05] S. Enoch, E. Popov, and N. Bonod. Analysis of the physical origin of surface modes on finite-size photonic crystals. *Physical Review B*, 72(15):155101, oct 2005.
- [FHA12] I C Fulga, F Hassler, and A R Akhmerov. Scattering theory of topological insulators and superconductors. *Phys. Rev. B*, 85(16):165409, 2012.
- [Fib] Leonardo Fibonacci. *Liber Abaci* (1202). Tre scritti inediti di Leonardo Pisano, 1.
- [Gay01] B Gayral. Controlling spontaneous emission dynamics in semiconductor microcavities; an experimental approach. *Ann. Phys. Fr.*, 26(1), 2001.
- [GG99] Jean-Michel Gerard and Bruno Gayral. Strong Purcell effect for InAs quantum boxes in three-dimensional solid-state microcavities. *Light-wave Technology, Journal of*, 17(11):2089–2095, 1999.

- [GG01] J M Gerard and B Gayral. InAs quantum dots: artificial atoms for solid-state cavity-quantum electrodynamics. *Physica E: Low-dimensional Systems and Nanostructures*, 9(1):131–139, 2001.
- [GJ72] David J Gross and R Jackiw. Effect of Anomalies on Quasi-Renormalizable Theories. *Phys. Rev. D*, 6(2):477–493, 1972.
- [GL92] C Godrèche and J M Luck. Indexing the diffraction spectrum of a non-Pisot self-similar structure. *Phys. Rev. B*, 45(1):176–185, 1992.
- [GO90] C Godrèche and Christophe Oguey. Construction of average lattices for quasiperiodic structures by the section method. *Journal de Physique*, 51(1):21–37, 1990.
- [GRGH83] Ph Goy, J M Raimond, M Gross, and S Haroche. Observation of cavity-enhanced single-atom spontaneous emission. *Physical review letters*, 50(24):1903, 1983.
- [Gur] Evgeni Gurevich. unpublished.
- [GV89] J-M Ghez and S Vaienti. On the wavelet analysis for multifractal sets. *Journal of Statistical Physics*, 57(1):415–420, 1989.
- [Haf14] Mohammad Hafezi. Measuring Topological Invariants in Photonic Systems. *Phys. Rev. Lett.*, 112(21):210405, 2014.
- [Har55] P G Harper. The general motion of conduction electrons in a uniform magnetic field, with application to the diamagnetism of metals. *Proceedings of the Physical Society. Section A*, 68(10):879, 1955.
- [Hat93a] Yasuhiro Hatsugai. Chern number and edge states in the integer quantum Hall effect. *Physical review letters*, 71(22):3697, 1993.
- [Hat93b] Yasuhiro Hatsugai. Edge states in the integer quantum Hall effect and the Riemann surface of the Bloch function. *Physical Review B*, 48(16):11851, 1993.
- [HG98] Xiuqing Huang and Changde Gong. Property of Fibonacci numbers and the periodiclike perfectly transparent electronic states in Fibonacci chains. *Physical Review B*, 58(2):739–744, jul 1998.
- [HJPH01] X. Huang, S. Jiang, R. Peng, and A. Hu. Perfect transmission and self-similar optical transmission spectra in symmetric Fibonacci-class multilayers. *Physical Review B*, 63(24):245104, may 2001.
- [HK10] M Z Hasan and C L Kane. Colloquium : Topological insulators. *Rev. Mod. Phys.*, 82(4):3045–3067, 2010.

- [HWG99] Xiuqing Huang, Yong Wang, and Changde Gong. Numerical investigation of light-wave localization in optical Fibonacci superlattices with symmetric internal structure. *Journal of Physics: Condensed Matter*, 11(39):7645, 1999.
- [Jan94] Christian Janot. *Quasicrystals*. Springer, 1994.
- [JJWM11] John D Joannopoulos, Steven G Johnson, Joshua N Winn, and Robert D Meade. *Photonic crystals: molding the flow of light*. Princeton university press, 2011.
- [Jol13] Timo Jolivet. *Combinatorics of Pisot Substitutions*. PhD thesis, 2013.
- [KDP80] K v Klitzing, Gerhard Dorda, and Michael Pepper. New method for high-accuracy determination of the fine-structure constant based on quantized Hall resistance. *Physical Review Letters*, 45(6):494, 1980.
- [Kes66] Harry Kesten. On a conjecture of Erdos and Szusz related to uniform distribution mod 1. *Acta Arithmetica*, 12(2):193–212, 1966.
- [KIM⁺07] Toshiyuki Komikado, Azusa Inoue, Koichi Masuda, Takashi Ando, and Shinsuke Umegaki. Multi-layered mirrors fabricated by spin-coating organic polymers. *Thin Solid Films*, 515(7):3887–3892, 2007.
- [KLR⁺12] Yaacov E. Kraus, Yoav Lahini, Zohar Ringel, Mor Verbin, and Oded Zilberberg. Topological States and Adiabatic Pumping in Quasicrystals. *Physical Review Letters*, 109(10):106402, sep 2012.
- [KM97] Anja König and N David Mermin. Electronic level degeneracy in nonsymmorphic periodic or aperiodic crystals. *Physical Review B*, 56(21):13607, 1997.
- [KM00] Anja König and N David Mermin. Symmetry, extinctions, and band sticking. *American Journal of Physics*, 68(6):525–530, 2000.
- [KMP⁺13] P. a. Kalozoumis, C. Morfonios, N. Palaiodimopoulos, F. K. Diakonou, and P. Schmelcher. Local symmetries and perfect transmission in aperiodic photonic multilayers. *Physical Review A*, 88(3):033857, sep 2013.
- [KSI87] Mahito Kohmoto, Bill Sutherland, and K Iguchi. Localization of optics: Quasiperiodic media. *Physical Review Letters*, 58(23):2436, 1987.
- [Kun86] H Kunz. Quantized currents and topological invariants for electrons in incommensurate potentials. *Physical review letters*, 57(9):1095, 1986.
- [KZ12] Yaacov E. Kraus and Oded Zilberberg. Topological Equivalence between the Fibonacci Quasicrystal and the Harper Model. *Physical Review Letters*, 109(11):116404, sep 2012.

- [LBFA15] E Levy, A Barak, A Fisher, and E Akkermans. Topological properties of Fibonacci quasicrystals: A scattering analysis of Chern numbers. arXiv preprint arXiv:1509.04028, 2015.
- [LBGS94] Nabil M Lawandy, R M Balachandran, A S L Gomes, and E Sauvain. Laser action in strongly scattering media. *Nature*, 368(6470):436–438, 1994.
- [LRG11] Netanel H Lindner, Gil Refael, and Victor Galitski. Floquet topological insulator in semiconductor quantum wells. *Nat Phys*, 7(6):490–495, jun 2011.
- [LS84] Dov Levine and Paul Joseph Steinhardt. Quasicrystals: A New Class of Ordered Structures. *Phys. Rev. Lett.*, 53(26):2477–2480, 1984.
- [LWY⁺15] Ling Lu, Zhiyu Wang, Dexin Ye, Lixin Ran, Liang Fu, John D Joannopoulos, and Marin Soljacic. Experimental observation of Weyl points. *Science*, 349(6248):622–624, aug 2015.
- [Ma06] Zhong-Qi Ma. The Levinson theorem. *Journal of Physics A: Mathematical and General*, 39(48):R625, 2006.
- [Mac06] Enrique Maciá. The role of aperiodic order in science and technology. *Reports on Progress in Physics*, 69(2):397, 2006.
- [Mer79] N D Mermin. The topological theory of defects in ordered media. *Rev. Mod. Phys.*, 51(3):591–648, 1979.
- [MM12] Alejandro J. Martínez and Mario I. Molina. Surface solitons in quasiperiodic nonlinear photonic lattices. *Physical Review A*, 85(1):013807, jan 2012.
- [MMB11] Dganit Meidan, Tobias Micklitz, and Piet W Brouwer. Topological classification of adiabatic processes. *Physical Review B*, 84(19):195410, 2011.
- [MSKD14] C. Morfonios, P. Schmelcher, P. a. Kalozoumis, and F. K. Diakonov. Local symmetry dynamics in one-dimensional aperiodic lattices: a numerical study. *Nonlinear Dynamics*, 78(1):71–91, may 2014.
- [MVA09] P.W. Mauriz, M.S. Vasconcelos, and E.L. Albuquerque. Optical transmission spectra in symmetrical Fibonacci photonic multilayers. *Physics Letters A*, 373(4):496–500, jan 2009.
- [NLR08] Gerardo G. Naumis and F.J. López-Rodríguez. The electronic spectrum of a quasiperiodic potential: From the Hofstadter butterfly to the Fibonacci chain. *Physica B: Condensed Matter*, 403(10-11):1755–1762, may 2008.

- [NN83] H.B. Nielsen and Masao Ninomiya. The Adler-Bell-Jackiw anomaly and Weyl fermions in a crystal. *Physics Letters B*, 130(6):389–396, nov 1983.
- [NTMDN09] R Nava, J Tagüeña-Martínez, J a Del Río, and G G Naumis. Perfect light transmission in Fibonacci arrays of dielectric multilayers. *Journal of physics. Condensed matter : an Institute of Physics journal*, 21(15):155901, apr 2009.
- [OP84] Stellan Ostlund and Rahul Pandit. Renormalization-group analysis of the discrete quasiperiodic Schrödinger equation. *Phys. Rev. B*, 29(3):1394–1414, 1984.
- [PDW10] Xiao-Ning Pang, Jian-Wen Dong, and He-Zhou Wang. Photonic localization of interface modes at the boundary between metal and Fibonacci quasiperiodic structure. *JOSA B*, 27(10):2009–2013, 2010.
- [PHQ⁺02] R. W. Peng, X. Q. Huang, F. Qiu, Mu Wang, A. Hu, S. S. Jiang, and M. Mazzer. Symmetry-induced perfect transmission of light waves in quasiperiodic dielectric multilayers. *Applied Physics Letters*, 80(17):3063, 2002.
- [PPH15] A V Poshakinskiy, A N Poddubny, and M Hafezi. Phase spectroscopy of topological invariants in photonic crystals. *Physical Review A*, 91(4):43830, 2015.
- [PTAV13] Siddharth A Parameswaran, Ari M Turner, Daniel P Arovas, and Ashvin Vishwanath. Topological order and absence of band insulators at integer filling in non-symmorphic crystals. *Nature Physics*, 9(5):299–303, 2013.
- [RZP⁺13] Mikael C Rechtsman, Julia M Zeuner, Yonatan Plotnik, Yaakov Lumer, Daniel Podolsky, Felix Dreisow, Stefan Nolte, Mordechai Segev, and Alexander Szameit. Photonic Floquet topological insulators. *Nature*, 496(7444):196–200, apr 2013.
- [Sam94] John David Samons. A Relationship Between the Fibonacci Sequence and Cantor’s Ternary Set. PhD thesis, University of North Florida, 1994.
- [SBGC84] D Shechtman, I Blech, D Gratias, and J W Cahn. Metallic Phase with Long-Range Orientational Order and No Translational Symmetry. *Physical Review Letters*, 53(20):1951–1953, nov 1984.
- [Sch13] Henning Schomerus. Topologically protected midgap states in complex photonic lattices. *Optics letters*, 38(11):1912–1914, jan 2013.

- [SDK⁺93] D R Smith, Rachida Dalichaouch, N Kroll, S Schultz, S L McCall, and P M Platzman. Photonic band structure and defects in one and two dimensions. *JOSA B*, 10(2):314–321, 1993.
- [Shu79] Mikhail Aleksandrovich Shubin. The spectral theory and the index of elliptic operators with almost periodic coefficients. *Russian Mathematical Surveys*, 34(2):109–157, 1979.
- [Sim82] Barry Simon. Almost periodic Schrödinger operators: A Review. *Advances in Applied Mathematics*, 3(4):463–490, dec 1982.
- [SÖ87] Paul Joseph Steinhardt and Stellan Östlund. *Physics of quasicrystals*. World Scientific, 1987.
- [SS86] Joshua E S Socolar and Paul J Steinhardt. Quasicrystals. II. Unit-cell configurations. *Phys. Rev. B*, 34(2):617–647, 1986.
- [TGB⁺14] Dimitrii Tanese, Evgeni Gurevich, Florent Baboux, Thibaut Jacqmin, Aristide Lemaître, Elisabeth Galopin, Isabelle Sagnes, Alberto Amo, Jacqueline Bloch, and Eric Akkermans. Fractal Energy Spectrum of a Polariton Gas in a Fibonacci Quasiperiodic Potential. *Physical Review Letters*, 112(14):146404, 2014.
- [TKNdN82] D J Thouless, M Kohmoto, M P Nightingale, and M den Nijs. Quantized Hall Conductance in a Two-Dimensional Periodic Potential. *Phys. Rev. Lett.*, 49(6):405–408, 1982.
- [TS09] Guillaume Tarel and Vincenzo Savona. Emission spectrum of a quantum dot embedded in a nanocavity. *Physica Status Solidi (C)*, 6(4):902–905, apr 2009.
- [Vaj07] Steven Vajda. *Fibonacci and Lucas numbers, and the golden section: theory and applications*. Courier Corporation, 2007.
- [VDML10] Aleksei P Vinogradov, Aleksandr V Dorofeenko, Aleksandr M Merzlikin, and Aleksandr a Lisyansky. Surface states in photonic crystals. *Physics-Usppekhi*, 53(3):243–256, jun 2010.
- [VGA04] Francisco Villa and J Gaspar-Armenta. Photonic crystal to photonic crystal surface modes: narrow-bandpass filters. *Optics express*, 12(11):2338–2355, 2004.
- [VM01] Julien Vidal and Rémy Mosseri. Generalized quasiperiodic Rauzy tilings. *Journal of Physics A: Mathematical and General*, 34(18):3927, 2001.

- [VZL⁺15] Mor Verbin, Oded Zilberberg, Yoav Lahini, Yaacov E Kraus, and Yaron Silberberg. Topological pumping over a photonic Fibonacci quasicrystal. *Phys. Rev. B*, 91(6):64201, 2015.
- [Wan78] G H Wannier. A Result Not Dependent on Rationality for Bloch Electrons in a Magnetic Field. *physica status solidi (b)*, 88(2):757–765, 1978.
- [XBA⁺15] Su-Yang Xu, Ilya Belopolski, Nasser Alidoust, Madhab Neupane, Guang Bian, Chenglong Zhang, Raman Sankar, Guoqing Chang, Zhujun Yuan, Chi-Cheng Lee, Shin-Ming Huang, Hao Zheng, Jie Ma, Daniel S Sanchez, BaoKai Wang, Arun Bansil, Fangcheng Chou, Pavel P Shibayev, Hsin Lin, Shuang Jia, and M Zahid Hasan. Discovery of a Weyl fermion semimetal and topological Fermi arcs. *Science*, 349(6248):613–617, aug 2015.
- [XKL⁺15] Jun Xiong, Satya K Kushwaha, Tian Liang, Jason W Krizan, Max Hirschberger, Wudi Wang, R J Cava, and N P Ong. Evidence for the chiral anomaly in the Dirac semimetal Na₃Bi. *Science*, 350(6259):413–416, 2015.
- [YLC⁺06] Jongseung Yoon, Wonmok Lee, Jean-Michel Caruge, Mounqi Bawendi, Edwin L. Thomas, Steven Kooi, and Paras N. Prasad. Defect-mode mirrorless lasing in dye-doped organic/inorganic hybrid one-dimensional photonic crystal. *Applied Physics Letters*, 88(9):091102, 2006.
- [ZD85] R K P Zia and W J Dallas. A simple derivation of quasi-crystalline spectra. *Journal of Physics A: Mathematical and General*, 18(7):L341, 1985.
- [ZFJ99] E. Zijlstra, A. Fasolino, and T. Janssen. Existence and localization of surface states on Fibonacci quasicrystals: A tight-binding study. *Physical Review B*, 59(1):302–307, jan 1999.
- [Zhu10] Sergei V. Zhukovsky. Perfect transmission and highly asymmetric light localization in photonic multilayers. *Physical Review A*, 81(5):053808, may 2010.

מחשב עבור הדוגמא של שרשראות פיבונאצ'י. מדידה זו גם כוללת ניתוח של העמידות של התופעה בפני אי-סדר מבני אקראי. בנוסף, אנו שבים למקור המבני של תיאורמת תיוג הפערים האסורים ושיאי העקיפה. אנו מראים כי מפה מרחבית דו-ממדית המתארת את היפוכי הפזון כפונקציה של ϕ הינה טורוס מושלם. תכונה זו מהווה הלכה למעשה תנאי שפה מחזוריים פנימיים למבנה הסופי כפונקציה של ϕ , ומובילים להגדרה של קוואזי-איזור-ברילואין במרחב ההופכי. כתוצאה מכך אנו מציעים ניתוח כמותי וביטויים מפורשים לכמות האפשרית של מספרי צ'רן, ולסטייה של תדירות הפערים האסורים ושיאי תמונת העקיפה מהערכים שלהם עבור השרשרת האינסופית. אנו מציגים מדידה ניסיונית ראשונה של הקוואזי-איזור-ברילואין עבור הדוגמא של שרשרת פיבונאצ'י, עם מדידה אחת ישירה של 89 מספרי צ'רן שונים. מובא גם דיון עקרוני בשאלת התפקיד של קוואזי-מחזוריות מלאה (שהינה אינסופית במהותה) בעיצוב התחזיות והמדידות שאנו מציגים, וכן בשאלת התפקיד של האורכים הטבעיים של שרשראות קוואזי-מחזוריות בעיצוב התחזיות והמדידות שאנו מציגים. העבודה הנוכחית נשענת על שרשראות פיבונאצ'י כדוגמא מובילה לשרשראות קוואזי-מחזוריות, אולם התוצאות המובאות כאן הינן ישימות לקבוצה גדולה מאד של שרשראות קוואזי-מחזוריות, וכן אנו סבורים כי ניתן יהיה להרחיב אותן גם לממדים גבוהים יותר. האופי של תוצאות העבודה הנוכחית הינו חיבור בסיסי הידע של קהילת הקוואזי גבישים (פיסיקה מתימטית) לזה של חקר התופעות הטופולוגיות במבנים סופיים (פיסיקת מצב מוצק), ולזה של פיסיקת מהודים (למשל באופטיקה), ליצירת תחום מאד אינטרדיסציפלינארי.

המגנטי. נושאי הזרם במערכת החשמלית הזו הינם מצבי קצה טופולוגיים שניטורם יכול ללמד על התכונות הטופולוגיות של התווך. בדוגמא זו, יחד גם דוגמאות פיסיקליות רבות אחרות, ניתן לזהות שדה חיצוני או סימטריה חבויה הקשורה לתכונות הטופולוגיות. בחקר התכונות הטופולוגיות של שרשראות קוואזי-מחזוריות אינסופיות לא נמצאה עדות לסימטריה כזו, והן מתקיימות ללא שדה חיצוני. במסגרת העבודה הנוכחית, לאחר ניתוח מבני של שרשראות קוואזי-מחזוריות סופיות, וכן ניתוח על ידי פיזור של גלים (שיטת מטריצת הפיזור), אנו מראים כי מספרי צ'רן המתייגים את הפערים האסורים בשרשראות קוואזי-מחזוריות אינסופיות קשורים לסימטריה חבויה בשרשראות קוואזי-מחזוריות סופיות. הסימטריה הזו הינה הסימטריה הפלינדרומית (סימטריה להיפוך) של מבנה סופי נתון. אנו מנטרים את הסטייה או ההפרה של סימטריה זו כפונקציה של דרגת חופש טרנסלציונית. הקיימת בשל סופיות המבנה ומתוארת ע"י הפרמטר ϕ הנקרא פזון, ונובע מאחת משיטות היצירה של השרשרת. פונקציית ההפרה הזו מתנהגת באופן מחזורי כפונקציה של ϕ עם תדירות כפולה בהשוואה ל- ϕ . אם נתחיל משרשרת קוואזי-מחזורית סופית ונסרוק את הפזון, נגלה כי המבנה משתנה באופן הנשלט ע"י שינויים מרחביים נקודתיים המכונים היפוכי-פזון. אם נתחיל משרשרת שהינה פלינדרום מושלם, נגלה כי היפוכי הפזון פוגעים יותר ויותר בסימטריה, ובשלב מסויים מתחילים לשפר את הסימטריה עד שהמבנה חוזר להיות פלינדרום מושלם, וחוזר חלילה עוד מחזור אחד. תיאורמת הסיווג הטופולוגי של פערים אסורים בספקטרום של שרשרת קוואזי-מחזורית נמצאה כקשורה לשתי פאזות בלתי תלויות של מטריצת הפיזור. הפאזה הראשונה היא פאזת הפיזור הכוללת, המתארת את הספקטרום של התווך הקוואזי-מחזורי, כולל ספקטרום ההעברה וספקטרום צפיפות המצבים, והיא לא רגישה לשינויים ב- ϕ . הפאזה השנייה היא פאזת הפיזור הכיראלית, הרגישה בעיקר לסימטריה של המבנה ונושאת מידע טופולוגי, היינו מספרי צ'רן, במספר הליפופים (השלם) שלה כפונקציה של ϕ . ההתנהגות של פאזת הפיזור הכיראלית הינה בהלימה מלאה להתנהגות המחזורית של פונקציית הסטייה מסימטריה פלינדרומית. תכונות אלו ניתנות למדידה נוחה יותר על ידי שימוש במצבי קצה, הנוצרים בתחומי התדירויות של הפערים האסורים בסכימה של קצה מוכלל שפיתחנו, ומבצעים בעצמם ליפוף ספקטראלי כפונקציה של ϕ הקשור ישירות למספרי צ'רן, ובכך מאפשרים לנטר את פאזת הפיזור הכיראלית. אנו מביאים כאן תיאור כמותי ונוח לקיומם של מצבי הקצה, והתדירות שלהם כפונקציה של ϕ בשפה של מהוד פברי-פרו אפקטיבי טופולוגי, בו התכונות הטופולוגיות של השרשרת מתמפות לשינויים באורך האפקטיבי של המהוד. בנושא זה, אנו מציגים מדידה ניסיונית ראשונה של התחזית הזו למספרי צ'רן במערכת של פולריטונים במהוד עבור הדוגמא של שרשראות פיבונאצ'י. ניתוח זהה בתוצאותיו לניתוח מטריצות הפיזור שלעיל, בוצע במרחב ההופכי. הסיווג הטופולוגי של שיאי תמונת העקיפה נמצאו קשורים לפאזת העקיפה הכיראלית, הנושאת אף היא את המידע הטופולוגי, היינו מספרי צ'רן, במספר הליפופים (השלם) שלה כפונקציה של ϕ . גם כאן, התנהגות פאזת העקיפה הכיראלית הינה בהלימה מלאה להתנהגות המחזורית של הסטייה מסימטריה פלינדרומית. תופעה של פיצול שיאי תמונת העקיפה במבנה המותאם לסכימת הקצה המוכלל מבצעת אף היא ליפוף על פני התדרים המרחביים כפונקציה של ϕ הקשור ישירות למספרי צ'רן, ובכך מאפשרת לנטר את פאזת העקיפה הכיראלית. בנושא זה, אנו מביאים כאן מדידה ניסיונית ראשונה של התופעה ושל מספרי צ'רן במערכת מדידה של שריג עקיפה אופטי מבוקר

תקציר

שרשראות קוואזי-מחזוריות הינן מבנים חד-ממדיים שאינם מחזוריים ואינם אקראיים. אלא נבנים על ידי כללי יצירה דטרמיניסטיים שאינם מחזוריים. דוגמא מפורסמת לשרשרת כזו הינה שרשרת פיבונאצ'י שניתן לייצר אותה בשיטות איטרטיביות. ליצירת שרשרת פיבונאצ'י, נתחיל מאלפבית של שתי אותיות, "א" ו-"ב", שיכולות ליצג שני ערכים מובחנים של פוטנציאל, מקדם שבירה, צפיפות או כל תכונה פיסיקלית אחרת. נתחיל מהדור ה-0 שמוגדר להיות "ב", והדור ה-1 שמוגדר להיות "א". החל מהדור השלישי של השרשרת, כל דור מורכב מן ההלחם של שני הדורות הקודמים כך שהדורות 2 עד 6 המתקבלים הם: "אב", "אבא", "אבאאב", "אבאאבא", ו-"אבאאבאאבאאב" בהתאמה. לשרשראות קוואזי-מחזוריות כמו שרשרת פיבונאצ'י, תכונות ספקטראליות לא טריוויאליות. הספקטרום של שרשראות אלה הינו רציף-נקודתי המכיל מספר אינסופי של פערים אסורים המסודרים במבנה מולטי-פרקטלי עם דמיון עצמי, ותכונות טופולוגיות ידועות. חקר התכונות הטופולוגיות של מבנים הינו כלי ניתוחי חזק במתימטיקה וגם בפיסיקה בהיותו הכללה של סיווג מבנים לפי קבוצות הסימטריה שלהם. טופולוגיה מאפשרת לזהות קבוצות מובחנות של מבנים כך שלא ניתן לעבור מקבוצה לקבוצה על ידי עיוות מרחבי רציף. המאפיין הטופולוגי של כל קבוצה ניתן על ידי מספרים שלמים שנקראים אינווריאנטים טופולוגיים. דוגמא מפורסמת לחלוקה כזו היא סיווג גאוס של משטחים תלת ממדיים. במקרה הזה האינווריאנט הטופולוגי הוא בקירוב מספר החורים המנקבים את המבנה. כך ספירה עם אפס חורים לא יכולה להפוך בתהליך רציף לטורוס שיש בו חור אחד, וכו'. במחקר זה אנו שבים לענף המחקר העוסק בתכונות הטופולוגיות של שרשראות קוואזי-מחזוריות. כבר משנות השמונים של המאה העשרים, ידוע כי מספרי צ'רן (שלמים) שהינם אינווריאנטים טופולוגיים, קיימים בשרשראות קוואזי מחזוריות. המספרים הללו הינם חלק מתיאורמה המתייגת את המספר האינסופי של הפערים האסורים בספקטרום, ושל שיאי תמונת העקיפה (ספקטרום פורייה) בשרשראות קוואזי-מחזוריות אינסופיות. בדוגמא של שרשרת פיבונאצ'י אינסופית, התיאורמה מתייגת את צפיפות המצבים האינטגרלית $\mathcal{N}(\epsilon)$ בתדרים המתאימים לפער אסור כלשהו ϵ_{gap} . על ידי הנוסחה $N(\epsilon_{gap}) = p + q/\tau$, כאשר p, q הם מספרים שלמים מסוג מספרי צ'רן. מספרי צ'רן, כאמור, משמשים לרוב בניתוח של תכונות מתימטיות ופיסיקליות. דוגמא פיסיקלית מוכרת היא אפקט הול הקוונטי, עבור מבנה מוליך למחצה דו ממדי בשדה מגנטי. בבעיה הפיסיקלית הזו מוליכות הול מתקיימת בערכים בדידים שהם מכפלה של יחידת מוליכות בסיסית במספר שלם. המספר השלם הזה, הינו מספר צ'רן המתאר את התכונות הטופולוגיות של רמות האנרגיה האלקטרוניות המלאות כפונקציה של השדה

המחקר בוצע בהנחייתם של פרופ' אריק אקרמן וד"ר אמנון פישר, בפקולטה לפיסיקה

רשימת פרסומים

חלק מן התוצאות בחיבור זה פורסמו כמאמרים מאת המחבר ושותפיו למחקר בכנסים ובכתבי-עת במהלך תקופת מחקר הדוקטורט של המחבר, אשר גרסאותיהם העדכניות ביותר הינן:

- [1] א. אקרמן, ג'. דן, ואלי לוי. ראה מידע באנגלית.
- [2] א. לוי, א. ברק, א. פישר, וא. אקרמן. ראה מידע באנגלית.
- [3] פ. בבו, א. לוי, א. למטיר, א. גלופין, י. סגנס, ל. לה-גרטיה, א. אמו, ז'. בלוך, וא. אקרמן. ראה מידע באנגלית.
- [4] א. דריו, א. לוי, מ. בוש-אגילרה, ר. בוגן, א. אקרמן, פ. גרבייה, ונ' בוניון. ראה מידע באנגלית.

תודות

תודותי נתונות
לאריק אקרמן, על דוגמה מופתית של ביצוע מחקר עיוני יסודי ודבקות בקידום משמעותי של הידע.
לאמנון פישר על התמיכה והעידוד בתקופות הלא קלות אדמיניסטרטיבית ומדעית.
לשימרת על שהייתה שותפה לדרך והעניקה לי תמיכה בלתי מתפשרת מאז הייתה בת זוגי כשיצאתי לדרך, ועד היום כשהיא אשתי ואם ילדיי מעיין ונילעד.

אני מודה לטכניון על התמיכה הכספית הנדיבה בהשתלמותי.

תכונות טופולוגיות של שרשראות קוואזי מחזוריות: ניתוח מבני וספקטראלי

חיבור על מחקר

לשם מילוי חלקי של הדרישות לקבלת התואר
דוקטור לפילוסופיה

אלי לוי

הוגש לסנט הטכניון — מכון טכנולוגי לישראל
סיוון תשע"ו חיפה יוני 2016

תכונות טופולוגיות של שרשראות
קוואזי מחזוריות: ניתוח מבני
וספקטראלי

אלי לוי